

Investigation of Practical Flight Control Systems for Small Aircraft

Wouter Falkena



Investigation of Practical Flight Control Systems for Small Aircraft

W. Falkena

Cover photo © 2012 by Mr. Pfaffstaller, Diamond Aircraft Industries GmbH.

Printed by Wöhrmann Print Service, Zutphen, The Netherlands.

Typeset by the author with the \LaTeX Document System.

Copyright © 2012 by W. Falkena. All rights reserved. No part of the material protected by this copyright notice may be reproduced or utilized in any form or by any means, electronic or mechanical, including photocopying, recording or by any information storage and retrieval system, without prior permission of the author.

Investigation of Practical Flight Control Systems for Small Aircraft

PROEFSCHRIFT

ter verkrijging van de graad van doctor
aan de Technische Universiteit Delft,
op gezag van de Rector Magnificus prof. ir. K. C. A. M. Luyben,
voorzitter van het College voor Promoties,
in het openbaar te verdedigen op maandag 17 december 2012 om 12:30 uur
door

Wouter FALKENA

ingenieur luchtvaart- en ruimtevaart
geboren te Leek.

Dit proefschrift is goedgekeurd door de promotor:

Prof. dr. ir. J. A. Mulder

Copromotor:

Dr. Q. P. Chu

Samenstelling promotiecommissie:

Rector Magnificus	voorzitter
Prof. dr. ir. J. A. Mulder	Technische Universiteit Delft, promotor
Dr. Q. P. Chu	Technische Universiteit Delft, copromotor
Prof. dr. ir. M. Verhaegen	Technische Universiteit Delft
Prof. Dr.-Ing. R. Luckner	Technische Universität Berlin
Prof. Dr.-Ing. F. Holzapfel	Technische Universität München
Prof. Dr.-Ing. R. Reichel	Universität Stuttgart
Dr. ir. G. Looye	Deutsches Zentrum für Luft- und Raumfahrt
Prof. dr. E. K. A. Gill	Technische Universiteit Delft, reservelid

Dr. ir. C. Borst heeft als begeleider in belangrijke mate aan de totstandkoming van het proefschrift bijgedragen.



Dit proefschrift is mede mogelijk gemaakt door de financiële ondersteuning van het Europese zevende kaderprogramma project SAFAR.

ISBN 978-94-6203-258-3

*To Ester,
my love, my life, my wife*

SUMMARY

Investigation of Practical Flight Control Systems for Small Aircraft

Wouter Falkena

In the future airspace, a growth in small aircraft movements is to be expected according to the US Small Aircraft Transportation System (SATS) and the European Personal Air Transportation System (EPATS) programs. The main reason for this growth is due to an increasing demand for people to access more communities in less time. With the introduction of improved and cost-efficient technologies, it is even expected to become an attractive alternative to road transportation. In the general aviation segment, however, fatal and non-fatal accidents are not rare. Currently, an average number of seven accidents per 100,000 flight hours dominates this segment. As this market is expected to grow significantly in future years, measures must be taken to guide this growth in a safe manner.

By looking more closely at accident analyses, frequent causes can be traced back to poor aircraft handling (72%) and pilot decision-making errors (36%). Simultaneously performing the tasks of aircraft handling, navigation, communication, and planning can be rather difficult, especially for less-experienced pilots. In terms of aircraft handling, misjudging the coupling of aircraft states, such as the additional pitching and yawing motion that occur when the aircraft starts to roll, and the effects of external disturbances can put pilots in unsafe regions of the flight envelope. In terms of decision-making, ambiguous and conflicting information from the airborne systems can result in poor pilot “situation awareness” and decision-making. To resolve these issues, control augmentation techniques can be used to create easy and safe aircraft handling characteristics and new ways of using and presenting information on flight displays can be explored to improve “situation awareness” and decision-making. This thesis, however, only deals with improving flight safety and easy aircraft handling.

Commercial aviation has a long history in using control systems to shape ideal aircraft responses. To increase safety, modern commercial aircraft, such as a Boeing 777 and an Airbus A380, are also equipped with a Flight Envelope Protection (FEP) system to protect for stall, exceeding over-speed, limit angle of attack and load factors. This has greatly reduced the number of handling and control accidents in the commercial aviation sector. However, simply downscaling these advanced Fly-By-Wire (FBW) platforms for general aviation aircraft is not an option as it would significantly increase the cost of such an aircraft. In the “Small Aircraft Future Avionics Architecture” (SAFAR) program, an ongoing European project, a low cost FBW platform will be developed for small aircraft by using a “Flexible Avionics Platform Approach”. This approach allows for potential cost savings, but also introduces a unique environment for the FCLs. In this environment, FCL designs are needed that have robustness against model uncertainties, sensor bias, sensor noise and time delays, while being fast and accurate enough to accommodate the relatively agile dynamics of a small aircraft. These FCL designs should also be usable in the near future to support the safe growth of the general aviation market. FCL designs that meet these requirements are called practical FCL designs in this thesis. To improve cost effectiveness of such designs, it is beneficial to allow the FCLs to be transferred easily to other small airplanes, ideally without any modification.

With the use of FEP, flying the aircraft can be made more safe. It does not make flying easier, however. Rate-Command/Attitude-Hold decouples the flight controls, thereby simplifying flying the aircraft, it rejects turbulence and is a proven concept, used at low speeds in the Airbus A320/330 and 340. Therefore this manual control mode is selected as one of the modes for which FCL designs are created in this thesis. A second, automatic 4D trajectory following mode (NAV mode) is used for FCL designs in this thesis as well. However, the emphasis lies on the manual mode, since an easy handling FCL remains essential in case of an emergency and for the fun of manual flying.

Based on a dynamic model of a Diamond DA 42 and a description of the dynamic properties of the FBW platform, two different FCL designs for each mode have been synthesized and analyzed in this thesis. The first design uses classical control theory, more specifically, loop shaping with focus on tracking performance, disturbance rejection and noise attenuation. Gain selection of this FCL is done using the combination of a rough pattern search method and a trust-region-reflective method. The second FCL design uses a newly developed nonlinear design method, based on backstepping, singular perturbation theory and approximate dynamic inversion. This method, called Sensor-Based Backstepping (SBB), uses no dynamic model information and relies solely on measurements. Both FCL designs have been

compared on sensitivity to parametric uncertainty, sensor noise, disturbances, time delays, Handling Qualities (HQs), performance metrics for automatic FCLs, design effort, certifiably and possibility to add FEP.

The influence of parametric uncertainties is tested by applying both FCL designs, without adaptation of the gains, to the airplane model of a fully different aircraft, a Cessna Citation II. Performance of the classical controller in this scenario is not bad, but the response does show oscillations. Performance of the SBB controller remains excellent and this design can therefore be seen as a first step towards a plug-and-play type of FCL. Noise attenuation and disturbance rejection are specifically taken into account while designing the classical controller. It is therefore no surprise that the classical FCL performs slightly better than the SBB controller in this regard. In the presence of worst case time delays caused by the FBW platform components, both FCL designs suffer in performance, but re-tuning the SBB controller is considerable easier. HQs are satisfactory for both designs, but differ in short period and aperiodic roll damping. The classical design is tuned to be fast and under-damped and the SBB design is inherently over-damped. Performance of the NAV mode is highly comparable for both FCL designs and is therefore not helpful in the selection of the FCL design method. Design effort in terms of gain tuning is easier for the SBB design as compared with the PID design and vice versa for certification effort.

In the scope of this thesis, SBB is selected as the preferred FCL design. This method produces good aircraft responses as long as the system is minimum phase, controllable and sufficiently time-scale separated. Further research is needed for a more scientific way of selecting the controller gains and pilot-in-the-loop simulations should show whether a less-experienced general aviation pilot appreciates and accepts the changes in dynamic behavior introduced by installing the FBW platform with FCLs on the aircraft.

CONTENTS

Summary	vii
Contents	x
1 Introduction	1
1.1 Research Context	1
1.2 Research Question and Approach	3
1.3 Thesis Outline	6
2 Aircraft Model Development	9
2.1 Introduction	10
2.2 Aircraft Dynamics	10
2.2.1 Reference Frames	10
2.2.2 Equations of Motion	11
2.3 Model Based Forces and Moments Description	13
2.3.1 Weight Model	14
2.3.2 Environment Model	15
2.3.3 Propulsion Model	18
2.4 Aerodynamic Model	19
2.4.1 Model Parameters	20
2.4.2 Model Validation	21
2.5 Conclusions	22
3 Influence of an Affordable Fly-by-wire Platform	25
3.1 Introduction	26
3.2 Platform Components	27
3.2.1 Stick and Throttle	28
3.2.2 Actuators	28
3.2.3 Engine Control Unit	30
3.2.4 Measurement Devices	31
3.2.5 Core Processing Module	35

3.2.6	Input Output Modules	36
3.3	Platform Delays	36
3.4	SAFAR Platform and Simulator Operation	37
3.5	Certification	37
3.6	Conclusions	41
4	Classical Flight Control Design	43
4.1	Introduction	44
4.2	Control Modes	44
4.2.1	Stability Augmentation	44
4.2.2	Control Augmentation	46
4.2.3	Cost of Automation	50
4.3	Performance Metrics	51
4.3.1	Performance Metrics for Manually Controlled FCLs	51
4.3.2	Performance Metrics for Automatic FCLs	55
4.4	Performance of the Unaugmented System	58
4.5	Robustness and Stability Metrics	60
4.5.1	Influence of Disturbances	63
4.5.2	Influence of System Uncertainties	65
4.5.3	Influence of Measurement Noise	66
4.5.4	Influence of Time-delays	67
4.6	Flight Control Law Design	70
4.6.1	Observability and Controllability	70
4.6.2	SAFAR Control Modes	72
4.6.3	SISO Design	74
4.6.4	MIMO Design	82
4.6.5	Handling Quality Evaluation of the ATT Law	83
4.6.6	Performance Evaluation of the NAV Law	87
4.6.7	Nonlinear Simulations	88
4.7	Conclusions and Recommendations	88
5	Nonlinear Flight Control Design	93
5.1	Introduction	94
5.2	Mathematical Notations	94
5.3	Performance Metrics	95
5.3.1	Performance Metrics for Manually Controlled FCLs	95
5.3.2	Performance Metrics for Automatic FCLs	95
5.4	Robustness Metrics	96
5.4.1	Lyapunov Stability	96
5.4.2	Disturbance Rejection	100

5.4.3	Noise Attenuation	101
5.4.4	Time-Delay Margin	101
5.5	Design Options	105
5.6	Nonlinear Flight Control Law Design	106
5.6.1	Backstepping	106
5.6.2	Backstepping and Singular Perturbation Theory	111
5.6.3	Backstepping with Taylor Series Expansions	130
5.6.4	Application to the DA 42 ATT Law	140
5.6.5	Application to the DA 42 NAV Law	147
5.6.6	Handling Quality Evaluation	151
5.6.7	Performance Evaluation of the NAV Law	155
5.7	Conclusions and Recommendations	157
6	Investigation of Practical FEP Systems for Small Aircraft	159
6.1	Introduction	160
6.2	Review of Flight Envelope Protection Strategies	160
6.2.1	Safe Flight Envelope Definition	160
6.2.2	Flight Envelope Protection	161
6.2.3	Pilot Authority at the Boundary	168
6.3	Aircraft Model Requirements	168
6.3.1	Importance of Modeling Nonlinearities	168
6.3.2	Mapping Functions and Aircraft Model Fidelity	169
6.4	Test Case Definition	170
6.4.1	Method	170
6.4.2	Flight Envelope Protection Strategies	173
6.4.3	Results	176
6.5	Discussion	176
6.5.1	Performance	176
6.5.2	Sensitivity to Parametric Uncertainty	177
6.5.3	Sensitivity to Sensor Noise and Bias	177
6.5.4	Sensitivity to Time Delays	178
6.5.5	Sensitivity to Wind Gusts and Turbulence	178
6.5.6	Implications for Small Aircraft	178
6.5.7	Scope of the Test Case	179
6.5.8	Future Investigations	179
6.6	Conclusions	180
7	Evaluation	185
7.1	Introduction	186
7.2	Offline Performance Comparison	186

7.2.1	Sensitivity to Parametric Uncertainty	187
7.2.2	Sensitivity to Sensor Noise and Bias	187
7.2.3	Sensitivity to Time Delays	187
7.2.4	Sensitivity to Wind Gusts and Turbulence	192
7.2.5	Handling Qualities	192
7.2.6	Performance Evaluation of the NAV Law	197
7.2.7	Design Effort	197
7.2.8	Certiability	200
7.2.9	Fault Tolerance	200
7.3	Exploratory Acceptance Study	201
7.3.1	Method	204
7.3.2	Flight Scenarios	207
7.3.3	Results and Discussion	207
7.4	Conclusions	215
8	Conclusions and Recommendations	217
8.1	Thesis Scope	217
8.2	Classical Flight Control Design	218
8.3	Nonlinear Flight Control Design	219
8.4	Addition of Flight Envelope Protection	220
8.5	Comparison of the Flight Control Designs	220
8.6	The Best Selection of a Practical FCL for Small Airplanes	221
8.7	Beyond the Scope	221
8.8	Recommendations	222
A	Rigid Body Aircraft Dynamics	225
A.1	Reference Frames	225
A.2	Equations of Motion	229
B	Parameter Determination using Flight Test Data	237
C	Aircraft Model Eigenmotions	243
D	Addition of a Landing Model	251
E	Classical Flight Control Design	255
E.1	Sideslip Compensator	255
E.2	Autothrottle	261
E.3	Pitch Rate Command/Attitude Hold Controller	264
E.4	Roll Rate Command/Attitude Hold Controller	268
E.5	3D Trajectory Following Controller	272

CONTENTS

E.6	Nonlinear Simulations using the ATT law	281
E.7	Nonlinear Simulations using the NAV law	285
F	Pilot Instructions for Simulator Trials	287
E.1	SAFAR Flight Control Law Concept	287
E.2	Objectives	288
E.3	Control Task	288
E.4	Apparatus	288
E.5	Procedure	289
	Bibliography	291
	Samenvatting	303
	Acknowledgements	307
	Curriculum Vitae	309

INTRODUCTION

1.1 Research Context

Personal air transportation utilizing general aviation aircraft is a market that is expected to grow significantly in the near future. The European Personal Air Transportation System (EPATS) program expects a growth of 93%¹ to 90,000 personal aircraft or 43 million EPATS flights in Europe in 2020 [67]. Similar growth is expected in the US by the US Small Aircraft Transportation System (SATS) program. The main reason for this growth is an increasing demand for people to access more communities in less time. With the introduction of improved and cost-efficient technologies, it is even expected to become an attractive alternative to road transportation.

In the general aviation segment, fatal and non-fatal accidents are not rare, however [90, 133]. Currently, an average number of seven accidents per 100,000 flight hours dominates this segment. For comparison, this figure is 70 times lower for the commercial aviation sector [91]. As the general aviation market is expected to grow significantly in future years, measures must be taken to guide this growth in a safe manner.

By looking more closely at accident analyses, frequent causes can be traced back to poor aircraft handling (72%) and pilot decision-making errors (36%) [90, 133].

¹The current number of personal aircraft is estimated at 46,000 using the ICAO recording of 36,100 personal aircraft in 1994 and an annual growth of 1,6%. [38]

Simultaneously performing the tasks of aircraft handling, communication, navigation, and planning can be demanding, especially for less-experienced pilots. While flying the states of the aircraft are coupled, meaning that for example an aileron deflection does not only induce a rolling motion, but also a yawing and pitching motion of the aircraft. In terms of aircraft handling, misjudging the coupling of aircraft states and the effects of external disturbances, such as wind gusts, can put pilots in unsafe regions of the flight envelope. In terms of decision-making, ambiguous and conflicting information from the airborne systems can result in poor pilot “situation awareness” and decision-making.

Safety can be increased by dealing with either cause. Control augmentation techniques can be used to create easy and safe aircraft handling characteristics [125] and new ways of using and presenting information on flight displays can be explored to improve “situation awareness” and decision-making [13, 127]. Flight Control Laws (FCLs) augment the stability and the controllability in many commercial aircraft, in order to reduce handling and control related accidents.

If FCLs are used to increase safety, a Fly-By-Wire (FBW) platform is required on-board the aircraft to facilitate the FCLs. Given the design of the aircraft, the way the aircraft responds to pilot commands can still be altered using FBW technology. The mechanical cables, pulleys and rods should then be replaced by electrical wiring and actuators. This makes it possible to include a computer, the Flight Control Computer (FCC), in the link between the pilot and the actuators connected to the control surfaces. The pilot provides commands to the FCC and the FCC translates these commands to control surface actions using the FCLs. When measurement devices, such as air-data sensors or inertial navigation systems, are connected to the FCC as well, directly or indirect through a Flight Data Computer, significant changes can be made to the way the aircraft responds to pilot commands. Improvements in aircraft stability and pilot workload become possible giving the FBW platform a clear advantage over its mechanical counterpart. To increase safety even further, modern commercial airplanes, such as a Boeing 777 and an Airbus A380, are also equipped with Flight Envelope Protection (FEP) systems to protect the airplane from going into unsafe regions of the flight envelope. Examples are automated stall protection, overspeed protection and limitation of the angle of attack and load factors.

Simply downscaling these advanced FBW platforms for general aviation airplanes is not an option as it would significantly increase the cost of such an airplane. In the Small Aircraft Future Avionics Architecture (SAFAR) program, an ongoing European project, a low cost FBW platform will be developed for small airplanes falling under the certification specification CS23, by using a “Flexible Avionics Platform Ap-

proach' [98]. The SAFAR approach allows for potential cost savings by using lower grade sensors compared with the commercial aviation systems and by using partly software- rather than hardware-based redundancy.

The SAFAR approach allows for potential cost savings, but also introduces a unique environment for the FCLs. In this environment, FCL designs are needed that have robustness against model uncertainties, sensor bias, sensor noise and time delays, while being fast and accurate enough to accommodate the relatively agile dynamics of a small aircraft. These FCL designs should also be usable in the near future to support the safe growth of the general aviation market. FCL designs that meet these requirements are called practical FCL designs in this thesis. To improve cost effectiveness of such designs, it is beneficial to allow the FCLs to be transferred easily to other small airplanes, ideally without any modification. Something that cannot be achieved using the FCL designs, based on classical control theory, that are commonly used in the commercial aviation sector.

1.2 Research Question and Approach

The main research question of this thesis can be formulated as follows:

What is the best selection of a practical flight control law for small fixed wing aircraft?

Two main options exist for FCL design. The design can be based on classical (linear) control theory or on nonlinear control theory. To answer the main research question, both options are investigated and compared in this thesis.

Many of the airplanes installed with FBW today use FCLs designed using classical control theory. An operating point is selected within the flight envelope around which a linear approximation is valid. This linearized model is then used in analysis and design tools, such as Root-Locus, Bode plots, Nyquist plots, etc., to select proper parameter values for the linear FCLs. The uncontrolled dynamic behavior of the aircraft changes throughout the flight envelope and so different linear FCLs must be designed for each region of the flight envelope. To keep adequate dynamic behavior of the controlled aircraft the gains of the FCLs should be adapted according to the different flight regimes. Gain scheduling uses scheduling variables, such as Mach number, true airspeed and altitude, to determine the current flight regime and update the gains in the FCLs accordingly. Gain scheduling is a simple nonlinear control strategy and is commonly associated with classical control theory.

The advantage of using a FCL design method based on classical control theory is that it has proven to work in practice and best practices are well documented. Moreover, classical FCL designs tend to have high functional visibility and certification authorities are used to dealing with them [95]. The drawback of this method is that tuning the FCLs is an extensive task and that gain scheduling has practical limits. The location and number of the operating points used in gain scheduling can be difficult to select. Gain values are interpolated linearly between operating points and when the system dynamics do not change linearly between these operating points, performance degradation may follow. Therefore, the spacing of the grid of operating points should be small enough, such that the transitions between the operating points are well defined and the rate of change in dynamic behavior is slow enough (quasi-linear behavior). However, a small grid spacing requires the development of more linear FCLs and is therefore more time consuming. Near the flight envelope limits, where most nonlinearities are present, or in case of a failure (e.g., actuator hard-over, engine out, structural damage, etc.), the number of scheduling variables and operating points increases dramatically up-to a point of impracticality.

In recent decades FCL design methods based on nonlinear control theory have gained in popularity in both academia and industry. Control methods such as, adaptive control, model-based predictive control, control using Lyapunov-analysis, and (recursive) linearizing control, are investigated to simplify implementation, improve closed-loop performance and to be fault-tolerant. Improved performance in this context means the ability to follow the reference signal more closely, or to decrease the control energy required to reach the reference values. However, different drawbacks of the different nonlinear control theories have prevented a shift in FCL design philosophy for modern commercial airplanes, such as the use of potentially numerically unstable matrix manipulations, lack of generating predictable output, decreased functional visibility and increased certification effort as compared with the classical FCL designs.

When designing the FCLs for a specific general aviation airplane, the use of classical control theory is arguably the best approach. Simpler certification then outweighs the drawback of extensive tuning. However, when designing the FCLs for personal air transportation systems in general, a FCL design based on nonlinear control theory with simpler tuning, or even no tuning at all, could outweigh the additional risk and cost of more elaborate certification.

To answer the main research question several objectives can be defined:

- Determine the basic (uncontrolled) dynamic behavior of the small aircraft selected as the testbed in the SAFAR project. In order to improve the dynamic behavior of a small aircraft using FCLs, first an accurate description is needed of the current behavior.
- Determine the influence of affordable FBW on designing a FCL. Making FBW affordable constraints the hardware selection and development procedures. The influence of the FBW components on the dynamic behavior of the system that is controlled by the FCLs should be investigated.
- Develop a FCL using classical control theory. A baseline FCL should be implemented that can be compared with subsequent nonlinear FCL designs.
- Develop a FCL using nonlinear control theories, while keeping the possibility of certification in mind. This requirement is essential for a FCL design, that is commercially applicable in the near future.
- Investigate a practical way to implement FEP for a small airplane. Since FEP is used to increase safety, the FCL designs are required to be extendable with a FEP system.
- Evaluate the classical and nonlinear FCL design options with offline and pilot-in-the-loop simulations.

The originality of this thesis shows in two ways. First, in the sense that FCLs currently do not exist for personal air transportation systems utilizing small aircraft with FBW technology. Affordable FBW comes with unique characteristics implying the need for a FCL design different from those used in commercial aviation, military aviation or unmanned aerial vehicles. The thesis is also original in the sense that the nonlinear control theory used, sensor-based backstepping, is a newly developed method. Due to the lack of adaptation and the inherent Lyapunov stability properties, this method could allow certification of advanced FCL concepts.

The results presented in this thesis contribute to work package deliverables D3.3A and D4.2A of the SAFAR project, resulted in two papers in the journal of Guidance, Control, and Dynamics of the American Institute of Aeronautics and Astronautics (AIAA), titled “Investigation of Practical Flight Envelope Protection Systems for Small Aircraft” [33] and “Sensor-Based-Backstepping” [Accepted for publication, 35], and have been presented at SAFAR meetings and at the AIAA Guidance, Navigation, and Control conferences in Toronto 2010 [34] and Portland 2011 [36].

1.3 Thesis Outline

From the objectives listed in the previous section, an outline for this thesis can be defined. Figure 1.1 shows this outline schematically.

Chapter 2 captures the current aircraft dynamic behavior in a modular six-degrees-of-freedom mathematical model. The goal of designing a FCL is to change the dynamic behavior of the aircraft. Before this behavior can be changed, first an accurate description of the unaugmented situation is needed.

Chapter 3 investigates the influence of the FBW platform on the FCL design. The FCLs are run on a FBW platform, and using an affordable FBW has impact on the FCL design. Therefore, Chapters 2 and 3 can be seen as the description of the environment in which the FCL designs of Chapters 4, 5 and 6 have to operate.

Chapter 4 designs the FCLs using classical control theory. The aircraft model from Chapter 2 and the FBW platform from Chapter 3 are used in this design. With the inclusion of this FCL design in this thesis, a baseline is created for the nonlinear FCL designs documented in Chapter 5.

Chapter 5 designs the FCLs using nonlinear control theory. Again, the aircraft model from Chapter 2 and the FBW platform from Chapter 3 are used in this design. The focus in this chapter lies on an advanced control strategy, while keeping certification in mind.

Chapter 6 extends the FCLs designed in Chapters 4 and 5 with FEP. FEP is used in modern commercial aircraft and can help also less- experienced pilots to maneuver “care free”.

Chapter 7 evaluates the different control strategies using offline as well as pilot-in-the-loop simulations. This latter evaluation is done using the SIMONA Research Simulator of the Faculty of Aerospace Engineering.

Chapter 8 provides the conclusions and recommendations.

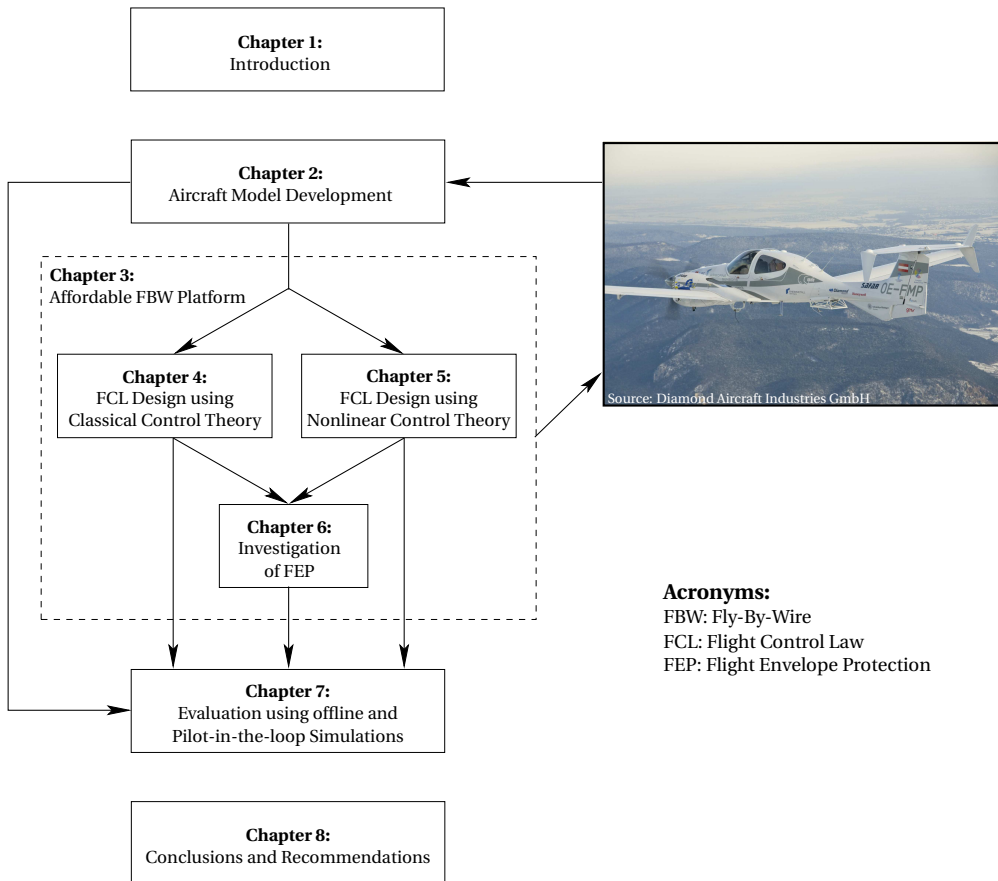


Figure 1.1: Thesis outline.

AIRCRAFT MODEL DEVELOPMENT

Abstract

This chapter introduces the dynamical aircraft model used for the flight control law design throughout the remainder of this thesis. A set of reference frames is presented to define the dynamic behavior of the aircraft and the equations of motion are used to determine this behavior. Forces and moments from different sources are described and included in a modular way. The dynamic aircraft model is validated by visual comparison to the Qualification Test Guide provided by Diamond Simulation GmbH. Due to the limited availability of validation data, the model is only usable in cruise condition for the design of the flight control laws and the control laws need to be robust to model uncertainties.

2.1 Introduction

Flight control software is used to change the dynamic behavior of an aircraft as seen from the pilot's perspective. Before this behavior can be redesigned, first an accurate description of the current aircraft behavior is needed. This chapter provides the mathematical model used to describe the behavior of a Diamond DA 42, the main study model of this thesis. First, Section 2.2 introduces rigid body aircraft dynamics. Next, Section 2.3 provides a description of the models used to determine the forces and moments acting on the aircraft. The aerodynamic forces and moments are treated separately in Section 2.4 and the chapter ends with conclusions in Section 2.5.

2.2 Aircraft Dynamics

The dynamic behavior, or the motion of a vehicle under the influence of forces and moments, can be described in a set of equations, called the Equations of Motion (EoM). Since motion only has meaning in a frame of reference, Section 2.2.1 starts with the definition of a set of reference frames. The EoM are derived next, in Section 2.2.2.

2.2.1 Reference Frames

The aircraft model, developed for this thesis, makes use of six reference frames. These reference frames are widely used for aircraft modeling and therefore merely listed here. For a more thorough introduction, the reader is referred to Appendix A.

- The Earth Fixed Reference Frame, RF_E , is fixed in position and attitude with respect to the earth and assumed to be inertial.
- The Vehicle Carried Local-Earth Reference Frame, RF_O , translates with the vehicle, but has the same attitude as RF_E .
- The Kinematic Reference Frame, RF_K , points in the direction of travel of the aircraft with respect to the ground (X_K along V_{GS}) and is obtained by rotating RF_O over the track angle χ_k , the flight path angle γ_k and the kinematic bank angle μ_k .
- The Body Fixed Reference Frame, RF_B , points towards the nose of the aircraft and is obtained by rotating RF_O over the yaw angle ψ , the pitch angle θ and the roll angle ϕ .

- The Aerodynamic Reference Frame, RF_A , points in the direction of travel of the aircraft with respect to the air (X_A along V_{TAS}) and is obtained by either rotating RF_B over the sideslip angle $-\beta$ and the angle of attack α or by rotating RF_O over the aerodynamic track angle χ_a , the flight path angle γ_a and the aerodynamic bank angle μ_a .
- The Trajectory Fixed Reference Frame, RF_T , is a right-handed orthogonal axis system of which X_T points along an earth fixed trajectory and is obtained by rotating RF_O over the track angle χ_T .

2.2.2 Equations of Motion

This section presents equations that can be used to describe the motion of a vehicle. These equations are also widely used and only the resulting twelve differential equations and a list of assumptions are given here. A more thorough introduction can be found in Appendix A.

The first three differential equations are used to compute the translational motion of the aircraft,

$$\begin{bmatrix} \dot{u} \\ \dot{v} \\ \dot{w} \end{bmatrix} = m^{-1} \begin{bmatrix} F_x \\ F_y \\ F_z \end{bmatrix} - \begin{bmatrix} p \\ q \\ r \end{bmatrix} \times \begin{bmatrix} u \\ v \\ w \end{bmatrix} \quad (2.1)$$

The second set of three differential equations is used to compute the rotational motion of the aircraft,

$$\begin{bmatrix} \dot{p} \\ \dot{q} \\ \dot{r} \end{bmatrix} = J^{-1} \begin{bmatrix} M_x \\ M_y \\ M_z \end{bmatrix} - J^{-1} \begin{bmatrix} p \\ q \\ r \end{bmatrix} \times \left(J \begin{bmatrix} p \\ q \\ r \end{bmatrix} \right) \quad (2.2)$$

The third set of three kinematic differential equations is used to describe the rotational rate of change of body attitude in RF_O ,

$$\begin{bmatrix} \dot{\phi} \\ \dot{\theta} \\ \dot{\psi} \end{bmatrix} = \begin{bmatrix} 1 & \sin\phi \tan\theta & \cos\phi \tan\theta \\ 0 & \cos\phi & -\sin\phi \\ 0 & \frac{\sin\phi}{\cos\theta} & \frac{\cos\phi}{\cos\theta} \end{bmatrix} \begin{bmatrix} p \\ q \\ r \end{bmatrix} \quad (2.3)$$

These equations are also known as the body orientation equations.

The last set of three differential equations, called the navigation equations, is used to describe the translation of the body in RF_E ,

$$\begin{bmatrix} \dot{x}_E \\ \dot{y}_E \\ \dot{z}_E \end{bmatrix} = Q_{BO}^T \begin{bmatrix} u \\ v \\ w \end{bmatrix} + V_{wind,E} \quad (2.4)$$

with $V_{wind,E}$ the constant velocity of the air with respect to the earth and,

$$Q_{BO} = \begin{bmatrix} \cos\theta \cos\psi & \cos\theta \sin\psi & -\sin\theta \\ -\cos\phi \sin\psi + \sin\phi \sin\theta \cos\psi & \cos\phi \cos\psi + \sin\phi \sin\theta \sin\psi & \sin\phi \cos\theta \\ \sin\phi \sin\psi + \cos\phi \sin\theta \cos\psi & -\sin\phi \cos\psi + \cos\phi \sin\theta \sin\psi & \cos\phi \cos\theta \end{bmatrix}$$

The foregoing differential equations are valid under the following assumptions,

- The earth is assumed flat, non-rotating, so that earth fixed reference frame is identical to the inertial reference frame.
- The aircraft is a rigid body, so any two points within the aircraft remain at fixed relative position. This assumption results in a substantial simplification of the EoM of the aircraft as described in Appendix A. Structural dynamics and aeroelasticity should be added in future work to finalize the FCL designs presented in this thesis. However, a certified CS-23 aircraft, such as the Diamond DA 42, is designed to be free from flutter, control reversal and divergence up to a certain limit velocity [41]. A large impact of these unmodeled dynamics on the FCL designs is therefore not expected.
- The mass of the aircraft is constant over the simulation time period. Hence, the integral over all mass elements can be evaluated outside the time derivative of the impulse equations.
- The pitch angle attained by the aircraft is bounded by $-\pi/2 < \theta < \pi/2$. This assumption prevents reaching the singularity in Equation (2.3).

The motion of the body relative to the earth can be calculated by solving the twelve differential equations. The complexity of solving these equations depends on the forces and moments that act on the vehicle. Sections 2.3 and 2.4 present several models for different sources of these forces and moments.

Additionally it is possible to express the EoM in different reference frames [69]. For example, the force equation in RF_A can be written as,

$$\begin{aligned}\dot{V}_{TAS} &= \frac{1}{m} [\cos \alpha \cos \beta \sin \beta \cos \beta \sin \alpha] F_B \\ \dot{\alpha} &= q - (p \cos \alpha + r \sin \alpha) \tan \beta + \frac{1}{m} \frac{1}{V_{TAS} \cos \beta} [-\sin \alpha \ 0 \ \cos \alpha] F_B \\ \dot{\beta} &= p \sin \alpha - r \cos \alpha + \frac{1}{m} \frac{1}{V_{TAS}} [-\cos \alpha \sin \beta \cos \beta \sin \alpha \sin \beta] F_B\end{aligned}\quad (2.5)$$

By substituting the forces from Equation (2.1), these derivatives can also be obtained from,

$$\begin{aligned}\dot{V}_{TAS} &= \frac{u\dot{u} + v\dot{v} + w\dot{w}}{V_{TAS}} \\ \dot{\alpha} &= \frac{u\dot{w} - w\dot{u}}{u^2 + w^2} \\ \dot{\beta} &= \frac{v\dot{V}_{TAS} - V_{TAS}\dot{v}}{\cos \beta V_{TAS}^2}\end{aligned}\quad (2.6)$$

The change in ground speed and track angles can be described in similar form using,

$$\begin{aligned}\dot{V}_{GS} &= \frac{u_E \dot{u}_E + v_E \dot{v}_E + w_E \dot{w}_E}{V_{GS}} \\ \dot{\gamma}_k &= \frac{-\dot{w}_E V_{GS} + \dot{V}_{GS} w_E}{\cos \gamma_k V_{GS}^2} \\ \dot{\chi}_k &= \frac{u_E \dot{v}_E - v_E \dot{u}_E}{u_E^2 + v_E^2}\end{aligned}\quad (2.7)$$

The expressions above are used in the flight control law design in Chapter 5.

2.3 Model Based Forces and Moments Description

The motion obtained by solving the EoM defined in Section 2.2.2 will only reflect the actual motion of the vehicle, when the modeled forces and moments also approximate the actual forces and moments on the vehicle. Adding too much detail in the forces and moments is not the best approach, since this may unnecessarily increase the computation time needed for the simulation of the vehicle dynamics and because implementing these detailed descriptions in a simulation environment can be time consuming. This section discusses several sources of forces and moments that act on the vehicle and the way in which they are modeled. The aerodynamic forces and moments are treated separately in Section 2.4.

2.3.1 Weight Model

Gravity acts on the body in positive Z_O -direction and has a magnitude of mg , in which m is the mass of the aircraft and g the gravitational acceleration. The influence of gravity on the body can be written as,

$$\begin{bmatrix} F_{W,X_B} \\ F_{W,Y_B} \\ F_{W,Z_B} \end{bmatrix} = Q_{BO} \begin{bmatrix} 0 \\ 0 \\ mg \end{bmatrix} \quad (2.8)$$

Since gravity acts on the Center of Gravity (CoG) of the aircraft it generates no moment in RF_B . The gravitational acceleration g is modeled to vary with the aircraft's altitude h_E as,

$$g = g_0 \frac{r_E^2}{(r_E + h_E)^2} \quad (2.9)$$

where $r_E = 6371009$ m is the mean radius of the earth, according to the International Union of Geodesy and Geophysics.

The mass of an aircraft can be divided into several parameters,

$$m = m_{empty} + m_{fuel} + m_{payload} \quad (2.10)$$

where m_{empty} is the mass of the aircraft when it is empty, m_{fuel} the mass of the fuel and $m_{payload}$ the mass of the passengers and the cargo. The mass of the fuel decreases during flight, questioning the assumption of constant mass made in the derivation of the EoM. However, the rate of change of mass, i.e., fuel flow, of an aircraft such as the DA 42 is small enough, that the error is negligible and therefore the assumption still holds.

The burning of fuel also influences the CoG position and the moments of inertia I_{xx} and I_{zz} . The influence on I_{yy} and I_{xz} is small due to the mass symmetry in the $X_B O Z_B$ -plane and assumed to be negligible. Plots of these influences are provided in the Airplane Flight Manual [3] and shown here in Figure 2.1.

The mass is assumed to be distributed symmetrically in the $X_B O Z_B$ -plane and therefore the moments of inertia I_{yz} and I_{xy} are zero. Uneven fuel loading causes a rolling moment on the aircraft. This moment is easily calculated from the fuel tank locations with respect to the CoG and the amount of fuel in each tank. However, flying with a significant fuel unbalance is not advisable and would violate the assumption of mass symmetry in the $X_B O Z_B$ -plane.

Values for this mass model have been provided by Diamond Aircraft Industries GmbH and are assumed to be validated.

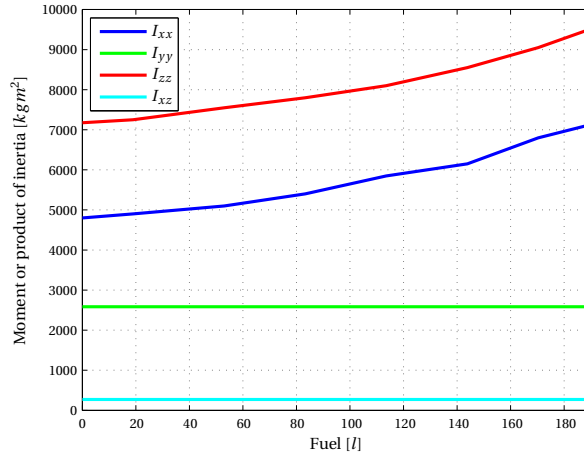


Figure 2.1: Influence of fuel on the inertia of the aircraft.

2.3.2 Environment Model

The surroundings of an aircraft consist of air, terrain and other flying objects. Forces and moments due to the latter factor are not included in this thesis and forces and moments due to terrain are only considered during landing in the unvalidated model extension in Appendix D. In this section both the gas properties as well as the constant and sudden movement of air are modeled.

Gas Properties

The gas properties of air are modeled as defined by the International Standard Atmosphere, ISA. The air is considered to be a perfect gas and the temperature T is related to the altitude of the aircraft h_E as follows,

$$T = T_0 + \lambda h_E \quad (2.11)$$

where $T_0 = 288.15$ K is the temperature at Mean Sea Level (MSL) and $\lambda = -0.0065$ is the lapse rate. As long as the aircraft stays in the troposphere $h_E < 11000$ m, the air density ρ can be calculated using,

$$\rho = \rho_0 \frac{T^{-\frac{g_0}{R\lambda+1}}}{T_0} \quad (2.12)$$

where $\rho_0 = 1.225$ kg/m³ is the air density at MSL, $g_0 = 9.80665$ m/s² is the gravitational acceleration at MSL and $R = 287.05287$ K m²/s² is the gas constant.

Wind

The constant movement of air, or wind, is modeled using the power law [137],

$$V_{wind,E} = \begin{bmatrix} \cos \psi_{wind} & -\sin \psi_{wind} & 0 \\ \sin \psi_{wind} & \cos \psi_{wind} & 0 \\ 0 & 0 & 1 \end{bmatrix} V_0 \left(\frac{h}{h_0} \right)^{1/7} \quad (2.13)$$

with V_0 the wind velocity at a reference height h_0 and ψ_{wind} the direction of the wind with respect to RF_E . More accurate wind models exist [48], but are considered beyond the scope of this thesis.

Atmospheric Disturbances

The sudden movement of air, or atmospheric disturbance, is modeled in two scenarios, turbulence and wind gusts. Turbulence is an excitation on the rigid body modes and on the structural modes of an aircraft. As explained in the assumptions of the EoM, the structural mode excitation is beyond the scope of interest in this thesis. For the purpose of evaluation of the FCL in the initial design phase turbulence modeling is important, but does not need high fidelity. Several possibilities exist for modeling turbulence, such as the paper of Etkin [30], the thesis of Van Staveren [116], lecture notes [86] and Section 3.7 of the Military Specification MIL-F-8785C [79]. The effects of turbulence have been modeled in this thesis according to the mathematical representation in MIL-F-8785C, due to its simplicity and adequate level of accuracy for the initial design of FCLs that aim at navigation and maneuvering of the aircraft.

Turbulence is seen in the MIL-F-8785C representation as a stochastic process defined by velocity spectra that are a function of the spatial frequency Ω . The assumption is made that turbulence is a stationary process, meaning that the turbulence seems frozen for an aircraft flying through it. This assumption allows the velocity spectra to be converted to the radial frequency ω , using, $\omega = \Omega V$ and therefore become a function of time, rather than distance. For computational simplicity the Dryden-form is chosen and the following power spectral density functions are used,

$$\begin{aligned} \Phi_u(\omega) &= \sigma_u^2 \frac{2L_u}{\pi V} \frac{1}{1 + (L_u \frac{\omega}{V})^2} \\ \Phi_v(\omega) &= \sigma_v^2 \frac{L_v}{\pi V} \frac{1 + 3(L_v \frac{\omega}{V})^2}{\left[1 + (L_v \frac{\omega}{V})^2\right]^2} \\ \Phi_w(\omega) &= \sigma_w^2 \frac{L_w}{\pi V} \frac{1 + 3(L_w \frac{\omega}{V})^2}{\left[1 + (L_w \frac{\omega}{V})^2\right]^2} \end{aligned} \quad (2.14)$$

where ω is the radial frequency, $L_{u,v,w}$ are scale lengths and $\sigma_{u,v,w}$ represent the turbulence intensities.

Section 3.7.5 of MIL-F-8785C states that for analysis purposes, in the absence of a proper structural model, the effect of asymmetric turbulence on the rigid-body airframe can be described by the resulting angular velocity components of the aircraft,

$$\begin{aligned}\Phi_p(\omega) &= \frac{\sigma_w^2}{VL_w} \frac{0.8 \left(\frac{\pi L_w}{4b}\right)^{1/3}}{1 + \left(\frac{4b\omega}{\pi V}\right)^2} \\ \Phi_q(\omega) &= \frac{\left(\frac{\omega}{V}\right)^2}{1 + \left(\frac{4b\omega}{\pi V}\right)^2} \Phi_w \\ \Phi_r(\omega) &= \frac{\left(\frac{\omega}{V}\right)^2}{1 + \left(\frac{3b\omega}{\pi V}\right)^2} \Phi_v\end{aligned}\tag{2.15}$$

where b is the wing span. The interested reader can find more details on the turbulence model in MIL-F-8785C.

Figure 2.2 shows the turbulence filter and the resulting velocity profile u_{turb} for cruise condition. Note that this figure shows the additional forward velocity of the aircraft due to turbulence and not the total forward velocity. The bode plot shows that amplification of the noise input signal is high at low frequencies and becomes lower at high frequencies. This results in a velocity profile that has large slow variations and rapid smaller changes.

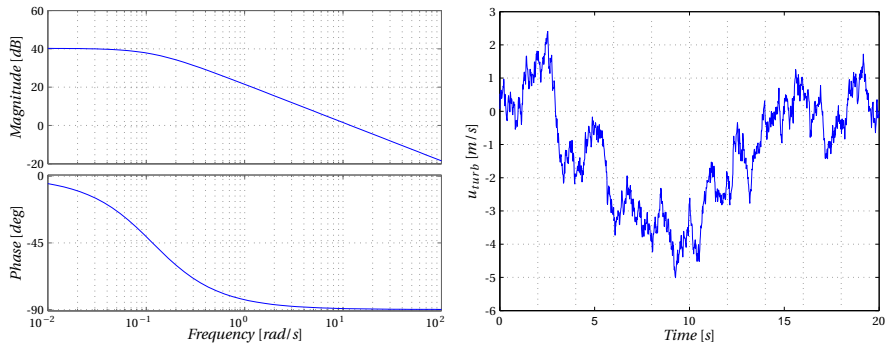


Figure 2.2: Turbulence shaping filter, with $\sigma_u = 10.3$ ft/s and $L_u = 1750$ ft (left) and velocity profile u_{turb} (right).

Section 3.7.1.3 of MIL-F-8785C defines a model for wind gusts using a ‘1-cosine’ shape. Although step or ramp functions are also permitted, gust can be modeled by the function,

$$V_{gust} = \begin{cases} 0, & \text{if } x < 0 \\ \frac{V_m}{2} (1 - \cos(\frac{\pi x}{d_m})), & \text{if } 0 \leq x \leq d_m \\ V_m, & \text{if } x > d_m \end{cases} \quad (2.16)$$

where V_m is the maximum gust velocity, x is the aircraft’s position and d_m is the gust length. The gust parameters are described in RF_B .

The total influence of the sudden movement of air on the velocity of the aircraft is the summation of turbulence and wind gust, expressed in RF_B ,

$$V_B = V_{steady,B} - V_{turb,B} - V_{gust,B} \quad (2.17)$$

$$\omega_B = \omega_{steady,B} + \omega_{turb,B} \quad (2.18)$$

Note that these resulting (angular) velocities are used in the evaluation of the EoM as well as the determination of the velocity dependent forces and moments, such as the propulsion model and the aerodynamic model described in Sections 2.3.3 and 2.4 respectively. The steady atmosphere velocity ($V_{steady,B}$) and angular velocity ($\omega_{steady,B}$) result from integrating the left hand sides of Equations (2.1) and (2.2) respectively.

The environment models are validated using large datasets by ISA and USAF.

2.3.3 Propulsion Model

The DA 42 is a twin propeller aircraft. The propulsive force, or thrust, is delivered by a lift force on each propeller blade, pulling the aircraft forwards. To create lift, the propellers are rotated by the engines. The thrust force T delivered by the propellers is equal to,

$$T = \frac{P}{V_{TAS}} \quad (2.19)$$

where the propeller power P is the product of efficiencies η , the power lever angle pla and the maximum power P_{max} of the engines,

$$P = \eta_{engine} \eta_{prop} pla P_{max} \quad (2.20)$$

The propeller efficiency in Equation (2.20) depends on engine rpm n , true airspeed V_{TAS} , altitude h , air temperature T_{air} , air density ρ and propeller diameter D , increasing the complexity of the engine model. Figure 2.3 shows a possible propeller efficiency profile at different altitudes, velocities and power lever angles.

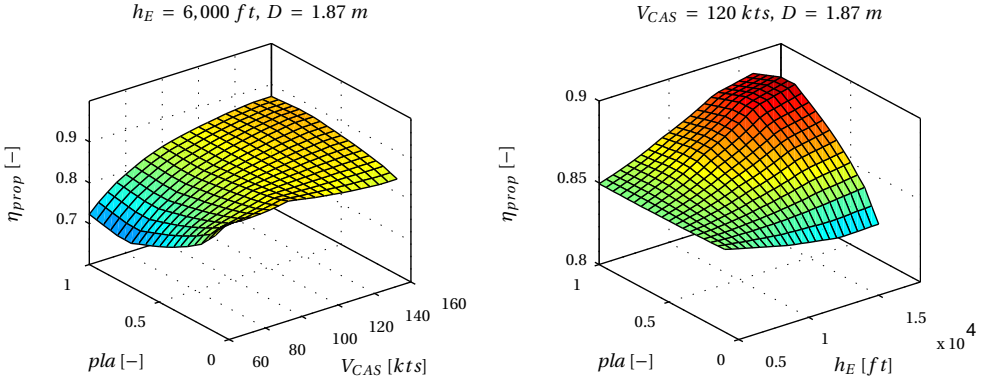


Figure 2.3: Example of the propeller efficiency at different flight conditions. The propeller efficiency data for the DA 42 is proprietary and therefore not shown in this thesis.

The assumption is made that the engines are perfectly aligned with the X_B -axis and an additional moment is introduced by shifting the forces from the propeller position to the CoG,

$$\begin{bmatrix} F_{T,X_B} \\ F_{T,Y_B} \\ F_{T,Z_B} \end{bmatrix} = \begin{bmatrix} T \\ 0 \\ 0 \end{bmatrix}, \quad \begin{bmatrix} M_{T,X_B} \\ M_{T,Y_B} \\ M_{T,Z_B} \end{bmatrix} = X_{prop} \times F_{T,B} \quad (2.21)$$

The propulsion model, including efficiencies, is also supplied by Diamond and assumed to be validated.

2.4 Aerodynamic Model

Aerodynamic forces and moments are caused by the deflection of air around the aircraft. This deflection depends on several variables such as, true airspeed (V_{TAS}), air density (ρ), rotational rate of the aircraft (p , q , r), angle of attack (α), angle of sideslip (β) and deflection of the control surfaces (δ_a , δ_e , δ_r). The aerodynamic forces and moments can be described by,

$$\begin{bmatrix} F_{A,X_B} \\ F_{A,Y_B} \\ F_{A,Z_B} \end{bmatrix} = \begin{bmatrix} X \\ Y \\ Z \end{bmatrix} = \frac{1}{2} \rho V_{TAS}^2 S \begin{bmatrix} C_X(\alpha, \dot{\alpha}, q, \delta_e, \dots) \\ C_Y(\beta, p, r, \delta_a, \delta_r, \dots) \\ C_Z(\alpha, \dot{\alpha}, q, \delta_e, \dots) \end{bmatrix} \quad (2.22)$$

$$\begin{bmatrix} M_{A,X_B} \\ M_{A,Y_B} \\ M_{A,Z_B} \end{bmatrix} = \begin{bmatrix} L \\ M \\ N \end{bmatrix} = \frac{1}{2} \rho V_{TAS}^2 S \begin{bmatrix} bC_L(\beta, p, r, \delta_a, \delta_r, \dots) \\ \bar{c}C_M(\alpha, \dot{\alpha}, q, \delta_e, \dots) \\ bC_N(\beta, p, r, \delta_a, \delta_r, \dots) \end{bmatrix} \quad (2.23)$$

in which three geometric parameters are used, that are obtained from the Aircraft Flight Manual [3]. The area of the wing planform, $S = 16.29$ meters, the distance between the wing tips, or the wing span, $b = 13.42$ meters and the mean aerodynamic chord, $\bar{c} = 1.271$ meters.

Parameterization of the aerodynamic model can be done in several ways, such as using multivariate splines [24], or Taylor expansions. Splines are particularly helpful if a global model is needed that is able to describe large nonlinearities. In this thesis the aircraft dynamics are quite linear and therefore Taylor expansions are used. For example, the pitch moment can be expanded as,

$$C_M = C_{M_0} + C_{M_\alpha} \alpha + C_{M_{\dot{\alpha}}} \dot{\alpha} + \dots \quad (2.24)$$

where $C_{M_\alpha} = \frac{\partial C_M}{\partial \alpha}$, etc. are dimensionless coefficients. A method for obtaining values for these parameters, also known as the stability and control derivatives, is treated in Section 2.4.1. Section 2.4.2 shows whether the model actually resembles the dynamic behavior of a DA 42.

2.4.1 Model Parameters

Different methods may be applied in order to find the stability and control derivatives, for instance wind tunnel tests, CFD computations, handbook methods based on empirical data, or flight tests. Appendix B provides an account of the failed attempt of using log files provided by Diamond Aircraft Industries GmbH for the latter method. This section presents a method that uses geometric data to estimate the aerodynamic model parameters.

In the 70's the United States Air Force combined many handbook methods into a data companion called DATCOM. Using this program the stability and control derivatives can be estimated based solely on the geometric data of the aircraft. Many small airplanes have quite conventional shapes and fly at low (subsonic) velocity, which are precisely the conditions for which DATCOM is known to have good results [50]. This method is therefore selected to determine values for the stability and control derivatives of the DA 42.

The input data required by DATCOM ranges from the location of the fuel tanks to the shape of the wing and the fuselage. In total 260 different parameters can be used, of which about 100 are critical for the proper modeling of the dynamic behavior of the aircraft. A large part of these parameters can be determined from the Airplane Flight Manual [3] and for proprietary data Diamond Aircraft Industries GmbH was contacted. This last step unfortunately prohibits inclusion of the aerodynamic model parameter values in this thesis.

After conversion to the body fixed reference frame, DATCOM provides the parameters for the following aerodynamic model:

$$\begin{aligned}
C_X &= C_{X_0} + C_{X_\alpha} \alpha + C_{X_{\delta_e}} \delta_e + C_{X_{\delta_f}} \delta_f \\
C_Y &= C_{Y_\beta} \beta + C_{Y_r} \frac{rb}{2V} \\
C_Z &= C_{Z_0} + C_{Z_\alpha} \alpha + C_{Z_{\dot{\alpha}}} \frac{\dot{\alpha} \bar{c}}{2V} + C_{Z_q} \frac{q \bar{c}}{2V} + C_{Z_{\delta_e}} \delta_e + C_{Z_{\delta_f}} \delta_f \\
C_L &= C_{L_\beta} \beta + C_{L_p} \frac{pb}{2V} + C_{L_r} \frac{rb}{2V} + C_{L_{\delta_a}} \delta_a \\
C_M &= C_{M_0} + C_{M_\alpha} \alpha + C_{M_{\dot{\alpha}}} \frac{\dot{\alpha} \bar{c}}{2V} + C_{M_q} \frac{q \bar{c}}{2V} + C_{M_{\delta_e}} \delta_e + C_{M_{\delta_f}} \delta_f \\
C_N &= C_{N_\beta} \beta + C_{N_p} \frac{pb}{2V} + C_{N_r} \frac{rb}{2V} + C_{N_{\delta_a}} \delta_a
\end{aligned} \tag{2.25}$$

Note that the rudder influence on roll ($C_{L_{\delta_r}}$) and yaw motion ($C_{N_{\delta_r}}$) are not provided by DATCOM and should be added from an alternative source.

DATCOM+ written by Bill Galbraith is a modern update for the DATCOM program of 1965. With a changed front-end and back-end, the user friendliness of the program has greatly been improved. The output of DATCOM+ consists of xml-files containing the stability and control derivatives. In order to easily test this aerodynamic model, a DATCOM to SIMULINK functionality has been implemented during the course of this thesis. The xml data is read in MATLAB and automatically converted to SIMULINK blocks, such as constants, lookup-tables, products, summations and dividers. This setup proved to be highly maintainable and therefore not only the aerodynamic model, but also the mass model, engine model, turbulence model and landing model were added in similar fashion.

With the data from the Airplane Flight Manual and Diamond Aircraft Industries GmbH, the dynamic behavior of a DA 42 is captured in a multi-model six-degrees-of-freedom nonlinear mathematical model. Although aircraft-like behavior is rapidly determined using desktop simulations, proper validation is needed before this model can be used for flight control law design.

2.4.2 Model Validation

Diamond Simulation GmbH (DS) a subsidiary company of Diamond Aircraft Industries GmbH specializes in full cockpit simulations of Diamond aircraft. The D-SIM-42 NG is scheduled to be certified as a Flight Training Device (FTD) on Level 6, according to 14 CFR Part 60, meaning that an aircraft model is used with specific DA 42 parameters. This level of certification requires a Qualification Test Guide (QTG)

to be written containing several test reports. The test reports are compiled using recorded flight data for specific flight trails, amongst which the eigenmotion behavior of the aircraft at different altitude and velocity. However, this document is confidential and therefore not distributed by DS.

After email discussions and signing a nondisclosure agreement, DS did agree to send the QTG they use for qualification of their Level 5 FTD. Level 5 means that a family of aircraft can be simulated rather than the DA 42 specifically. The resulting model accuracy can therefore be questioned and the flight control laws need to be designed with robustness to model uncertainty in mind. Furthermore, the eigenmotions included in this QTG show the dynamic behavior only in cruise configuration and around 120 kts at 6,000 ft and not in the entire flight envelope. Validation of the model is therefore limited to this operating condition as well. This should also be kept in mind, while designing the flight control laws.

Validation of the aerodynamic parameters used in this thesis is done using the Level 5 QTG. A summary of the results is shown in Figure 2.4, in which each row shows a different eigenmotion of the aircraft. The complete set of comparison figures can be found in Appendix C. Since the results are highly comparable to the QTG provided by DS, the assumption is made that the aircraft model behaves similar to a DA 42 in the neighborhood of 120 kts at 6,000 ft and in cruise configuration. Rough validation of the aircraft model is therefore complete.

2.5 Conclusions

This chapter presented a six degrees-of-freedom nonlinear model of the dynamic behavior of a Diamond DA 42. This model is used as the main study model throughout this thesis. It contains a validated weight model, environment model, propulsion model and aerodynamic model.

The purpose of a Flight Control Law (FCL) is to change the dynamic behavior of the aircraft. The model developed in this chapter describes the current dynamic behavior of the aircraft and may therefore serve as a basis for the FCL design. Due to difficulties in the validation process, the accuracy and fidelity of the developed model is questionable. When designing the FCLs, robustness is needed for parameters uncertainties and unmodeled dynamics. Also, FCLs designed using this model should be restricted to cruise configuration and around 120 kts at 6,000 ft.

Installing a Fly-By-Wire platform on the aircraft changes the dynamic behavior perceived by the FCLs. Before designing the FCLs this change in behavior should be investigated, which is done in the next chapter.

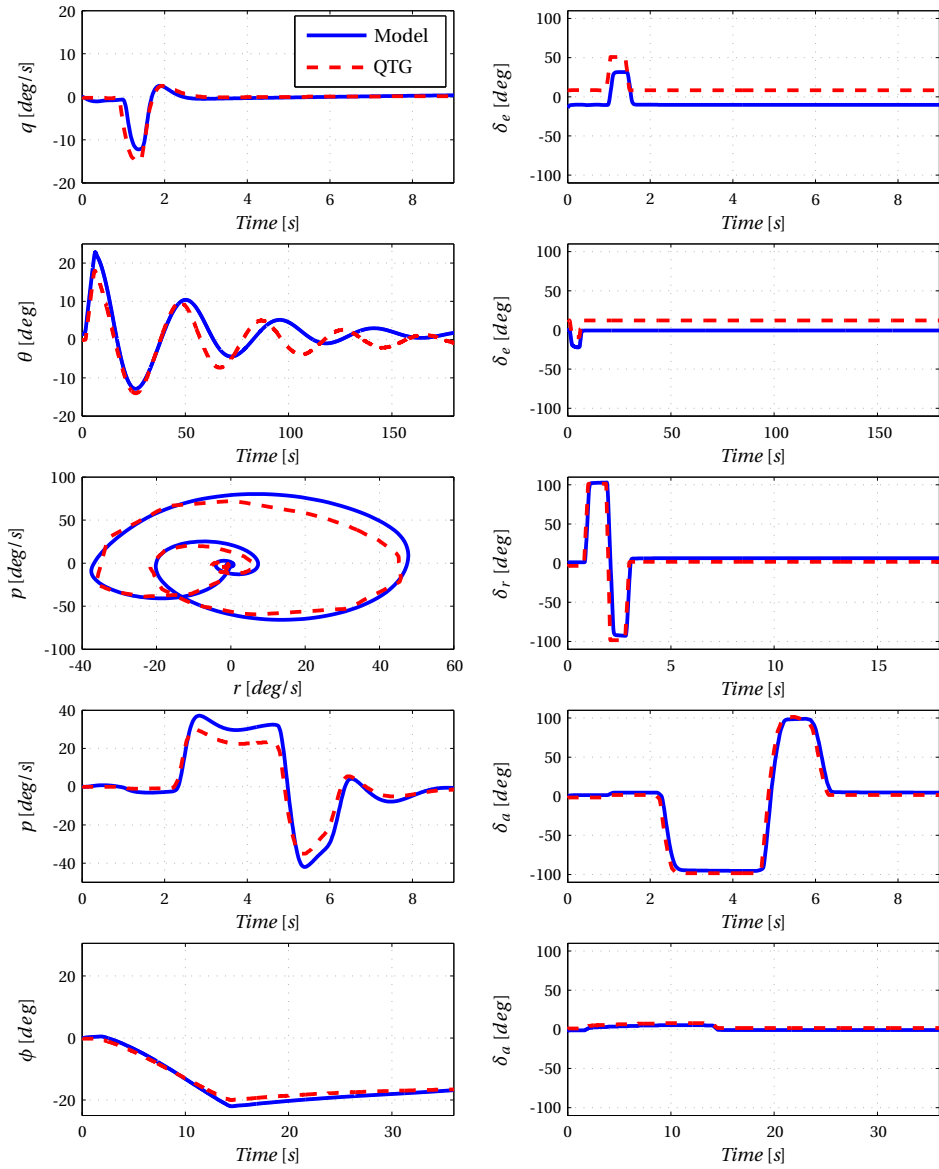


Figure 2.4: Eigenmotion behavior of the DA 42 aircraft model in cruise configuration.

INFLUENCE OF AN AFFORDABLE FLY-BY-WIRE PLATFORM

Abstract

This chapter briefly introduces an affordable Fly-By-Wire (FBW) platform for general aviation aircraft, that will be used in the “Small Aircraft Future Avionics aRchitecture” project and installed onto a Diamond DA 42. Together with the aircraft model the FBW platform serves as the definition of the operating environment for the flight control laws and determines the dynamic characteristics of the system that is controlled. The FBW platform components and specifications described in this chapter show that the FCL must be designed with robustness to sensor noise and time delays in addition to the required robustness to model uncertainty mentioned in Chapter 2.

3.1 Introduction

Given the design of the aircraft, the way the aircraft responds to pilot commands can still be altered using Fly-By-Wire (FBW) technology. The mechanical cables, pulleys and rods should then be replaced by electrical wiring and actuators. This makes it possible to include a computer, the Flight Control Computer (FCC), in the link between the pilot and the actuators connected to the control surfaces. The pilot provides commands to the FCC and the FCC translates these commands to control surface actions using the FCLs. When measurement devices, such as air-data sensors or inertial navigation systems, are connected to the FCC as well, directly or indirect through a Flight Data Computer, significant changes can be made to the way the aircraft responds to pilot commands. Improvements in aircraft stability and pilot workload become possible giving the FBW platform a clear advantage over its mechanical counterpart [15].

The drawback of the FBW platform is that it is more expensive than the mechanical system. Even more so, since the full potential is only obtained in combination with expensive measurement devices. In order to get a positive outcome in a cost-benefit analysis, the full FBW platform must be affordable, while satisfying safety regulations. Spending two million euro on a flight control system for a sixty million euro aircraft is acceptable, however, spending the same amount for a one million euro general aviation aircraft is absurd. This implies that for a general aviation FBW platform low-cost components should be used, that still have satisfactory properties. Bandwidth and noise characteristics of FBW components affect the FCL design by changing the dynamic behavior of the system that is controlled. For low-cost components this change can be significant and should be modeled before designing the FCLs.

Aiming at an affordable platform can also affect the amount of time-delay in the signals that are used by the FCLs. Safety regulations require such a low probability of failure of the FBW platform, that a single failure should not result in any degradation of the FBW platform functionality. In other words the FBW platform should be at least fail-operational for a single failure. In commercial aviation, failure passivity is obtained through hardware redundancy [15]. This means all FBW platform components are installed three or four times, in order to maintain a working system when failures are detected. For a general aviation FBW platform a more advanced, software-based method of redundancy management may be needed in order to reduce the cost of the platform. However, such a management system would use more computational time, thereby creating time-delays in the signals processed by the FCLs.

When designing the FCLs, the control engineer should be aware of the dynamic properties of the aircraft as described in Chapter 2, but also of the constraints and the dynamic properties of the FBW platform. Constraints, such as available processing power, available measurement devices, certification guidelines, financial budget, development time, etc., can sometimes be changed, but are more often fixed. In general, the earlier the system should be operational, the more constraints are fixed. This chapter investigates constraints and influences on the dynamic behavior perceived by the FCL, posed by the FBW platform. As such it describes a crucial step for the FCL design process in order to end up with practical FCLs that are usable by small aircraft in the near future.

Section 3.2 comments on the development of an affordable FBW platform as determined in the European project: “Small Aircraft Future Avionics aRchitecture” (SAFAR) [107]. This section provides a brief description of the components, such as sensors and actuators, and their influence on the dynamic properties of the system controlled by the FCLs. Section 3.3 provides information about the time-delays in the signals processed by the FCL caused by the data transportation and redundancy management of the SAFAR FBW platform. Section 3.4 roughly defines the operational scope of the SAFAR platform by combining the knowledge of this chapter and the previous one. Section 3.5 contains a short review of the certification guidelines applicable to FCL development. It will roughly indicate the amount of work needed for certification of linear FCLs and indicate a gap in the certification procedures prohibiting certification of nonlinear FCLs. Actual FCL certification is beyond the scope of this thesis, however. Section 3.6 ends this chapter with conclusions.

3.2 Platform Components

A FBW platform consists of several components. The pilot provides inputs to the platform using stick and throttle movements. These inputs are pre-processed by the Input-Output Modules (IOMs) and send to the Core Processing Module (CPM) which acts as FCC. The FCC translates these commands based on the FCLs and using sensor data, into actuator commands and power lever angle commands, which are send to the actuator and engine control modules. The actuators move the control surfaces, which results in a change in airflow over the aircraft and therefore in a change in aerodynamic forces and moments. The engine control module sets the engine throttle, which results in a change of engine thrust. Both actions enable the pilot to fly the aircraft and reach a certain location at a given time. The subsequent sections will discuss the components in a FBW platform and specific attention is given to the FBW platform components used in SAFAR.

3.2.1 Stick and Throttle

The stick and throttle used on the SAFAR platform are depicted in Figure 3.1. Both are manufactured by Spohn & Burkhardt GmbH & Co. and convert the movements provided by a pilot into an electrical signal. The side-stick is spring centered, meaning that the pilot has to maintain force on the stick in order to keep it deflected. The throttle does not contain a spring, giving the pilot the ability to select a setting between zero (fully pulled back) and one (fully pushed forward). One of the FCLs presented in Chapter 4 is the DRCT mode, in which the pilot directly controls the control surfaces. This stick-to-surface mode contains only a stick-shaping function, that maps the deflection of the stick and the throttle to the deflection of the control surfaces and the engine throttle respectively. Other FCL modes use sensor information to change the interaction the pilot has with the aircraft. Control modes can be selected using the green button on the side-stick and the other buttons are used for platform calibration and initialization. The rudder pedals are not linked to the SAFAR platform, meaning that a rudder controller is needed in the FCLs, or in case of the DRCT law, that the safety pilot will provide rudder commands.

3.2.2 Actuators

In a FBW platform the control surfaces are moved using actuators. For SAFAR these actuators contain synchron brushless DC motors, harmonic drive gears and electromagnetic clutches [107]. These clutches close when the FBW platform is engaged and open on disengage or loss of power. The SAFAR actuators are manufactured by SET GmbH and one of them is shown in Figure 3.2.

After installing the FBW platform on the DA 42, the dynamic behavior of the aircraft changes as seen from the FCL perspective. The aircraft model therefore needs to be extended with an actuator model. Figure 3.3 shows a detailed representation of the actuator dynamics. This model was provided by the University of Stuttgart and is printed with permission. The inputs of this model are the commanded actuator rotation ϕ_{cmd} and the number of actuators active n_{act} . In normal operation (Degradation Mode 0), two actuators will move one control surface in order to be fail-operational in a single failure. The output of this model is the actual actuator rotation ϕ , which is used to compute the control surface deflection using a lookup-table. Three distinct subsystems can be identified in the actuator model. First, the actuator control loop running on the actuator control module, which determines the current (I_{cmd}) send to the actuator motor. Second, the actuator mechanics, consisting of the motor and a gear with a transmission ration of 120:1, which influences the torque applied by the actuator. And third, the aerodynamic moments acting on the control surface, which effects the actuators as an external load. Using this data



Figure 3.1: Side-stick and throttle manufactured by Spohn & Burkhardt GmbH & Co.



Figure 3.2: Actuator manufactured by SET GmbH.

and combining it with the inertia of the actuators and the control surface, the rotational acceleration of the actuator can be obtained ($\ddot{\phi}$). Integrating this acceleration twice provides the output of this model, the rotation of the actuator itself (ϕ).

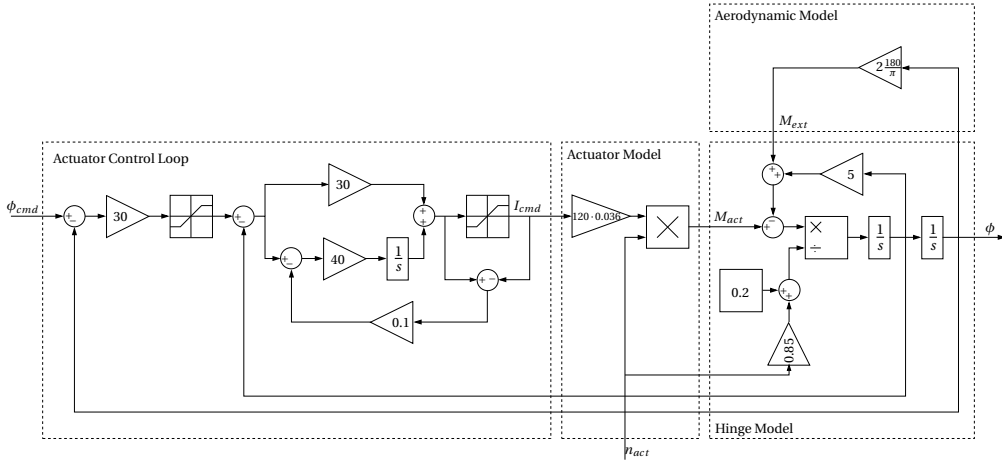


Figure 3.3: Actuator model developed by the University of Stuttgart.

For nonlinear FCL design purposes it may be desirable to have a simple analytical representation of the actuator dynamics. Literature suggests that the dynamics of this actuator could also be modeled with a simple low-pass filter [23],

$$H(s) = \frac{12}{s + 12} \tag{3.1}$$

Figure 3.4 shows the response of both actuator models to a step input of 20 degrees and a chirp input ranging from 0.1 rad/s to 50 rad/s in 100 seconds. Clearly the difference between both models is small and the low-pass filter representation may be used for FCL design. For simulation the full actuator model will be used.

3.2.3 Engine Control Unit

The engines of a DA 42 are equipped with a Full Authority Digital Engine Control (FADEC) system. This system selects optimal engine settings, given a certain power lever angle, air density, engine temperatures, engine pressures, and many other parameters. Since no specific model was available for the FADEC, it is modeled as a low-pass filter with a larger time constant than used in the actuators [23],

$$H(s) = \frac{3}{s + 3} \tag{3.2}$$

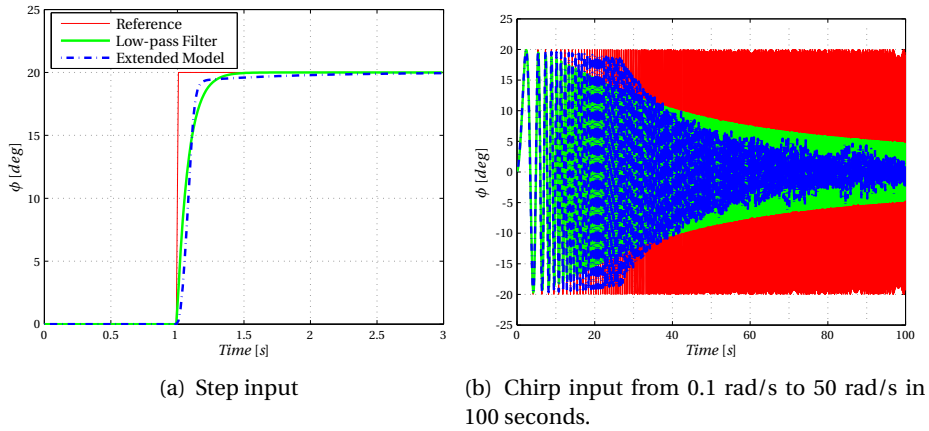


Figure 3.4: Dynamic response of the actuator.

3.2.4 Measurement Devices

Measurement devices are used in a FBW platform to determine the state of the aircraft. This state information is used by the FCC to evaluate the FCLs and thereby change the dynamic behavior of the system controlled by the pilot. When measurements are incorrect the change in dynamic behavior can be different from the designed change, possibly leading to undesired dynamic behavior of the aircraft. To deal with this problem, sensor fusion and sensor modeling can be applied. Sensor fusion combines information from different types of sensors, to determine the state more accurately than would be possible using each sensor individually. Sensor modeling adds the dynamic characteristics of the sensors to the aircraft model in the FCL design process, thereby ensuring that the designed FCLs are able to operate satisfactory while using the modeled sensors. In this section we will focus on the sensor modeling and assume that the sensor fusion is done properly by the sensor manufacturers.

Two types of state information can be distinguished, namely state information regarding the aircraft with respect to the earth's surface and state information regarding the aircraft with respect to the air. The first part of the state is referred to as the navigation part and contains the aircraft's position (X_E), velocity (V_E), acceleration (A_E), attitude ($[\phi \ \theta \ \psi]^T$), angular rate (ω), ground speed (V_{GS}) and flight path ($[\chi_k \ \gamma_k \ \mu_k]^T$) information. Navigational sensors commonly used are accelerometers, gyroscopes, magnetometers and Global Navigation Satellite System (GNSS) receivers. Integrated sensor packages are also commercial-of-the-shelf available, such as Inertial Measurement Units (IMUs), combining accelerometers

and gyroscopes, Attitude and Heading Reference Systems (AHRS), combining IMUs and magnetometers, Inertial Navigation Systems (INS), combining IMUs and GNSS receivers, Inertial Reference Units (IRUs), combining more fancy IMUs and GNSS receivers, etc. The second part of the state is referred to as the air-data part and contains the airspeed (V_{TAS}), aerodynamic flow angles (α, β), outside air temperature (T_{OAT}), static pressure (p_s) and total pressure (p_t). Air-data sensors commonly used are angle of attack vanes, angle of sideslip vanes, Pitot tubes and air-data booms.

In the SAFAR FBW platform several navigational sensors and algorithms are developed in parallel. The cheapest option combines the IMU and GNSS receiver shown in Figure 3.5. A highly optimized navigation algorithm is used to combine the sensor information from both sources and provide the navigation solution. Due to proprietary reasons, the full sensor models including navigational algorithm could not be included in the aircraft model. Instead the resulting dynamic properties of the fused state is mimicked and applied to the aircraft model output signals.



(a) iIMU-MM-02 Inertial Measurement Unit manufactured by iMar. (b) AsteRx2eH Global Navigation Satellite System receiver manufactured by Septentrio.

Figure 3.5: IMU and GNSS receiver used in the SAFAR FBW platform.

The noise and bias characteristics of sensors can be modeled as [132],

$$x_{noisy} = x_{true} + \omega_x + b \quad (3.3)$$

where x_{noisy} is the noisy state, x_{true} is the true state, ω_x is zero mean wide-band noise with variance σ_x^2 and b is the bias drift, that can be described by a first order Gauss-Markov process,

$$\dot{b} = -b/\gamma + \omega_b \quad (3.4)$$

where γ is the time constant or correlation time and ω_b is zero mean wide-band noise with variance σ_b^2 . The IMU product datasheet does not provide values for

σ_x and σ_b directly, but using the Angular Random Walk (ARW) and Allan Variance (AVAR) [53, 5]. Values for γ are not mentioned at all on the datasheet and can be determined from the autocorrelation of a recorded time history of the sensor output. The autocorrelation function shows how much a current time segment resembles a γ second delayed time segment. Since the sensor can be modeled as a first order Gauss-Markov process, the autocorrelation function is usually an exponential function, $\psi = \sigma_b^2 e^{-t/\gamma}$. The correlation time γ can be read from the autocorrelation plot at the point where the current time segment resembles the delayed segment for only 36.8% [100].

AVAR is a method of analyzing a time sequence to pull out the intrinsic system noise as a function of the averaging time [118]. It is otherwise difficult to measure the process noise ω_b , as it is much smaller than the measurement noise ω_x . Figure 3.6(a) shows a 5,5 hour time history of the sensor model output, modeling a gyroscope using $\sigma_x = 0.008$ deg/s and $\sigma_b = 0.0023$ deg/s. By dividing this time history in a number of bins of τ seconds wide and comparing the data contained in each bin, using the following equation,

$$AVAR^2(\tau) = \frac{1}{2(n-1)} \sum_i (y(\tau)_{i+1} - y(\tau)_i)^2 \quad (3.5)$$

with y_i being the average value of bin i and n the number of bins in the dataset for this averaging time τ , leads to a quantitative measure of how much the average value changed at that particular value of τ .

Figure 3.6(b) shows the AVAR for different values of τ on a log-log scale. For small values of τ the slope of this plot is $-1/2$, which corresponds to the ARW part of the sensor output. The ARW value in the datasheet can be obtained by fitting the function $ARW \cdot \tau^{-1/2}$, to the AVAR plot. Alternatively, the ARW value can be calculated using,

$$ARW = AVAR\sqrt{\tau} \quad (3.6)$$

for the range of τ matching the $-1/2$ slope. In this case, conveniently looking at the AVAR value at $\tau = 1$ seconds leads to an ARW value of $0.48 \text{ deg}/\sqrt{\text{hr}}$, which closely matches the value provided in the datasheet [53]. For large values of τ the slope of the plot becomes $+1/2$ due to the rate random walk, which is the inherent instability in the sensors output. The standard definition of bias instability used by inertial sensor manufacturers is the minimum point on the AVAR curve. In this case the bias instability occurs at 16 deg/hr at $\tau = 7.6$ seconds, again close to the value specified by the datasheet. The parameters used in the simple gyroscope model are therefore assumed to be good enough. Parameters for the accelerometer model can be determined in the same way. Due to the use of sensor fusion, the sensor characteristics

for the position, velocity and attitude sensor models can not be directly determined using the datasheet. For these signals, the characteristics are determined by an engineering guess.

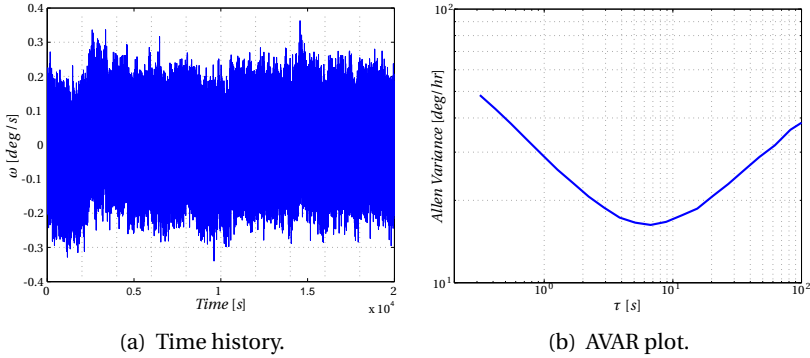


Figure 3.6: Simple sensor model parametrization, $\sigma_x = 0.008$ deg/s, $\sigma_b = 0.0023$ deg/s.

The sensor model, Equation (3.3), does not include terms for temperature effects or scale factor present in many sensors, as these errors are assumed to be removable by preliminary calibration methods. For the accelerometers and gyroscopes the sensor bandwidth can be ignored as well, since these are assumed much faster than the dynamics of the actuators or the aircraft itself. Position, velocity and attitude resulting from the sensor fusion algorithm have much slower dynamics and should be included in the model. Literature suggests that the dynamics of these signals may be modeled as [74],

$$\dot{x}_m = -Bx_m + Bx_{true} \quad (3.7)$$

where x_m is the measured state and B the bandwidth of the signal. Note that when a bandwidth is used, Equation (3.3) should be altered slightly to use x_m rather than x_{true} directly. The sensor characteristics used in the aircraft model are listed in Table 3.1 and a block diagram of the sensor model is shown in Figure 3.7. Note that $N_2\sigma_x$ produces the high frequent measurement noise and that $N_1\sigma_b\frac{\gamma}{\gamma s+1}$ results in the lower frequent process noise of the sensors.

The air-data boom used in the SAFAR platform is shown in Figure 3.8. The IcaSim air-data boom is a flush air-data sensor, with accurate readings for angle of attack and angle of sideslip in a narrow range. Unfortunately a high fidelity model for this sensor was not available and therefore again the sensor model in Equations (3.3) and (3.7) is used. The IcaSim datasheet does not supply detailed sensor characteristics [111], but luckily one of these sensors could be piggy-bagged on a DA 42

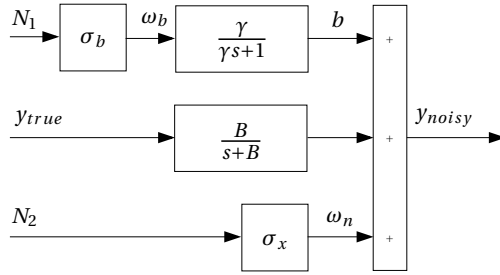


Figure 3.7: Block diagram of a sensor model.

test flight. After flight-data analysis, sensor experts from Honeywell determined the noise characteristics for the IcaSim air-data sensor. The bandwidth for the air-data boom is chosen at 50 rad/s, as suggested by Magni *et al.* [74].



Figure 3.8: IcaSim Air-data boom manufactured by SimTec.

Table 3.1: Equivalent sensor characteristics for the fused states.

Measured State	Init. Bias	σ_x	γ [s]	σ_b	B [rad/s]
ω [deg/s]	0.2	0.008	300	0.0023	∞
ϕ, θ, ψ [deg]	0.2	0.01	50	0.02	40
A_E [m/s ²]	0.004	0.003	300	0.0005	∞
V_E [m/s]	0.2	0.01	5	0.06	10
X_E [m]	0.5	0.1	200	0.18	1
V_{TAS} [m/s]	0.6	0.4	N/A	N/A	50
α, β [deg]	0.6	0.12	N/A	N/A	50

3.2.5 Core Processing Module

Two CPMs are used in the platform for redundancy reasons. Inside each CPM two identical lanes are present, performing the same calculations. The results of both lanes are compared and when differences occur, the CPM sets itself into a passive state converting control to the other CPM. For this reason, the states of the integrators used in the FCLs are shared between the CPMs and should be a part of the FCL input and output data streams.

The processors in the CPMs are optimized for single precision operations. This means care must be taken when a FCL is designed that uses many finite precision matrix manipulations [49]. Work is done in the field of automatically testing whether the control laws in finite precision closely match the intended operations [7], but for SAFAR this test is done manually.

Also the instruction set usable on the CPMs is limited to instructions available to the MATLABs Real-Time Workshop Embedded Coder. This means only discrete blocks may be used in the Simulink model and that first-order hold is not supported. For more information, the interested reader is referred to the Real-Time Workshop Embedded Coder user guide [75].

3.2.6 Input Output Modules

The input devices (side-stick and throttle), the control effectors (actuators and engine controllers) and the measurement devices (GNSS receivers, IMUs and air-data probes) all connect to the CPM through IOMs. Each IOM acts as a gateway to the platform and has no knowledge of other platform components. Its function is to provide some pre-processing and data (un)packing to allow external devices to be interfaced to the CPMs. The only impact that the IOMs have on the FCL design is that they delay the signals. Section 3.3 comments on the time delays present inside the SAFAR platform in more detail.

3.3 Platform Delays

This section comments on the time-delays caused by the FBW platform that must be taken into account in the FCL design. The different components and connections within the SAFAR FBW platform cause different types of delays. The influence of each type of delay will be investigated in Chapter 4. Because the platform itself has an update frequency of 62.5 Hz, each time step in the platform will take 16 ms. For FCL design in the SAFAR project the following delays are used:

- Reference delay, from pilot commands to the FCLs, $2t_s = 32$ ms.
- Actuator delay, from the FCLs to the aircraft, $3t_s = 48$ ms.
- Measurement delay, from the aircraft to the FCLs, $3t_s = 48$ ms.

It should be noted that during flight test of the SAFAR demonstrator aircraft delay times (sensor to surface) of 64-80 ms are measured. Furthermore, a significant

part of the delay time is caused by allowing three different sensor fusion approaches to be developed on the SAFAR platform. In case of reducing to a single approach the overall time delay will go down to 32-48 ms, due to reduction of bus load. It should also be noted that for SAFAR the CPU used in the CPM of the platform is the same as used in the IOM and the Actuator Control Model, i.e., it is basically a controller. When the much more powerful CPU, that is currently used in automotive applications, would be used in SAFAR, the time delay reduces to 20-30 ms.

3.4 SAFAR Platform and Simulator Operation

This section describes the intended purpose of the FCLs that will be designed in the remainder of this thesis. Two scenarios are identified, one leading to tight design constraints and one with more relaxed constraints.

The first scenario is the SAFAR demonstrator aircraft. Due to the limited range of validity of the aircraft model developed in Chapter 2 and in order to obtain permission to flight from EASA, the SAFAR platform is only engaged during cruise flight. This means the FCLs should be designed around the operating point at 120 kts and 6,000 ft. Note that for safety reasons, the unvalidated changes in dynamic behavior resulting from velocity and altitude changes should be included in the FCL design but flying into these regions of the flight envelope should not be encouraged. Furthermore, every implication of the FBW platform components must be taken into account, including FCL design restrictions coming from the CPM component.

The second scenario is the simulator environment, in which more maneuverability is possible. The aircraft model is usable in a far larger flight envelope than merely the cruise condition, even including landing. For simulator flights, the validity of the model is not a large issue, but caution is needed when drawing conclusions using these flight. The restrictions imposed by using the CPM in the FBW platform can be relieved, making more academic FCL designs possible. Chapter 5 treats these design options in more detail.

3.5 Certification

As a last aspect of using a FCL design outside a simulation environment, this section will look briefly into certification. Certification of airborne systems is done by the Federal Aviation Authority (FAA) in the US and the European Aviation Safety Agency (EASA) in Europe. Small aircraft with less than nine passengers, excluding the pilot seat(s), are certified using CS-23 [40]. CS-23 does not offer clear criteria on certification of FBW platforms, however. To get some indication for certifica-

tion requirements of a FBW platform, we can look at the certification document for large aircraft, CS-25 [39]. However, this document provides the accepted means of certification rather than the certification requirements themselves. The Radio Technical Commission for Aeronautics (RTCA) and the European Organization for Civil Aviation Equipment (EUROCAE) have jointly written the DO-178B (US) and ED-12B (Europe) documents that are accepted by the FAA and EASA as means for certification [106, 31, 42]. Since most applicants use DO-178B rather than showing that other means are equivalent to DO-178B, the International Organization for Standardization (ISO) officially recognizes DO-178B as the *de facto* standard [115].

DO-178B, or Software Considerations in Airborne Systems and Equipment Certification, is a self-contained document, meaning that no other software standards are referred therein [106]. It consists of twelve sections, two annexes and three appendices. Sections 2 and 10 show the relation of DO-178B to the overall certification procedure. Sections 3, 4 and 5 support the software life cycle process. Sections 6, 7, 8 and 9 provide guidelines to the integration process. Section 11 shows details on life cycle data and Section 12 ends with additional considerations. The document does not provide specific requirements for certification of flight control software, but rather a description of software development processes that should be used in order to end up with software that has been properly verified and validated.

To get an impression on the amount of work needed for certification of a FCL design, first Section 2.2 should be read. Table 3.2 summarizes the contents of this section. Five levels of failure conditions are defined, ranging from catastrophic to no effect, each of which is linked to a Design Assurance Level (DAL) required for the software development. Since failures in the FCL designs have the potential to lead to a large negative impact on safety or performance, or may even lead to a crash, this software may be classified as hazardous or catastrophic. The precise classification depends on the availability of degradational modes of the FBW platform and lies beyond the scope of interest of this thesis. Lower classifications could be obtained by using a mechanical backup, which allows the FCLs to be switched off when failures are detected. Using a mechanical backup in a future personal air transportation system is not an economically viable option, however.

The next step in determining the amount of work required for certification is found in Section 11. This section provides a list of deliverables and their contents that should be provided by the applicant. A few of these deliverables are repeated in Table 3.3. Not every deliverable is needed for each DAL, however. Annex A defines which deliverables are needed and which items of a deliverable are required at each level. Table 3.4 shows the number of deliverables required for each DAL.

Table 3.2: Failure conditions and related software DAL.

Failure condition	Explanation	DAL
Catastrophic	Failure may cause a crash.	A
Hazardous	Failure has a large negative impact on safety or performance, or reduces the ability of the crew to operate the aircraft due to physical distress or a higher workload, or causes serious or fatal injuries among the passengers.	B
Major	Failure is significant, but has a lesser impact than a Hazardous failure (for example, leads to passenger discomfort rather than injuries).	C
Minor	Failure is noticeable, but has a lesser impact than a Major failure (for example, causing passenger inconvenience or a routine flight plan change)	D
No Effect	Failure has no impact on safety, aircraft operation, or crew workload.	E

Table 3.3: Some of the deliverables defined by DO-178B.

	Deliverable	Process
PSAC	Plan for Software Aspects of Certification	Planning
SDP	Software Development Plan	
SVP	Software Verification Plan	
SCMP	Software Configuration Management Plan	
SQAP	Software Quality Assurance Plan	
SDS	Software Design Standards	
SCS	Software Code Standards	Development
SRD	Software Requirements Data	
SDD	Software Design Description Source code Executable object code	
SVCP	Software Verification Cases and Procedures	Verification
SVR	Software Verification Results	
SCI	Software Configuration Index	Configuration management
SECI	Software life cycle Environment Conf. Index	
SQAR	Software Quality Assurance Records	Quality assurance
SCR	Software Conformity Review	
SAS	Software Accomplishment Summary	

Table 3.4: Number of deliverables (objectives) required per software DAL.

DAL	Failure condition	Deliverables
A	Catastrophic	66
B	Hazardous	65
C	Major	57
D	Minor	28
E	No effect	0

From Table 3.4 it is clear that certification of any FCL design, linear or nonlinear, requires a considerable amount of work and is also beyond the scope of this thesis. Moreover, the aircraft model developed in Chapter 2 will not be qualified as a tool usable for FCL design as well. As indicated in Table 3.3 an important document for the development phase in the certification procedure is the Software Requirements Data document. It is possible to make a distinction between certification effort required for linear FCL designs as compared with nonlinear FCL designs, based on this document. For certification of linear FCL designs, requirements, or stability and performance metrics in terms of gain and phase margins, are well known. For nonlinear FCL designs, phase margin has no meaning and cannot be used to evaluate the requirements [55].

Certification of nonlinear FCLs translates into the question: How to quantify how far a nonlinear system is away from instability? Two paths are pursued in answering this question, high fidelity simulation and mathematical analysis [55]. The former method starts with desktop simulation with increasing complexity, such as addition of nonlinear aerodynamics, actuator models, sensor models and structural dynamics. Next, actual hardware is placed in the control loop, such as the flight control computer, cockpit controls and the real sensors and actuators, in a setup called the “Iron-bird”. This may be followed by motion-based simulation, where the simulation is flown by a test pilot who receives both visual and motion feedback of the simulated flight. A last step is testing the new FCLs on a demonstrator aircraft. Instability quantification using mathematical analysis usually involves a Lyapunov based method that guarantees system stability. However, this method only guarantees the ultimate stability of the system and does not indicate how fast this stable situation is reached. The method also relies on analytical evaluation of the closed-loop system. These analytical expressions can be difficult to evaluate, particularly when the nonlinear aircraft model is combined with a FBW platform model. For more details on the Lyapunov analysis of closed-loop systems, the reader is referred to Chapter 5.

Besides presenting software development process guidelines, DO-178B has a focus on safety. Table 3.5 shows the accepted probability of failure for each DAL. You can imagine that achieving an probability of 10^{-9} , or once in a billion flying hours, requires both the FBW platform as well as the FCL designs to be able to withstand failures in hardware and software. The FBW platform needs to be fail-operational for a single failure [107, 15], as discussed in Section 3.3. For the FCL designs requirement can be robustness to model uncertainty, sensor noise, time delays and disturbances and fault tolerance to engine or actuator failures or even structural damage throughout the full extent of the flight envelope. This thesis will focus primarily on the robustness properties of the FCL designs. The thesis of Lombaerts is a good example for the design of a fault-tolerant FCL [71].

Table 3.5: Level System Failure Frequency Description FAR/JAR Definition.

DAL	Failure condition	Failure Probability
A	Catastrophic	Extremely improbable: $P < 10^{-9}$
B	Hazardous	Extremely remote: $10^{-9} < P < 10^{-7}$
C	Major	Remote: $10^{-7} < P < 10^{-5}$
D	Minor	Probable: $10^{-5} < P$
E	No effect	-

3.6 Conclusions

This chapter briefly introduced an affordable Fly-By-Wire (FBW) platform for general aviation aircraft, that will be used in the “Small Aircraft Future Avionics aRchitecture” (SAFAR) project and installed onto a Diamond DA 42. Together with the aircraft model developed in Chapter 2, the FBW platform serves as the definition of the operating environment for the Flight Control Laws (FCLs) and determine the dynamic behavior of the system controlled by the FCLs.

Two target platforms can be identified, each with a different impact on the FCL design options. The first is the SAFAR demonstrator aircraft, for which the FCLs designs should comply to all aspects of the FBW platform, including the requirements posed by the core processing module. The second is the SIMONA Research Simulator, for which the design restrictions can be relaxed, making application of more academic FCL designs possible. For both platforms, the FCL must be designed with robustness to model uncertainty, sensor noise and time delays. The remainder of this thesis focuses primarily on designing and evaluating several FCL designs in a simulation environment. The FCL designs for the demonstrator aircraft are reported in a SAFAR deliverable and derived from the classical FCL designs presented in Chapter 4.

CLASSICAL FLIGHT CONTROL DESIGN

Abstract

This chapter presents six classical Flight Control Law (FCL) designs for the Diamond DA 42. These FCLs are usable in two separate modes, a manually controlled mode and an automatic mode. Evaluating the handling qualities for the unaugmented aircraft shows that no stability augmentation is needed, except for sideslip compensation. The manual control mode therefore consist of a sideslip compensator and additionally uses an autothrottle and a pitch- and roll rate-command/attitude-hold FCL with the aim to simplify aircraft handling. The design of these FCLs focuses on performance in terms of handling qualities and reference tracking and robustness in terms of noise attenuation and disturbance rejection. The automatic mode adds two FCLs that react on the horizontal and vertical deviation to a given reference trajectory. These FCLs are evaluated using general time- and frequency-based metrics.

4.1 Introduction

This chapter uses the aircraft model developed in Chapter 2 and the FBW platform described in Chapter 3 to design the Flight Control Laws (FCLs) for a Diamond DA 42 using classical (linear) control theory. Many books have been written on this subject and this chapter serves partly as a review of that literature. A good starting point for the design of linear FCLs, is the book *Airplane Flight Dynamics and Automated Flight Controls* written by Dr. Jan Roskam [102, 103]. Also the works of K. Ogata [92] and Richard C. Dorf and Robert H. Bishop [26] provide valuable insight, although they focus on general control theory rather than FCL design specifically.

The control theory used in this chapter is not new. Application of this theory to the design of the FCLs for a DA 42 is new, however. The developed classical FCLs will be used on the SAFAR demonstrator aircraft and have to comply with all requirements posed in the previous chapter. Furthermore, with the inclusion of classical FCLs in this thesis, a baseline is created for the nonlinear FCLs documented in Chapter 5. Both of these designs are compared in Chapters 6 and 7.

Section 4.2 starts with the review of several control modes. Section 4.3 provides performance indicators for classical FCLs in order to determine the performance of the FCL designed in this chapter. Section 4.4 uses these performance indicators to show the performance of the unaugmented system. Section 4.5 investigates the influence of the off-nominal conditions defined in Chapters 2 and 3, i.e., model uncertainty, sensor noise and bias, and time delays, on the FCL design. Section 4.6 uses Single-Input-Single-Output (SISO) and Multiple-Input-Multiple-Output (MIMO) representations of the aircraft dynamics to design the FCLs and Section 4.7 ends this chapter with conclusions and recommendations.

4.2 Control Modes

This section presents different FCL designs at a functional level. Flight control software can be used for two purposes, to improve the stability of the aircraft and to improve the ease and safety of controlling of the aircraft [103]. Both types of FCL designs are treated in this section.

4.2.1 Stability Augmentation

In extreme cases stability augmentation can make an inherently unstable aircraft, such as the F-16, stable [27]. For stable aircraft, such as the DA 42, stability augmentation can be used to increase the damping of undesired dynamical modes, with the goal of increasing safety and travel comfort. Three examples will be discussed

briefly, yaw damping, pitch damping and sideslip-angle-to-rudder feedback. More information on each stability augmentation system can be found in Chapter 11 of the book of Roskam [103].

Yaw Damping

The Dutch roll is an eigenmotion of the aircraft that is commonly experienced as unpleasant. To improve travel comfort, most aircraft are therefore equipped with yaw dampers to improve Dutch roll suppression. The rudder is deflected when a non-zero yaw rate is measured to counter the yawing motion. This setup works well for suppression of the Dutch roll, but also works against a pilot who is trying to set up a constant bank angle turn. There are two solutions to this problem. Either the reference yaw-rate can be computed, requiring more state measurements, or a washout filter is included in the yaw damper design. A washout filter has the following transfer function,

$$H = \frac{\tau s}{\tau s + 1} \quad (4.1)$$

with τ representing the washout time constant. Using this filter the yaw damper will stop working against the pilot to a large extent after a little more than τ seconds. If τ is too small, the yaw damper will not work at all, however. Typically a compromise value of $\tau = 4$ seconds is used [103].

Pitch Damping

Most high performance aircraft suffer from low short period damping at high altitudes and/or low speed flight conditions. To improve this behavior, a pitch damper may be used. This stability augmentation system is highly comparable to the yaw damper, but deflects the elevator when a non-zero pitch rate is measured. Again a computed reference input or washout filter is needed to prevent this system from working against the pilot.

Sideslip-Angle-to-Rudder Feedback

When an airplane is designed with insufficient inherent static directional stability, an sideslip feedback system to the rudder will increase travel comfort. However, a more important use of this mode is for control augmentation. When a turn is initiated by the pilot, both ailerons deflect in opposite direction leading to a difference in lift, due to which the aircraft starts rolling, but also to a difference in induced drag, due to which the aircraft starts yawing. In addition the roll rate itself can be viewed as a difference in vertical velocity of both wings, resulting in a change in local angle of attack and therefore also a difference in induced drag. This combined effect is known as adverse yaw and experienced pilots compensate this motion by

deflecting the rudder. A sideslip-angle-to-rudder feedback controller automatically deflects the rudder when a sideslip angle is measured, thereby making flying easier. Sideslip feedback could introduce a low frequency lateral oscillation, sometimes referred to as the lateral phugoid. Emergence of such an oscillation must be checked in the FCL design.

4.2.2 Control Augmentation

The second purpose for which a FCL can be designed is control augmentation. A pilot wanting to steer an aircraft along a predefined earth-fixed trajectory, mentally has to close three loops (attitude in the inner loop, flight-path vector in the middle loop and position in the outer loop) each having their own constraints and response characteristics [84]. Figure 4.1 shows an approximation of the pilot-aircraft control loop for lateral positioning. A similar figure can be drawn for longitudinal positioning. Besides position control, the pilot also influences the time of arrival at a certain position in a fixed trajectory using the engine throttles. This temporal aspect will become even more important when SESAR's user defined 4D trajectories become operational [16]. Depending on the desired level of automation, a number of these loops can be closed by an autopilot using control augmentation with the aim of making flying easier. This section provides short descriptions of some of these control augmentation systems. Each subsequent control mode that is discussed, increases the level of automation and places the pilot further from active (manual) control of the aircraft.

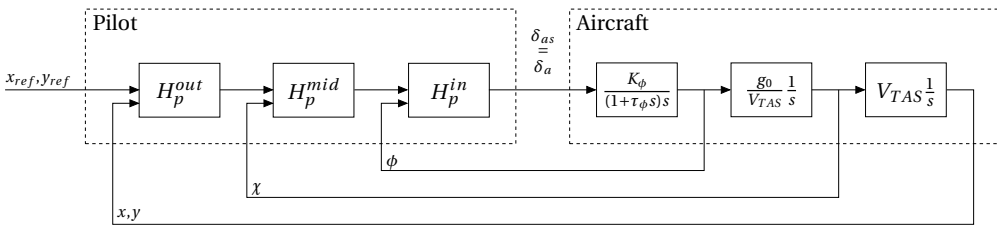


Figure 4.1: Approximation of the lateral pilot-aircraft control loop.

Attitude Command

In the attitude command FCL mode, the pilots stick movements are interpreted as attitude commands, as shown in Figure 4.2. The attitude controller, on-board the FBW platform, will try to minimize the error between the commanded reference attitude and the measured attitude of the aircraft. This FCL mode changes the way the pilot interacts with the aircraft significantly. For example, a turn in this control mode would require a constant deflection.

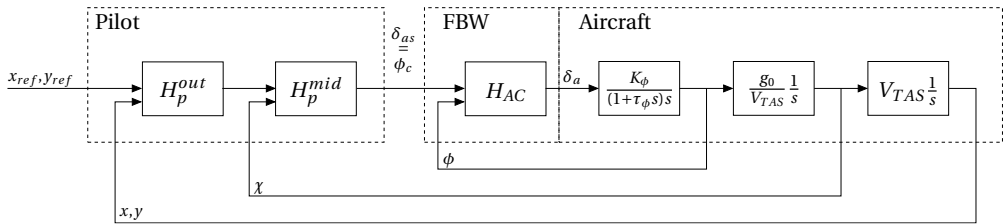


Figure 4.2: Lateral pilot-aircraft control loop approximation with attitude control.

Attitude Rate Command

In order to make the pilot-aircraft interaction more similar to that of the unaugmented aircraft, the pilots stick movements are interpreted as attitude rate commands in the attitude-rate-command FCL mode. These attitude rate commands are integrated and used as a reference value for the attitude angles. When the pilot is not applying any stick input, the current reference attitude is held and this FCL mode is therefore also known as the Rate Command/Attitude Hold (RCAH) mode. In this way, disturbances on the aircraft attitude are canceled automatically and the control becomes decoupled. For example, when initiating a turn, the pilot only needs to deflect the stick laterally, because the pitch down motion of the aircraft is automatically canceled when the pitch reference is not changed [85]. A drawback of this method is that speed stability is removed. When a large pitch reference is given, the aircraft decelerates even when the throttle setting is set at its maximum. To prevent the aircraft from stalling, Flight Envelope Protection (FEP) should be added to push the nose down in this situation. Chapter 6 treats FEP in more detail.

Airbus uses a mode similar to the RCAH in longitudinal control (pitch). The C* (pronounced “C-star”) control law, used in the A320/330 and 340, blends the control of pitch rate and load factor. At low speeds pitch rate is the controlling factor, meaning that for low speeds a certain stick deflection results in a certain pitch rate, which is the same as the RCAH law. At high speeds the load factor dominates the control. The C* control law is reported to result in reduction in pilot workload, to have the possibility of generating a family concept, in which a range of aircraft have similar handling qualities, and to have the option of adding FEP [37].

Boeing uses an extension of this mode, the C*U control law, in the 777. The added “U” term denotes that any speed change away from the trim speed will cause a pitch change to return to the trim speed. In other words, this additional property restores speed stability to the C* control mode [115].

Flight Path Vector Rate Command

Closing another control loop using a control law results in a flight-path-vector-rate-command mode, as shown in Figure 4.3. Again the stick inputs are integrated, here resulting in a flight-path-vector reference. By closing both the inner and middle control loops using FCLs, the pilot can fly the aircraft using where-to-go commands. Since late 1970s NASA is working on these types of control systems and successful implementation is achieved in the Boeing 7J7, although the aircraft itself was never actually build [85].

Note that this control mode also changes the pilot-aircraft interaction considerably. The flight-path-vector cannot be determined by looking outside (head up) and therefore it must be controlled by looking at the primary flight display (head down). For example, if the aircraft is pitched up, such that the nose is pointing above the horizon, but with a negative vertical velocity, then the flight-path-vector would point below the horizon. The primary flight display should therefore show a flight-path-vector symbol that is controlled by the pilot, and indicates the reference that is tracked by the FCL. Without this symbol, or when loosing focus on this symbol, the control mode is reported to cause pilot involved oscillations, due to lack of reference [14].

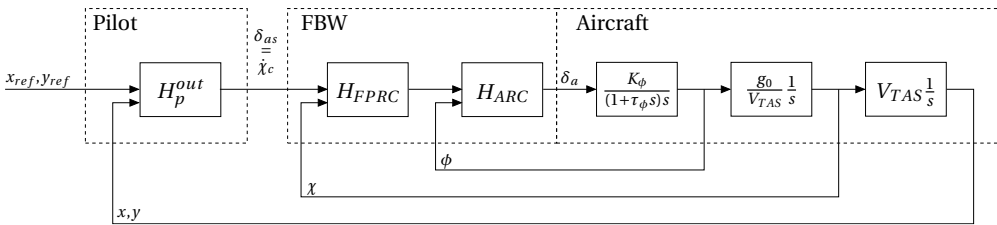


Figure 4.3: Lateral pilot-aircraft control loop approximation with flight path vector rate control.

Lateral Navigation and Longitudinal Navigation

Closing yet another control loop, removes the pilot from direct interaction with the aircraft, as shown in Figure 4.4. In this control mode the pilot only sets way points and the FCL will make the aircraft fly towards these points. An example of a lateral navigation control mode is the localizer intercept and hold, found on many aircraft. Longitudinal navigation examples are the glideslope intercept and hold, the flare mode and the landing mode.

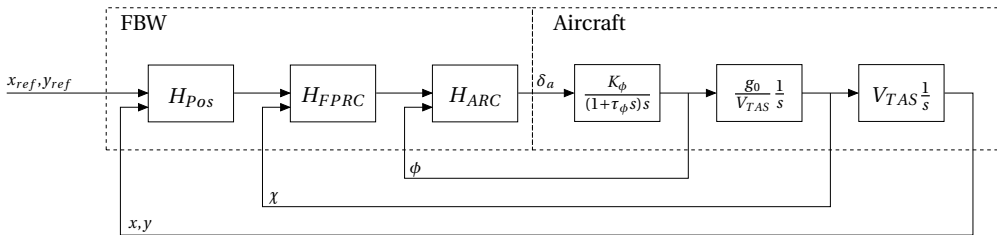


Figure 4.4: Lateral pilot-aircraft control loop approximation with automated lateral navigation.

3D Trajectory Following

An extension of the previous control mode is the 3D trajectory following mode, in which the lateral navigation and longitudinal navigation modes are combined. In this mode, the aircraft will automatically follow a 3D trajectory. This trajectory may come from the Flight Management System (FMS) and could be optimized to save fuel or time.

4D Trajectory Following

The 4D trajectory following mode fully automates the control of the aircraft. In this mode, not only the position is completely controlled by the FCL, but also the speed. The SASAR 4D trajectory can therefore be followed without any interaction of the pilot. This mode seems to be perfect to negate human errors, but there are drawbacks. Section 4.2.3 comments on these drawbacks of automation.

Total Energy Control

Instead of controlling position and velocity, Lambregts envisioned another control strategy, called the Total Energy Control System (TECS) [66, 32]. As implied by the name, this mode lumps the kinetic and potential energy together and controls this state using both the elevator and throttle. After numerous variations of the TECS design, the best overall configuration was found to be one in which the thrust command is determined from the energy rate demand, using the sum of flight path angle error and longitudinal acceleration error, and the elevator command from the energy rate distribution error, using the difference between longitudinal acceleration error and flight path angle error. The advantages of using TECS are that it results in a fully integrated system that has predictable consistent performance in all operating modes and that a part of the design is aircraft independent and therefore reusable [17]. Although research into this control mode is ongoing for the past 30 years, practical use in commercial aircraft could not be found in literature.

Hold Modes

Besides the side-stick or column and throttles, there are additional knobs and wheels in the aircraft cockpit to select reference values for hold modes, such as, altitude hold, speed/Mach hold and climb or descent rate hold. More information on these modes can be found in [103].

4.2.3 Cost of Automation

As mentioned in the 4D Trajectory Following control mode, full automation of the control task seems perfect to negate human errors. However, people are still involved in designing and using automation. When using automation, the effect of the human error changes and can be moved further into the future. The coupling between human input to machine output is loosened and a few human inputs can lead to machine output during many hours. This makes it more difficult to detect mismatches between human intention and process behavior [45]. An example of such a mismatch, where the pilots lost track of the automation mode changes, is the crash of Air Inter Flight 148. The pilots of the Airbus A320 inadvertently left the autopilot in Vertical Speed mode, instead of the intended Flight Path Angle mode, and then entered “33” for a 3.3° descent angle. The autopilot interpreted this command as a descent rate of 3,300 ft/min and crashed the aircraft in the Vosges Mountains [10].

The previous section showed that automation can be used to make the aircraft easier to fly. When closing more inner control loops, the level of automation is increased, creating more distance between the pilot and the manual flying task. In other words, automation hides flying complexity. In case of an unanticipated event such as, sensor, software or airframe failures or local weather phenomena, the automation may take the wrong actions or return to a deprecated mode. Because the pilot is not actively in the control loop anymore, the errors in automation may not be noticed in time and could result in accidents. The crash of Air France Flight 447 is an example of this. Due to a faulty velocity sensor, the FEP was disabled by automation while reverting to a deprecated mode. The pilots, unaware of this fact, pulled the stick in order to make the aircraft climb. Because FEP was disabled, the pilot input resulted in a stall situation in which the aircraft lost altitude, rather than gained it, and finally the aircraft crashed in the Atlantic Ocean [11].

Of course automation is intended by the control engineer to enhance safety and the ease of flying. Years of experience in commercial aviation has thought us, that the best intentions are sometimes accompanied by unanticipated problems. When designing FCLs for a general aviation aircraft this side note should not be forgotten.

4.3 Performance Metrics

In order to compare different implementations of the same control mode, a proper definition of FCL performance is required. This section first provides performance metrics intended for control modes without control augmentation. When the level of control augmentation increases many of these metrics become less applicable and when the pilot is not actively in the control loop anymore, the FCL designer should use more general performance indicators. These more general metrics are discussed second. Besides performance, the safety of each implementation must be evaluated. This is done using stability and robustness metrics, which are discussed in Section 4.5. Note that the performance and robustness metrics described in this chapter are intended for linear FCLs. Metrics for nonlinear FLCs are discussed in Chapter 5.

4.3.1 Performance Metrics for Manually Controlled FCLs

Specifications for performance metrics, or handling qualities, of manually (or actively) controlled linearized models of military aircraft are given in [79] and [80]. The handling qualities for a DA 42 type aircraft are documented in [19] and [56], but these sources provide fairly general terms and only few numerical guidelines. Therefore the military guidelines are used to evaluate the performance of the FCLs determined in this chapter. The civil aviation authorities often take the same approach in the process of certification [102]. Using the performance metrics described in this section, it is also possible to determine the performance of the manually-controlled unaugmented aircraft and see whether stability augmentation is required in the FCL design.

The aircraft model defined in Chapter 2 could only be validated for a single operating condition of 120 kts at 6,000 ft and in cruise configuration. Therefore, the practical use of the FCLs developed in this chapter is also restricted to the non-terminal flight phases that are accomplished using gradual maneuvers, i.e, category B of MIL-STD-1797A and MIL-F-8785C. The requirements presented in this section are valid for class I (small and lightweight) aircraft in flight phases of category B. Readers interested in handling qualities for categories A and C are referred to MIL-STD-1797A and MIL-F-8785C.

Three levels of handling qualities are defined by MIL-F-8785C, where level I indicates that the handling qualities are clearly adequate for the mission and level III that the aircraft is safely controllable, but the pilots workload will be excessive. In this section the handling qualities for the nominal FCL will be presented, which has to comply to level I.

A part of the requirements on the handling qualities deal with the dynamic behavior of the aircraft in relation to the forces on the pilot controls. This part is not included in this section, because the design of the side-stick, or stick shaping, is considered to be outside the scope of this thesis.

Longitudinal Handling Qualities

Page 171 of MIL-STD-1797A states that any oscillation in the pitch angle longer than 15 seconds, should have a damping ratio, ζ_{ph} , larger than 0.04. This damping ratio is determined from the equivalent 3-DOF transfer function, also referred to as the Low Order Equivalent System (LOES) description,

$$\frac{\theta(s)}{\delta_{es}(s)} = \frac{K_{\theta}(s + 1/T_{\theta_1})(s + 1/T_{\theta_2})e^{-\tau_e s}}{\left[s^2 + 2\zeta_{ph}\omega_{ph}s + \omega_{ph}^2\right] \left[s^2 + 2\zeta_{sp}\omega_{sp}s + \omega_{sp}^2\right]} \quad (4.2)$$

in which the parameters can be determined from a (locally) best-fit match to the actual frequency response of the High Order System (HOS). The difference in frequency response over a number of equi-spaced frequency points on a logarithmic scale between 0.1 and 10 radians per second, is defined by [51] as,

$$M = \Sigma (G_{HOS} - G_{LOES})^2 + K \Sigma (\phi_{HOS} - \phi_{LOES})^2 \quad (4.3)$$

in which M is the difference, G is the magnitude in dB, ϕ is the phase in degrees and K is a weighing factor of around 0.02. Note that for some HOS, the phase is shifted over n times 360 degrees with respect to the LOES. This offset must be compensated before the difference is calculated. The (locally) best-fit match is found using MATLAB's *lsqnonlin* method, which uses a trust-region-reflective algorithm. This algorithm is a subspace trust-region method and is based on the interior-reflective Newton method described in [21, 22]. More detailed information on parameter estimation, including determination of parameter accuracy and the degree of parameterizability using the Fischer information matrix, can be found in [105]. Further, the optimization method used in this thesis to find the LOES descriptions produces good results, but if a global best-fit match is needed other algorithms, such as interval analysis [129], can be used.

In case a FCL is designed that removes the phugoid from the dynamic behavior of the aircraft, MIL-STD-1797A also provides a LOES description without the poles and zeros related to the phugoid,

$$\frac{\theta(s)}{\delta_{es}(s)} = \frac{K_{\theta}(s + 1/T_{\theta_2})e^{-\tau_e s}}{s^2 + 2\zeta_{sp}\omega_{sp}s + \omega_{sp}^2} \quad (4.4)$$

Short period oscillations should be damped with a ratio, ζ_{sp} , between 0.3 and 2.0. This damping ratio is determined using the derivative of the transfer function in Equation (4.2),

$$\frac{q(s)}{\delta_{es}(s)} = s \frac{K_{\theta}(s + 1/T_{\theta_1})(s + 1/T_{\theta_2})e^{-\tau_e s}}{\left[s^2 + 2\zeta_{ph}\omega_{ph}s + \omega_{ph}^2\right] \left[s^2 + 2\zeta_{sp}\omega_{sp}s + \omega_{sp}^2\right]} \quad (4.5)$$

in which again the parameters are determined by a best-fit match to the HOS.

MIL-F-8785C states a requirement on the short period natural frequency, ω_{sp} , that depends on the gust- or load-factor-sensitivity $n_{\alpha} = \partial n / \partial \alpha$. Using,

$$n_{\alpha} = \frac{L_{\alpha}}{W} = \frac{\bar{q}C_{L_{\alpha}}}{W/S} \quad (4.6)$$

this parameter can be determined with some knowledge about the aircraft. For a DA 42 weighing 15.5 kN and flying at 6000 ft, the gust- or load-factor-sensitivity reduces to, $n_{\alpha} = 0.0033V_{TAS}^2$. For level I handling qualities, $0.3\sqrt{n_{\alpha}} \leq \omega_{sp} \leq 2\sqrt{n_{\alpha}}$. MIL-STD-1797A defines the requirements on the short period natural frequency in a slightly different way. The Control-Anticipation-Parameter (CAP) is written as,

$$CAP = \frac{\omega_{sp}^2}{n_{\alpha}} \quad (4.7)$$

and should lie between 0.085 and 3.6 for level 1 handling qualities. Since n_{α} is positive, the CAP requirement can also be written as, $\sqrt{0.085n_{\alpha}} \leq \omega_{sp} \leq \sqrt{3.6n_{\alpha}}$ and is therefore nearly identical to the requirements posed by MIL-F-8785C.

MIL-STD-1797A also puts a requirement on the equivalent pitch time delay, τ_{θ} . For level I handling qualities the maximum time delay is 0.1 seconds. Adding a flight control system that processes the pilot's inputs and calculates required control surface deflections will contribute to this time delay and therefore time consumption of this system should be minimized.

Please keep in mind that these values are valid for the level I handling qualities of a class I aircraft in flight phase category B only. Other flight phases and other types of aircraft have different requirements for each handling quality level.

Lateral Handling Qualities

Page 424 of MIL-STD-1797A provides a LOES for a conventional roll rate response of an aircraft,

$$\frac{p(s)}{\delta_{as}(s)} = \frac{Ks \left(s^2 + 2\zeta_{\phi}\omega_{\phi}s + \omega_{\phi}^2 \right) e^{-\tau_{ep}s}}{(s + 1/T_s)(s + 1/T_r)(s^2 + 2\zeta_d\omega_d s + \omega_d^2)} \quad (4.8)$$

in which the parameters are determined by a (locally) best-fit match to the HOS.

MIL-F-8785C provides requirements for the dutch roll damping and natural frequency in section 3.3.1.1. The damping, ζ_d , should be at least 0.08, the natural frequency, ω_d , should be at least 0.4 and the product of both should exceed 0.15.

MIL-F-8785C also provides requirements for the roll subsidence and spiral mode time constants. The roll subsidence mode time constant, T_r , should be smaller than 1.4 seconds. For an unstable spiral, $T_s < 0$, the time to double amplitude, T_2 , must be larger than 20 seconds for level I handling qualities. The relation between T_2 and T_s can be derived as,

$$e^{-(t+T_2)/T_s} = e^{-t/T_s} e^{-T_2/T_s} = 2e^{-t/T_s} \quad (4.9)$$

$$T_2 = -T_s \ln(2)$$

This means the spiral mode time constant, T_s , should be larger than -28.85 seconds.

In some cases the roll subsidence mode and spiral mode can become coupled. In this case the LOES in Equation (4.8) should be changed to,

$$\frac{p(s)}{\delta_{as}(s)} = \frac{Ks \left(s^2 + 2\zeta_\phi \omega_\phi s + \omega_\phi^2 \right) e^{-\tau_{ep}s}}{(s^2 + 2\zeta_{rs} \omega_{rs} s + \omega_{rs}^2)(s^2 + 2\zeta_d \omega_d s + \omega_d^2)} \quad (4.10)$$

The coupled mode, or lateral phugoid, is permitted as long as the product of natural frequency, ω_{rs} , and damping, ζ_{rs} , exceeds 0.5.

After a step command on the aileron or the roll controller, the roll rate oscillations can be obtained from the HOS, from the full nonlinear system, or from measured flight test data. There are two requirements on this oscillating motion. First, the roll rate at the first minimum after the first peak should exceed 25% of the roll rate at the first peak and have the same sign for level I handling qualities. Second, the ratio between the oscillatory component and the average component of the roll rate, p_{osc}/p_{av} , should comply to Figure 4.5. The ratio can be calculated as follows,

$$\frac{p_{osc}}{p_{av}} = \begin{cases} \frac{p_1 + p_3 - 2p_2}{p_1 + p_3 + 2p_2} & \text{if } \zeta_d \leq 0.2 \\ \frac{p_1 - p_2}{p_1 + p_2} & \text{if } \zeta_d > 0.2 \end{cases} \quad (4.11)$$

with p_1 , p_2 and p_3 being the roll rates at the i -th peak, positive and negative, in the roll rate response. This latter requirement applies to step commands up to the magnitude that causes a 60 degrees bank angle in $1.7 T_d$ seconds, where the Dutch roll damped period, $T_d = 2\pi / (\omega_d \sqrt{1 - \zeta_d^2})$.

Bank angle oscillations following from an impulse command on the roll control, ϕ_{osc}/ϕ_{av} , are restricted in similar fashion and are also shown in Figure 4.5.

Limitations on the sideslip angle following from a step roll control command are presented as a maximum increment, $\Delta\beta$, occurring within a time window of $T_d/2$ or 2 seconds, whichever is longer. MIL-F-8785C defines requirements for large inputs, where the step input should be held until the bank angle changed at least 90 degrees. These requirements are 10 degrees maximum increment per k for adverse sideslip, where a right roll control command causes right sideslip, and 3 degrees maximum increment per k for proverse sideslip, where a right roll control command causes left sideslip. The parameter k is a ratio between the roll control command and a roll control performance requirement, $k = \phi_{cmd}/\phi_{req}$. For a DA 42, the performance requirement, ϕ_{req} , is 60° in 1.7 seconds. MIL-F-8785C also defines requirements on the maximum sideslip increment for small inputs, up to the magnitude which causes a 60 degrees bank angle change, within $T_d/2$ or 2 seconds, whichever is longer. All three requirements on the sideslip angle are depicted in Figure 4.5.

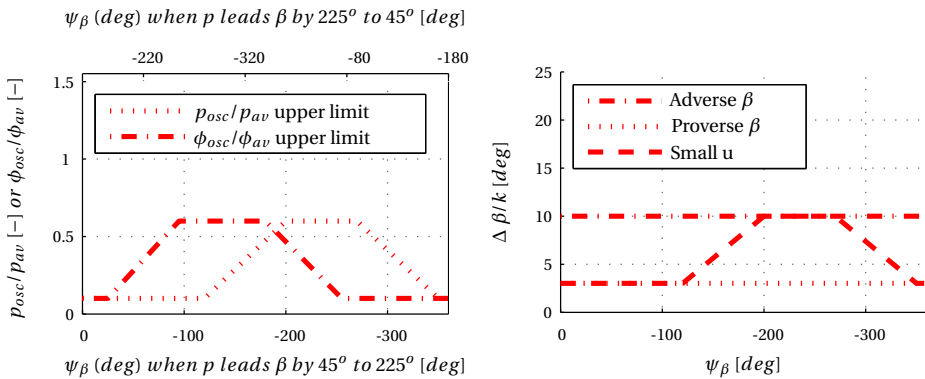


Figure 4.5: Roll (rate) oscillation requirements and sideslip requirements.

4.3.2 Performance Metrics for Automatic FCLs

For automatic (or passively controlled) FCLs, more general performance metrics must be used. These metrics exist in both the time domain and the frequency domain. For example, rise time, peak time, settling time, percent overshoot, and steady state error are important time domain indices and resonance peak and bandwidth are valuable frequency domain indices [26].

Figure 4.6 shows performance indicators in the frequency domain [103]. The resonance peak M_p at the resonance frequency ω_p , is defined as the maximum value

of magnitude of the closed loop system response. Large values of M_p imply large oscillatory overshoots and poor transient time domain behavior of the system. Generally the behavior is acceptable, when $1 \leq M_p \leq 1.7$ dB. The cut-off frequency ω_c is defined at the frequency for which the magnitude of the close loop system has dropped 3 dB and the range of frequencies until the cut-off frequency is called the bandwidth. Increasing the bandwidth implies less attenuation of the reference signal, more effective disturbance rejection, and a faster response [101]. The gain and phase margins are robustness metrics and will be described in Section 4.5.

Figure 4.7 shows performance indicators in the time domain domain for the transient part of the response to a unit step input [103]. The overshoot is determined from the maximum difference between the transient response and the steady state response of the aircraft to a unit step input. The delay time T_d is defined as the time required for the output to reach 50% of the steady state value and the rise time T_r as the time required for the response to rise from 10% to 90% of the steady state value. The settling time indicates the time at which the transient part died out sufficiently to keep the response within 5% of the steady state value. The transient performance is sometimes also compacted into a single metric, such as the Integral Square Error index [68],

$$ISE = \int_0^T (x(t) - x_{ref}(t))^2 dt$$

the Integral Time Absolute Error index,

$$ITEA = \int_0^T t|x(t) - x_{ref}(t)|dt$$

or the normalized transient performance metric [117],

$$M = \frac{\|x(t) - x_{ref}(t)\|_{\infty}}{\|x_{ref}(t)\|_{\infty}}$$

which requires specification of the reference dynamics rather than a target value. Using only one of these metrics would hide specific strengths and weaknesses of the FCL under evaluation. Instead every metric is used to demonstrate FCL performance in this thesis.

Besides performance indicators for the transient part of the response, other indicators can be defined for the steady state part of the response. The steady state error describes the difference between the reference signal and the output signal

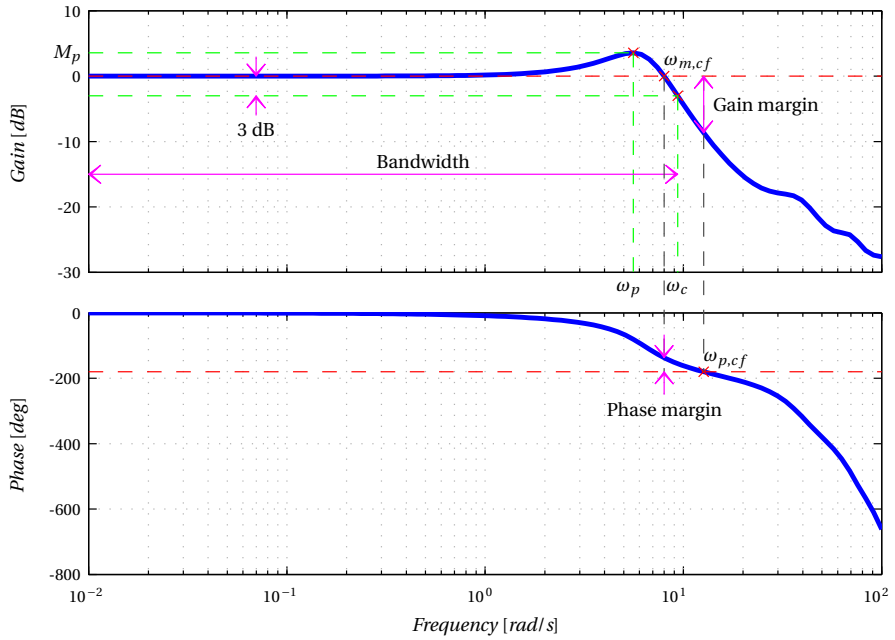


Figure 4.6: Indicators in the frequency domain.

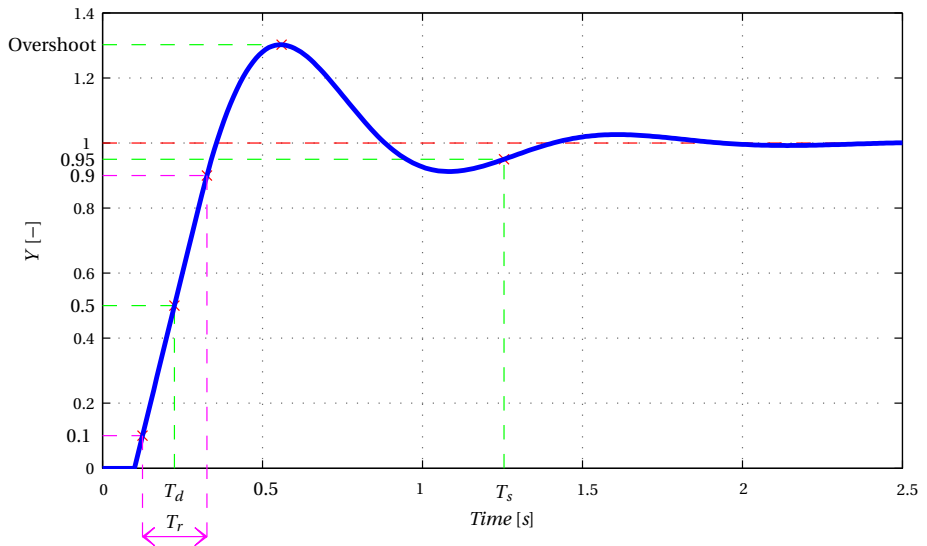


Figure 4.7: Transient performance indicators in the time domain.

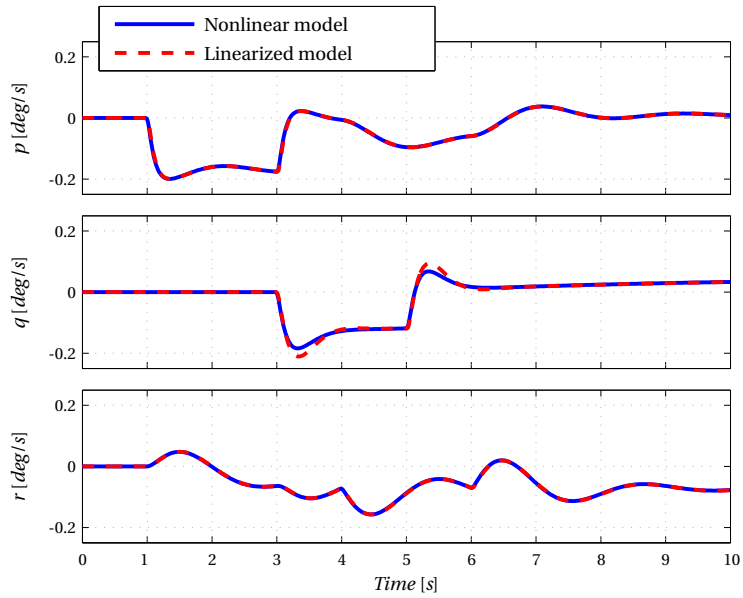
when the transient part of the response has died out. The steady state error is usually defined for a step input, a ramp input and a parabolic input. The resulting error is called the position error, velocity error and acceleration error respectively for these inputs. The normalized transient performance metric can also be used to evaluate steady state performance. In this case, the metric should be evaluated over a time interval corresponding to the steady state behavior of the system [117].

4.4 Performance of the Unaugmented System

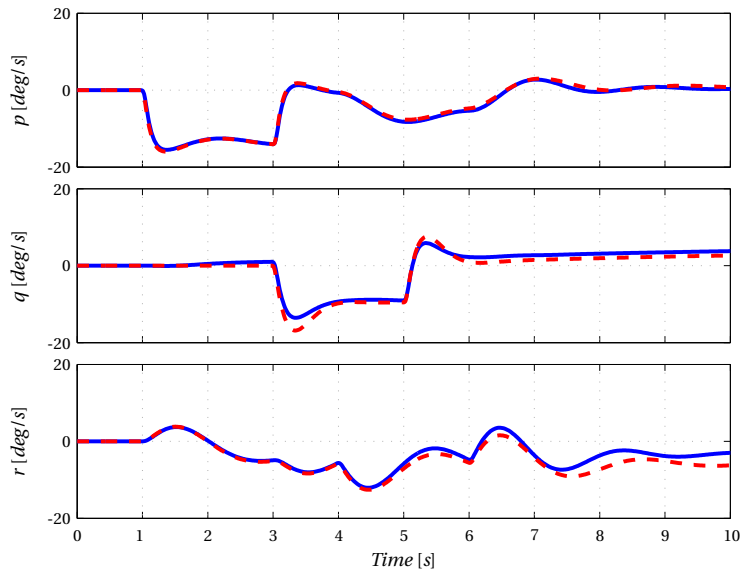
This section describes the performance of the unaugmented system. This system is defined using the aircraft model created in Chapter 2 and the FBW platform described in Chapter 3. Unaugmented means that the pilots inputs are directly fed to the actuators and can be seen as control surface deflection commands. This stick-to-surface FCL mode is also referred to as the direct law (DRCT). DRCT law does not manipulate the command signal and is therefore not influenced by model uncertainty or sensor dynamics. Application of the FBW platform does introduce some time delay in the order of 80 ms, however. The performance of the unaugmented system is determined by the handling qualities introduced in the previous section. This procedure is repeated for several points in the flight envelope defined as $80 \leq V_{TAS} \leq 160$ kts and $2,000 \leq h \leq 12,000$ ft. It should be noted that the model validity was only demonstrated at 120 kts, 6,000 ft and in cruise configuration. The handling qualities obtained for other points in the flight envelope should therefore be used with caution.

In order to determine the performance of the unaugmented system, the nonlinear system first needs to be linearized. Simulink uses pre-programmed Jacobian matrices in the so-called block-by-block exact linearization method. The blocks that do not have analytical linearization representations are linearized using the numerical perturbation method that can be found in [76]. The validity of the linearized system can be determined by comparing a time history of the aircraft dynamics. Figure 4.8 shows the angular rates of the nonlinear system and the linearized system resulting from singlets on the different control surfaces at a true airspeed of 120 kts and an altitude of 6,000 ft. Nearly identical responses are obtained for small inputs as shown in Figure 4.8(a) and even when larger inputs are used, the responses are quite similar as shown in Figure 4.8(b).

The linearized system is a collection of HOS, that need to be fitted onto LOES descriptions in order to determine the systems handling qualities. This is done using the method provided in Equation (4.3). As example, Figure 4.9 shows that a close match is found for the transfer function, $q/\delta_e(s)$, at 120 kts and 6,000 ft.



(a) $A = 0.1$ deg



(b) $A = 8$ deg

Figure 4.8: Comparison between the nonlinear and linearized system, using two second singlets on the aileron, elevator and rudder with an amplitude A .

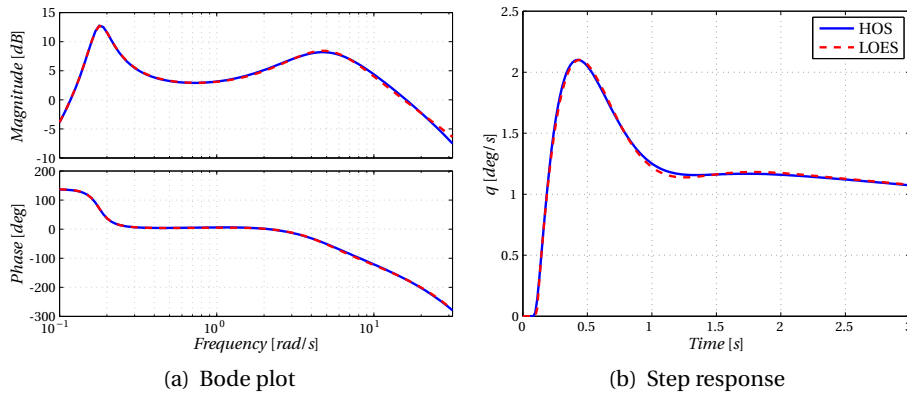


Figure 4.9: Fitting the High Order System (HOS) of the pitch rate response, $q(s)/\delta_{es}(s)$, onto a Low Order Equivalent System (LOES), system (4.5).

The longitudinal and lateral performance of the manually controlled unaugmented system is shown in Figures 4.10 and 4.11 respectively. The bottom left plot in Figure 4.10 shows that the addition of the FBW platform introduces too much time delay. Without the FBW platform the aircraft dynamics has 28 ms equivalent pitch delay and addition of 80 ms introduced by the platform itself, puts the total over 100 ms delay. The level 2 handling quality requirement for this indicator is 200 ms delay, which indicates that 108 ms delay will not result in terrible handling qualities, but merely not perfect. The bottom right plot shows that the short period natural frequency is also on the high side for many points in the flight envelope. For the FCL design point, at which the aircraft model has been validated, the level 1 requirement is met, however. The sideslip angle following from a step roll control command shown in the bottom right plot of Figure 4.11 seems to be inadequate. When turning this aircraft, the pilot must be aware of the sideslip buildup and counter this with rudder control actions. All other performance indicators are satisfactory. This result is not surprising, since the aircraft has been certified and complies to regulations.

4.5 Robustness and Stability Metrics

This section identifies four factors that influence the FCL design. These factors deteriorate the nominal closed loop performance of the FCL, defined using the performance metrics. For certification purposes it should be clear how large each factor may be before system stability is compromised (stability margins). Here, a stable system is defined as a system that has a bounded (limited) system response to a bounded input [26]. It is also important to know how sensitive the system perfor-

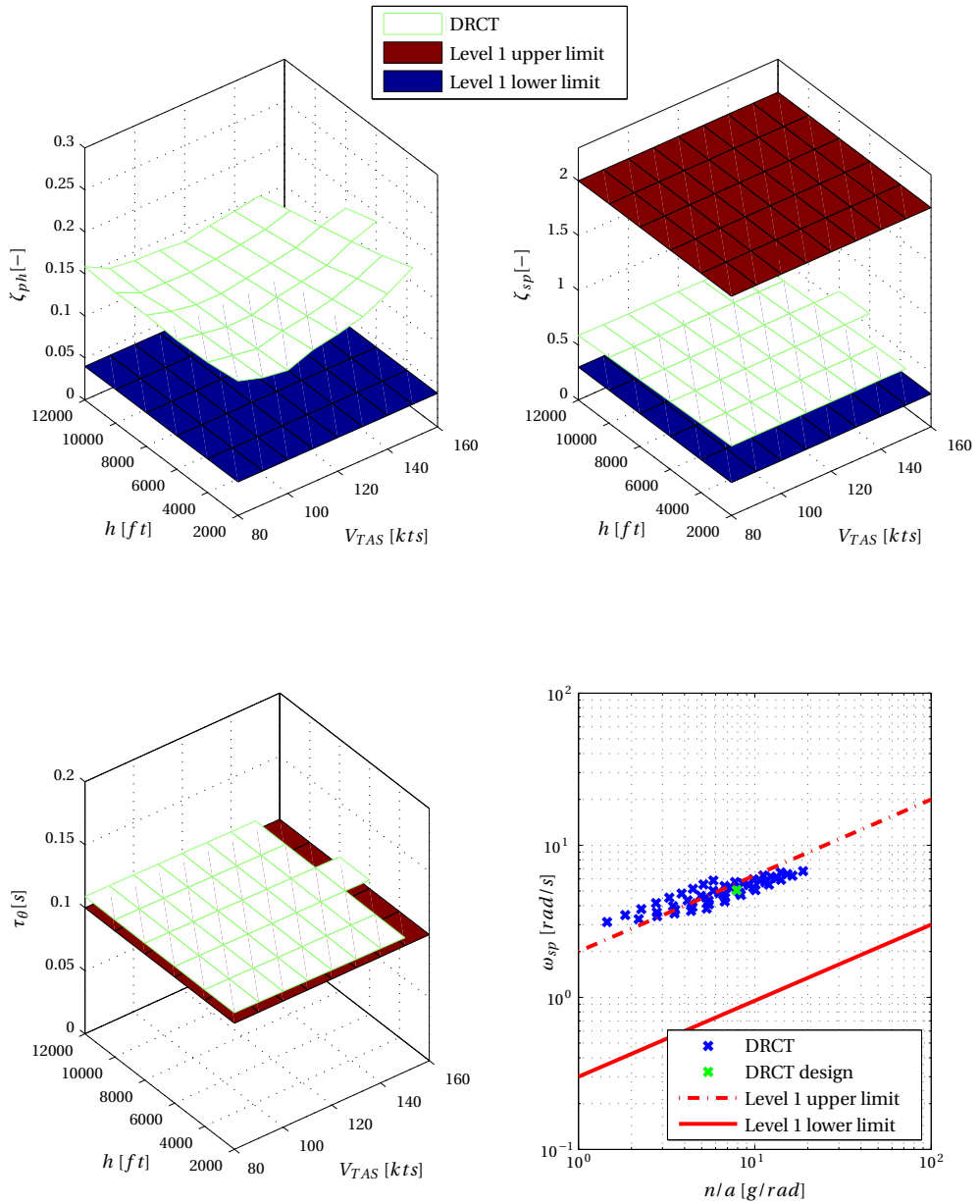


Figure 4.10: Longitudinal performance of the unaugmented system.

4. CLASSICAL FLIGHT CONTROL DESIGN

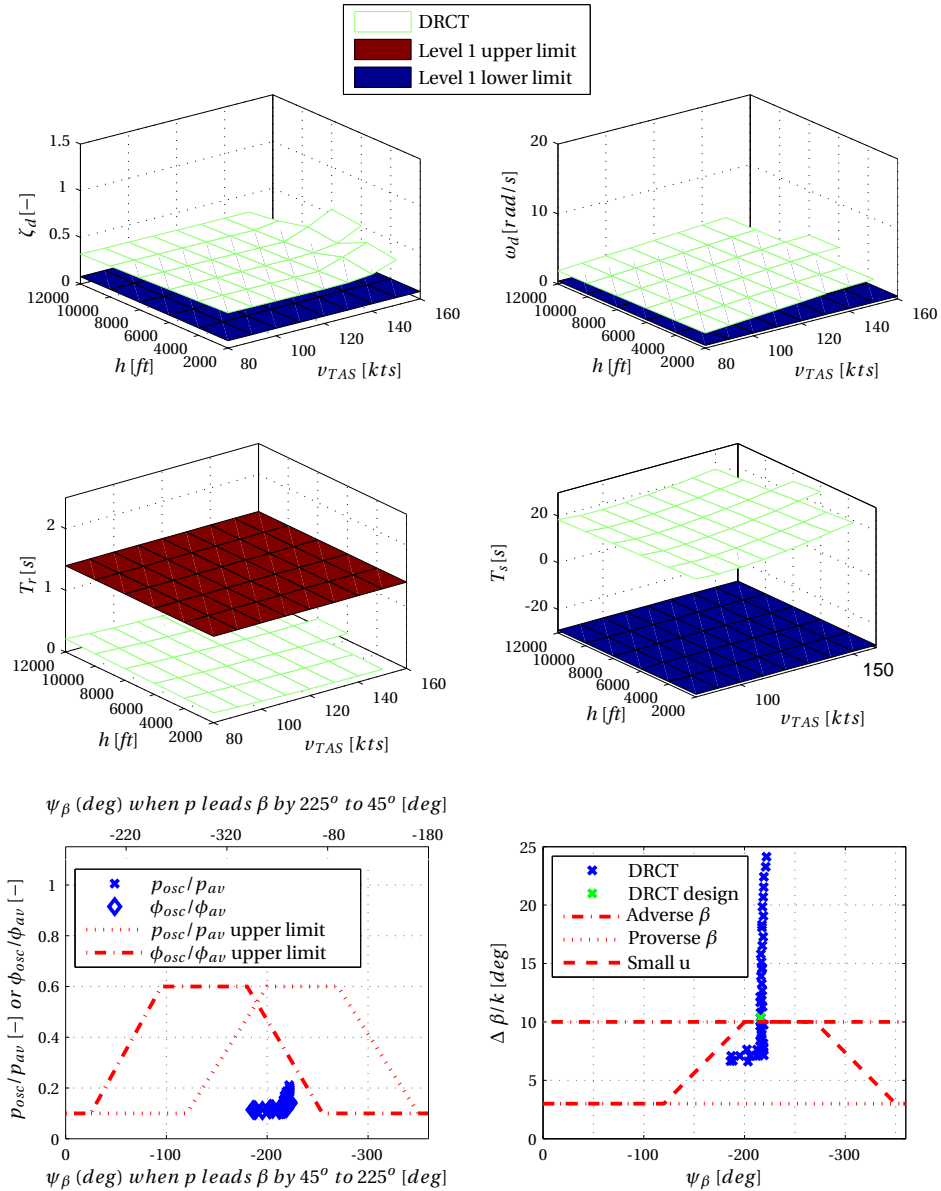


Figure 4.11: Lateral performance of the unaugmented system.

mance is to off-nominal conditions (robustness metrics). Off nominal is defined in this context as operating under dynamic-behavior conditions other than the conditions for which the controller was synthesized. Figure 4.12 shows a block diagram of the linearized aircraft model with FBW platform $G(s)$, the flight control laws $C(s)$, a reference signal $R(s)$, a disturbance signal $D(s)$, an output signal $Y(s)$, a noise signal $N(s)$, the sensor filter model $H(s)$, and the time delays of the reference signal $e^{-\tau_r s}$, the actuator command signal $e^{-\tau_a s}$ and the measurement signal $e^{-\tau_m s}$. All blocks are presented in the Laplace domain. From this figure three factors influencing the closed-loop performance are easily identified as disturbance, noise and time delays. A fourth factor is added since the model dynamics $G(s)$ used in controller synthesis may behave differently in reality, or in other words the system dynamics may be uncertain.

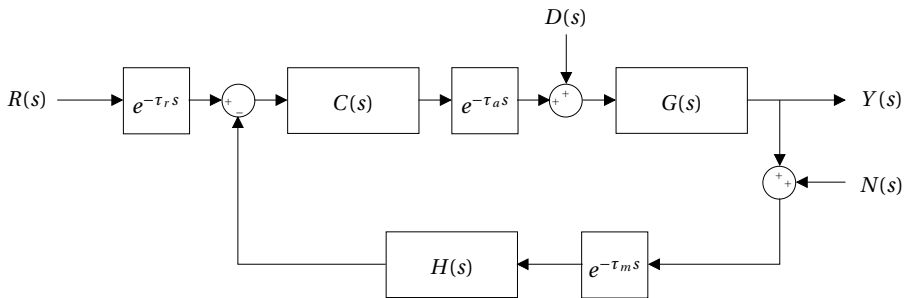


Figure 4.12: Block diagram of a closed loop control system.

4.5.1 Influence of Disturbances

Disturbances act as additional (unwanted) inputs to the aircraft. To reject disturbances, or to be robust with respect to disturbances, feedback is used in the FCL design. The influence of disturbances on the closed-loop system performance can be investigated by introducing the tracking error [26]. The tracking error is defined as the difference between the reference signal and the output,

$$E(s) = R(s) - Y(s) \quad (4.12)$$

Assuming zero time-delay (i.e., $\tau_r = \tau_a = \tau_m = 0$), unit feedback (i.e., $H(s) = 1$), and after some block diagram manipulations, the tracking error can be written as,

$$E(s) = \frac{den(s) - C(s)G(s)}{den(s)} R(s) - \frac{G(s)}{den(s)} D(s) + \frac{C(s)G(s)}{den(s)} N(s) \quad (4.13)$$

$$den(s) = 1 + C(s)G(s)$$

From this expression it becomes clear that increasing the loop gain, $C(s)G(s)$, will decrease the influence of disturbance, $D(s)$, on the tracking performance. However, by increasing the loop gain, the influence of measurement noise, $N(s)$, on the tracking performance is also increased. Figure 4.13 shows two systems, one with high loop gain and the other with low loop gain. The response of both systems to a sinusoidal disturbance and noise signal are given in the bottom two plots in the figure. Indeed the low loop gain system has poor disturbance rejection and good noise attenuation, while the high loop gain system has good disturbance rejection and poor noise attenuation. Clearly an optimum should be found. The guidelines for reaching this optimum are discussed in Section 4.5.3.

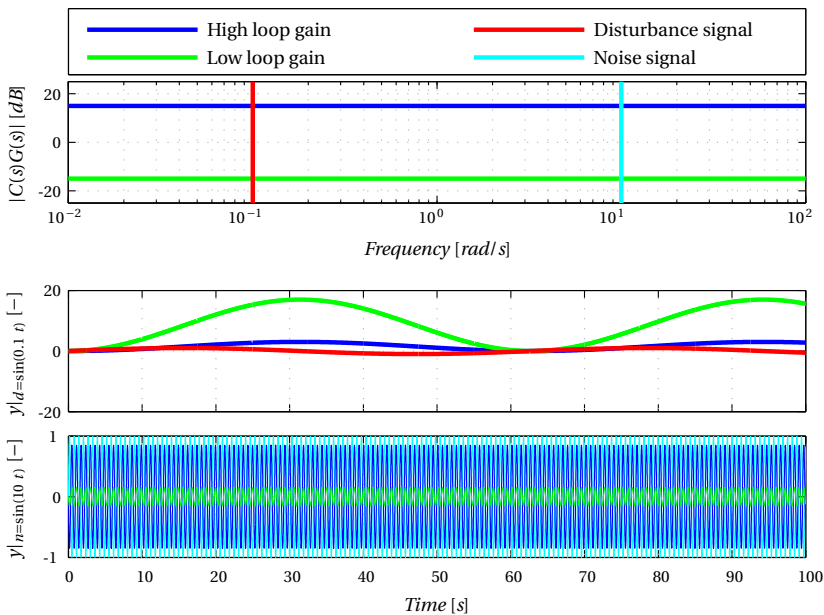


Figure 4.13: Example bode magnitude plot and time histories plots for disturbance rejection and noise attenuation.

Increasing the loop gain has another effect, it changes the relative stability of the system, or in other words it changes how far a system is from becoming (un)stable. The gain margin is shown in Figure 4.6 and is determined from the difference between the magnitude of the system at the frequency where the phase crosses the -180 degrees line and 0 dB [92]. This margin indicates by how much the loop gain can be increased before the closed-loop system becomes marginally stable. For many systems $GM \approx 9.5$ dB will result in good stability properties [103]. Note that the gain margin and phase margin indicate the stability of the closed-loop system based on the bode plot of the open-loop system.

4.5.2 Influence of System Uncertainties

Parametric uncertainty can also be seen as an additional (unwanted) input on the system [26]. Suppose the aircraft model $G(s)$ behaves in reality as $G(s) + \Delta G(s)$. Then an input u would result in the output,

$$Y(s) = G(s)U(s) + \Delta G(s)U(s) \quad (4.14)$$

which is $\Delta G(s)U(s)$ larger or smaller than in the nominal situation. Relying on the principle of superposition, only the change in the aircraft model is examined, so $D(s) = N(s) = 0$. The tracking error can then be written as,

$$E(s) + \Delta E(s) = \frac{\text{den}(s) - G(s)C(s) - \Delta G(s)C(s)}{\text{den}(s)} R(s) \quad (4.15)$$

$$\text{den}(s) = G(s)C(s) + \Delta G(s)C(s) + 1$$

and the change in tracking error is therefore,

$$\Delta E(s) = \frac{-C(s)\Delta G(s)}{(G(s)C(s) + 1)\text{den}(s)} R(s) \quad (4.16)$$

Again it can be seen that increasing the loop gain will decrease the influence of the parametric uncertainty.

Stability margins for parametric uncertainty depend on the system description. In-depth analysis using the Routh-Hurwitz stability criterion is needed to demonstrate worst case parameter sets and their effect. For more details the reader is referred to Chapter 6 of [26].

Besides parametric uncertainty a system can have unmodeled dynamics, or unstructured uncertainty. A number of models are used in robust control theory to account for unstructured uncertainty [1]. One of these models, that captures a wide variety of uncertainties, is the multiplicative perturbation model,

$$\bar{G}(s) = (1 + W_{\Delta}(s)\Delta(s))G(s) \quad (4.17)$$

where the perturbation $\Delta(s)$ is assumed to satisfy $\|\Delta(s)\|_{\infty} \leq 1$ and $W_{\Delta}(s)$ is a weighing function. Using the small gain theory documented in [25], the uncertain closed-loop system is stable when,

$$\|W_{\Delta}(s)T(s)\|_{\infty} \leq 1 \quad (4.18)$$

with $T(s)$ the transfer function of the closed-loop system and assuming that the non-perturbed system ($\Delta(s) = 0$) is internally stable. The importance of this result can be demonstrated using a simple example. Suppose the aircraft model matches

quite well for the lower frequencies ($|W_{\Delta}(j\omega)| = 0.1$ for $\omega \leq 10\pi$ rad/s), but has up to 200% error for the higher frequencies ($|W_{\Delta}(j\omega)| = 2.0$ for $\omega > 10\pi$ rad/s) due to the lack of a structural vibration model. The weighing model could then be described by the transfer function,

$$W_{\Delta}(s) = 2 \frac{s + 10\pi \cdot 0.1}{s + 10\pi \cdot 2} \tag{4.19}$$

Figure 4.14 shows both the weighing model and the inverse of this model. The robust stability criterion claims that as long as $|T(s)| < |W_{\Delta}(j\omega)|^{-1}$ for all frequencies, the closed-loop system will be stable. A physical interpretation of this criterion is that remaining below the $|W_{\Delta}(j\omega)|^{-1}$ line prevents energy at these frequencies from exciting the unmodeled dynamics and, therefore, prevents the possible loss of stability [20].

Although stability is assured in this case, performance is not. By preventing higher frequencies for the closed-loop system, effectively the bandwidth of the system is limited. In other words, good performance cannot be expected at the frequencies where significant modeling errors are taken into account.

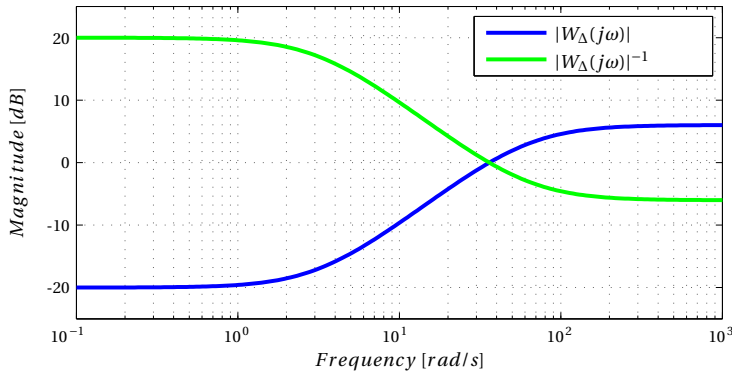


Figure 4.14: Example bode plot for an unstructured uncertainty weighing function and its inverse.

4.5.3 Influence of Measurement Noise

Section 4.5.1 shows that the loop gain ($C(s)G(s)$) should be large for good disturbance rejection and small for good noise attenuation. In order to facilitate both properties, the FCL should be designed such that the loop gain is large over the frequency range associated with disturbances and small for frequencies associated with noise [26]. The sensor models introduced in Section 3.2.4 show that measurement noise is a signal with power at high frequency. If sensor selection has not

been fixed, the sensor should be chosen such that the noise frequency exceeds the desired bandwidth of the system. Disturbances are often low frequency signals, e.g., fuel sloshing, passenger movement, etc., and therefore both signals are frequency separated. Figure 4.15 shows an example of a properly designed loop gain. Some disturbances, such as turbulence, are also high frequent and require special attention. In this case it may be possible to increase the loop gain at the specific frequencies associated with the high frequency disturbance using a band-pass filter.

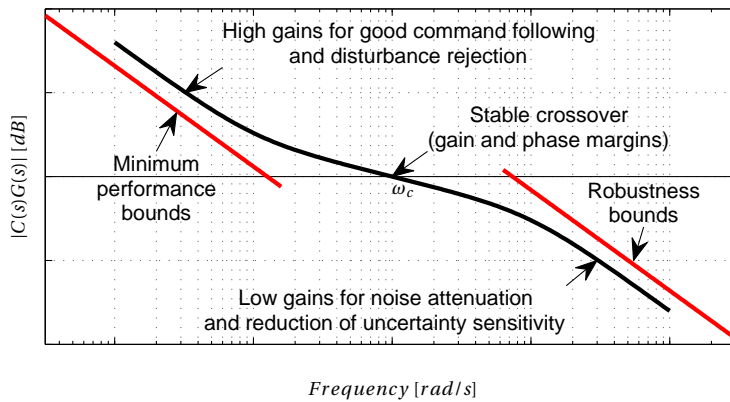


Figure 4.15: Bode magnitude plot for loop gain $|C(s)G(s)|$, source: Figure 12.12 in [26].

4.5.4 Influence of Time-delays

Time delays are introduced by sensors, actuators and by the FBW platform itself. On the FBW platform, redundancy management and the packing and unpacking of data can cause a substantial part of the total time delay of the system. Three types of time delay influence the FCL as presented in Figure 4.12. These types are, reference delay, actuator delay and measurement delay. The effect of the delays depends on the characteristics of the closed-loop system. As example, Figure 4.16 shows the effects of time delays in a bode plot, for an integrating system, $G(s) = 1/s$, without sensor filter, $H(s) = 1$, and with a proportional controller with gain 10, $C(s) = 10$, i.e., the closed-loop system,

$$\frac{Y(s)}{R(s)} = e^{-\tau_r s} \frac{10e^{-\tau_a s}}{s + 10e^{-(\tau_a + \tau_m)s}} \quad (4.20)$$

Clearly, the controlled system is influenced by the presence of time delay. When time delays are not dealt with correctly, the high performance controller designed in a simulation environment may perform worse or even lead to system instability in practice.

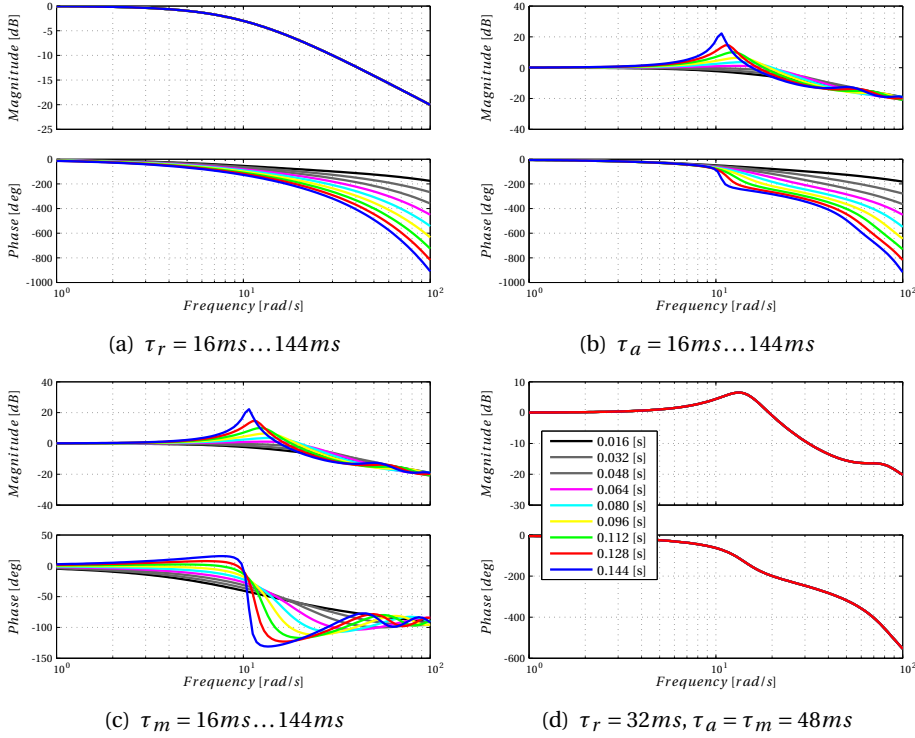


Figure 4.16: Bode plots of the influence of time delays to the system (4.20).

The stability margin with respect to time delays is also referred to as the time-delay margin. This margin can be determined by looking at the closed-loop system transfer function of the block diagram presented in Figure 4.12. Again ignoring noise and disturbances ($D(s) = N(s) = 0$), and assuming unity feedback ($H(s) = 1$), this transfer function is given by,

$$\frac{Y(s)}{R(s)} = e^{-\tau_r s} \frac{C(s)G(s)e^{-\tau_a s}}{1 + C(s)G(s)e^{-(\tau_a + \tau_m)s}} \quad (4.21)$$

The characteristic equation for this transfer function is written as,

$$1 + C(s)G(s)e^{-(\tau_a + \tau_m)s} = 0 \quad (4.22)$$

and the largest root(s) of this equation should have a zero real part for marginal stability of the system. The time-delay at which this happens, is called the time-delay margin. Solving this equation analytically is generally not possible, but numerical solvers can produce correct results. Alternatively Padé approximations can be used

to obtain a solvable polynomial, but this can produce non-conservative (over estimated) results [117]. A third method is to use Lyapunov-Krasovskii Functionals [43] to obtain a set of linear matrix inequalities, which can be solved efficiently and produces conservative (under estimated) results. This method is used in Chapter 5. However, the most simple method is to increase the time delays until marginal stability is obtained in the system response. Marginal stability is indicated by a periodically oscillating steady state response.

The time delay margin can be related to the phase margin using,

$$\text{time delay margin} = \frac{\text{phase margin}}{\text{crossover frequency}} \quad (4.23)$$

The phase margin is shown in Figure 4.6 and determined by adding 180 degrees to the phase angle at the frequency where the magnitude of the system crosses the 0 dB line. The larger the phase angle, the better the relative stability of the system with respect to phase shifts. For many systems $PM > 35$ degrees results in good stability properties [103].

Improving the time-delay margin by lowering the loop gain, i.e., increasing the phase margin and decreasing the crossover frequency, is generally not the best option. Lowering the loop gain will not only change the phase, but also the magnitude of the system response and therefore decrease the tracking performance, the bandwidth and the disturbance rejection. Lead compensation is essentially a high pass filter that adds phase to the system at a certain (high) frequency [92]. A single lead compensator can add at most 65 degrees phase to the system, but when even more lead is required multiple lead filters may be designed in series. The drawback of a lead filter is that it decreases the loop gain at low frequencies thereby influencing the disturbance rejection and command following performance of the system. Lag compensation is essentially a low pass filters that permits high gains at low frequencies, thereby increasing the steady state performance. Combining best of both worlds results in a lead-lag filter as shown in Figure 4.17. This filter decreases the magnitude only over a small frequency range and consists of a phase lag and phase lead portion. It can be written as [92],

$$G_{LL}(s) = K_c \frac{s + 1/T_1}{s + \gamma/T_1} \frac{s + 1/T_2}{s + 1/(\beta T_2)} \quad (4.24)$$

where $\beta > 1$ and $\gamma > 1$. The lead part of this filter is determined by,

$$\frac{s + 1/T_1}{s + \gamma/T_1} = \frac{1}{\gamma} \frac{T_1 s + 1}{(T_1/\gamma)s + 1} \quad (4.25)$$

and the lag part by,

$$\frac{s + 1/T_2}{s + 1/(\beta T_2)} = \beta \frac{T_2 s + 1}{\beta T_2 s + 1} \tag{4.26}$$

As shown in the figure, the time constant T_1 determines the frequency range that affects the phase and magnitude of the filter. The frequency at which a lead-lag filter crosses the zero phase line is calculated by $\omega_c = 1/\sqrt{T_1 T_2}$.

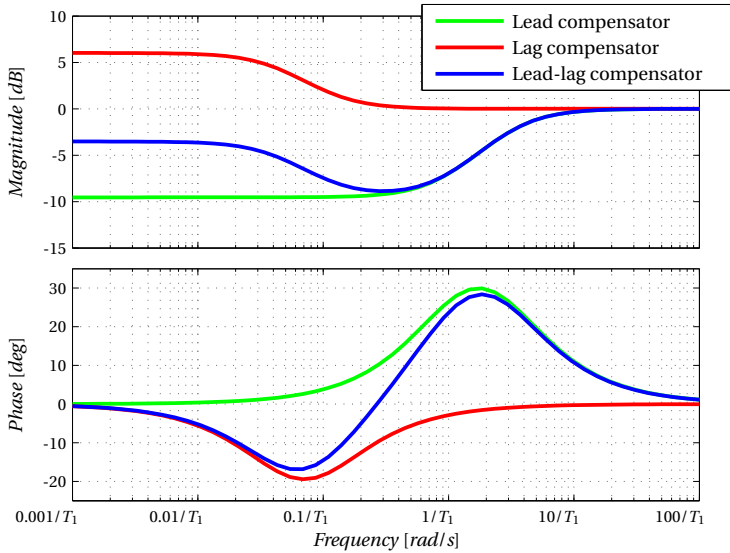


Figure 4.17: Lead, Lag and Lead-Lag Compensators with $K_c = 1$, $\gamma = 3$, $\beta = 2$ and $T_2 = 10T_1$.

4.6 Flight Control Law Design

This section determines a suitable FCL design for the Diamond DA 42 using the knowledge from the previous section. The design starts by identifying the controllability and observability of the system. Next, the SAFAR control mode is selected, followed by the determination of the necessary control loop components using Single-Input-Single-Output (SISO) representations of the system. Then, the design is completed using Multiple-Input-Multiple-Output (MIMO) representations and flying quality evaluations. Finally, the FCL is tested using the nonlinear aircraft model developed in Chapter 2 combined with the FBW platform described in Chapter 3.

4.6.1 Observability and Controllability

The first step in designing a FCL is to check whether all necessary state variables can be measured or in other words are observable and whether all desired state

changes can be made using the available inputs or in other words are controllable. The concepts of controllability and observability were introduced by Kalman [59].

Consider the linear time-invariant system,

$$\begin{aligned}\dot{x} &= Ax + Bu \\ y &= Cx + Du\end{aligned}\tag{4.27}$$

with $x \in \mathbb{R}^n$ being the state vector, $u \in \mathbb{R}^m$ the input vector, $y \in \mathbb{R}^q$ the output vector, $A \in \mathbb{R}^{n \times n}$ the system matrix, $B \in \mathbb{R}^{n \times m}$ the input matrix, $C \in \mathbb{R}^{q \times n}$ the output matrix and $D \in \mathbb{R}^{q \times m}$ the direct feed-through matrix.

The observability of this linear system can be determined using the observability matrix O , which is defined as,

$$O = \begin{bmatrix} C \\ CA \\ CA^2 \\ \vdots \\ CA^{n-1} \end{bmatrix}\tag{4.28}$$

The system is said to be fully observable if and only if the rank of the observability matrix is equal to the number of states n .

The controllability of this linear system can be determined using the controllability matrix R , which is defined as,

$$R = [B \quad AB \quad A^2B \quad \dots \quad A^{n-1}B]\tag{4.29}$$

The system is said to be fully controllable if and only if the rank of the controllability matrix is equal to the number of states n .

Although the rank conditions of the controllability and observability matrices are easy to test, these can be poorly conditioned computational operations to perform. An alternative test uses the controllability and observability gramians, [104]

$$\begin{aligned}W_c &= \int_0^\infty e^{At} B B^T e^{A^T t} dt \\ W_o &= \int_0^\infty e^{A^T t} C^T C e^{At} dt\end{aligned}\tag{4.30}$$

where $W_c \in \mathbb{R}^{n \times n}$ is the controllability gramian and $W_o \in \mathbb{R}^{n \times n}$ the observability gramian. For this test, the system should clearly be stable. Again these matrices must have rank n for full controllability and observability, or equivalently they should be invertible.

Besides the on-off criteria mentioned above, it is convenient to know the degree of controllability or observability of each state. In other words is a state almost uncontrollable or fully controllable. The degree of controllability δ_c can be defined as, [4]

$$\delta_c = \frac{\sqrt{\lambda(RR^T)}}{\sqrt{\lambda_{max}(RR^T)}} \quad (4.31)$$

where $\lambda(x)$ are the eigenvalues of x . Note that Equation (4.31) is the same as the singular values of R obtained from a singular value decomposition. In similar fashion the degree of observability δ_o can be obtained from,

$$\delta_o = \frac{\sqrt{\lambda(O^T O)}}{\sqrt{\lambda_{max}(O^T O)}} \quad (4.32)$$

Table 4.1 provides the degree of controllability and observability for the DA 42 combined with FBW platform. The system is fully controllable and observable.

Table 4.1: Degree of controllability and observability.

State (x)	δ_c	δ_o
<i>p</i>	0.012057	0.0080902
<i>q</i>	0.012154	0.0098696
<i>r</i>	0.016463	0.011928
<i>u</i>	0.018175	0.026435
<i>v</i>	0.028673	0.033954
<i>w</i>	0.02889	0.035354
ϕ	0.045202	0.061443
θ	0.17766	0.066003
ψ	0.26034	0.090537
<i>x</i>	0.99994	0.09226
<i>y</i>	0.99995	0.19304
<i>z</i>	1	1
<i>fuel_{left}</i>	0.012004	0.0023124
<i>fuel_{right}</i>	0.012022	0.0030577

4.6.2 SAFAR Control Modes

The first control mode used in SAFAR is the DRCT mode. This mode is a stick-to-surface mode, which does not change the pilot-aircraft interaction as already introduced in Section 4.4. In DRCT mode the safety pilot will provide rudder commands, such that no sensor data is needed to operate this FCL mode.

The second control mode is the ATT mode. This mode uses RCAH for elevator and aileron commands, which simplifies flying, while posing moderate sensor requirements. A reference attitude is set by the pilot and disturbances on pitch and roll angle, such as turbulence, are rejected by the FCL. Also, since the reference attitudes can be set independently, the FCL decouples the control of the aircraft states. For example, a larger elevator deflection command is automatically issued as soon as a turn is initiated, to prevent the aircraft from pitching down while banking. Ideally only gyroscopic measurements are needed for this control law. In reality the bias of the gyroscope needs to be compensated using accelerometer and GPS measurements. The resulting angular rate and attitude measurements usually have low noise characteristics. Another argument for selecting the RCAH mode is that it does not require the pilot to fly head down, thereby keeping the pilot-aircraft interaction close to the DRCT mode. As mentioned in Section 4.2 the RCAH mode lacks speed stability. A FEP system will therefore be designed and added to the FCL, but the treatment hereof is postponed until Chapter 6. Rudder commands in the ATT mode are generated using a sideslip compensator. Section 4.4 shows that sideslip buildup cannot be neglected and since the pilot has no rudder control, a sideslip compensator is needed in the ATT mode. Because cruise flight is selected as operating condition for the FCL, a de-crabbing mode, needed in cross-wind landings, is not designed in this chapter. Speed is controlled by interpreting the throttle setting as a speed command. Deviation from this reference speed results in a change in engine throttle. Since the FCLs are designed for the cruise phase of the flight, the strategy of this control mode matches the strategy often used by pilots. In other flight phases controlling speed using elevator deflections may be more appropriate.

The third and final mode used in SAFAR is a fully automated 3D trajectory following mode called the NAV mode. This mode uses the horizontal and vertical offset to a reference trajectory as well as the difference between flight-path vector and the reference trajectory to compute elevator and aileron commands. It requires additional sensor information, such as the position $[x_e \ y_e \ z_e]^T$, the flight-path angle γ and the track angle χ and also uses an on-board database that should contain a properly defined reference trajectory. This mode is therefore only used in a simulation environment and not actually implemented on the SAFAR demonstrator aircraft. The rudder and engine throttle are controlled using the same sideslip compensator and autothrottle used in the ATT mode respectively.

For safety reasons an elevator trim tab control law, that controls the hinge moment to zero, should be added to the ATT and NAV modes. This controller can be slow (low frequent) and should not interfere with the other FCL designs. However, the trim tab is currently not connected to the SAFAR platform and is therefore left

for future work. It is strongly advised to include this functionality to the FBW platform and FCL designs in a subsequent project.

4.6.3 SISO Design

The SISO description is a simplified representation of reality using only one-to-one relations. For example, the influence of an elevator deflection on the pitch angle can be described using a SISO system. The benefit of using such descriptions lies in the rapid evaluations that can be made of the system. This section uses SISO descriptions for the design of a sideslip compensator, autothrottle, RCAF FCL and a 3D trajectory following FCL.

There are many design methodologies for linear models, such as root locus, Bode plots, LQR-optimal control, Eigenstructure assignment, H_∞ -synthesis, linear matrix inequalities, etc. Each of these methods can be used to achieve stabilization, tracking, disturbance rejection and similar design objectives. This chapter uses Bode plots and loop shaping to synthesize the different classical FCLs.

One of the most challenging tasks in the design of a classical FCL is the gain selection, or weighing factor selection when an optimal control design method is used. The gain selection in this chapter is done using an optimization function over tracking performance, disturbance rejection and noise attenuation. For each of the FCLs a different weight is used on each of these factors as will be explained in the remainder of this section. First an initial gain set is found using a rough pattern search algorithm, documented in [70]. Then, the trust-region-reflective method documented in [22] is used to fine tune these gains. This procedure does not guarantee that a global minimum of the cost function is found, but does lead to good results for the FCLs described in this chapter. Future research could improve the gain selection using an algorithm that is guaranteed to find the global minimum, such as interval analysis [129].

Sideslip Compensator

Figure 4.18 shows a block diagram of the sideslip compensator developed for SAFAR. The complete design can be found in Appendix E.1, here merely the resulting controller is presented. The gains for this FCL design are determined with a primary focus on disturbance rejection. Using the following transfer functions,

$$C(s) = \left(K_p + \frac{K_I}{s} \right) \left(\frac{s + 1/T_1}{1 + \gamma/T_1} \right) \left(\frac{s + 1/T_2}{s + 1/(\beta T_2)} \right) \quad (4.33)$$

$$H(s) = 1$$

and,

$$\begin{aligned} C_{IL}(s) &= 1 \\ H_{IL}(s) &= K_{IL} \frac{\tau s}{\tau s + 1} \end{aligned} \quad (4.34)$$

with $K_P = 1.7$, $K_I = 0.6$, $T_1 = 0.56$ seconds, $T_2 = 0.91$ seconds, $\gamma = 2.77$, $\beta = 3.71$, $K_{IL} = -0.41$ and $\tau = 1.53$ seconds, results in the open and closed loop behavior shown in Figure 4.19. The open-loop system shows good gain and phase margins, the closed-loop system of disturbance to output $Y(s)/D(s)$ shows good disturbance rejection and the closed-loop system of noise to output $Y(s)/N(s)$ indicates proper noise attenuation at the high frequencies. Similar characteristics are obtained throughout the flight envelope and gain scheduling is therefore not needed. Further, the sideslip compensator introduces fast well-damped lateral oscillations rather than a “lateral phugoid”.

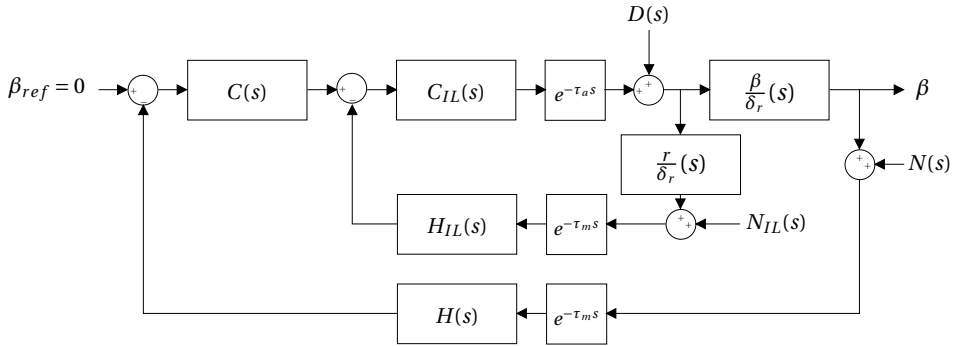


Figure 4.18: Block diagram for the sideslip compensator, in which β/δ_r represents the transfer function of the sideslip response due to rudder input of the aircraft combined with the FBW platform, $C(s)$ the FCL and $H(s)$ the measurement filter. r/δ_r , $C_{IL}(s)$ and $H_{IL}(s)$ represent a yaw-rate inner-loop controller.

Autothrottle

Figure 4.20 shows a block diagram of the autothrottle developed for SAFAR. The complete design can be found in Appendix E.2, again only the resulting controller is presented. The gains for this FCL design are determined by focusing on noise attenuation. Using the following transfer functions,

$$\begin{aligned} C(s) &= K_P + K_I/s \\ H(s) &= \frac{1}{1 + Ts} \end{aligned} \quad (4.35)$$

with $K_P = 0.4$, $K_I = 0.15$ and $T = 0.2$ seconds, results in the open and closed loop behavior shown in Figure 4.21. The open-loop system shows good gain and phase mar-

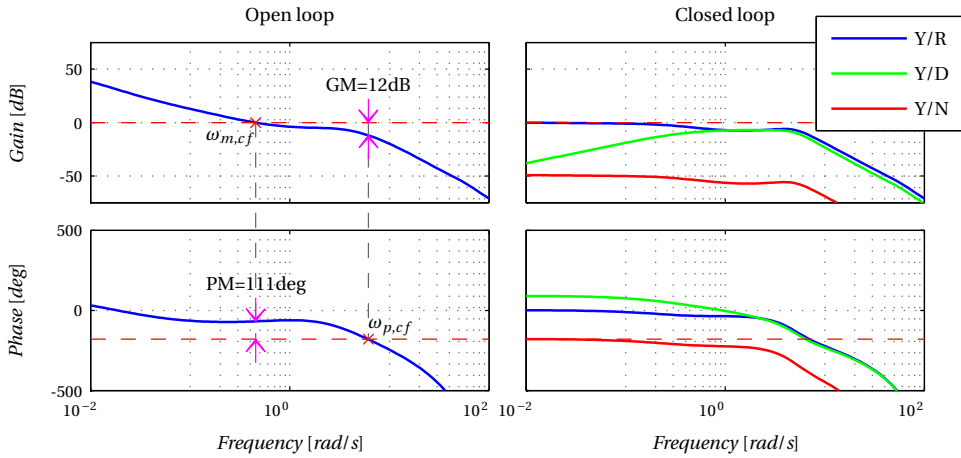


Figure 4.19: Bode plot of the sideslip controller with $C = (1.7 + 0.6/s)(s + 1/0.56)/(1 + 2.77/0.56)(s + 1/0.91)/(s + 1/(3.71 \cdot 0.91))$, $H = 1$, $C_2 = 1$ and $H_2 = -0.41 \cdot 1.53s/(1.53s + 1)$.

gins, the closed-loop system of noise to output $Y(s)/N(s)$ indicates proper noise attenuation at the high frequencies. The acceptable noise attenuation comes at the cost of lower disturbance rejection around 1 rad/s. For now this is not regarded as a problem and the autothrottle design is considered to be acceptable. Again similar characteristics are obtained throughout the flight envelope and gain scheduling is not needed. Note that the low frequency resonance and anti-resonance shown in the open loop bode plot is also found in mechanical systems where motor and load are compliantly coupled [28]. Acceleration feedback in combination with a bilinear quadratic filter improves the performance for those systems and future work should show if this strategy also works for the autothrottle design.

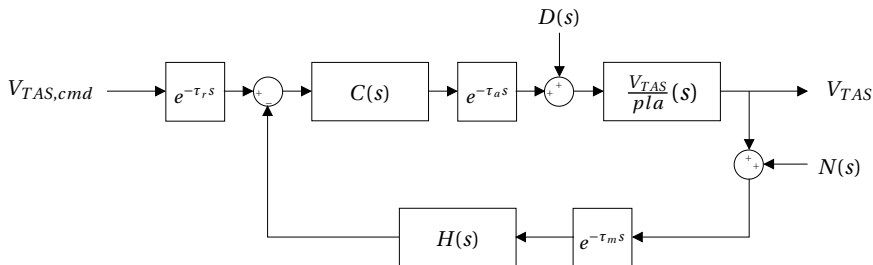


Figure 4.20: Block diagram for the autothrottle, in which V_{TAS}/pla represents the transfer function of the true airspeed response due to power lever angle input of the aircraft combined with the FBW platform, $C(s)$ the FCL and $H(s)$ the measurement filter.

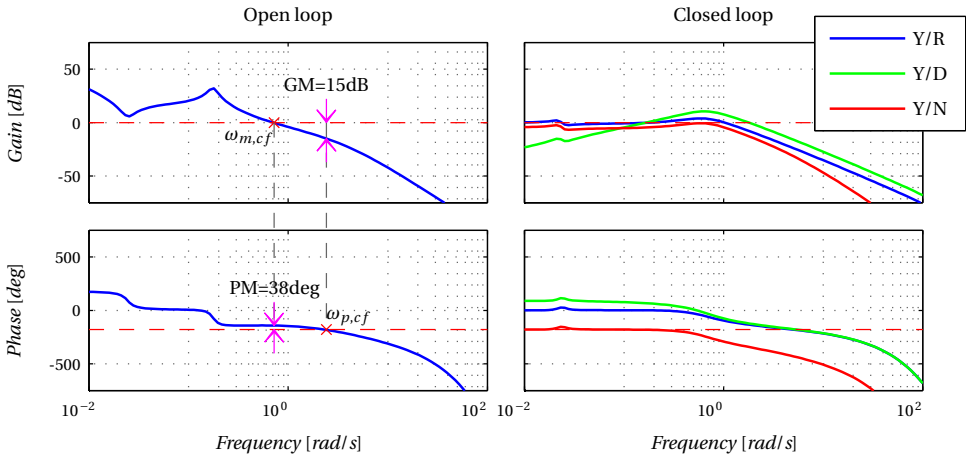


Figure 4.21: Bode plot of the autothrottle with $C = 0.4 + 0.15/s$ and $H = 1/(1 + 0.2s)$.

Rate Command/Attitude Hold

The RCAH controller is designed using a similar strategy as applied to the sideslip controller and the autothrottle. The design is split into two parts, one for the elevator and one for the ailerons. The gain selection for these FCLs is done with focus on tracking performance.

Figure 4.22 shows a block diagram for the elevator control loop developed for SAFAR. Note that the pitch-rate command is integrated to a pitch-angle reference, which the FCL should track. The complete design can be found in Appendix E.3, here only the resulting controller is presented. Using the following transfer functions,

$$\begin{aligned}
 C(s) &= \left(K_P + \frac{K_I}{s} \right) \left(\frac{s + 1/T_1}{1 + \gamma/T_1} \right) \left(\frac{s + 1/T_2}{s + 1/(\beta T_2)} \right) \\
 H(s) &= 1 \\
 C_{IL}(s) &= 1 \\
 H_{IL}(s) &= K_{IL} \frac{\tau s}{\tau s + 1}
 \end{aligned} \tag{4.36}$$

with $K_P = -1$, $K_I = -0.3$, $T_1 = 0.54$ seconds, $T_2 = 0.1$ seconds, $\gamma = 3.0$, $\beta = 6.2$, $K_{IL} = -0.4$, $\tau = 5$ seconds, results in the open and closed loop behavior shown in Figure 4.23. In order to get similar closed-loop behavior throughout the flight envelope K_P and K_{IL} are scheduled as shown in Figure 4.24.

Figure 4.25 shows a block diagram for the aileron control loop developed for

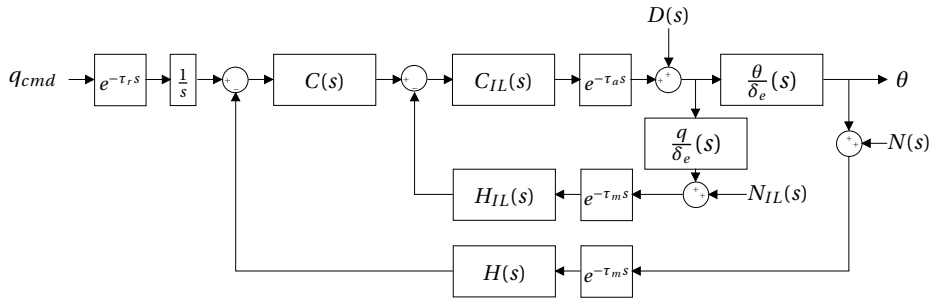


Figure 4.22: Block diagram for the pitch RCAH controller, in which θ/δ_e represents the transfer function of the pitch-angle response due to elevator deflections of the aircraft combined with the FBW platform, $C(s)$ the FCL and $H(s)$ the measurement filter. q/δ_e , $C_{IL}(s)$ and $H_{IL}(s)$ represent a pitch-rate inner-loop controller.

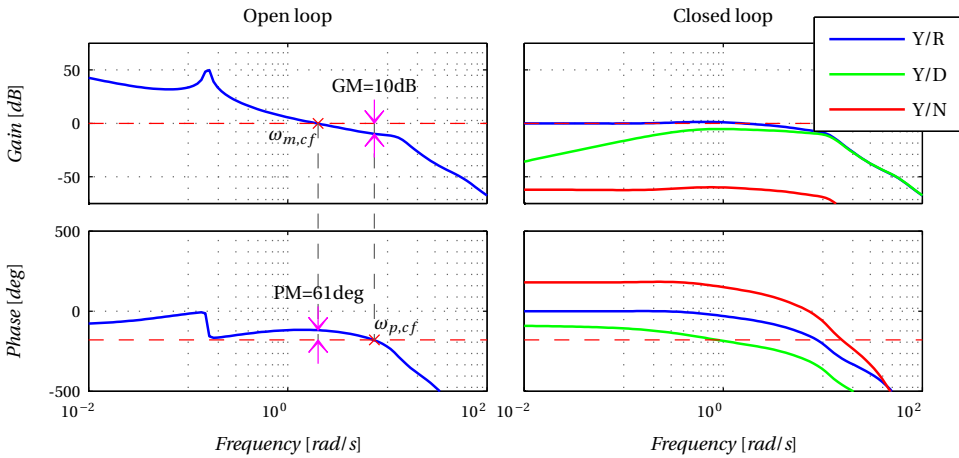


Figure 4.23: Bode plot of the pitch RCAH controller with $C = (-1 - 0.3/s)(s + 1/0.54)/(s + 3.0/0.54)(s + 1/0.1)/(s + 1/(6.2 \cdot 0.1))$, $H = 1$, $C_{IL} = 1$ and $H_{IL} = -0.4 \cdot 5s/(5s + 1)$.

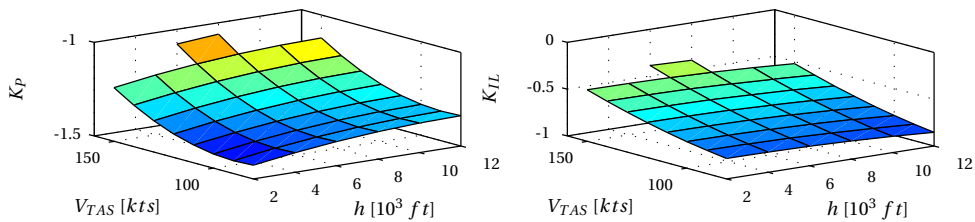


Figure 4.24: Gain schedule of K_P and K_{IL} for altitude and speed.

SAFAR. Also the roll-rate command is integrated to a roll-angle reference. The complete design can be found in Appendix E.4. Using the following transfer functions,

$$\begin{aligned}
 C(s) &= \left(K_P + \frac{K_I}{s} \right) \left(\frac{s + 1/T_1}{1 + \gamma/T_1} \right) \left(\frac{s + 1/T_2}{s + 1/(\beta T_2)} \right) \\
 H(s) &= 1 \\
 C_{IL}(s) &= 1 \\
 H_{IL}(s) &= K_{IL} \frac{\tau s}{\tau s + 1}
 \end{aligned}
 \tag{4.37}$$

with $K_P = -3.6$, $K_I = -0.6$, $T_1 = 0.11$ seconds, $T_2 = 0.07$ seconds, $\gamma = 6.0$, $\beta = 2.7$, $K_{IL} = -0.2$, $\tau = 5$, results in the open and closed loop behavior shown in Figure 4.26. In order to get similar closed-loop behavior throughout the flight envelope K_P and K_{IL} are scheduled as shown in Figure 4.27.

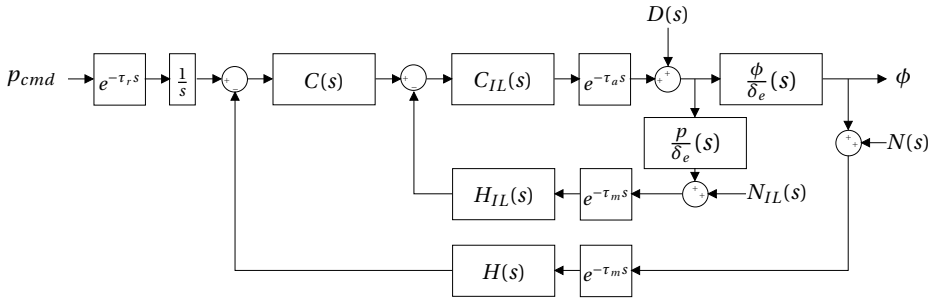


Figure 4.25: Block diagram for the roll RCAH controller, in which ϕ/δ_a represents the transfer function of the roll-angle response due to aileron deflections of the aircraft combined with the FBW platform, $C(s)$ the FCL and $H(s)$ the measurement filter. p/δ_a , $C_{IL}(s)$ and $H_{IL}(s)$ represent a roll-rate inner-loop controller.

3D Trajectory Following

The 3D trajectory following controller closes two additional control loops on top of the RCAH controller. The complete design can be found in Appendix E.5. Figure 4.28 shows the vertical trajectory following controller. The inner loop of this controller determines the pitch-angle command, that is used as an input to the RCAH controller, based on a flight path angle reference. The outer loop computes the flight path angle reference based on the vertical position of the aircraft. Figure 4.29 shows the open and closed-loop characteristics of this system. Clearly both noise attenuation and disturbance rejection are poor. The cause for these poor properties lies in the high noise levels on the position measurement. Using this FCL results in slow altitude variations of several feet due to measurement noise. For the cruise phase this is not deemed a problem and no additional filtering is used.

4. CLASSICAL FLIGHT CONTROL DESIGN

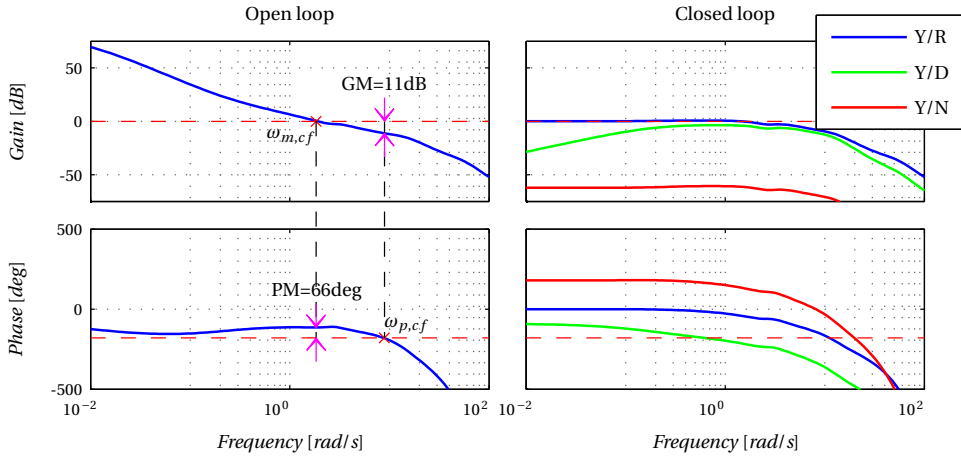


Figure 4.26: Bode plot of the roll RCAH controller with $C = (-3.6 - 0.6/s)(s + 1/0.11)/(s + 6.0/0.11)(s + 1/0.07)/(s + 1/(2.7 \cdot 0.07))$, $H = 1$, $C_{IL} = 1$ and $H_{IL} = -0.2 \cdot 5s/(5s + 1)$.

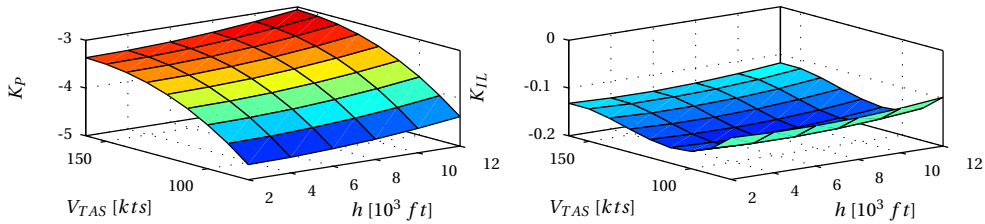


Figure 4.27: Gain schedule of K_P and K_{IL} for altitude and speed.

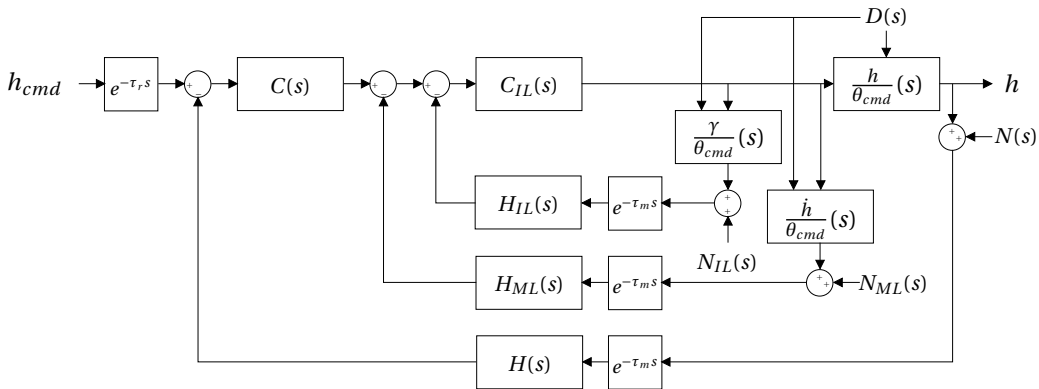


Figure 4.28: Block diagram for the vertical trajectory following controller with flight-path-angle feedback in the inner loop, vertical speed feedback in the middle loop and vertical position feedback in the outer loop.

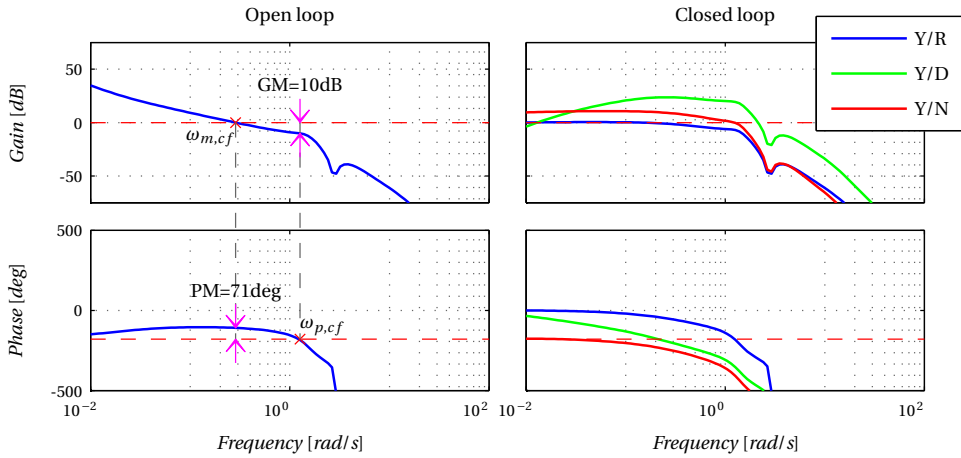


Figure 4.31: Bode plot of the horizontal trajectory following controller with, $C_{IL} = 5$, $H_{IL} = 1$, $H_{ML} = 5/1000$, $C = (6 + 0.1/s)/1000$ and $H = 1$.

4.6.4 MIMO Design

SISO design neglects the cross-coupling between inputs and aircraft states. For example, sideslip is not only caused by rudder deflections, but also by aileron deflections. This section provides two improvements that become apparent when the aircraft model is combined with the previously defined controllers in a MIMO environment.

First the sideslip controller is adjusted. Applying an input to the roll RCAF not only causes the aircraft to roll, but also to yaw and to sideslip. Therefore, this input can be seen as a disturbance on the sideslip compensator control loop. By adding roll-rate feedback to the inner loop of the sideslip compensator, improvements should be possible. Adding roll rate feedback to the sideslip compensator, i.e., $H_{IL,p}(s) = 0.3$, results in the disturbance rejection shown in Figure 4.32. Clearly the roll-rate inner-loop is beneficial for the sideslip compensator. In order to keep this contribution constant over the flight envelope, the gain is scheduled with velocity and altitude.

The second improvement aims at the autothrottle. Adding pitch-angle feedback in the inner loop of the autothrottle lets the controller anticipate velocity changes due to pitching and thereby perform better. Figure 4.33 presents the block diagram for the autothrottle with pitch-angle feedback in the inner loop. Figure 4.34 shows the SISO open and closed-loop system characteristics when this controller is used

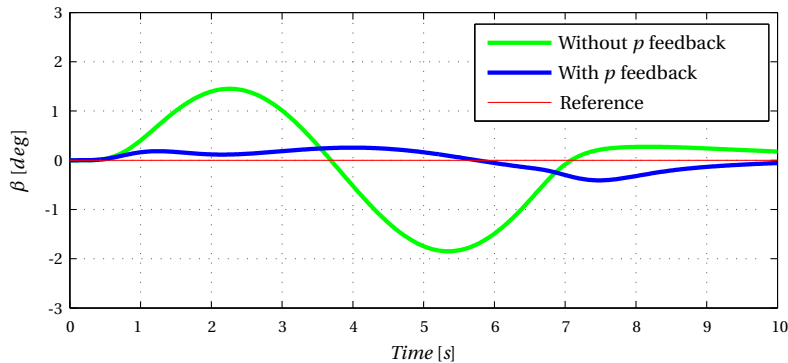


Figure 4.32: Time histories of the MIMO system with and without roll-rate feedback in the sideslip compensator inner loop.

with a simple gain in the feedback part of the inner-loop controller, $H_{IL}(s) = K_{IL}$, with $K_{IL} = -5.5$. Comparing this figure to Figure 4.21 does not reveal any advantages of using the inner loop. However, Figure 4.35 shows the time-histories obtained by simulating the MIMO system using a cosine input on the pitch-rate command. Clearly adding the autothrottle inner loop improves the disturbance rejection.

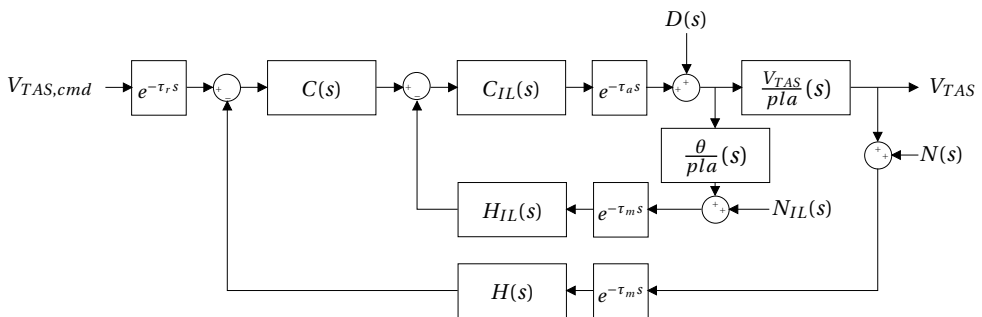


Figure 4.33: Block diagram for the autothrottle with pitch-angle feedback in the inner loop.

4.6.5 Handling Quality Evaluation of the ATT Law

Section 4.3.1 presented an evaluation method for the performance of a manually controlled FCL, such as the ATT law. The results of the longitudinal handling quality analysis are presented in Figure 4.36 and compared with the handling qualities of the unaugmented system presented in Section 4.4. The upper limit of the equivalent time-delay τ_θ is exceeded by both the ATT law as well as the DRCT law. The

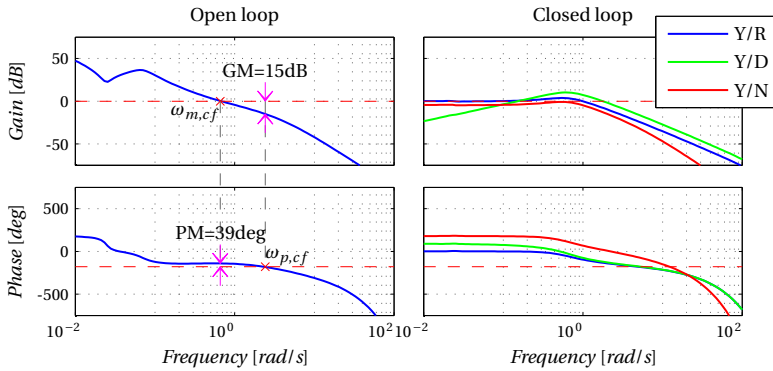


Figure 4.34: Bode plot of the autothrottle with $C = 0.3 + 0.15/s$, $H = 1/(1 + 0.2s)$, $C_{IL} = 1$ and $H_{IL} = -5.5$.

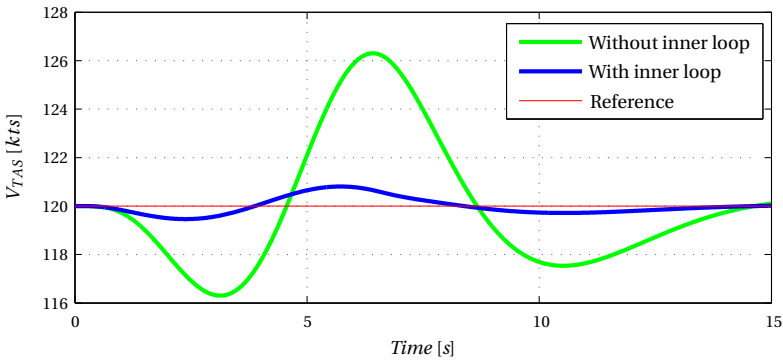


Figure 4.35: Time histories of the MIMO system with and without pitch angle feedback in the autothrottle inner loop at an operating condition of 120 kts.

cause for this lies in the FBW platform, which has 32 ms reference delay, 48 ms actuator delay and 48 ms measurement delay. Note that the phugoid damping is not provided for the ATT law, since the RCAH controller suppresses this eigenmode of the aircraft. The requirement on the short period natural frequency is met throughout the flight envelope by the ATT law, whereas the DRCT law shows minor excesses of the upper limit. Similar results are obtained for the lateral handling qualities, shown in Figure 4.37. The handling qualities of the ATT law are adequate and occasionally better than the handling qualities of the unaugmented system.

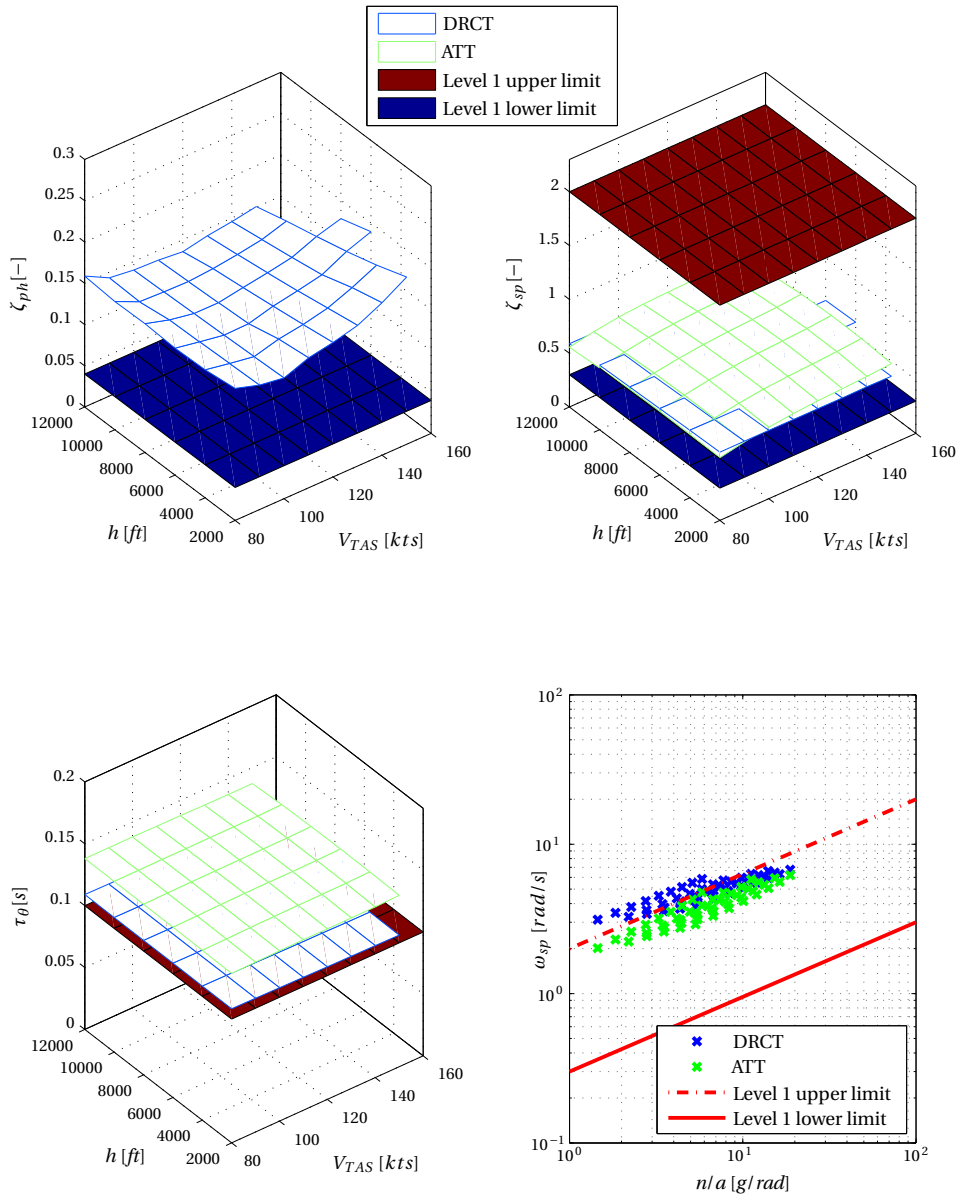


Figure 4.36: Longitudinal performance of the ATT law controlled system.

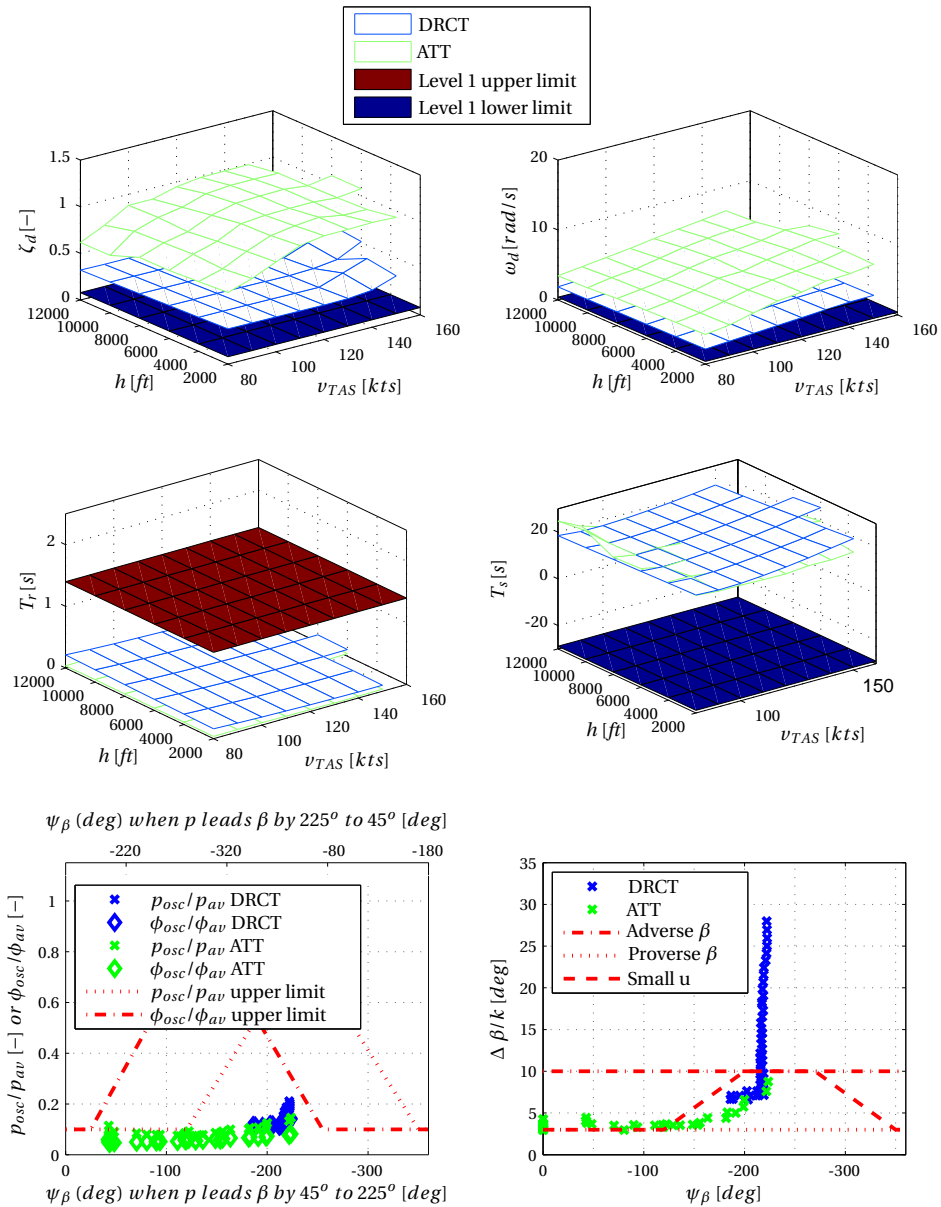


Figure 4.37: Lateral performance of the ATT law controlled system.

4.6.6 Performance Evaluation of the NAV Law

Table 4.2 provides the performance metrics for automatic FCLs as described in Section 4.3.2. The rise time, settling time and overshoot are obtained from the response of the aircraft to a unit step input. The V-NAV column shows that the FCL is fairly aggressive in altitude control, letting the response rise from 10% to 90% of the reference value in only 3.2 seconds with an overshoot of 12.2%. However, the settling of the response takes quite long, 23.8 seconds. The H-NAV controller is more relaxed and somewhat slower, but has almost no overshoot, which is beneficial for passenger comfort. The ISE and ITEA values are determined with respect to the unit step reference and show that the response is not excessively over-damped, nor under-damped, but also that substantial errors remain for quite some time, which was also indicated by the large settling time. Evaluation of the M-metric requires the definition of reference dynamics and since the focus lies on a NAV controller, a sigmoid function is selected,

$$x_{ref}(t) = \frac{1}{1 + e^{-1.2t+4.4}} \quad (4.38)$$

Values of M close to zero indicate a response similar to the reference response, i.e., a smooth transition to a unit step input reference. The M value for the V-NAV controller is quite large and therefore the response differs substantially from the sigmoid function, which was also indicated by the overshoot. The M value for the H-NAV controller is reasonably small indicating a smoother horizontal motion to the reference trajectory. Note that none of the metrics have strict requirements, but they do indicate whether the FCL design is satisfactory and they can be used for comparison with the nonlinear FCLs designed in the next chapter.

Table 4.2: NAV law performance.

Metric	V – NAV	H – NAV
Rise time [s]	3.2	5.4
Settling time [s]	23.8	9.8
Overshoot [%]	12.2	0.9
ISE [ms]	1.7	2.3
ITEA [ms]	31.3	25.5
M [-]	0.49	0.25
Bandwidth [rad/s]	0.6	0.1
Resonance peak [dB]	1.2 @ 0.1 rad/s	N/A

4.6.7 Nonlinear Simulations

The classical FCLs designed in this chapter are implemented on linearized SISO or MIMO system descriptions. The actual aircraft dynamics are nonlinear as demonstrated in Chapter 2 and therefore the classical FCLs need to be implemented and tested on the nonlinear model as well. Ideally the dynamic behavior resulting from control actions should be identical for both the linear and nonlinear models. In this way the performance, defined in the previous sections, also remains the same. Two sources of nonlinearities are already taken into account in the FCL design, velocity and altitude changes. Where necessary gain scheduling has been applied in order to compensate for the change in dynamic behavior due to these two sources. In the nonlinear model, interpolation is used between the gains derived for the different operating points. Appendices E.6 and E.7 present the full comparison between the linear and nonlinear dynamics resulting from control actions of the RCAF and the NAV laws, respectively. Figure 4.38 and 4.39 show a summary of this analysis for the design operating condition of flying at 120kts and 6,000ft. The classical FCLs clearly perform similar on the linear as well as the nonlinear system for small input signals. When larger inputs are given and the control effectors saturate, differences become apparent. This behavior is found throughout the flight envelope and therefore the conclusion can be drawn that the classical FCLs properly control the nonlinear aircraft model in the neighborhood of the operating condition.

4.7 Conclusions and Recommendations

This chapter presented six classical Flight Control Law (FCL) designs for the Diamond DA 42. These FCLs are usable in two separate modes, a manually controlled mode and a fully automated mode. The performance of both modes is demonstrated using different metrics, handling qualities for the former and general time- and frequency-based metrics for the latter mode. Evaluating the handling qualities for the unaugmented aircraft shows that no stability augmentation is needed, except for sideslip compensation. The DA 42 has a considerable adverse yaw. Linearizing the aircraft at the operating conditions for which the model was validated in Chapter 2, i.e., 120 kts at 6,000 ft and cruise configuration provides the Single-Input-Single-Output (SISO) descriptions used in the sideslip compensator design. The design steps taken are based upon commonly used robustness and stability metrics, such as gain and phase margin, noise attenuation and disturbance rejection.

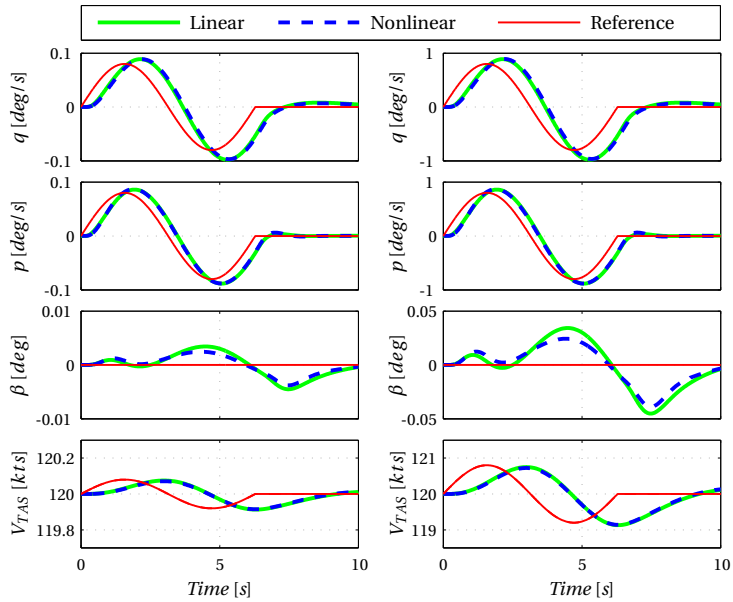


Figure 4.38: Time histories of the linear and nonlinear aircraft dynamics influenced by small inputs to the RCAH controller.

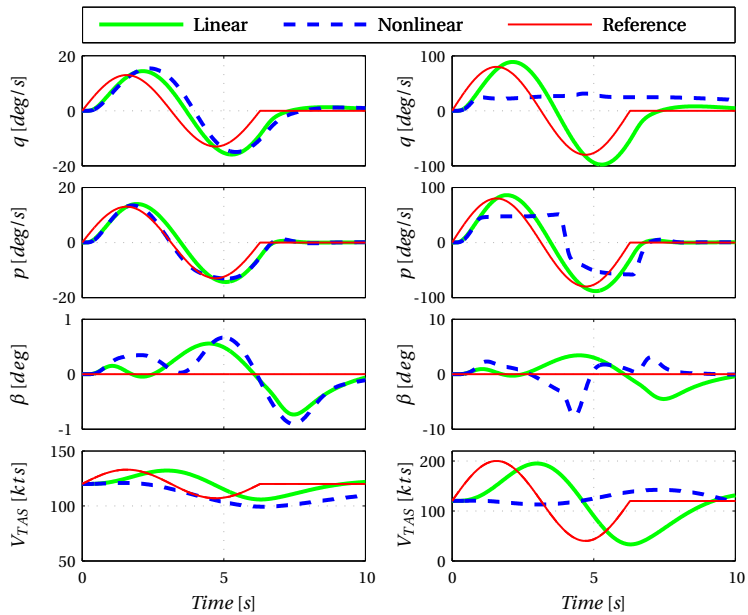


Figure 4.39: Time histories of the linear and nonlinear aircraft dynamics influenced by larger inputs to the RCAH controller.

The sideslip compensator is tested at different operating points in the flight envelope defined by $80 \leq V_{TAS} \leq 160$ kts and $2,000 \leq h \leq 12,000$ ft. This flight envelope lies in the neighborhood of the validated operating point and is possibly encountered during test flights. The sideslip compensator performs adequately throughout the flight envelope and gain scheduling is not needed.

The second FCL is designed to keep the speed constant using throttle commands and is referred to as the autothrottle. Additional filtering of the speed measurements is used to obtain acceptable noise levels for the throttle commands and the controller gains are kept as low as possible. Again no gain scheduling is needed throughout the flight envelope.

The third and fourth FCL are Rate-Command/Attitude-Hold (RCAH) controllers for pitch and roll. The pitch-rate and roll-rate commands are integrated and the resulting pitch-angle and roll-angle references are tracked by the FCLs. This is done using pitch-rate and roll-rate feedback in an inner loop and the pitch-angle and roll-angle feedback in the outer loop. Lead-lag compensation is used to compensate for the effects of measurement, actuator and reference delay and gain scheduling is applied to compensate for the change in dynamics at the different operating conditions the flight envelope.

The first four FCLs are combined into the manually controlled mode, called the ATT mode. It is worth noting that for each of the FCLs the design is done from a different perspective. The focus in the sideslip compensator design lies on disturbance rejection, whereas for autothrottle design the focus shifts to noise attenuation. Finally, the RCAH controller design is done from a reference tracking point of view. Evaluation of this mode is done using the handling qualities. Slight improvements can be noted compared with the already properly performing unaugmented system. However, the ATT mode was not developed for performance increase, but for simplifying flying by decoupling the flight controls and rejecting disturbances.

The last two FCLs are added on top of the RCAH FCLs and close the flight-path vector and the position loop. The resulting fully automated mode, called the NAV mode is evaluated using time-based metrics and will be compared with the nonlinear FCL designs in the later chapters of this thesis.

Both the ATT mode and the NAV mode are implemented and tested on the nonlinear model and, as long as the aircraft stays in the linear region of the dynamics, the FCLs perform as designed. In order to prevent the aircraft from entering the highly nonlinear part of the flight envelope, flight envelope protection is used, which is described in Chapter 6.

The FCL designs presented in this chapter are of course not fully finalized products, but rather a good starting point for further research. Several topics are addressed in this chapter that have not been included in the design, such as the stick shaping part of the handling quality evaluation, the determination of the stability margins for parametric model uncertainty and the influence of turbulence as a high frequency disturbance. Disturbances with a frequency around 1 rad/s are shown to have a large negative influence on the autothrottle performance. Sources of such disturbances should be identified and an autothrottle redesign may be needed.

Other recommendations are to improve the evaluation of the manually controlled FCLs, by including more handling quality indicators, such as the Gibson Dropback criterion, the Phase-rate criterion and the Thumbprint criterion. The robustness properties determined for the SISO controllers do not always extend to the MIMO system. In order to determine the robustness of the MIMO designs alternative methods, such as μ -analysis need to be applied. Also the number of implemented modes is rather limited and could be extended with an autothrottle thrust mode, a de-crab mode, a flare mode and a landing mode, for more intensive use of the FBW platform in all flight phases. However, the NAV law already showed to produce altitude variations of several feet due to measurement noise. Additional filtering, or better sensors may be needed when a position-based FCL is designed for the landing phase.

NONLINEAR FLIGHT CONTROL DESIGN

Abstract

This chapter presents two nonlinear flight control law designs using a modification of the conventional backstepping design method. The first is based on singular perturbation theory and is named Sensor-Based Backstepping and the second is based on Taylor expansions and is called Incremental Backstepping. Both methods use measurement data rather than model knowledge in their implementation and should therefore be usable on a broad family of aircraft. Good tracking performance with or without uncertainty is obtained using either method for simple scalar systems, but also for flight control of the DA 42. The influence of measurement noise is shown to be small and comparable to that obtained using conventional backstepping. Since the Backstepping controllers are based on Lyapunov analysis, stability of the controlled system is guaranteed. The new controllers developed in this chapter have the advantage over conventional backstepping that model uncertainties have a smaller impact on performance and therefore they may very well be a significant step towards certification of advanced flight control laws.

5.1 Introduction

This chapter again uses the aircraft model developed in Chapter 2 and the FBW platform described in Chapter 3, to design the Flight Control Laws (FCLs) for a Diamond DA 42. Chapter 4 showed that the design using classical control theory is quite tedious work. In this chapter, nonlinear control theory is used, which should simplify the design. The theory itself is more mathematically complex, however.

Section 5.2 starts with mathematical notations that are used throughout this chapter. Sections 5.3 and 5.4 provide the performance and robustness metrics used to evaluate the designed FCLs, respectively. Section 5.5 explains why backstepping is used as the core methodology in this thesis and Section 5.6 provides a short recap on backstepping and introduces two new nonlinear FCL designs, sensor based backstepping and incremental backstepping. The sensor based backstepping design will be compared with the classical FCL design of Chapter 4, in Chapters 6 and 7. Section 5.7 ends this chapter with conclusions and recommendations.

5.2 Mathematical Notations

The set of real numbers is indicated by \mathbb{R} and the time t is a scalar that lies in the positive part of this set, indicated by $t \in \mathbb{R}_+$. The state variables or simply states of a system are indicated by x . Generally a system has n states, each being a real number, i.e., $x \in \mathbb{R}^n$. A time-varying nonlinear system can be written as,

$$\dot{x}(t) = f(x(t), t), \quad x(t_0) = x_0 \quad (5.1)$$

in which f is a function from states and time to state derivatives, i.e., $f: \mathbb{R}^n \times \mathbb{R}_+ \rightarrow \mathbb{R}^n$. We can make the assumptions that this function is (locally) Lipschitz in x and (piecewise) continuous in t . These assumptions limit the state derivatives to be (locally) finite and defined throughout the time (interval). More formally, [29]

Definition 5.1 (*Lipschitz continuity*)

A function $f(x, t)$ satisfies the Lipschitz condition on a domain $\mathcal{D} \in \mathbb{R}^n \times \mathbb{R}_+$ with Lipschitz constant L if,

$$|f(x, t) - f(y, t)| \leq L|x - y| \quad (5.2)$$

for all points (x, t) and (y, t) in \mathcal{D} .

The initial condition of system (5.1) (at $t = t_0$) is indicated by x_0 and the state is called an equilibrium state x_e when $\dot{x} = f(x_e, t) = 0, \forall t$ (for all t).

5.3 Performance Metrics

This section introduces specifications of performance metrics of nonlinear FCLs for both manually controlled and automatic flight control modes. Section 4.3 already introduced performance indicators for linear FCLs and some of these metrics can be extended to be applicable to nonlinear FCLs as well.

5.3.1 Performance Metrics for Manually Controlled FCLs

As mentioned in Section 4.3.1, literature only provides performance metrics for manually controlled linearized FCLs. These metrics are based on Low Order Equivalent System (LOES) descriptions, given in the frequency domain. Therefore, application of these metrics for nonlinear systems requires linearization and LOES estimation. In the previous chapter the aircraft model and FBW platform are linearized using Jacobian linearization and used in the FCL design. The resulting closed-loop High Order System (HOS) is then fitted on to the LOES description using least-squares optimization and with this LOES description the Handling Qualities (HQs) are evaluated. The nonlinear FCLs are designed using the nonlinear aircraft model directly. Therefore, evaluation of the HQs of the nonlinear FCLs requires Jacobian linearization of the entire closed loop of aircraft model, FBW platform and FCL. Note that in this case the entire closed-loop should be in equilibrium to determine a useful HOS representation. Again the LOES can be fitted onto the HOS and can be used to evaluate the HQs.

When no nonlinear model is available, for instance when analyzing test flight data, the HQs can be evaluated using a different method. Given a properly defined input signal, that has power at the frequencies used in HQ evaluation, the time response resulting from that input can be transformed to the frequency domain. The magnitude and phase of this frequency data can again be fitted to a LOES using least-squares optimization and the HQs can be evaluated. Several options exist for the transformation from the time domain to the frequency domain, such as the fast Fourier transform or the chirp z transform [97]. Figure 5.1 shows that all three methods obtain highly comparable results.

5.3.2 Performance Metrics for Automatic FCLs

Section 4.3.2 introduced two types of performance metrics for automatic linear FCLs. The time-based metrics, such as overshoot, delay time, rise time, settling time, ISE index, ITEA index and the normalized transient performance metrics are directly applicable to nonlinear FCLs as well. For the frequency-based methods

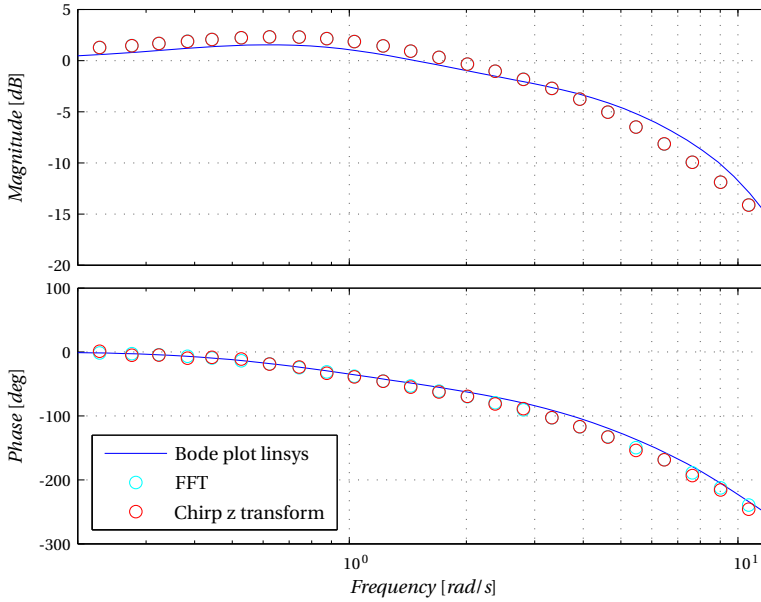


Figure 5.1: Bode plot of a Jacobian linearization of $q(s)/q_{ref}(s)$ versus the FFT and Chirp z transform of a pitch rate time response to a sum of sinusoids on the reference pitch rate.

linearization or frequency response estimation is needed of the entire closed-loop system.

5.4 Robustness Metrics

Stability of linear systems is described in Section 4.5 in terms of obtaining a bounded (limited) system response for a bounded input. For nonlinear systems this notion also holds. However, for nonlinear FCL design an alternative notion of stability is used more commonly. This section starts with a compact overview of Lyapunov stability. An in-depth review can of Lyapunov stability can be found in Appendix A of Krstić *et al.* [64].

5.4.1 Lyapunov Stability

Consider the nonlinear time-varying system,

$$\dot{x}(t) = f(x(t), t), \quad x(t_0) = x_0 \tag{5.3}$$

with $t \in \mathbb{R}_+$, $x(t) \in \mathbb{R}^n$ and $f : \mathbb{R}_+ \times \mathbb{R}^n \rightarrow \mathbb{R}^n$ locally Lipschitz in x and piecewise continuous in t . Without loss of generality the system (5.3) is assumed to have an

equilibrium point at the origin, $x_e = 0$. The following definition gives the stability of this equilibrium point [60].

Definition 5.2 (Stability in the sense of Lyapunov)

The equilibrium point $x_e = 0$ of the system (5.3) is,

- **stable** if for each $\epsilon > 0$ and any $t_0 > 0$, there exists a $\delta(\epsilon, t_0) > 0$ such that,

$$|x(t_0)| < \delta(\epsilon, t_0) \Rightarrow |x(t)| < \epsilon, \forall t \geq t_0; \quad (5.4)$$

- **uniformly stable** if for each $\epsilon > 0$ and any $t_0 > 0$, there exists a $\delta(\epsilon) > 0$ independent of t_0 such that,

$$|x(t_0)| < \delta(\epsilon) \Rightarrow |x(t)| < \epsilon, \forall t \geq t_0; \quad (5.5)$$

- **asymptotically stable** if it is stable, and for any $t_0 > 0$, there exists a positive constant $c = c(t_0)$ such that,

$$|x(t_0)| < c \Rightarrow \lim_{t \rightarrow \infty} |x(t)| = 0; \quad (5.6)$$

- **uniformly asymptotically stable** if it is uniformly stable and there exists a positive constant c independent of t_0 , such that $\forall |x(t_0)| < c, \lim_{t \rightarrow \infty} |x(t)| = 0$, uniformly in t_0 , that is, $\forall \eta > 0$, there is a $T = T(\eta) > 0$ such that,

$$|x(t_0)| < c \Rightarrow |x(t)| < \eta, \forall t \geq t_0 + T(\eta); \quad (5.7)$$

- **exponentially stable** if for any ϵ there exists a $\delta(\epsilon) > 0$ and a positive constant α such that,

$$|x(t_0)| < \delta \Rightarrow |x(t)| < \epsilon e^{-\alpha(t-t_0)}, \forall t \geq t_0 > 0; \quad (5.8)$$

- **unstable** if it is not stable.

To clarify stability in the sense of Lyapunov a bit further, the $\epsilon - \delta$ requirement can be seen in a challenge-answer form [60]. The origin is stable if, for any value of ϵ that a challenger poses, we can answer with a δ , possibly dependent on ϵ , such that a trajectory starting in the neighborhood of δ never leaves the neighborhood of ϵ . Figure 5.2 provides a graphical representation of this stability definition.

Asymptotic stability only has one requirement, the state should go to the origin, or in other words the origin should be attractive, when time goes to infinity. If a constant c can be selected for which this occurs, the origin is called asymptotically stable. In the figure this constant is chosen coincidentally in the neighborhood of δ . For uniform asymptotic stability, a slightly different definition is used. This definition is constructed as follows. However small a positive η is chosen, $|x(t)|$ will be smaller than that after $t_0 + T$ seconds.

Asymptotic stability does not provide a rate of convergence, or in other words it only shows if the origin is reached, not when the origin is reached. In the case of exponential stability, the origin it is not only attractive, but the rate of convergence is guaranteed to be exponential.

The reader should note that the system itself is not stable, but the origin (or equilibrium) of the system is stable. However, for brevity, the system is called stable in the remainder of this thesis, when actually the stable equilibrium of the system is meant.

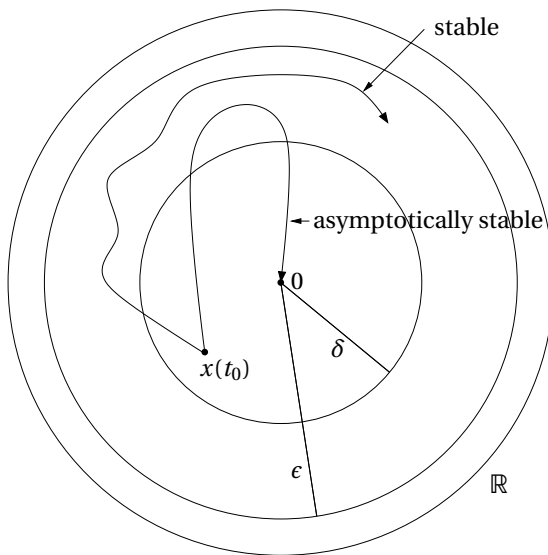


Figure 5.2: Graphical representation of stability in the sense of Lyapunov, source [58].

Demonstration of the stability of a system using only Definition 5.2 would require the analytical solution of system (5.3). This solution is generally not available and therefore an alternative method of demonstrating stability must be used. In 1892 Lyapunov showed a different method to assert stability, referred to as Lyapunov's second method, or direct method [72]. In short this methods claims, when

a system contains some “measure of energy”, the rate of change of this energy will provide insight into the stability of that system. Before providing a more formal definition of this method, let us first define function properties that can describe the “measure of energy”.

Definition 5.3 (Lyapunov function properties)

Let $B(r)$ be a ball of size r around the origin, $B(r) = \{x \in \mathbb{R}^n : |x| < r\}$. A continuous function $V(x)$ is,

- **positive definite** on $B(r)$, if $V(0) = 0$ and $V(x) > 0$, $\forall x \in B(r)$ without the origin;
- **positive semi-definite** on $B(r)$, if $V(0) = 0$ and $V(x) \geq 0$, $\forall x \in B(r)$ without the origin;
- **negative (semi-)definite** on $B(r)$, if $-V(x)$ is positive (semi-)definite;
- **radially unbounded** if $V(0) = 0$, $V(x) > 0$ on \mathbb{R}^n without the origin, and $V(x) \rightarrow \infty$ as $|x| \rightarrow \infty$.

A continuous time-varying function $V(x, t)$ is,

- **positive definite** on $\mathbb{R} \times B(r)$, if $V(0, t) = 0$, $\forall t \geq 0$ and $V(x, t) > \alpha(x)$, $\forall t \geq 0$, $x \in B(r)$, in which $\alpha(x)$ is a positive definite function on $B(r)$;
- **radially unbounded** if $V(0, t) = 0$, $\forall t \geq 0$ and $V(x, t) > \alpha(x)$, $\forall t \geq 0$, $x \in \mathbb{R}^n$, in which $\alpha(x)$ is a radially unbounded function;
- **decreasing** on $\mathbb{R} \times B(r)$ if there exists a positive definite function $\alpha(x)$ on $B(r)$ such that, $V(x, t) \leq \alpha(x)$, $\forall t \geq 0$, $x \in B(r)$.

Given a Lyapunov (energy) function $V(x, t)$ for the system (5.3), the stability of this system can be studied using the time derivative of V along the trajectories of the system,

$$\dot{V}(t, x) = \frac{\partial V}{\partial t} + \frac{\partial V}{\partial x} f(t, x) \quad (5.9)$$

Theorem 5.1 (Lyapunov's direct method)

Let $V(x, t) : \mathbb{R}_+ \times \mathcal{D} \rightarrow \mathbb{R}_+$ be a continuously differentiable and positive definite function, where \mathcal{D} is an open region containing the origin. The equilibrium

point $x_e = 0$ is,

- **stable** if $\dot{V}(t, x)$ is negative semi-definite for $x \in \mathcal{D}$;
- **uniformly stable** if $V(t, x)$ is decrescent and $\dot{V}(t, x)$ is negative semi-definite for $x \in \mathcal{D}$;
- **asymptotically stable** if $\dot{V}(t, x)$ is negative definite for $x \in \mathcal{D}$;
- **uniformly asymptotically stable** if $V(t, x)$ is decrescent and $\dot{V}(t, x)$ is negative definite for $x \in \mathcal{D}$;
- **exponentially stable** if there exist three positive constants, c_1 , c_2 and c_3 , such that $c_1|x|^2 \leq V(t, x) \leq c_2|x|^2$ and $\dot{V}(t, x) \leq -c_3|x|^2$ for $x \in \mathcal{D}$.

Proof: The proof can be found in Chapter 4 of Khalil [60].

Lyapunov's direct method's primary benefit is that it can be applied without explicitly solving the differential Equation (5.3). However, Theorem 5.1 only gives sufficient conditions for stability and does not provide any means of constructing the Lyapunov function $V(t, x)$. Section 5.6 continues this discussion, but first let us look at other robustness issues, such as disturbance rejection, noise attenuation and the time-delay margin.

5.4.2 Disturbance Rejection

General robustness metrics for disturbance rejection and noise attenuation, comparable to the loop gain shaping used in linear FCL design, could not be found for nonlinear systems. Also the concepts of gain and phase margin, indicating how far the system is from instability and how robust it is to perturbations, are not directly applicable to nonlinear systems [119]. Instead the influence of unknown disturbances can be included in the system description and taken into account in the nonlinear FCL design. The synthesized nonlinear FCL should then be able to achieve asymptotic (or exponential) stability for every disturbance within a range of possible disturbances. Consider the disturbed nonlinear system,

$$\dot{x}(t) = f(x(t), u(t), d(t), t), \quad x(t_0) = x_0 \quad (5.10)$$

with $t \in \mathbb{R}_+$, $x(t) \in \mathbb{R}^n$, $u(t) \in \mathbb{R}^m$, $d(t) \in \mathbb{R}^m$ and $f: \mathbb{R}_+ \times \mathbb{R}^n \times \mathbb{R}^m \times \mathbb{R}^m \rightarrow \mathbb{R}^n$. The nonlinear FCL should be synthesized such that,

$$\dot{V}(t, x) = \frac{\partial V}{\partial t} + \frac{\partial V}{\partial x} f(x(t), u(t), d(t), t) < 0 \quad (5.11)$$

with $V(t, x)$ a decrescent Lyapunov function. Even though the resulting controller stabilizes the system for a set of disturbances, it remains unknown how well these disturbances are actually rejected.

5.4.3 Noise Attenuation

The influence of measurement noise on the closed loop nonlinear system can be written as,

$$\begin{aligned}\dot{x}(t) &= f(x(t), u(t, y), t), & x(t_0) &= x_0 \\ y(t) &= h(x(t), n(t), t)\end{aligned}\quad (5.12)$$

with $t \in \mathbb{R}_+$, $x(t) \in \mathbb{R}^n$, $y(t) \in \mathbb{R}^p$, $n(t) \in \mathbb{R}^p$, $u: \mathbb{R}_+ \times \mathbb{R}^p \rightarrow \mathbb{R}^m$, $f: \mathbb{R}_+ \times \mathbb{R}^n \times \mathbb{R}^m \rightarrow \mathbb{R}^n$ and $h: \mathbb{R}_+ \times \mathbb{R}^n \times \mathbb{R}^p \rightarrow \mathbb{R}^p$. The system input u is determined by the controller based on the measured output y , which contains measurement noise n . Again a Lyapunov function can be constructed for the asymptotic stability of this system using,

$$\dot{V}(t, x) = \frac{\partial V}{\partial t} + \frac{\partial V}{\partial x} f(x(t), u(t, y), t) < 0 \quad (5.13)$$

However, this result would not indicate the actual amount of attenuation.

One branch of control theory dealing with noise attenuation is that of minimum variance controllers. These controllers are synthesized to minimize the variance of the output signal [120]. If an error state is chosen as the controlled output signal, the synthesized controller would maximize noise attenuation. Extensions of this theory to nonlinear systems, using an ANOVA-like variance decomposition method can also be found in literature [134]. Possible application of lessons learned from these theories, to the controllers developed in this chapter, is left for future work.

5.4.4 Time-Delay Margin

Stability of nonlinear systems with time delays is studied thoroughly in literature [78, 44, 43]. Consider the time-delay system,

$$\dot{x}(t) = A_0 x(t) + A_1 x(t - \tau) \quad (5.14)$$

with $t \in \mathbb{R}_+$, $x(t) \in \mathbb{R}^n$ and $\tau \in \mathbb{R}_+$. The initial condition for this system depends on the state at $t = 0$ as well as $t = -\tau$ and cannot be specified as a point $x(0) = x_0$. Instead the initial condition is a function,

$$x(t) = \phi(t), \quad t \in [-\tau, 0] \quad (5.15)$$

where $\phi: [-\tau, 0] \rightarrow \mathbb{R}^n$ is given. The system (5.14) is therefore called a functional differential equation. Moreover system (5.14) is a functional differential equation

of the retarded type, because the highest order derivative does not contain delayed variables. Alternatively, the time-delay system,

$$\dot{x}(t) - C\dot{x}(t - \tau) = A_0x(t) + A_1x(t - \tau) \quad (5.16)$$

is not of the retarded type, but of the neutral type.

The general form of a retarded functional differential equation is,

$$\dot{x}(t) = f(t, x_t) \quad (5.17)$$

with $t \in \mathbb{R}_+$, $x(t) \in \mathbb{R}^n$ and $f: \mathbb{R} \times \mathcal{C} \rightarrow \mathbb{R}^n$, where \mathcal{C} is a short hand notation for the set of continuous function mappings $\mathcal{C}([-\tau, 0], \mathbb{R}^n)$ to which ϕ belongs. Studying the stability of a time-delay system also requires the use of functionals. The Lyapunov-Krasovskii Functional (LKF) is defined using a differentiable $V(t, \phi)$ and $x_t(\eta, \phi)$ as the solution of system (5.17) at time t with the initial condition $x_\eta = \phi$. The derivative of $V(t, x_t)$ is calculated with respect to t and evaluated at $t = \eta$ [63],

$$\begin{aligned} \dot{V}(\eta, \phi) &= \left. \frac{d}{dt} V(t, x_t) \right|_{t=\eta, x_t=\phi} \\ &= \limsup_{\Delta t \rightarrow 0} \frac{1}{\Delta t} [V(\eta + \Delta t, x_{\eta+\Delta t}(\eta, \phi)) - V(\eta, \phi)] \end{aligned} \quad (5.18)$$

Theorem 5.2 (Lyapunov-Krasovskii Stability Theorem)

Suppose that $f: \mathbb{R} \times \mathcal{C} \rightarrow \mathbb{R}^n$ in system (5.17), maps $\mathbb{R} \times$ (bounded sets in \mathcal{C}) into a bounded set in \mathbb{R}^n , and $u, v, w: \mathbb{R}_+ \rightarrow \mathbb{R}_+$ are continuous nondecreasing functions, where $u(s)$ and $v(s)$ are positive for $s > 0$, and $u(0) = v(0) = 0$. The equilibrium, $\dot{x}(t) = 0$, is,

- **uniformly stable** if there exists a continuous differentiable functional $V: \mathbb{R} \times \mathcal{C} \rightarrow \mathbb{R}$, such that,

$$\begin{aligned} u(|\phi(0)|) &\leq V(t, \phi) \leq v(|\phi|_c) \\ \dot{V}(t, \phi) &\leq -w(|\phi(0)|); \end{aligned} \quad (5.19)$$

- **uniformly asymptotically stable** if Equation (5.19) holds with $w(s) > 0$ for $s > 0$;
- **globally uniformly asymptotically stable** if it is asymptotically stable and $\lim_{s \rightarrow \infty} u(s) = \infty$.

Proof: The proof can be found in Chapter 1 of Gu *et al.* [43].

The basics on how to apply Theorem 5.2 can be demonstrated using a simple example, adopted from Nguyen *et al.* [88] as presented in [62].

Example 5.1 (Lyapunov-Krasovskii Stability)

Consider the linear scalar system with input delay,

$$\dot{x}(t) = ax(t) + bu(t - \tau) \quad , \tau \in \mathbb{R}_+ \quad (5.20)$$

which is controlled using a state feedback controller $u(t) = -kx(t)$ with $bk > 0$. The closed-loop system will therefore be a retarded type system,

$$\dot{x}(t) = ax(t) - bkx(t - \tau) \quad (5.21)$$

Using a LKF we can find the controller gain k that would stabilize system (5.21), given a certain time delay τ . For this, consider the positive definite LKF,

$$V(x(t)) = \frac{1}{2}x^2(t) + \frac{1}{\tau} \int_{t-\tau}^t x^2(\theta) d\theta \quad (5.22)$$

with its time derivative along the solutions of (5.21),

$$\begin{aligned} \dot{V}(x(t)) &= x(t)\dot{x}(t) + \frac{1}{\tau} [x^2(t) - x^2(t - \tau)] \\ &= \left(a + \frac{1}{\tau}\right)x^2(t) - bkx(t - \tau)x(t) - \frac{1}{\tau}x^2(t - \tau) \\ &= \left(a + \frac{1}{2}bk + \frac{1}{\tau}\right)x^2(t) + \left(\frac{1}{2}bk - \frac{1}{\tau}\right)x^2(t - \tau) \dots \\ &\quad - \frac{1}{2}bk(x(t) + x(t - \tau))^2 \end{aligned} \quad (5.23)$$

using the relation $-bkx(t)x(t - \tau) = \frac{1}{2}bk(-[x(t) + x(t - \tau)]^2 + x^2(t) + x^2(t - \tau))$. The last term is negative, since $bk > 0$ and for \dot{V} , the other two terms must be negative as well, leading to the inequalities,

$$a + \frac{1}{2}bk + \frac{1}{\tau} < 0 \quad \text{and} \quad \frac{1}{2}bk - \frac{1}{\tau} < 0 \quad (5.24)$$

which can be expressed in controller gain limits, $bk < -2a - \frac{2}{\tau}$ and $bk < \frac{2}{\tau}$, or in terms of time delay margin, $\frac{-1}{a - \frac{1}{2}bk} < \tau < \frac{2}{bk}$. Note that a different choice in LKF leads to different inequalities, one being more conservative than the other. For instance, choosing,

$$V(x(t)) = x^2(t) + \frac{1}{\tau} \int_{t-\tau}^t x^2(\theta) d\theta \quad (5.25)$$

leads to the time delay margin, $\frac{-1}{2a-bk} < \tau < \frac{1}{bk}$. Inequalities, such as (5.24), arising from the LKF method can be presented as Linear Matrix Inequalities (LMIs) for which efficient solvers are available. For more information on determination of the time-delay margin the reader is referred to the book of Gu *et al.* [43].

The Lyapunov-Krasovskii functional requires the state variable $x(t)$ in the interval $[t - \tau, t]$, which makes applications of the Lyapunov-Krasovskii Stability Theorem rather difficult. This difficulty can sometimes be avoided using Razumikhin's theorem. Suppose,

$$\bar{V}(x_t) = \max_{\theta \in [-\tau, 0]} V(x(t + \theta)) \quad (5.26)$$

can serve as a measure for the size of x_t . If $V(x(t)) < \bar{V}(x_t)$, then $\dot{V}(x) > 0$ does not necessarily make $\bar{V}(x_t)$ grow. To keep $\bar{V}(x_t)$ from growing it is only necessary that $\dot{\bar{V}}(x_t) \leq 0$ whenever $V(x(t)) = \bar{V}(x_t)$. More formally,

Theorem 5.3 (Razumikhin Theorem)

Suppose that $f : \mathbb{R} \times \mathbb{C} \rightarrow \mathbb{R}^n$ in system (5.17), maps $\mathbb{R} \times$ (bounded sets in \mathbb{C}) into a bounded set in \mathbb{R}^n , and $u, v, w : \mathbb{R}_+ \rightarrow \mathbb{R}_+$ are continuous nondecreasing functions, where $u(s)$ and $v(s)$ are positive for $s > 0$, and $u(0) = v(0) = 0$, v strictly increasing. The equilibrium, $\dot{x}(t) = 0$, is,

- **uniformly stable** if there exists a continuous differentiable functional $V : \mathbb{R} \times \mathbb{R}^n \rightarrow \mathbb{R}$, such that,

$$\begin{aligned} u(|x|) &\leq V(t, x) \leq v(|x|) \\ \dot{V}(t, x(t)) &\leq -w(|x(t)|) \text{ whenever } V(t + \theta, x(t + \theta)) \leq V(t, x(t)) \end{aligned} \quad (5.27)$$

for $\theta \in [-\tau, 0]$;

- **uniformly asymptotically stable** if there exists a continuous differentiable functional $V : \mathbb{R} \times \mathbb{R}^n \rightarrow \mathbb{R}$, $w(s) > 0$ for $s > 0$ and there exists a nondecreasing function $p(s) > s$ for $s > 0$ such that,

$$\begin{aligned} u(|x|) &\leq V(t, x) \leq v(|x|) \\ \dot{V}(t, x(t)) &\leq -w(|x(t)|) \text{ whenever } V(t + \theta, x(t + \theta)) \leq pV(t, x(t)) \end{aligned} \quad (5.28)$$

for $\theta \in [-\tau, 0]$;

- **globally uniformly asymptotically stable** if it is asymptotically stable and $\lim_{s \rightarrow \infty} u(s) = \infty$.

Proof: The proof can be found in Chapter 1 of Gu *et al.* [43].

5.5 Design Options

Numerous design options exist for the control of a nonlinear system. Adaptive (self-learning) control, robust control, (recursive) linearizing control, predictive control and combinations of these methodologies have emerged to control a wide variety of nonlinear systems. The focus of this thesis lies on practical FCL design for general aviation aircraft. Because each aircraft type behaves different from the other, the nonlinear FCL method that is selected should not be highly model dependent. Thereby the necessity of detailed model identification is avoided and cost can be reduced. The method should not be computationally expensive as well. The hardware described in Chapter 3 has a 16 ms cycle and FCL calculations should not take longer than one cycle for minimal effective time delay. After the design is complete it should be clear what the stability properties of the closed loop system are in terms that the certification authorities understand, i.e., indicate how far the system is from becoming unstable for any state in the flight envelope [55]. In this way the designed FCL is usable in the near future.

Backstepping control is deemed a good candidate for a certifiable advanced control law, due to its use of Lyapunov analysis that guarantees system stability. However, conventional backstepping is sensitive to model uncertainties [109]. This problem is commonly approached from two sides. Robust backstepping incorporates specific uncertainties (e.g., an unknown parameter θ lying in a known interval $[\theta_{min}, \theta_{max}]$) in the controller design or imposes a dominating stable nonlinearity on the closed loop system, such that stability can be guaranteed even in the presence of these uncertainties [61]. Alternatively, adaptive backstepping incorporates parameter estimation in the backstepping controller to adapt uncertain parameters or even failures [113]. However, as mentioned by Jacklin [55], giving the FCL the capability to make rapid automated changes to enable self-healing in case of failures, also carries the risk that it makes a healthy aircraft unflyable in case of software malfunction.

This thesis proposes two new backstepping control methodologies based primarily on sensor data rather than model information. These methodologies are less sensitive to model uncertainties, while keeping the benefit that stability guarantees can be given using Lyapunov analysis. The resulting nonlinear FCLs are computational inexpensive and could therefore be used on the SAFAR platform. By linearizing the closed-loop system of aircraft, FBW platform and each FCL it is possible to express the performance, stability and robustness of the system using the metrics described in Section 4.3.

5.6 Nonlinear Flight Control Law Design

This section provides two design methods for a sensor-based backstepping algorithm. One uses singular perturbation theory and high-gain design and the second uses Taylor expansions to obtain an incremental form. First the principles of conventional backstepping are introduced. Note that the controller gains in this section are selected using trail and error, unless specifically stated otherwise.

5.6.1 Backstepping

Backstepping belongs to the class of the recursive nonlinear design strategies [109]. The main idea is to design a Control Lyapunov Function (CLF) based on a small subsystem and then reapply this design step-by-step to an augmented subsystem at each step. The design is complete when the augmentations recover the whole system. Backstepping starts with the subsystem that is removed by the largest number of integration steps from the control input. Each step the subsystem is stabilized using a “virtual control input” and then augmented with an integration equation until finally the original control input and complete system are obtained. In a block-diagram starting with the integrator farthest from the control input and adding integrating equation at each step, appears as moving “backwards”. Hence the name backstepping. Two detailed textbooks that deal with backstepping are written by Krstić *et al.* and Khalil [64, 60].

The definition of a CLF is introduced by Artstein and Sontag [8, 114].

Definition 5.4 (*Control Lyapunov Function*)

A smooth, positive definite, and radially unbounded function $V(x)$ is called a Control Lyapunov Function (CLF) for the system $\dot{x} = f(x) + g(x)u$ if for all $x \neq 0$,

$$L_g V(x) = 0 \Rightarrow L_f V(x) < 0 \quad (5.29)$$

The reason for using CLFs in the design of a backstepping controller is that the existence of a CLF is equivalent to the existence of a globally stabilizing control law [8]. In other words when a CLF is found, the backstepping control law will be globally stabilizing. The terms $L_g V(x)$ and $L_f V(x)$ in the CLF definition are Lie derivatives, which are defined as follows.

Definition 5.5 (Lie derivative)

Given a scalar function $h(x)$ and a vector field $f(x)$, the first order Lie-derivative of h with respect to f , $L_f^1 h(x)$, is defined as,

$$L_f^1 h(x) = \nabla h(x) f(x) \quad (5.30)$$

in which $\nabla h(x) = \frac{\partial h(x)}{\partial x}$ is the Jacobian of h . The Lie derivative can be interpreted as the directional derivative of h along f . Higher order Lie-derivatives are defined recursively,

$$\begin{aligned} L_f^0 h(x) &= h(x) \\ L_f^i h(x) &= \frac{\partial L_f^{i-1} h(x)}{\partial x} f(x) \end{aligned} \quad (5.31)$$

The function h and vector field f are assumed to be smooth, such that the function is differentiable any finite number of times and therefore the k -th Lie-derivative exists, with $k \in \mathbb{R}_+$.

The backstepping method can be applied to a broad class of systems. More precisely, backstepping is applicable to strict feedback systems, that is systems in the following feedback (lower triangular) form [109],

$$\begin{aligned} \dot{z} &= f(z) + \psi(z, \xi_1) \xi_1 \\ \dot{\xi}_1 &= a_1(\xi_1, \xi_2) \\ \dot{\xi}_2 &= a_2(\xi_1, \xi_2, \xi_3) \\ &\vdots \\ \dot{\xi}_n &= a_n(\xi_1, \xi_2, \xi_3, \dots, \xi_n, u) \end{aligned} \quad (5.32)$$

which, for the input-output pair (u, ξ_1) , has relative degree n . For systems having an upper triangular form, forwarding may be used, but this design methodology is not pursued here. More information on forwarding may be found in [109]. The relative degree of a system is defined as follows.

Definition 5.6 (Relative degree)

The relative degree of a nonlinear system,

$$\begin{aligned} \dot{x} &= f(x) + g(x)u \\ y &= h(x) + j(x)u \end{aligned} \quad (5.33)$$

with $x \in \mathbb{R}^n$ and $u, y \in \mathbb{R}^m$ is $\{r_1, \dots, r_m\}$ at $x = x_0$ if

- $L_{g_j} L_f^k h_i(x) = 0$ for all $1 \leq (i, j) \leq m$, for all $k < r_i - 1$ and for all x in a neighborhood of $x = x_0$,
- the matrix $m \times m$ matrix,

$$R(x) = \left[\frac{\partial y_i^{r_i}}{\partial u_j} \right]_{1 \leq i, j \leq m} = \begin{pmatrix} L_{g_1} L_f^{r_1-1} h_1(x) & \dots & L_{g_m} L_f^{r_1-1} h_1(x) \\ \vdots & & \vdots \\ L_{g_1} L_f^{r_m-1} h_1(x) & \dots & L_{g_m} L_f^{r_1-1} h_m(x) \end{pmatrix} \quad (5.34)$$

is nonsingular at $x = x_0$.

For a SISO system ($n = m = 1$) this reduces to, the relative degree is the integer r such that,

- $L_g L_f^k h(x) = 0$ for all $k = 0, \dots, r - 2$ and for all x in a neighborhood of $x = x_0$,
- $L_g L_f^{r-1} h(x_0) \neq 0$.

An advantage of backstepping over other linearizing control laws, such as Feedback Linearization (FBL), also known as Nonlinear Dynamic Inversion (NDI) in aerospace applications, is the possibility to retain stabilizing nonlinearities in the closed-loop system description. The next example is adopted from Khalil [60] and shows the advantage of backstepping over FBL.

Example 5.2 (Scalar system example)

Consider the nonlinear scalar system,

$$\dot{x} = ax - bx^3 + u \quad (5.35)$$

with $x, u \in \mathbb{R}$ and a, b positive constants. A CLF for this system would be,

$$V = \frac{1}{2}x^2$$

and its time derivative along the solutions of (5.35),

$$\dot{V} = x\dot{x} = x(ax - bx^3 + u)$$

A control law that renders this expression negative definite could be,

$$u = bx^3 - (k + a)x \quad (5.36)$$

in which $k > 0$. This control law cancels the nonlinearity (cubic term) and is equivalent to the control law obtained by FBL. Note that the control activity is large for large values of x to cancel the cubic term. When the constant b is uncertain it can even happen that this controller destabilizes the closed-loop system if the estimate used in the controller synthesis is larger than the real value of b . Alternatively the Lyapunov derivative could also be rendered negative definite using,

$$u = -(k + a)x \quad (5.37)$$

in which the cubic term is kept in the closed-loop system description, providing “non-linear damping”, irrespective of the actual value of b . Figure 5.3 shows the time histories of the state and input for both control laws, when $a = b = 1$, $x(0) = 5$ and $k = 2$. Clearly the FBL control law uses much control effort to cancel the beneficial nonlinearity, resulting in worse stabilizing performance.

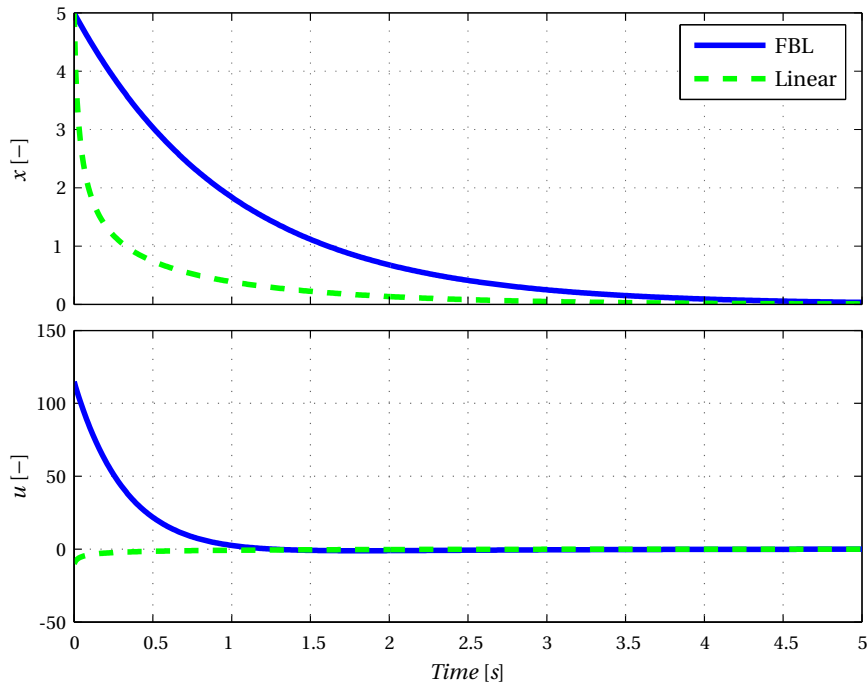


Figure 5.3: Time histories of system (5.35) with $a = b = 1$ and $x(0) = 5$, controlled by (5.36) and (5.37) with $k = 2$.

The following example is again adopted from Khalil [60] and shows the backstepping design methodology for higher-order systems.

Example 5.3 (Backstepping)

Consider the second-order system,

$$\begin{aligned}\dot{x}_1 &= x_1^2 - x_1^3 + x_2 \\ \dot{x}_2 &= u\end{aligned}\tag{5.38}$$

A stabilizing backstepping controller can be constructed for this system as follows.

Step 1: Take the scalar system furthest from the input, that is,

$$\dot{x}_1 = x_1^2 - x_1^3 + x_2\tag{5.39}$$

with x_2 viewed as the virtual input and proceed to design the feedback control $x_2 = \alpha(x_1)$ to stabilize the origin $x_1 = 0$. For this the CLF, $V_1 = \frac{1}{2}x_1^2$ may be used with its time derivative along the solutions of (5.39),

$$\dot{V}_1 = x_1 \dot{x}_1 = x_1^3 - x_1^4 + x_1 \alpha(x_1)$$

The stabilizing function used in this example is,

$$\alpha(x_1) = -x_1^2 - x_1$$

resulting in,

$$\dot{V}_1 = -x_1^2 - x_1^4 \leq -x_1^2, \forall x_1 \in \mathbb{R}$$

Hence, the origin of (5.39) is globally exponentially stable.

Step 2: To step back, a change in variables can be used,

$$y = x_2 - \alpha(x_1)$$

resulting in the new system description,

$$\begin{aligned}\dot{x}_1 &= x_1^2 - x_1^3 + y + \alpha(x_1) = -x_1 - x_1^3 + y \\ \dot{y} &= \dot{x}_2 - \dot{\alpha}(x_1) = u + (2x_1 + 1)(-x_1 - x_1^3 + y)\end{aligned}\tag{5.40}$$

Using the composite CLF, $V_2 = V_1 + \frac{1}{2}y^2$, with its time derivative along the solutions of (5.40),

$$\dot{V}_2 = x_1 \dot{x}_1 + y \dot{y} = -x_1^2 - x_1^4 + y(u + x_1 + (2x_1 + 1)(-x_1 - x_1^3 + y))$$

the stabilizing backstepping control law for system (5.38) can be obtained. Taking,

$$u = -x_1 - (2x_1 + 1)(-x_1 - x_1^3 + y) - y$$

yields

$$\dot{V}_2 = -x_1^2 - x_1^4 - y^2$$

Hence, the origin is globally asymptotically stable. Figure 5.4 shows a block-diagram of the resulting closed-loop system. The green arrows indicate the model information used to determine the backstepping control law.

The backstepping procedure of Example 5.3 can be extended to n -th order strict feedback systems (5.32). Figure 5.5 shows the generalization of Figure 5.4 required to deal with such n -th order systems. From this figure and Example 5.3 it becomes clear that backstepping depends largely on system information and can be cumbersome to derive. In the next two sections alternative backstepping methods are presented that replace the use system information with an increased use of sensor information.

5.6.2 Backstepping and Singular Perturbation Theory

This section uses singular perturbation theory, Tikhonov's Theorem [60, 124], and a backstepping design in order to control uncertain systems. Hovakimyan *et al.* [52] proposed a controller for non-affine systems based on Tikhonov's Theorem in 2007. Their Approximate Dynamic Inversion (ADI) controller, is modified in this section to incorporate a backstepping framework. Also the focus is shifted from control of non-affine systems to control of uncertain systems with respect to the previous work. The resulting control law depends on sensor information, rather than model information, for determination of the system dynamics. Dealing with uncertainties in this way could be a major benefit for certification of advanced control laws. The reason for this is twofold. First, the backstepping design, using Lyapunov analysis, guarantees the stability of the controlled system. Second, by using state derivative measurements rather than relying on perfect knowledge of the system, the need for adaptation to uncertain parameters or unknown model structure is removed. To emphasize that this method uses mainly measurements rather than a model to evaluate the system dynamics, the developed control law will be referred to as Sensor-Based Backstepping (SBB) in this thesis. It should be noted that this method uses even less model information than the Incremental Backstepping method introduced in Section 5.6.3.

Singular Perturbation Theory

Singular perturbations, i.e., small perturbations that cannot be approximated as zero, cause time-scale separated behavior in systems [60]. This can be seen from slow and fast transients in the reaction of the system to an external input. Consider

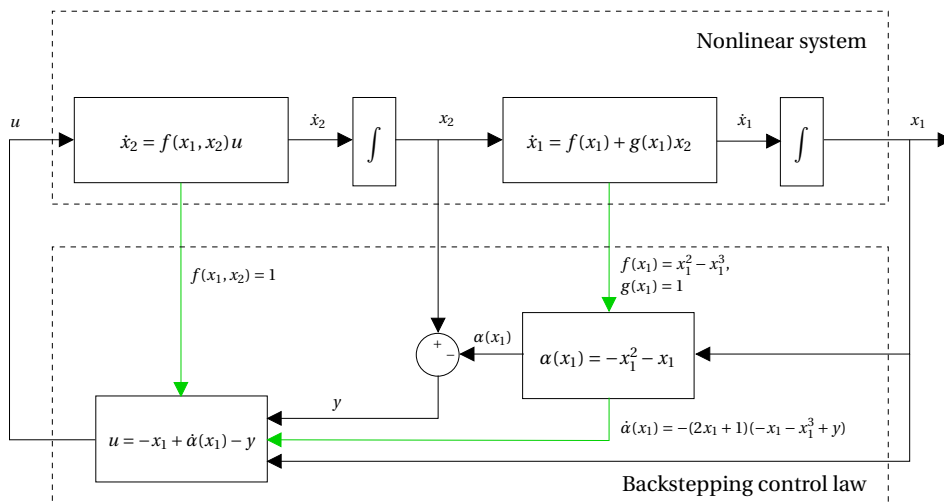


Figure 5.4: Block-diagram of the closed-loop system second order nonlinear system and backstepping control law. The green arrows indicate model information used in the controller design.

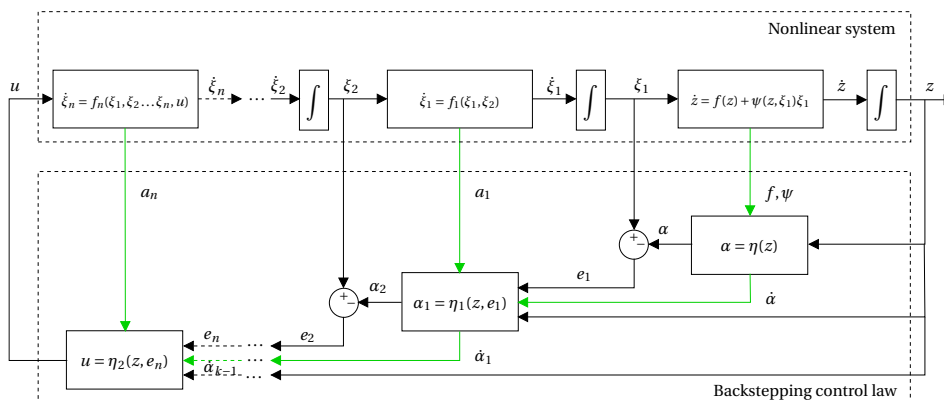


Figure 5.5: Block-diagram of the closed-loop system of nonlinear system and backstepping control law. The green arrows indicate model information used in the controller design. Source [2]

a singularly perturbed, nonlinear system with the following state space description:

$$\begin{aligned}\dot{x} &= f(t, x, u, \epsilon), \quad x(0) = \xi(\epsilon) \\ \epsilon \dot{u} &= g(t, x, u, \epsilon), \quad u(0) = \eta(\epsilon)\end{aligned}\tag{5.41}$$

where ξ and η depend smoothly on the small positive parameter ϵ . Assume that f and g are continuously differentiable in their arguments for $(t, x, u, \epsilon) \in \mathbb{R}_+ \times D_x \times D_u \times [0, \epsilon_0]$, where $D_x \in \mathbb{R}^n$, $D_u \in \mathbb{R}^m$ are domains and $\epsilon_0 > 0$. In addition, let the system, Eq. (5.41), be in *standard form*, i.e., $0 = g(t, x, u, 0)$ has $k \geq 1$ isolated real roots $u = h_i(t, x)$, $i \in \{1, \dots, k\}$ for each $(t, x) \in \mathbb{R}_+ \times D_x$. To obtain the i -th model, the roots can be substituted in Eq. (5.41) at $\epsilon = 0$,

$$\dot{x} = f(t, x, h(t, x), 0), \quad x(0) = \xi(0)\tag{5.42}$$

Equation (5.42) is also referred to as the reduced (slow) system. In singular perturbation theory, the system given by,

$$\frac{dv}{d\tau} = g(t, x, v + h(t, x), 0), \quad v(0) = \eta_0 - h(0, \xi_0)\tag{5.43}$$

is called the boundary layer (fast) system, where $v(t, x) = u - h(t, x)$, the normal time-scale t is replaced by the new time-scale $\tau = \frac{t}{\epsilon}$ and $\eta_0 = \eta(0)$ and $\xi_0 = \xi(0)$, $(t, x) \in \mathbb{R}_+ \times D_x$ are treated as fixed parameters.

Then the following result is due to Tikhonov [60, 124],

Theorem 5.4 (Tikhonov's Theorem)

Consider the singular perturbation system, Eq. (5.41), and let $u = h(t, x)$ be an isolated root of $g(t, x, u, 0)$. Assume that the following conditions hold for all $(t, x, u - h(t, x), \epsilon) \in \mathbb{R}_+ \times D_x \times D_v \times [0, \epsilon_0]$ for some domains $D_x \in \mathbb{R}^n$ and $D_v \in \mathbb{R}^m$, which contain the corresponding origins.

- (a) On any compact subset of $D_x \times D_v$ the function f , g , their first partial derivatives with respect to (x, u, ϵ) , and the first partial derivative of g with respect to t are continuous and bounded, $h(t, x)$ and $\frac{\partial g}{\partial u}(t, x, u, 0)$ have bounded first derivatives with respect to their arguments, $\frac{\partial f}{\partial x}(t, x, h(t, x))$ is Lipschitz in x uniformly in t , and the initial conditions for ξ and η are smooth functions of ϵ .
- (b) The origin is an exponentially stable equilibrium point of the reduced system, Eq. (5.42). There exists a Lyapunov function $V : \mathbb{R}_+ \times D_x \rightarrow \mathbb{R}_+$ that

satisfies

$$W_1(x) \leq V(t, x) \leq W_2(x), \quad (5.44)$$

$$\frac{\partial V(t, x)}{\partial t} + \frac{\partial V(t, x)}{\partial x} f(t, x, h(t, x), 0) \leq -W_3(x)$$

for all $(t, x) \in \mathbb{R}_+ \times D_x$, where W_1 , W_2 , and W_3 are continuous positive definite functions on D_x . Let c be a nonnegative number such that $x \in D_x | W_1(x) \leq c$ is a compact subset of D_x .

(c) The origin is an equilibrium point of the boundary layer system, Eq. (5.43), which is exponentially stable uniformly in (t, x) .

Let $R_v \in D_v$ denote the region of attraction of the autonomous system,

$$\frac{dv}{d\tau} = g(0, \xi_0, v + h(0, \xi_0), 0) \quad (5.45)$$

and let W_v be a compact subset of R_v . Then for each compact set $W_x \in \{x \in D_x | W_2(x) \leq \rho c, 0 < \rho < 1\}$, there exists a positive constant ϵ_* such that for all $t \geq 0, \xi_0 \in W_x, \eta_0 - h(0, \xi_0) \in W_v$ and $0 < \epsilon < \epsilon_*$. The nonlinear system, Eq. (5.41), has a unique solution x_ϵ on \mathbb{R}_+ and $x_\epsilon(t) - x_{00}(t) = O(\epsilon)$ holds uniformly for $t \in \mathbb{R}_+$, where $x_{00}(t)$ denotes the solution of the reduced system.

Proof: The proof can be found in Chapter 11 of Khalil [60].

In words Tikhonov's theorem can be explained as follows. Given a sufficiently time-scale separated nonlinear system ($0 < \epsilon < \epsilon_*$), that describes physical phenomena (Theorem 5.4.a), with stabilizable slow dynamics (Theorem 5.4.b) and stable fast dynamics (5.4.c), then the solutions of the complete nonlinear system will be stable and tend to the solutions of the slow system ($x_\epsilon(t) - x_{00}(t) = O(\epsilon)$).

Aproximate Dynamic Inversion

Hovakimyan *et al.* proposed a controller based on the time-scale separation properties of a singularly perturbed system [52]. Consider the nonlinear system,

$$\dot{x} = f(t, x, u) \quad (5.46)$$

where $x(0) = x_0$ for $(x, u) \in D_x \times D_u$ and where $D_x \subset \mathbb{R}^n$ and $D_u \subset \mathbb{R}^m$ are domains that contain the corresponding origins. Here x denotes the state vector and u the input vector. The function f is continuously differentiable in its arguments. Furthermore assume $\partial f / \partial u$ is bounded away from zero for $(x, u) \in \Omega_{x,u} \subset D_x \times D_u$, where $\Omega_{x,u}$ is a compact set of possible initial conditions, i.e., there exists a $b_0 > 0$ such that $|\partial f / \partial u| > b_0$.

A reference signal y_r is defined for the state x and the tracking error between the state and this reference is given by, $e = x - y_r$. Therefore, the error dynamics of the system can be written as,

$$\dot{e} = f(t, e + y_r, u) - \dot{y}_r \quad (5.47)$$

An ADI controller for Eq. (5.47) can be constructed based on the following fast dynamics,

$$\epsilon \dot{u} = -\text{sign} \left(\frac{\partial f}{\partial u} \right) \mathbf{f}(t, e, u) \quad (5.48)$$

where $\mathbf{f}(t, e, u)$ is the mapping $D_e \times D_u \rightarrow \mathbb{R}^m$. Application of Tikhonov's Theorem leads to the following result.

Theorem 5.5 (Approximate Dynamic Inversion)

Assume that the following conditions hold for all $(t, e, u - h(t, e), \epsilon) \in \mathbb{R}_+ \times D_e \times D_v \times [0, \epsilon_0]$ for some domains $D_e \in \mathbb{R}^n$ and $D_v \in \mathbb{R}^m$, which contain the corresponding origins.

(a) On any compact subset of $D_e \times D_v$ the function f and the first partial derivatives with respect to (t, e, u) , are continuous and bounded, $h(t, e)$ and $\frac{\partial f}{\partial u}(t, e, u)$ have bounded first derivatives with respect to their arguments, $\frac{\partial f}{\partial e}(t, e, h(t, e))$ is Lipschitz in e , uniformly in t .

(b) The origin is an exponentially stable equilibrium point of the reduced system,

$$\dot{e} = f(t, y_r, h(t, e)) \quad (5.49)$$

The mapping $e \rightarrow f(e + y_r, h(t, e))$ is continuously differentiable and Lipschitz in e , uniformly in t .

(c) The mapping $(t, e, v) \rightarrow \frac{\partial f}{\partial u}(t, e, v + h(t, e))$ is bounded from below by some positive number for all $(t, e) \in \mathbb{R}_+ \times D_e$

Then the origin of the boundary layer system,

$$\frac{dv}{d\tau} = -\text{sign} \left(\frac{\partial f}{\partial u} \right) \mathbf{f}(t, e, v + h(t, e)) \quad (5.50)$$

is exponentially stable. Moreover, let Ω_v be a compact subset of R_v , where $R_v \subset D_v$ denotes the region of attraction of the autonomous system,

$$\frac{dv}{d\tau} = -\text{sign} \left(\frac{\partial f}{\partial u} \right) \mathbf{f}(0, e_0, v + h(0, e_0)) \quad (5.51)$$

Then for each compact subset $\Omega_e \subset D_e$, there exists a positive constant ϵ_* such that for all $t \geq 0$, $e_0 \in \Omega_e$, $u_0 - h(0, e_0) \in \Omega_v$, and $0 < \epsilon < \epsilon_*$. The nonlinear system, Eqs. (5.46, 5.48), has a unique solution x_ϵ on \mathbb{R}_+ and $x_\epsilon(t) = y_r(t) + O(\epsilon)$ holds uniformly for $t \in [T, \infty)$.

Proof: The proof can be found in the paper of Hovakimyan *et al.* [52].

In other words, given a sufficiently time-scale separated nonlinear system ($0 < \epsilon < \epsilon_*$), that describes physical phenomena (Theorem 5.5.a), is minimum phase (Theorem 5.5.b) and controllable (Theorem 5.5.c), then the fast dynamics will be stable and follow the reference signal ($x_\epsilon(t) = y_r(t) + O(\epsilon)$). The advantage of using the stabilizing controller described in Eq. (5.48) becomes clear in the following sections.

Sensor-Based Backstepping

Suppose that the function $\mathbf{f}(t, e, u)$ in Eq. (5.48) can be written as,

$$\mathbf{f}(t, e, u) = \dot{x} - \dot{x}_{des} \quad (5.52)$$

in which \dot{x} is a measurement of the state derivative and \dot{x}_{des} the desired state derivative. The latter can be defined using a backstepping framework as follows. Again consider the system in Eq. (5.46), $\dot{x} = f(t, x, u)$, and the tracking error, $e = x - y_r$. A backstepping controller can be designed using the positive definite, radially unbounded CLF, $V(e)$, of which the time derivative should be negative definite for asymptotic stability in the sense of Lyapunov,

$$\dot{V}(e) = \frac{\partial V(e)}{\partial e} \dot{e} = \frac{\partial V(e)}{\partial e} (\dot{x} - \dot{y}_r) \quad (5.53)$$

Promoting \dot{x} to the control variable \dot{x}_{des} , it follows that,

$$\dot{x}_{des} = -c \frac{\partial V(e)}{\partial e} + \dot{y}_r \quad (5.54)$$

with the design parameter $c > 0$, will lead to a negative definite $\dot{V}(e)$ and hence to guaranteed asymptotic stability of the error dynamics. Substituting \dot{x}_{des} in Eqs. (5.52, 5.48) yields the following controller,

$$\epsilon \dot{u} = -\text{sign} \left(\frac{\partial f}{\partial u} \right) \left[\dot{x} - \dot{y}_r + c \frac{\partial V(e)}{\partial e} \right] \quad (5.55)$$

hereafter referred to as the SBB controller. Note that this controller will stabilize the error dynamics, given a sufficiently time-scale separated nonlinear system ($0 <$

$\epsilon < \epsilon_*$), that describes physical phenomena (Theorem 5.5.a), is minimum phase (Theorem 5.5.b) and controllable (Theorem 5.5.c). This will be referred to as the SBB assumption in the remainder of this thesis. Also note that, since the time-scale separation parameter ϵ is small, the controller gain will be high. The CLF offers some design freedom to the control engineer. The benefit of this framework can be shown using several examples. Figure 5.6 shows the SBB controller in a block diagram.

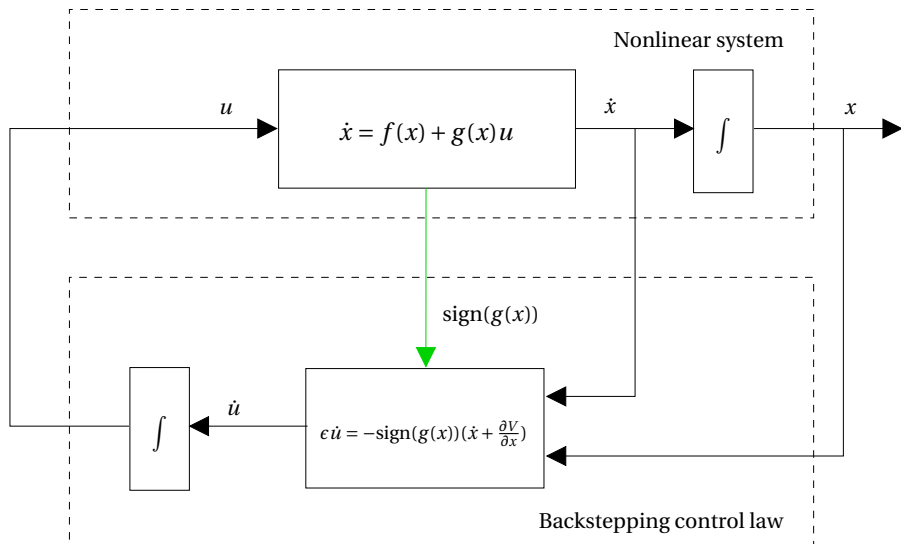


Figure 5.6: Block diagram of sensor based backstepping. The green arrow indicates model information used in the controller design.

Example 5.4 (Simple linear system)

Consider the scalar linear system,

$$\dot{x} = h(u) = f + gu \quad (5.56)$$

with $x(0) = 0$, $x \in \mathbb{R}$, $u \in \mathbb{R}$ and f and g non-zero constants. Again the tracking error, $e = x - y_r$, is introduced.

A SBB controller can be designed using the most simple CLF $V(e) = \frac{1}{2}e^2$, as,

$$\epsilon \dot{u} = -\text{sign}(g) [\dot{x} - \dot{y}_r + c_1(x - y_r)] \quad (5.57)$$

with $c_1 > 0$ to asymptotically stabilize the error dynamics. The system, Eqs. (5.56, 5.57), clearly satisfies the assumptions of Theorem 5.5.a and 5.5.c. For compliance to as-

sumption 5.5.b the exponential stability of the equilibrium point of the reduced system needs to be demonstrated. The isolated root, $\epsilon = 0$, can be written as,

$$0 = -\text{sign}(g) [\dot{x} - \dot{y}_r + c_1(x - y_r)] = \dot{e} + c_1(x - y_r) \quad (5.58)$$

leading to the reduced system definition,

$$\dot{e}(t, x, h(x, t), 0) = -c_1(x - y_r) \quad (5.59)$$

with equilibrium point $x_{eq} = y_r$. Application of Lyapunov's direct method, Theorem 5.1, shows exponential stability of the reduced system, thereby verifying Theorem 5.5.b. The controller in Eq. (5.57) should indeed stabilize the system, Eq. (5.56). Note that the selection of ϵ is arbitrary in this example, since Eq. (5.56) is not a physical system. It should be chosen smaller than one, however.

Also a conventional backstepping controller can be designed using the CLF, $V(e) = \frac{1}{2}e^2$, of which the derivative should be negative definite for asymptotic stability in the sense of Lyapunov,

$$\begin{aligned} \dot{V}(e) &= e\dot{e} = e(\dot{x} - \dot{y}_r) = e(f + gu - \dot{y}_r) \\ u &= g^{-1}(-c_2e + \dot{y}_r - f) \end{aligned} \quad (5.60)$$

If $c_2 > 0$, then $\dot{V}(e)$ will be negative definite for the control law, Eq. (5.60), and hence the stability of the closed-loop system is guaranteed.

Figure 5.7(a) shows the response of the system, Eq. (5.56), to the different controllers. Note that the initial response, from zero to two seconds, of the SBB controlled system is caused by starting the control actions when the system starts not in an equilibrium condition. Adding a trim input, $u_0 = g^{-1}(-f)$, such that $\dot{x}(0) = 0$, results in the response shown in Figure 5.7(b). Clearly the tracking error has been reduced. Figure 5.8 shows a magnification of the tracking error for both controllers. The conventional backstepping control law tracks the reference signal with zero error, whereas the SBB control law tracks the reference signal closely, but not perfectly. However, the maximum tracking error of the SBB control law is small, approximately 0.1% of the amplitude of the reference signal and therefore acceptable.

The advantage of using SBB becomes clear in the presence of uncertainty. Considering parametric uncertainty, the system can be written as,

$$\dot{x} = \theta_x f + \theta_u g u \quad (5.61)$$

with θ_x and θ_u representing the state and input matrix uncertainty. Increasing f by 10% (i.e., $\theta_x = 1.1$) without changing the controllers, leads to the response shown in Figure 5.9(a). Increasing g by 10% leads to the response shown in Figure 5.9(b). The normal backstepping controller needs some time to stabilize the error dynamics, thereby creating a large steady state error. The SBB controller only uses the sign of $\partial h / \partial u$ and is therefore unaffected by the parameter changes.

Example 5.5 (Simple nonlinear system)

A slightly more complex scalar system can be written as,

$$\dot{x} = f x^a + g u \quad (5.62)$$

with $x \in \mathbb{R}$, $u \in \mathbb{R}$, and f , g and a non-zero constants. Again it is possible to construct a conventional backstepping controller as,

$$u = g^{-1}(-c_3 e + \dot{y}_r - f x^{a_c}) \quad (5.63)$$

with a_c the non-zero constant used during controller synthesis. Since the SBB controller does not make use of $f(x)$, it may remain the same. Also the compliance to the assumptions 5.5.a, 5.5.b and 5.5.c can be demonstrated in the same way as in Example 5.4.

Figure 5.10 shows the response of the system, Eq. (5.61), to the different controllers with and without uncertainty in the nonlinearity. Figure 5.10(a) shows that perfect tracking is obtained for both controllers when the system is nonlinear ($a = 2$) and the controller knows this nonlinearity ($a_c = 2$). Figure 5.10(b) shows the response of the system, Eq. (5.61), when linearity ($a_c = 1$) is used in the synthesis of the controllers, while the system actually behaves nonlinearly. The SBB controller still tracks properly, whereas the conventional backstepping method is notably influenced by the assumption of linearity during the controller synthesis.

Although uncertainties have little influence on the tracking performance, internal dynamics do affect performance. Since these dynamics are not measured, they are also not compensated. The next example shows how to deal with internal dynamics.

Example 5.6 (Effect of Internal Dynamics)

Consider the system,

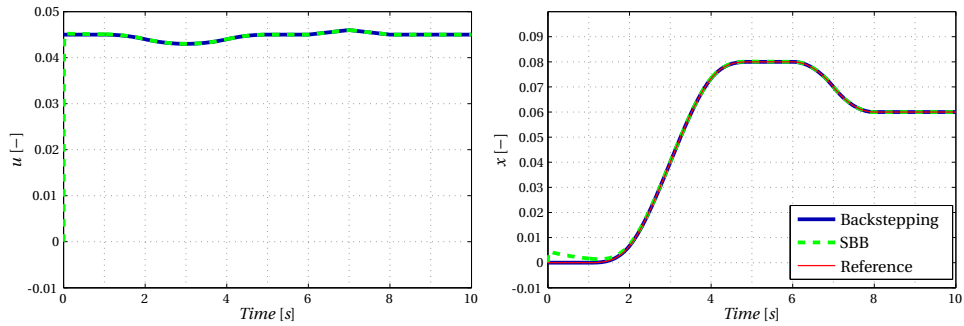
$$\begin{aligned} \dot{x}_1 &= f_1 x_2 \\ \dot{x}_2 &= f_2 x_1 + f_3 x_2 + g u \end{aligned} \quad (5.64)$$

Suppose this system is controlled using the SBB controller,

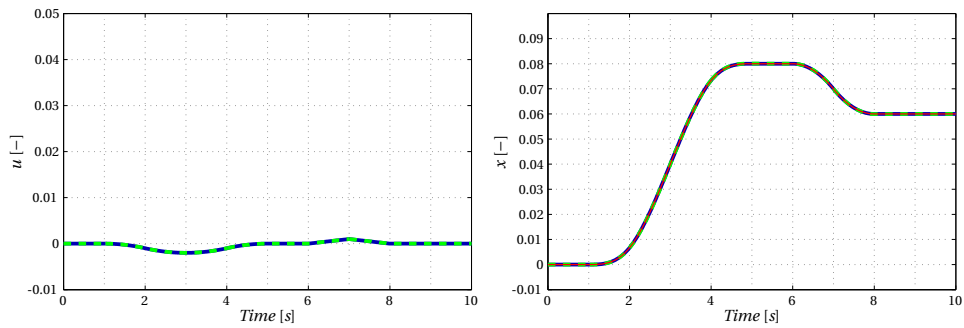
$$\epsilon \dot{u} = -\text{sign}(g) [\dot{x}_2 - \dot{y}_r + c_1(x_2 - y_r)] \quad (5.65)$$

Note that the state x_1 is not influenced by the controller directly and therefore part of the internal dynamics.

The left plot of Figure 5.11 shows that the SBB controller has difficulty stabilizing the error dynamics. By changing the CLF used in the SBB derivation to $V(e) = \frac{1}{2} e^2 + k \frac{1}{2} \lambda^2$, where $\lambda = \int e dt$ and $k > 0$, this problem can be solved. The time-derivative of this CLF



(a) SBB without trim.



(b) SBB with trim $u_0 = g^{-1}(-f)$.

Figure 5.7: Response of the system, Eq. (5.56) with $f = 0.9$ and $g = -20$, using a backstepping ($c_2 = 1$) and a sensor based backstepping controller ($c_1 = 1, \epsilon = 0.1$).

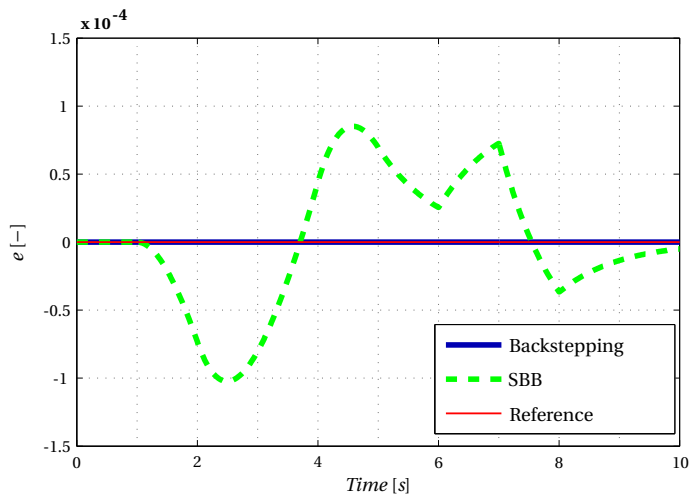
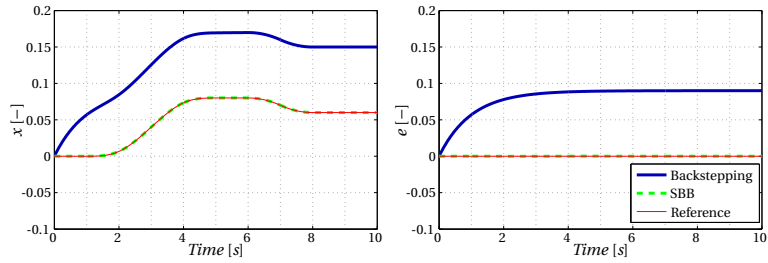
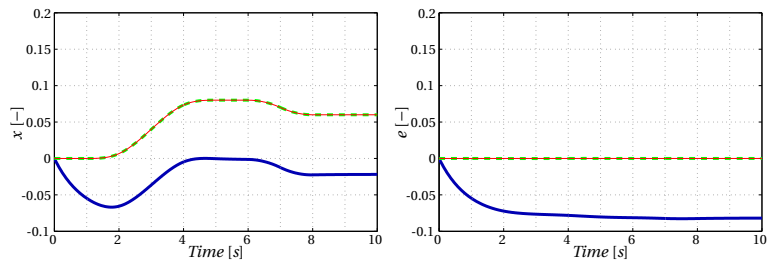


Figure 5.8: Magnification of the tracking error.

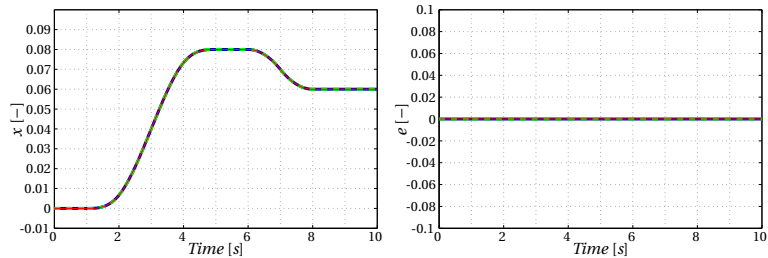


(a) Uncertainty in f

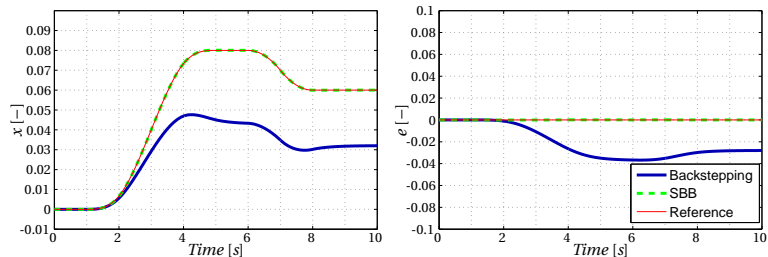


(b) Uncertainty in g

Figure 5.9: Response of the system, Eq. (5.61) with $f = 0.9$ and $g = -20$, using a backstepping ($c_2 = 1$) and a sensor based backstepping controller ($c_1 = 1, \epsilon = 0.1$).



(a) B: $c_3 = 1, a_c = 2$, SBB: $c_1 = 1, \epsilon = 0.1$



(b) B: $c_3 = 1, a_c = 1$, SBB: $c_1 = 1, \epsilon = 0.1$

Figure 5.10: Response of the system, Eq. (5.62), with $a = 2, f = 0.9$ and $g = -20$ using a backstepping and a sensor based backstepping controller.

is,

$$\dot{V}(e) = e\dot{e} + \lambda e = e(\dot{x} - \dot{y}_r + k\lambda) \quad (5.66)$$

and therefore,

$$\dot{x}_{des} = \dot{y}_r - ce - k\lambda \quad (5.67)$$

Inserting this into Eq. (5.52) yields the SBB controller,

$$e\dot{u} = -\text{sign}(g) \left[\dot{x}_2 - \dot{y}_r + c_1(x_2 - y_r) + k \int (x_2 - y_r) dt \right] \quad (5.68)$$

with $c_1 > 0$ and $k > 0$ to asymptotically stabilize the error dynamics when the assumptions of SBB control are met. The right plot of Figure 5.11 shows that the tracking performance increases using this new SBB controller.

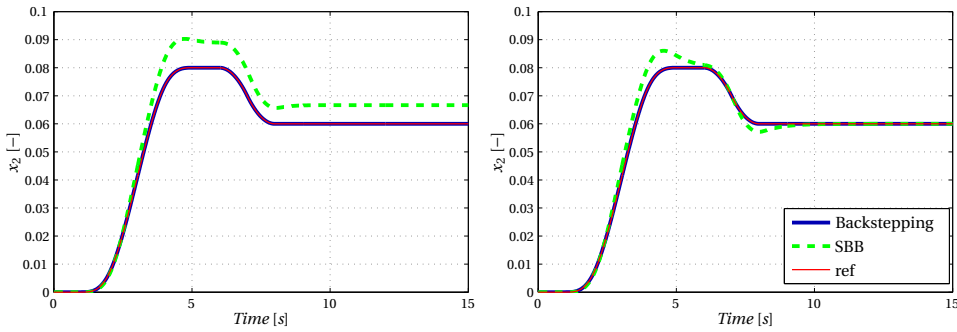


Figure 5.11: Response of system (5.64) with $f_1 = 2$, $f_2 = 1$, $f_3 = 1$ and $g = 1$ under influence of a Backstepping controller with $c = 2$ and a SBB controller with $c = 2$ and $k = 0$ (left plot) or $k = 1$ (right plot).

Additional information can be obtained by analyzing the SBB controller in a state-space description. This is demonstrated in the following example.

Example 5.7 (State-space representation of the SBB controller)

Consider again the system and SBB controller from Example 5.5, with $a = 1$,

$$\begin{aligned} \dot{x} &= f x + g u \\ e\dot{u} &= -\text{sign}(g) [\dot{x} - \dot{y}_r + c_1(x - y_r)] \end{aligned} \quad (5.69)$$

Rewriting this expression into a state-space description gives,

$$\begin{bmatrix} \dot{x} \\ \dot{u} \end{bmatrix} = \underbrace{\begin{bmatrix} f & g \\ P(f+c_1) & Pg \end{bmatrix}}_A \begin{bmatrix} x \\ u \end{bmatrix} + \begin{bmatrix} 0 & 0 \\ -Pc_1 & -P \end{bmatrix} \begin{bmatrix} y_r \\ \dot{y}_r \end{bmatrix} \quad (5.70)$$

with $P = -\text{sign}(g)/\epsilon$ and assuming that \dot{x} is measured perfectly. The stability of this system can be determined by calculating the roots of the determinant of $(sI - A)$, i.e.,

$$\begin{aligned}
 0 &= (s - f)(s - Pg) - gP(f + c_1) = s^2 - s(f + Pg) - gPc_1 \\
 s_{1,2} &= \frac{1}{2} (f + Pg) \pm \frac{1}{2} \sqrt{(f + Pg)^2 + 4Pg c_1} \\
 s_{1,2} &= \frac{1}{2} \left(f - \frac{|g|}{\epsilon} \right) \pm \frac{1}{2} \sqrt{\left(f - \frac{|g|}{\epsilon} \right)^2 - 4 \frac{|g|}{\epsilon} c_1}
 \end{aligned} \tag{5.71}$$

Figure 5.12 shows the stability of this system depending on f , g , ϵ and c_1 . Note that for negative values of f the system is (marginally) stable for any value of g , ϵ and c_1 . When f is larger than zero, stability depends on the combination of g and ϵ . If g is small, time-scale separation between input and state is insufficient unless the time-scale separation parameter ϵ is made small enough as well. This is shown in Figures 5.12(a)-5.12(c) in which the value of ϵ is changed with a constant value of c_1 . The controller tuning parameter c_1 does not change whether a certain value of g will be stabilizing, but it does change the location of the poles. Figures 5.12(d)-5.12(f) show the real part of the largest pole for a constant ϵ and a varying value of c_1 . In stable regions, large values of c_1 clearly makes the stabilization faster. However, if $c_1 > (|g| - \epsilon f)^2 / (4\epsilon|g|)$ the poles become imaginary and the system will oscillate.

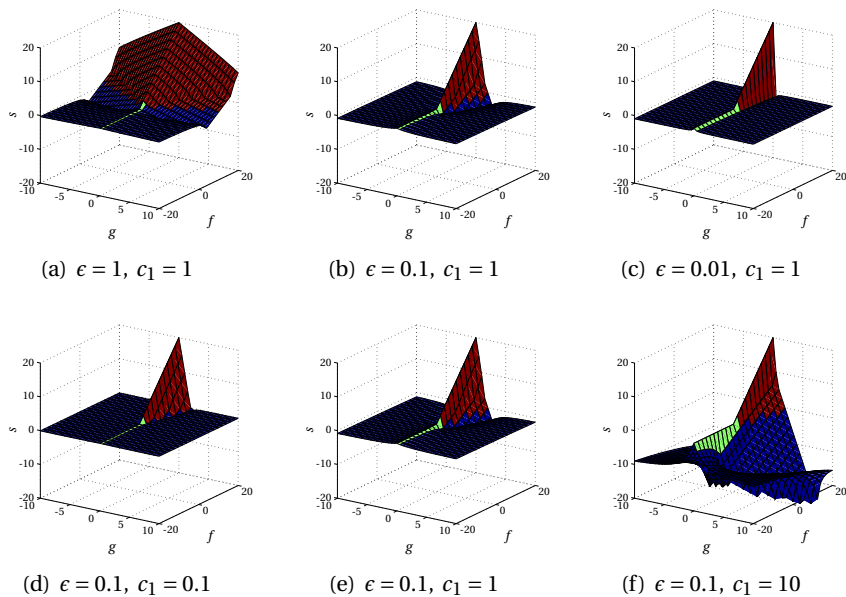


Figure 5.12: Real part of the largest pole in Equation (5.71). In the red part of each plot the system is unstable, the green part indicates marginal stability and the blue part stability.

SBB uses sensor information rather than model knowledge. This naturally gives rise to the question, what is the sensitivity of the SBB method to sensor noise. Again a simple example is used to investigate the noise sensitivity.

Example 5.8 (Influence of sensor noise)

Consider the noisy linear system,

$$\begin{aligned} \dot{x} &= f + gu \\ y &= \begin{bmatrix} x + \omega_x \\ \dot{x} + \omega_{\dot{x}} \end{bmatrix} \end{aligned} \tag{5.72}$$

where ω_x and $\omega_{\dot{x}}$ are zero mean wide-band noise signals with variances σ_x^2 and $\sigma_{\dot{x}}^2$, respectively. The SBB controller can then be written as,

$$\begin{aligned} \epsilon \dot{u} &= -\text{sign}(g) \left([0 \ 1] y - \dot{y}_r + c_1 ([1 \ 0] y - y_r) \right) \\ &= -\text{sign}(g) \left(\dot{x} + \omega_{\dot{x}} - \dot{y}_r + c_1 (x + \omega_x - y_r) \right) \end{aligned} \tag{5.73}$$

and the conventional backstepping controller as,

$$\begin{aligned} u &= g^{-1} (-c_2 ([1 \ 0] y - y_r) + \dot{y}_r - f) \\ &= g^{-1} (-c_2 (x + \omega_x - y_r) + \dot{y}_r - f) \end{aligned} \tag{5.74}$$

Figure 5.13 shows the influence of sensor noise on both controllers. Clearly both controllers result in similar noise attenuation properties. The amount of attenuation depends on the frequency, but is at least a factor 10.

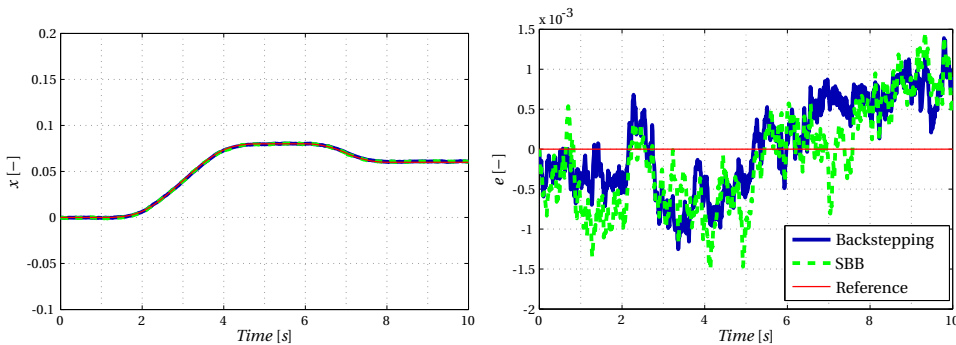


Figure 5.13: Response of the system, Eq. (5.72) with $\sigma_x^2 = \sigma_{\dot{x}}^2 = 10^{-4}$, $f = 0.9$ and $g = -20$, using a backstepping and a sensor based backstepping controller.

Also disturbance rejection can be investigated using a simple example.

Example 5.9 (Influence of disturbances)

Consider the linear system with additive disturbance,

$$\dot{x} = f + g(u + w) \quad (5.75)$$

The disturbance is treated as unanticipated and unmeasured and therefore the backstepping (Eq. 5.60) and SBB (Eq. 5.57) controllers are not altered. Figure 5.14 shows that the backstepping controller is influenced substantially more by the additive disturbance compared with the SBB controller. In this scenario the disturbance rejection of both controllers differs by a factor 85. The reason for the improved disturbance rejection can be traced to the high gain nature of the SBB controller.

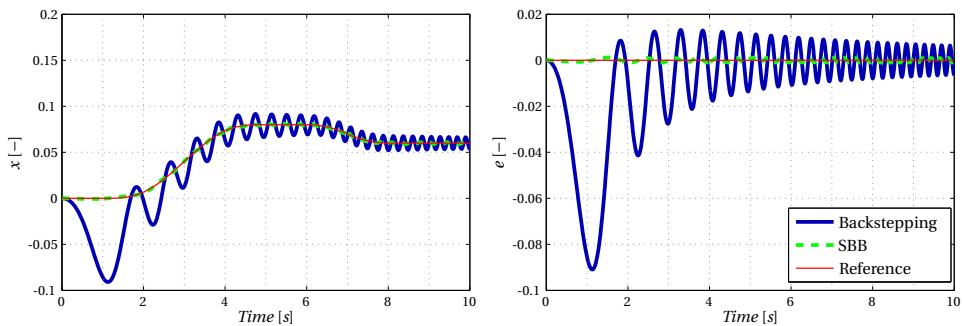


Figure 5.14: Response of the system, Eq. (5.75) with $f = 0.9$, $g = -20$ and w equal to a chirp signal with an amplitude of 0.01 and a frequency linearly increasing from 0.1 Hz to 5 Hz in 10 seconds, using a backstepping and a sensor based backstepping controller.

The last off-nominal condition tested in this section is the influence of time-delays in the closed loop system.

Example 5.10 (Influence of time delays)

Consider the linear system with actuator delay,

$$\dot{x} = f x + g u(t - \tau) \quad (5.76)$$

Figure 5.15 shows the system response, using a delay of 10 milliseconds, without changing the control laws. In the first 10 seconds, the SBB controller is slightly more robust to the time delay than the conventional backstepping controller. However, the integrator of the SBB controller winds up, resulting in instability of the closed-loop system.

This problem is analyzed by writing the SBB controlled system in state-space form and

focusing just on stabilization ($y_r = \dot{y}_r = 0$),

$$\begin{bmatrix} \dot{x} \\ \dot{u} \end{bmatrix} = \underbrace{\begin{bmatrix} f & 0 \\ P(f+c_1) & 0 \end{bmatrix}}_{A_0} \begin{bmatrix} x \\ u \end{bmatrix} + \underbrace{\begin{bmatrix} 0 & g \\ 0 & Pg \end{bmatrix}}_{A_1} \begin{bmatrix} x \\ u \end{bmatrix} (t-\tau) \quad (5.77)$$

According to Proposition 5.22 in Gu et al. [43], the system given by,

$$\dot{x}(t) = A_0 x(t) + A_1 x(t-\tau) \quad (5.78)$$

is asymptotically stable if there exist $n \times n$ matrices $P = P^T$, Q_p , $S_p = S_p^T$, $R_{pq} = R_{pq}^T$, $p = 0, 1$, $q = 0, 1$ such that the LMIs,

$$\begin{pmatrix} P & \tilde{Q} \\ \tilde{Q}^T & \tilde{R} + \tilde{S} \end{pmatrix} > 0 \quad (5.79)$$

with,

$$\begin{aligned} \tilde{Q} &= (Q_0 \ Q_1) \\ \tilde{R} &= \begin{pmatrix} R_{00} & R_{01} \\ R_{10} & R_{11} \end{pmatrix} \\ \tilde{S} &= \frac{1}{\tau} \text{diag}(S_0 \ S_1) \end{aligned}$$

and

$$\begin{pmatrix} \Delta & -D^s & -D^a \\ -D^{sT} & R_d + S_d & 0 \\ -D^{aT} & 0 & 3S_d \end{pmatrix} > 0 \quad (5.80)$$

with,

$$\begin{aligned} \Delta &= \begin{pmatrix} \Delta_{00} & \Delta_{01} \\ \Delta_{01}^T & \Delta_{11} \end{pmatrix} \\ \Delta_{00} &= -PA_0 - A_0^T P - Q_0 - Q_0^T - S_0 \\ \Delta_{01} &= Q_N - PA_1 \\ \Delta_{11} &= S_N \end{aligned}$$

and

$$\begin{aligned} S_d &= S_{p-1} - S_p \\ R_d &= \tau(R_{00} - R_{11}) \\ D^s &= \begin{pmatrix} \frac{\tau}{2} A_0^T (Q_0 + Q_1) + \frac{\tau}{2} (R_{00} + R_{01}) - (Q_0 - Q_1) \\ \frac{\tau}{2} A_1^T (Q_0 + Q_1) - \frac{\tau}{2} (R_{10} + R_{11}) \end{pmatrix} \\ D^a &= \begin{pmatrix} \frac{\tau}{2} A_0^T (Q_0 - Q_1) - \frac{\tau}{2} (R_{00} - R_{01}) \\ \frac{\tau}{2} A_1^T (Q_0 - Q_1) + \frac{\tau}{2} (R_{10} - R_{11}) \end{pmatrix} \end{aligned}$$

have a solution. This method is only slightly conservative and often comes close to the "true" time-delay margin. Rewriting these LMIs into an explicit expression of time delay margin (τ_{max}) as function of g , c and ϵ is generally not possible, however. Using Eqs.

(5.79 and 5.80), the time-delay margin of the closed-loop system (5.77) with $f = 0.9$, $g = -20$, $c = 1$ and $\epsilon = 0.1$ is determined to be $\tau_{max} = 7.8$ milliseconds. This time-delay margin is too low for practical use. The time-scale separation parameter, ϵ , could be increased (lowering the controller gains), but this also lowers the general closed-loop stability as indicated in Example 5.7.

Integrator windup prevention can be implemented in several ways, such as disabling the integral until the controlled variable is in the controllable region, or saturating the integrator state [12]. A “classical” tracking anti windup scheme will be implemented in this example, as shown in Figure 5.16. By comparing the achieved input and the commanded input, the difference can be used to reduce the integrator input. The difference signal is multiplied by the anti-windup gain H , which has to be tuned based on values of g , f , τ , ϵ and c_1 . Figure 5.17 shows that satisfactory tracking is obtain even when the actuator delay is 100 milliseconds. The time delay margin can be obtained by writing the system,

$$\begin{aligned} \dot{x} &= fx + gu(t - \tau) \\ \epsilon \dot{u} &= \epsilon H(u(t - \tau) - u) - \text{sign}(g)(\dot{x} + cx) \end{aligned} \quad (5.81)$$

in state-space form,

$$\begin{bmatrix} \dot{x} \\ \dot{u} \end{bmatrix} = \underbrace{\begin{bmatrix} f & 0 \\ P(f + c_1) & -H \end{bmatrix}}_{A_0} \begin{bmatrix} x \\ u \end{bmatrix} + \underbrace{\begin{bmatrix} 0 & g \\ 0 & Pg + H \end{bmatrix}}_{A_1} \begin{bmatrix} x \\ u \end{bmatrix} (t - \tau) \quad (5.82)$$

Again using Proposition 5.22 in Gu *et al.* [43] with $f = 0.9$, $g = -20$, $c = 1$, $\epsilon = 0.1$ and $H = 150$ gives a time-delay margin of $\tau_{max} = 0.64$ seconds. Which is an improvement by a factor 82.5 with respect to the SBB controller without anti-windup. The dependency of the anti-windup gain H on the model parameters could be a major drawback of this method, since SBB is developed to be model independent.

Figure 5.18 shows the influence of model uncertainty on the time delay margin. Clearly not much knowledge is required on the system function (f) parameters. Even when 50% is added to or subtracted from this function, the time-delay margin changes by only 10%. Also the input function (g) parameters do not need to be very accurate. However, if the mismatch in this case is larger than 40%, the designed controller is more sensitive to time delays in reality. As a last note, this anti-windup scheme makes use of direct actuator output measurements. These measurements are not always available and the anti-windup scheme could be altered to use the output of an actuator model instead. Simulations show that this actuator model should be fairly accurate as well.

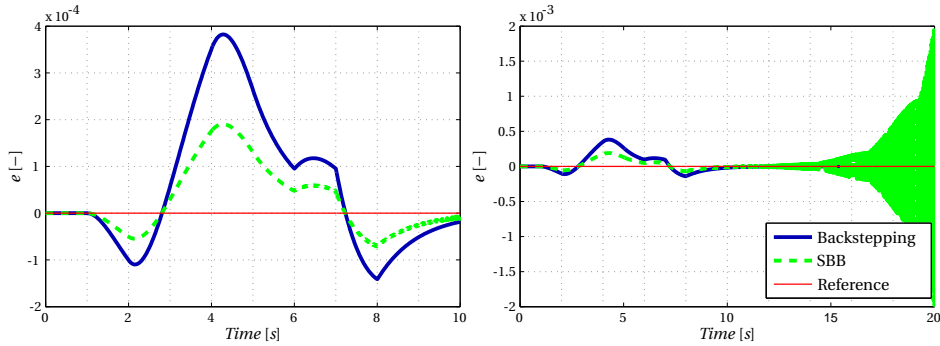


Figure 5.15: Response of the system, Eq. (5.76) with $f = 0.9$, $g = -20$ and $\tau = 0.01$ seconds, using a backstepping and a sensor based backstepping controller.

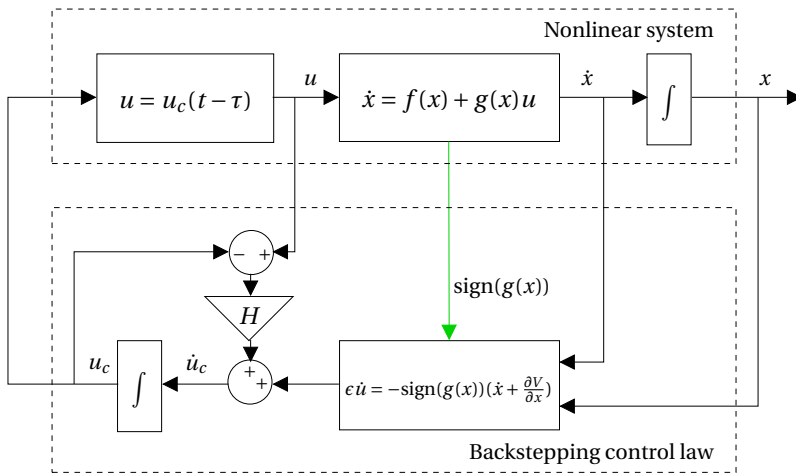


Figure 5.16: Block diagram of sensor based backstepping with anti windup.

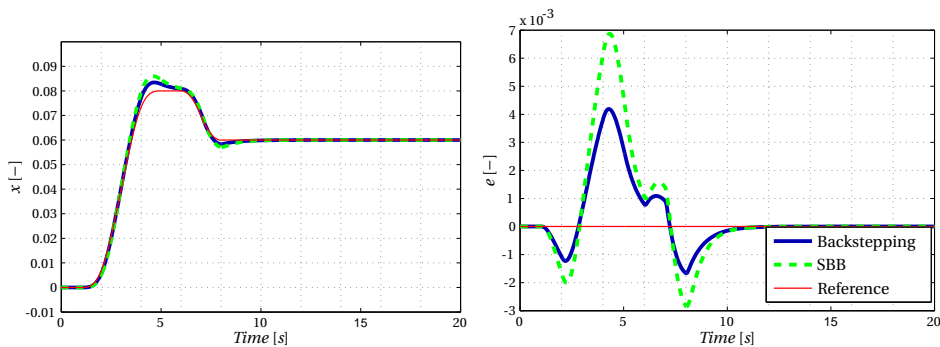


Figure 5.17: Response of the system, Eq. (5.76) with $f = 0.9$, $g = -20$, $\tau = 0.1$ seconds and $H = 150$, using a backstepping and a sensor based backstepping controller with anti windup.

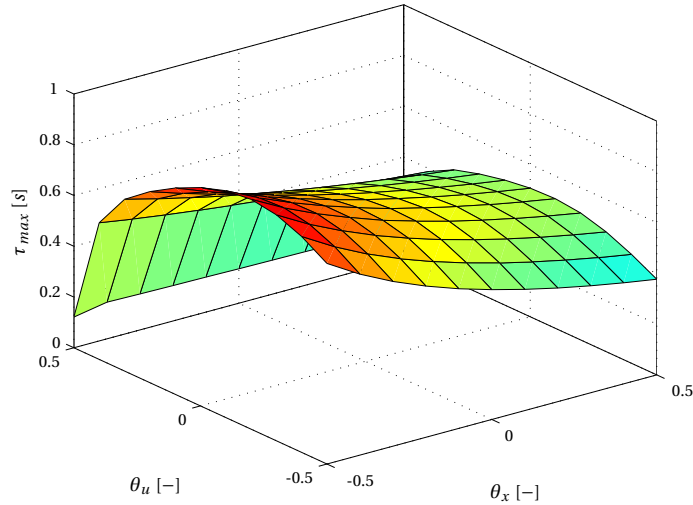


Figure 5.18: Influence of model uncertainty on time delay margin τ_{max} with $f = 0.9(1 + \theta_x)$, $g = -20(1 + \theta_u)$, $\tau = 0.1$ seconds and $H = 150$.

Comparison to PI Control

When looking more closely at the SBB control law for systems with a relative degree of one, e.g., Eq. (5.57), one may argue that this control law is actually a Proportional-Integral (PI) control law. Indeed, integrating both sides of this equation results in,

$$\epsilon u = -\text{sign}(g) \left(e + c_4 \int_0^t e \, dt \right) \quad (5.83)$$

This result was also obtained by Teo *et al.* in 2010 [123]. In that paper, the authors claim that although the ADI controller is equivalent to the PI controller in some aspects, in the robustness aspect it is not.

Example 5.11 (SBB versus PI)

Consider the simple nonlinear system (5.62),

$$\dot{x} = f x^a + g u$$

Using a SBB controller, the closed-loop error dynamics can be written as,

$$\dot{e} = f x^a - \frac{|g|}{\epsilon} \int_0^t (\dot{e} + c_1 e) dt \quad (5.84)$$

Instead using a PI controller, results in the closed-loop error dynamics,

$$\dot{e} = f x^a - \frac{|g|}{\epsilon} \left(e + c_4 \int_0^t e dt \right) \quad (5.85)$$

Figure 5.19 shows that indeed identical results are obtain when using SBB and PI controllers on system (5.62) with $a = 1$ and $a = 2$.

Adding sensor noise changes the SBB and PI controlled closed-loop system descriptions to,

$$\dot{e} = f x^a - \frac{|g|}{\epsilon} \int_0^t (\dot{e} + \omega_{\dot{x}} + c_1(e + \omega_x)) dt \quad (5.86)$$

and,

$$\dot{e} = f x^a - \frac{|g|}{\epsilon} \left(e + \omega_x + c_4 \int_0^t (e + \omega_x) dt \right) \quad (5.87)$$

respectively. Figure 5.20 shows that PI control is influenced more by sensor noise than the SBB controller. The SBB controller is influenced only by integrated noise on the \dot{x} and x resulting in a lower noise level than the PI controller which is influenced by direct and integrated noise on the x signal. However, when \dot{x} is not measured, but calculated from differentiating x , this ‘advantage’ disappears.

Figures 5.21(a) and 5.21(b) show that robustness to disturbances and time-delays is again equivalent for the SBB and PI controller. Furthermore, it is also possible to construct an anti-windup scheme, similar to the one presented in Example 5.10, for the PI controller, improving time-delay robustness.

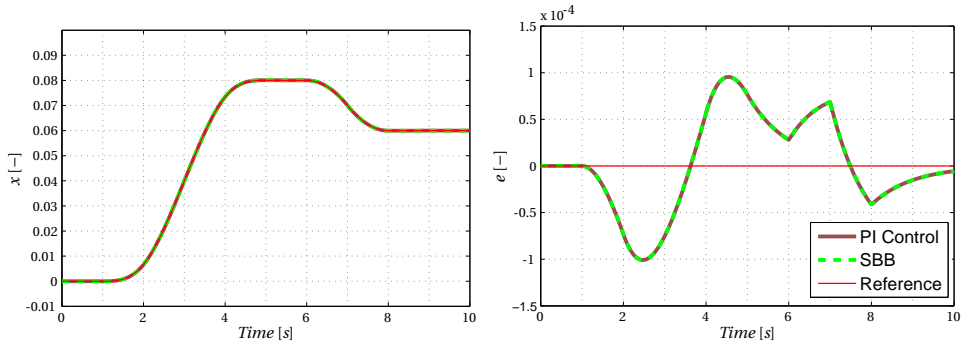
Example 5.11 shows that the SBB controller could be seen as a motivation why PI control can be used to control some nonlinear systems with a relative degree of one. However, keeping the backstepping framework has benefits for higher order systems, which will be discussed in Section 5.6.4.

5.6.3 Backstepping with Taylor Series Expansions

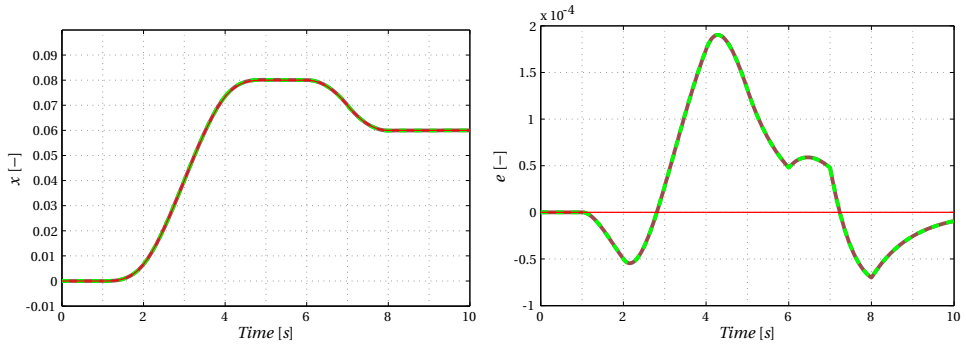
This section presents the second new backstepping method that uses limited model information, called incremental backstepping. The name of this method is derived from the method Incremental Nonlinear Dynamic Inversion (INDI) [110] to which it bears resemblance.

Consider the affine-in-control nonlinear system,

$$\dot{x} = f(x) + g(x)u \quad (5.88)$$



(a) SBB: $c_1 = 1, \epsilon = 0.1$, PI: $c_1 = 1, \epsilon = 0.1$, System: $a = 2$



(b) SBB: $c_1 = 1, \epsilon = 0.1$, PI: $c_1 = 1, \epsilon = 0.1$, System: $a = 1$

Figure 5.19: Response of the system, Eq. (5.62), using a sensor based backstepping controller and a PI controller.

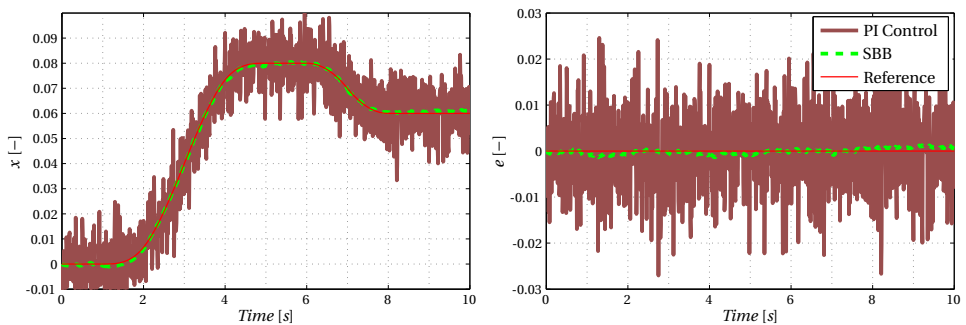


Figure 5.20: Response of the system, Eq. (5.72) with $\sigma_x^2 = \sigma_{\dot{x}}^2 = 10^{-4}$, $f = 0.9$ and $g = -20$, using a sensor based backstepping controller and a PI controller.

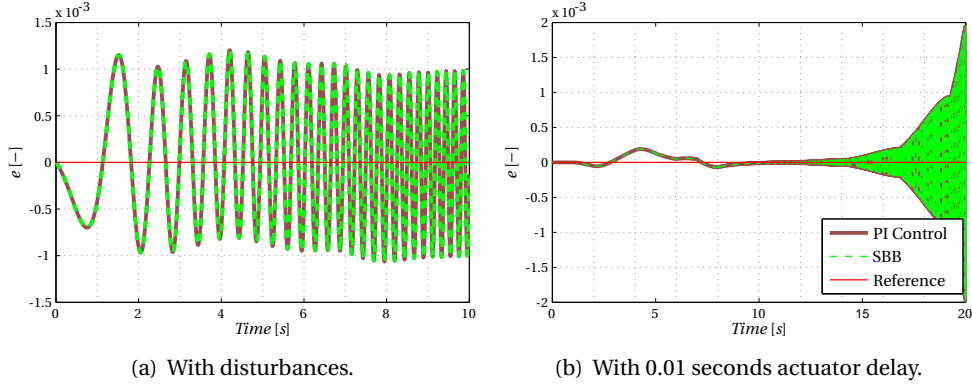


Figure 5.21: Response of the system, Eq. (5.75) and Eq. (5.76) with, $f = 0.9$ and $g = -20$, using a sensor based backstepping controller and a PI controller.

Using a first-order Taylor series expansion of this system around the current solution of the system $[x_0, u_0]$ gives,

$$\begin{aligned} \dot{x} &\approx \dot{x}\Big|_{\substack{x=x_0, \\ u=u_0}} + \frac{\partial \dot{x}}{\partial x}\Big|_{\substack{x=x_0, \\ u=u_0}} (x - x_0) + \frac{\partial \dot{x}}{\partial u}\Big|_{\substack{x=x_0, \\ u=u_0}} (u - u_0) + \dots \\ &\approx f(x_0) + g(x_0)u_0 + \frac{\partial}{\partial x}[f(x) + g(x)u_0]\Big|_{x=x_0} (x - x_0) + g(x_0)(u - u_0) + \dots \end{aligned} \quad (5.89)$$

which is a linearization of \dot{x} in the small neighborhood of $[x_0, u_0]$. The differences $(x - x_0)$ and $(u - u_0)$ can be viewed as increments in state and input respectively with respect to the current solution.

When the system is sufficiently time-scale separated, the increment in state will be much smaller than the increment in both state derivative and input, allowing to neglect the former. The system description then becomes,

$$\dot{x} \approx \dot{x}_0 + g(x_0)\Delta u \quad (5.90)$$

with $\dot{x}_0 = f(x_0) + g(x_0)u_0$ and $\Delta u = (u - u_0)$. A backstepping controller designed for this linearized time-scale separated system is referred to as Incremental Backstepping (IB) in the remainder of this thesis. Given the CLF $V(x) = \frac{1}{2}x^2$, with its time-derivative along the solutions of (5.90), $\dot{V}(x) = x\dot{x} = x(\dot{x}_0 + g(x_0)\Delta u)$ results in the IB controller,

$$\Delta u = -g(x_0)^{-1}(\dot{x}_0 + cx) \quad (5.91)$$

with $c > 0$ to asymptotically stabilize the (approximated and linearized) system.

The closed-loop system description of system (5.88) and IB controller (5.91) is,

$$\begin{aligned}
 \dot{x} &= f(x) + g(x)(u_0 - g(x_0)^{-1}(\dot{x}_0 + cx)) \\
 &= f(x) + g(x)(u_0 - g(x_0)^{-1}(f(x_0) + g(x_0)u_0 + cx)) \\
 &= f(x) - g(x)g(x_0)^{-1}(f(x_0) + cx)
 \end{aligned} \tag{5.92}$$

When the dependence of g on x is slow varying this can be approximated to,

$$\dot{x} \approx f(x) - f(x_0) - cx \tag{5.93}$$

which is asymptotically stable as long as $(f(x) - f(x_0))x < cx^2$.

Example 5.12 (Incremental Backstepping with Dynamics and Kinematics)

Consider the second-order nonlinear system,

$$\dot{\xi} = f_k(\xi) + g_k(\xi)x \tag{5.94}$$

$$\dot{x} = f_d(\xi, x) + g_d(\xi, x)u \tag{5.95}$$

where (5.94) and (5.95) describe the kinematics and dynamics of a vehicle respectively. Although both equations are similar in form, the functions f_k , g_k and f_d , g_d are fundamentally different. As mentioned in Chapter 2, the dynamics of a vehicle is the motion of that vehicle under influence of forces and moments. The kinematic equations are analytical equations that evolve the reference frames used to describe the forces and moments. They contain no uncertainties and are one integration step slower than the dynamic equations. The dynamic equations evaluate the modeled forces and moments and are therefore influenced by model uncertainties. Hence, the IB controller will be designed such that the dependence on f_d is removed, but keeping the dependence on g_k . In accordance with the backstepping design methodology, the IB controller is constructed in two steps.

Step 1: The system furthest from the input, i.e., the kinematic equations, are written as,

$$\dot{\xi} = f_k(\xi) + g_k(\xi)x \tag{5.96}$$

A backstepping control law can be designed for (5.96) using the CLE, $V_1 = \frac{1}{2}\xi^T\xi$ with its time derivative along the solutions of (5.96),

$$\dot{V}_1 = \xi^T (f_k(\xi) + g_k(\xi)\alpha) \tag{5.97}$$

The stabilizing function,

$$\alpha = -g_k^{-1}(\xi) (c_1\xi + f_k(\xi)) \tag{5.98}$$

with $c_1 > 0$ asymptotically stabilizes the kinematic state variables. Note that other CLFs and stabilizing functions are possible as well and could improve the closed-loop system in terms of control effort and stabilization time, depending on f_k and g_k .

Step 2: To step back a change in variables is used, $r = x - \alpha$, yielding the system description,

$$\begin{aligned}\dot{\xi} &= f_k(\xi) + g_k(\xi)(r + \alpha) \\ \dot{r} &= f_d(\xi, x) + g_d(\xi, x)u - \dot{\alpha}\end{aligned}\quad (5.99)$$

Instead of using backstepping for this step, IB is used to get rid of the dependence on f_d . Using the approximation of Eq. (5.90), yields the system description,

$$\begin{aligned}\dot{\xi} &= f_k(\xi) + g_k(\xi)(r + \alpha) \\ \dot{r} &\approx \dot{x}_0 + g_d(\xi, x_0)\Delta u - \dot{\alpha}\end{aligned}\quad (5.100)$$

The time derivative of the CLF, $V_2 = \frac{1}{2}\xi^T \xi + \frac{1}{2}r^T r$, along the solutions of (5.100) is,

$$\begin{aligned}\dot{V}_2 &= \xi^T (f_k(\xi) + g_k(\xi)(r + \alpha)) + r^T (\dot{x}_0 + g_d(\xi, x_0)\Delta u - \dot{\alpha}) \\ &= -c_1 \xi^T \xi + r^T (\dot{x}_0 + g_d(\xi, x_0)\Delta u - \dot{\alpha} + (\xi^T g_k(\xi))^T)\end{aligned}\quad (5.101)$$

The IB controller that asymptotically stabilizes the complete system is therefore,

$$\Delta u = -g_d^{-1}(\xi, x_0)(\dot{x}_0 - \dot{\alpha} + c_2 r + (\xi^T g_k(\xi))^T)\quad (5.102)$$

with $c_1, c_2 > 0$.

Example 5.13 (Incremental Backstepping versus Sensor Based Backstepping)

Consider system (5.62) from Example 5.5,

$$\dot{x} = f x^a + g u$$

An IB controller can be constructed that stabilizes the error dynamics $e = x - y_r$ of this system using the linearized system approximation,

$$\dot{e} \approx \dot{x}_0 + g \Delta u - \dot{y}_r\quad (5.103)$$

and the CLF, $V = \frac{1}{2}e^2$. The derivative of this CLF

$$\dot{V} = e(\dot{x}_0 - \dot{y}_r + g \Delta u)\quad (5.104)$$

becomes negative definite, when the incremental control,

$$\Delta u = -g^{-1}(\dot{x}_0 - \dot{y}_r + c_1(x - y_r))\quad (5.105)$$

is used, with $c_1 > 0$.

Figure 5.22 shows the IB controller and the SBB controller stabilizing the error dynamics of the system with $a = 1$ and $a = 2$. Minor differences exist in favor of either controller depending on the scenario, but both controllers are satisfactory.

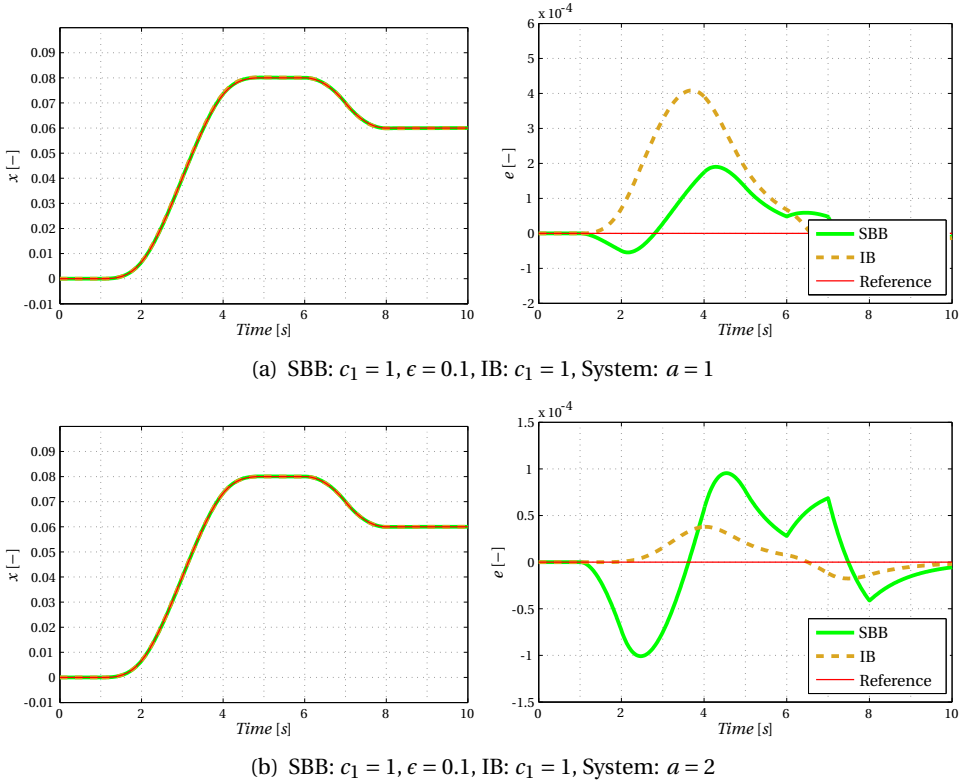


Figure 5.22: Response of the system, Eq. (5.62) with $f = 0.9$ and $g = -20$, using a sensor based backstepping controller and a incremental backstepping controller.

Example 5.13 shows an IB controller which is not dependent on the system function f . Changing the nonlinearity in the system does not influence the tracking performance of the controller negatively. However, the IB controller is dependent on the input function g . Therefore, uncertainties in this function are also investigated using a simple example.

Example 5.14 (Incremental Backstepping with Parametric Uncertainty)

Adding parametric uncertainty to system (5.62) results in,

$$\dot{x} = f x + \theta_u g u \tag{5.106}$$

The IB controller (5.105) is not changed and Figure 5.23 shows that the uncertainty has little effect on the stabilization properties of the IB controller.

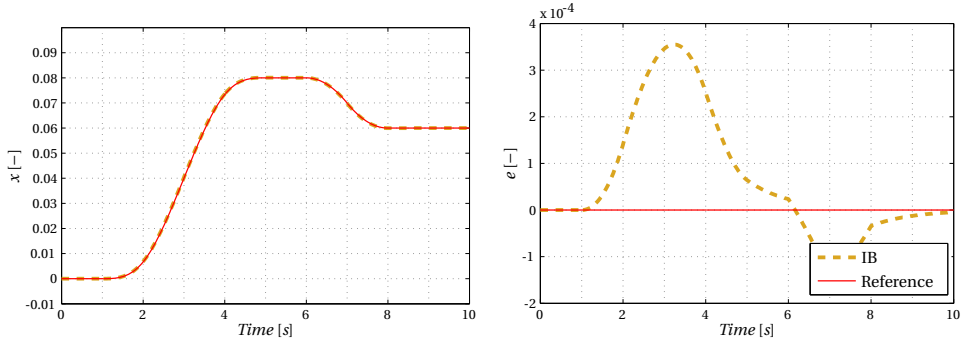


Figure 5.23: Response of the system, Eq. (5.106) with $f = 0.9$, $g = -20$ and $\theta_u = 1.5$, using a incremental backstepping controller.

Example 5.15 (Incremental Backstepping with Sensor Noise)

Consider the system from Example 5.8,

$$\begin{aligned} \dot{x} &= f + gu \\ y &= \begin{bmatrix} x + \omega_x \\ \dot{x} + \omega_{\dot{x}} \end{bmatrix} \end{aligned}$$

An IB controller for this system could be,

$$\Delta u = -g^{-1}(\dot{x}_0 + \omega_{\dot{x}} - \dot{y}_r + c(x + \omega_x - y_r)) \tag{5.107}$$

Figure 5.24 shows that the IB controller has nearly the same noise characteristics as the SBB controller. This could be expected, since both controllers use the same sensor information.

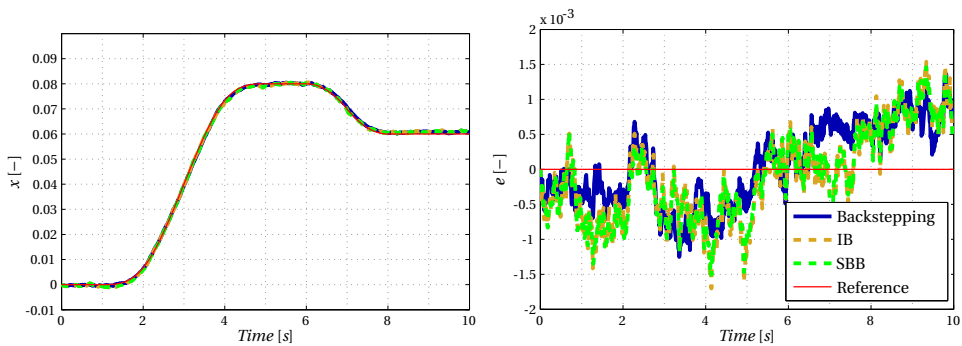


Figure 5.24: Response of the system, Eq. (5.72) with $\sigma_x^2 = \sigma_{\dot{x}}^2 = 10^{-4}$, $f = 0.9$ and $g = -20$, using a backstepping, a sensor based backstepping and a incremental backstepping controller.

Example 5.16 (Incremental Backstepping with Disturbances)

Consider the linear system with additive disturbance from Example 5.9,

$$\dot{x} = f + g(u + w)$$

The disturbance is again treated as unanticipated and unmeasured and therefore the IB controller (Eq. 5.105) is not altered. Figure 5.25 shows that the IB controller is influenced more by the additive disturbance compared with the SBB controller. In this scenario the disturbance rejection of both controllers differs by a factor 3. Additional simulations showed that changing the IB controller gain c_1 improves disturbance rejection at low frequencies, but not at high frequencies. The reason for this is that a small e produces high gains on both x and \dot{x} for the SBB controller, whereas c_1 only increases the gain on x for the IB controller. The gain on \dot{x} is fixed to g^{-1} in that case.

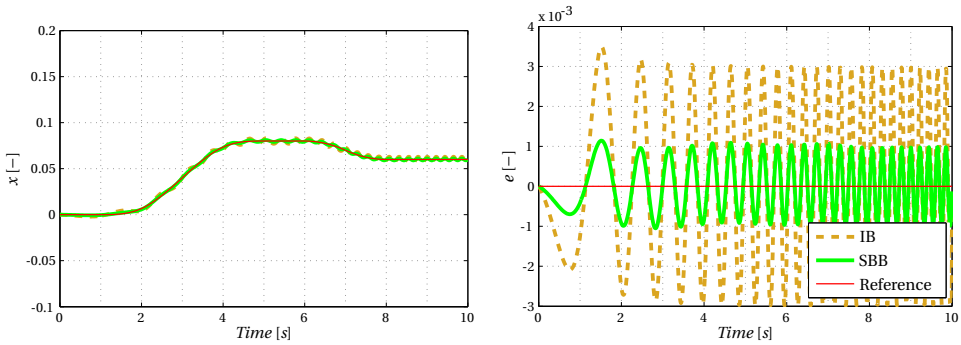


Figure 5.25: Response of the system, Eq. (5.75) with $f = 0.9$, $g = -20$ and w equal to a chirp signal with an amplitude of 0.01 and a frequency linearly increasing from 0.1 Hz to 5 Hz in 10 seconds, using a sensor based backstepping and an incremental backstepping controller.

Example 5.17 (Incremental Backstepping with Time Delays)

Consider the linear system with actuator delays from Example 5.10,

$$\dot{x} = f x + g u(t - \tau)$$

Figure 5.26 shows the system response, using a delay of 10 milliseconds, without changing the control laws. In the first 10 seconds, the IB controller is slightly more robust to the time delay than the conventional backstepping controller. However, also the incremental term of the IB controller winds up, resulting in instability of the closed-loop system.

The IB control action calculated at the delayed time is,

$$u(t - \tau) = u(t - \tau - t_s) - g^{-1}(\dot{x}(t - \tau - t_s) + c x(t - \tau)) \quad (5.108)$$

and the closed-loop system description therefore becomes,

$$\begin{aligned}
 \dot{x}(t) &= f x(t) + g u(t - \tau - t_s) - g g^{-1}(\dot{x}(t - \tau - t_s) + c x(t - \tau)) \\
 &= f x(t) + g u(t - \tau - t_s) - \dot{x}(t - \tau - t_s) - c x(t - \tau) \\
 &= f x(t) - f x(t - t_s) + \dot{x}(t - t_s) - \dot{x}(t - \tau - t_s) - c x(t - \tau) \\
 &\approx \dot{x}(t - t_s) - \dot{x}(t - \tau - t_s) - c x(t - \tau)
 \end{aligned} \tag{5.109}$$

When t_s would vanish to zero, the closed-loop system becomes $\dot{x}(t - \tau) = -c x(t - \tau)$ which is stable. Unfortunately t_s does not vanish to zero in practice. Substituting the expressions for $\dot{x}(t - \tau - t_s)$ in Eq. (5.109) leads to,

$$\begin{aligned}
 \dot{x}(t) &= f x(t) + g u(t - \tau - t_s) + g g^{-1}(-f x(t - \tau - t_s) - g u(t - 2\tau - t_s) - c x(t - \tau)) \\
 &= f x(t) - c x(t - \tau) - f x(t - \tau - t_s) + g u(t - \tau - t_s) - g u(t - 2\tau - t_s)
 \end{aligned} \tag{5.110}$$

which is a retarded type system. Proposition 7.9 in Gu *et al.* [43] could be used to determine the time-delay margin of this multiple delayed system, but as indicated by Figure 5.26, the delay margin would be impractically small.

To overcome this deficit of IB, we can analyze Eqs. (5.110) and (5.92) in more detail. Equation (5.92) shows that without time-delay, the input dependent part of the \dot{x} -measurement i.e., $g(x_0)u_0$, is canceled by the incremental construct, $u = u_0 + \Delta u$. Assuming that the input is directly present in the \dot{x} -measurement, the IB controller could then also be simplified to,

$$\begin{aligned}
 u &= u_0 - g^{-1}(\dot{x}_0 + c x) \\
 &= u_0 - g^{-1}(f x_0 + g u_0 + c x) \\
 &= -g^{-1}(f x_0 + c x)
 \end{aligned} \tag{5.111}$$

which is nearly equivalent to the backstepping controller, $u = -g^{-1}(f x + c x)$. With time delay, this cancellation no longer occurs and u grows with,

$$\begin{aligned}
 u &= u_0 - g^{-1}(\dot{x}_0 + c x) \\
 &= u_0 - g^{-1}(f x_0 + g u_0(t - \tau) + c x) \\
 &= u_0 - u_0(t - \tau) - g^{-1}(f x_0 + c x)
 \end{aligned} \tag{5.112}$$

Instead of using the increment $\Delta u = u - u_0$ an alternative could be to use a measurement of the achieved input, that is present in the \dot{x} -measurement, i.e., $\Delta u = u - u_0(t - \tau)$ for this example. The IB controller would then again reduce to,

$$\begin{aligned}
 u &= u_0(t - \tau) - g^{-1}(\dot{x}_0 + c x) \\
 &= u_0(t - \tau) - g^{-1}(f x_0 + g u_0(t - \tau) + c x) \\
 &= -g^{-1}(f x_0 + c x)
 \end{aligned} \tag{5.113}$$

resulting in the closed-loop system,

$$\begin{aligned}
 \dot{x}(t) &= f x(t) + g u(t - \tau) \\
 &= f x(t) + g(g^{-1}(-f x_0(t - \tau) - c x(t - \tau))) \\
 &= f x(t) - f x_0(t - \tau) - c x(t - \tau) \\
 &\approx f x(t) - (f + c)x(t - \tau)
 \end{aligned} \tag{5.114}$$

Figure 5.27 shows that using this new method provides better results and when the time delay increases, the closed-loop response becomes indeed almost equivalent to that of the conventional backstepping controller.

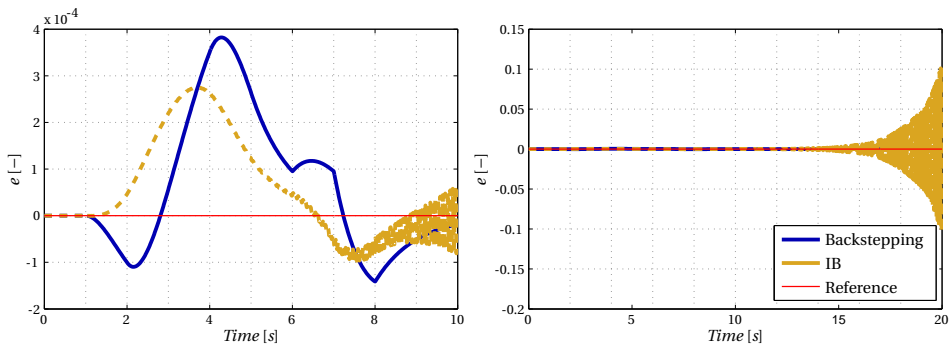


Figure 5.26: Response of the system, Eq. (5.76) with $f = 0.9$, $g = -20$ and $\tau = 0.01$ seconds, using a backstepping and an incremental backstepping controller.

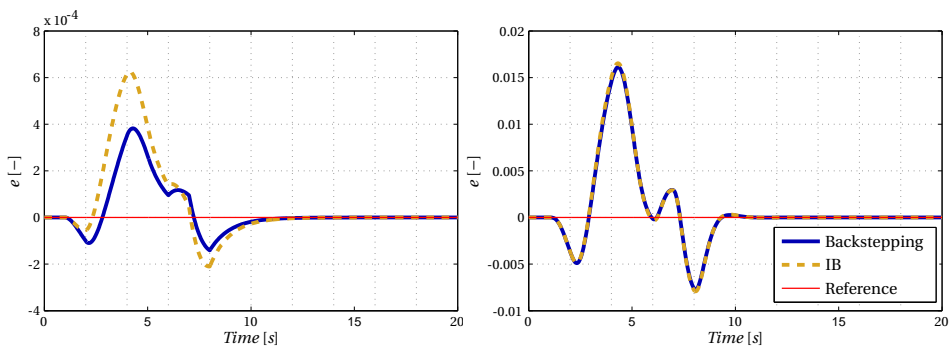


Figure 5.27: Response of the system, Eq. (5.76) with $f = 0.9$, $g = -20$ and $\tau = 0.01$ (left) and $\tau = 0.3$ (right) seconds, using a backstepping and an incremental backstepping controller.

5.6.4 Application to the DA 42 ATT Law

This section shows the application of SBB and IB to the manually controlled ATT mode, introduced in Section 4.6.2. In recent years angular accelerometers have become commercially-of-the-shelf available, giving the control engineer the capability to choose between using extensive modeling information or additional sensor information. The FCL designs presented in this section are synthesized for the DA 42. However, both strategies are (almost) model independent and should therefore be applicable to other small airplanes as well.

To design the ATT mode of Section 4.6.2 using nonlinear FCLs, first a clear system description is needed. Recall the moment equation, Eq. (2.2),

$$\dot{\omega} = J^{-1}(M - \omega \times J\omega) \quad (5.115)$$

For now we concentrate only on the aerodynamic moments and treat the other moments as disturbances on the system. The aerodynamic moments can be described using Eq. (2.23),

$$M = \bar{q}S \begin{bmatrix} bC_l(\beta, p, r, \delta_a, \delta_r) \\ \bar{c}C_m(\alpha, \dot{\alpha}, q, \delta_e) \\ bC_n(\beta, p, r, \delta_a, \delta_r) \end{bmatrix} \quad (5.116)$$

where the aerodynamic moment coefficients can be determine from Eq. (2.25). The inputs of the aerodynamic model are the control surface deflections, $u = [\delta_a \delta_e \delta_r]^T$. Under the assumption that the moment equation is linearly dependent on the input, i.e., affine-in-control, these can be extracted as,

$$M = \underbrace{\bar{q}SC_1 \begin{bmatrix} C_l(\beta, p, r) \\ C_m(\alpha, \dot{\alpha}, q) \\ C_n(\beta, p, r) \end{bmatrix}}_{M_{aero}} + \underbrace{\bar{q}SC_1 \begin{bmatrix} C_{l\delta_a} & 0 & C_{l\delta_r} \\ 0 & C_{m\delta_e} & 0 \\ C_{n\delta_a} & 0 & C_{n\delta_r} \end{bmatrix}}_{M_c} u \quad (5.117)$$

with $C_1 = \text{diag}(b, \bar{c}, b)$. Note that the major part of the uncertainties in the aircraft model is contained in the parameter M_{aero} and to lesser extend in M_c . The aerodynamic flow angles α and β can be related to the rotational rates of the aircraft using Eq. (2.5),

$$\begin{aligned} \dot{V}_{TAS} &= \frac{1}{m} [\cos \alpha \cos \beta \sin \beta \cos \beta \sin \alpha] F_B \\ \dot{\alpha} &= q - (p \cos \alpha + r \sin \alpha) \tan \beta + \frac{1}{m} \frac{1}{V_{TAS} \cos \beta} [-\sin \alpha \ 0 \ \cos \alpha] F_B \\ \dot{\beta} &= p \sin \alpha - r \cos \alpha + \frac{1}{m} \frac{1}{V_{TAS}} [-\cos \alpha \sin \beta \ \cos \beta \ \sin \alpha \sin \beta] F_B \end{aligned} \quad (5.118)$$

in which F_B represents the sum of forces acting on the aircraft, which also contains uncertain parameters. The influence of the control surface deflections and the power lever angle ($pl_a = u_t$) on F_B can be written as,

$$F_B = T^* u_t + \bar{q} S \underbrace{\begin{bmatrix} 0 & C_{X_{\delta_e}} & 0 \\ 0 & 0 & 0 \\ 0 & C_{Z_{\delta_e}} & 0 \end{bmatrix}}_{F_c} u + \dots \quad (5.119)$$

with T^* representing the propulsion model and again assuming that the system is affine-in-control. In the ATT mode the pitch and roll angles are controlled using a RCAH strategy, the sideslip should be suppressed and the velocity is held. To achieve RCAH control, the body orientation equation, Eq. (2.3), is added,

$$\begin{bmatrix} \dot{\phi} \\ \dot{\theta} \\ \dot{\psi} \end{bmatrix} = \begin{bmatrix} 1 & \sin \phi \tan \theta & \cos \phi \tan \theta \\ 0 & \cos \phi & -\sin \phi \\ 0 & \frac{\sin \phi}{\cos \theta} & \frac{\cos \phi}{\cos \theta} \end{bmatrix} \begin{bmatrix} p \\ q \\ r \end{bmatrix} \quad (5.120)$$

By combining the controlled states from Eqs. (2.5 and 2.3), the complete system can be written as,

$$\begin{aligned} \dot{V}_{TAS} &= [\cos \alpha \cos \beta \sin \beta \cos \beta \sin \alpha] \frac{T^* u_t + \bar{q} S F_c u + \dots}{m} \\ \dot{x}_1 &= \underbrace{\begin{bmatrix} 1 & \sin \phi \tan \theta & \cos \phi \tan \theta \\ 0 & \cos \phi & -\sin \phi \\ \sin \alpha & 0 & -\cos \alpha \end{bmatrix}}_{f_1(x_1)} x_2 + \\ &\quad \underbrace{\begin{bmatrix} 0 & 0 & 0 \\ 0 & 0 & 0 \\ -\cos \alpha \sin \beta & \cos \beta & \sin \alpha \sin \beta \end{bmatrix}}_{a(x)} \frac{T^* u_t + \bar{q} S F_c u + \dots}{m V_{TAS}} \\ \dot{x}_2 &= \underbrace{J^{-1} \bar{q} C_1 (M_{aero}(x_1, x_2)) - J^{-1} (x_2 \times J x_2)}_{f_2(x_1, x_2)} + \underbrace{J^{-1} \bar{q} C_1 M_C}_{g(x)} u \end{aligned} \quad (5.121)$$

with $x_1 = [\phi \ \theta \ \beta]^T$ and $x_2 = \omega$. Note that the system (5.121) is not a strict feedback system, due to the input terms appearing in \dot{V}_{TAS} and \dot{x}_1 . By making the choice that only u_t is used to control the velocity and by noticing that mainly input independent forces in Y_B -direction have influence on the sideslip, the system can be put into strict feedback form.

Example 5.18 (ATT law using Sensor Based Backstepping)

The autothrottle part of the SBB controller is a system with a relative degree of one and can be designed in a single step. Consider the SBB controller,

$$\epsilon \dot{u}_t = -\text{sign}\left(\frac{\partial \dot{V}_{TAS}}{\partial u_t}\right) [\dot{V}_{TAS} - \dot{V}_{TAS,r} + c_1(V_{TAS} - V_{TAS,r})] \quad (5.122)$$

with $c_1 > 0$. The sign of $\frac{\partial \dot{V}_{TAS}}{\partial u_t} = [\cos \alpha \cos \beta \sin \beta \cos \beta \sin \alpha] \frac{T^*}{m}$ is positive, since T^* is positive and acts mainly in the X_B direction, m is positive and the cosines are positive as well for $-\frac{\pi}{2} \leq (\alpha, \beta) \leq \frac{\pi}{2}$, i.e., always for the aircraft considered. Therefore the SBB autothrottle becomes,

$$\epsilon \dot{u}_t = -[\dot{V}_{TAS} - \dot{V}_{TAS,r} + c_1(V_{TAS} - V_{TAS,r})] \quad (5.123)$$

The RCAH part and sideslip compensating part of the SBB controller are designed in two steps.

Step 1: The system furthest from the input can be written as,

$$\dot{x}_1 = f_1(x_1)x_2 + a(x) \quad (5.124)$$

Using the tracking error $e_1 = x_1 - x_{1r}$, yields the error dynamics,

$$\dot{e}_1 = f_1(x_1)x_2 + a(x) - \dot{x}_{1r} \quad (5.125)$$

A backstepping control law can be designed for (5.125) using the CLF $V_1 = \frac{1}{2}e_1^T e_1$ with it's time derivative along the solutions of (5.125),

$$\dot{V}_1 = e_1^T (f_1(x_1)\alpha_1 + a(x) - \dot{x}_{1r}) \quad (5.126)$$

The stabilizing function,

$$\alpha_1 = -f_1(x_1)^{-1} (c_2 e_1 + a(x) - \dot{x}_{1r}) \quad (5.127)$$

with $c_2 > 0$ asymptotically stabilizes the e_1 error dynamics.

Step 2: To step back, a change in variables is used,

$$r_1 = x_2 - \alpha_1 \quad (5.128)$$

resulting in the new system description,

$$\begin{aligned} \dot{e}_1 &= f_1(x_1)(r_1 + \alpha_1) + a(x) - \dot{x}_{1r} \\ \dot{r}_1 &= \dot{x}_2 - \dot{\alpha}_1 = f_2(x_1, x_2) + g(x)u - \dot{\alpha}_1 \end{aligned} \quad (5.129)$$

Using conventional backstepping would lead to a control law sensitive to model uncer-

tainties, so instead the SBB method is applied to this new system,

$$\epsilon \dot{u} = -\text{sign}\left(\frac{\partial \dot{r}}{\partial u}\right)(\dot{r} - \dot{r}_{des}) = -\text{sign}\left(\frac{\partial \dot{r}}{\partial u}\right)(\dot{x}_2 - \dot{\alpha}_1 - \dot{r}_{des}) \quad (5.130)$$

in which the angular accelerations \dot{x}_2 are assumed to be measured. The stabilizing function \dot{r}_{des} is found using the CLE, $V_2 = \frac{1}{2}e_1^T e_1 + \frac{1}{2}r^T r$ with it's time derivative,

$$\begin{aligned} \dot{V}_2 &= e_1^T (f_1(x_1)(r + \alpha_1) + a(x) - \dot{x}_{1r}) + r^T \dot{r}_{des} \\ &= -e_1^T c_2 e_1 + r^T (\dot{r}_{des} + (e_1^T f_1(x_1))^T) \end{aligned} \quad (5.131)$$

Therefore we can define the stabilizing function,

$$\dot{r}_{des} = -c_3 r - (e_1^T f_1(x_1))^T \quad (5.132)$$

with $c_3 > 0$ to asymptotically stabilize the system, Eq. (5.129). The SBB controller thus becomes,

$$\epsilon \dot{u} = -\text{sign}\left(\frac{\partial \dot{r}}{\partial u}\right)(\dot{x}_2 - \dot{\alpha}_1 + c_3 r + (e_1^T f_1(x_1))^T + k\lambda) \quad (5.133)$$

with $c_3 > 0$ and $k > 0$ to stabilize the whole system when the assumptions of SBB are met. Note that $\lambda = \int r dt$ is added to cancel the effect of internal dynamics as explained in Example 5.6. Evaluating the partial derivative of \dot{r}_1 to u gives,

$$\frac{\partial \dot{r}_1}{\partial u} = J^{-1} \bar{q} C_1 M_c < 0 \quad (5.134)$$

Since J , \bar{q} , C_1 are all positive (definite), the only matrix of influence is the control effectiveness matrix M_c . The eigenvalues of this matrix are all negative when the direction of control surface deflections are defined as done by Mulder [83] and a conventional fixed wing aircraft is considered. This means $\text{sign}\left(\frac{\partial \dot{r}_1}{\partial u}\right)$ will be minus one. Note that this assumption is wrong when structural damage, or structural dynamics, causes a sign reversal of the control surface effectiveness. Optionally a crude form of online aerodynamic model identification [71] may be used to prevent these control algorithm failures. In this thesis effects of structural damage and structural dynamics are not further pursued and the SBB controller is therefore written as,

$$\epsilon \dot{u} = \dot{x}_2 - \dot{\alpha}_1 + c_3 r + (e_1^T f_1(x_1))^T + k\lambda \quad (5.135)$$

Note that the SBB controller uses measurements of the angular accelerations \dot{x}_2 , rather than evaluating the system dynamics from the aerodynamic model in $f_2(x_1, x_2)$.

Figures 5.28 and 5.29 show the aircraft response influenced by the SBB controllers (5.123 and 5.135) with the anti windup scheme of Example 5.10. Note that the aircraft response refers here to the response of the aircraft model described in Chapter 2, combined with the FBW platform documented in Chapter 3, including time delays. The controller gains are listed in Table 5.1 and were selected by trial and error. Clearly the

controller tracks the attitude rate command signals and holds the attitude angles when no input is given. Whether the controller is robust to model uncertainty, disturbances and noise is checked in later examples and whether performance is good in terms of handling qualities is analyzed in Section 5.6.6.

Table 5.1: SBB and IB controller gains.

Signal	c_1	c_2	c_3	k	H
$\dot{\phi}_{cmd}$	-	2	5	0.5	150
$\dot{\theta}_{cmd}$	-	2	5	0.5	150
β_{cmd}	-	0.5	2	0.5	150
$V_{TAS,cmd}$	1.5	-	-	-	150

Example 5.19 (ATT law using Incremental Backstepping)

The IB methodology can also be used to derive a controller for the system (5.121).

Under the assumptions of IB control, the autothrottle can be written as,

$$u_t = u_{t,0,m} - g(x)^{-1} [\dot{V}_{TAS} - \dot{V}_{TAS,r} + c_1(V_{TAS} - V_{TAS,r})] \quad (5.136)$$

with $c_1 > 0$ to asymptotically stabilize the error dynamics.

For the RCAH and sideslip controller again two steps are used. Since step 1 is identical to step 1 of the SBB controller in Example 5.18 it is skipped here. An IB controller for system (5.129) is constructed using,

$$u = u_{0,m} - g(x)^{-1} [\dot{x}_2 - \dot{\alpha}_1 + c_3 r + (\xi^T g_k(\xi))^T + k\lambda] \quad (5.137)$$

with $c_3 > 0$. Note that this result was also obtained in Example 5.12, with a slight change to use input measurements ($u_{0,m}$) to improve time-delay robustness and with an integral term (λ) to cancel the effect of internal dynamics.

Figures 5.28 and 5.29 also show the aircraft response influenced by the IB controllers (5.136 and 5.137). The controller gains are selected equivalent to those of the SBB controller. The response is comparable to that of the SBB controller for pitch and roll and even better than the SBB controller for velocity and sideslip tracking.

Using measurements of the angular accelerations for control of the attitude rate naturally gives rise to the question what would happen in the presence of sensor noise. This is investigated in the next example.

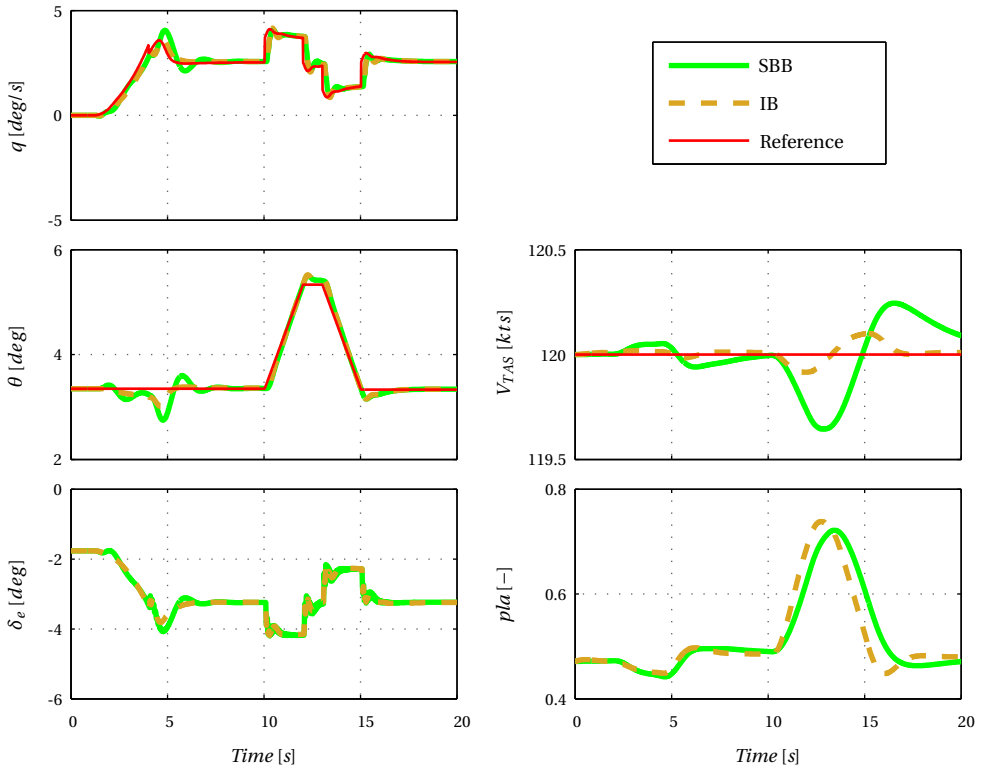


Figure 5.28: Longitudinal aircraft response, controlled by Sensor Based Backstepping and Incremental Backstepping.

Example 5.20 (Effects of Sensor Noise)

The measured input and output signals are made noisy using the sensor models provided in Chapter 3. An additional model for angular accelerations is added to the simulation environment for research purpose. Since the angular rate sensors (gyro's) have been researched and developed longer than the commercially-of-the-shelf available angular acceleration sensors, the latter has been given a noise variance ten times larger than the former, i.e., $\sigma_{\omega}^2 = 10\sigma_{\dot{\omega}}^2$. The results are shown in Figures 5.30 and 5.31. Clearly both controllers are still able to track the reference signals. In the first five seconds of each plot offsets are visible, which exist due to the sensor bias of the angular accelerometers. The bottom right plot in Figure 5.30 shows that the SBB controller generates smoother pla -commands compared with the IB controller. The right side of Figure 5.31 shows that the advantage of IB over SBB in dealing with sideslip is removed when noise is present. The rudder commands generated by the SBB controller are again smoother compared with those generated by the IB controller.

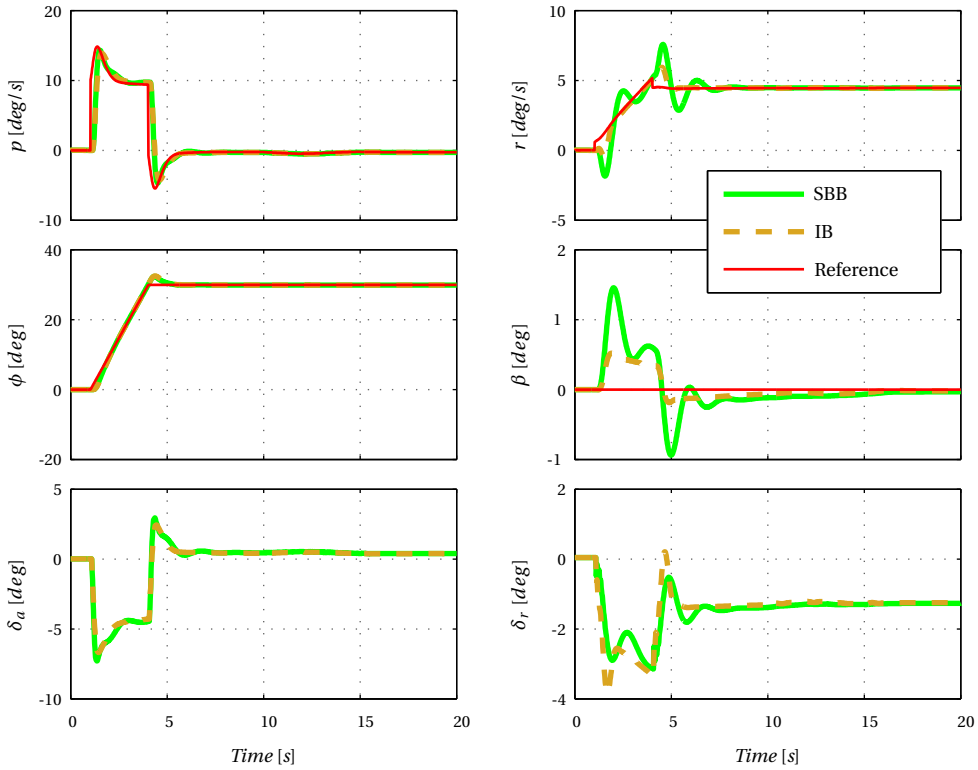


Figure 5.29: Lateral aircraft response, controlled by Sensor Based Backstepping and Incremental Backstepping.

Since the goal of this thesis is to investigate a practical FCL for a small aircraft, the assumed availability of angular accelerometers is questionable. The next example shows whether the developed controllers are able to use differentiated angular rate signals rather than angular accelerations measurements.

Example 5.21 (Gyro Differentiation)

Figures 5.32 and 5.33 show the aircraft response in the presence of sensor noise and under control of SBB and IB. In this example, the angular accelerations are obtained by differentiation instead of measurement. Clearly the results are very good. Due to the differentiation the measurement bias is removed, which improves the tracking performance considerably. The SBB controller still generates smoother p and rudder commands compared with the IB controller, but the better sideslip compensation is again achieved by the IB controller.

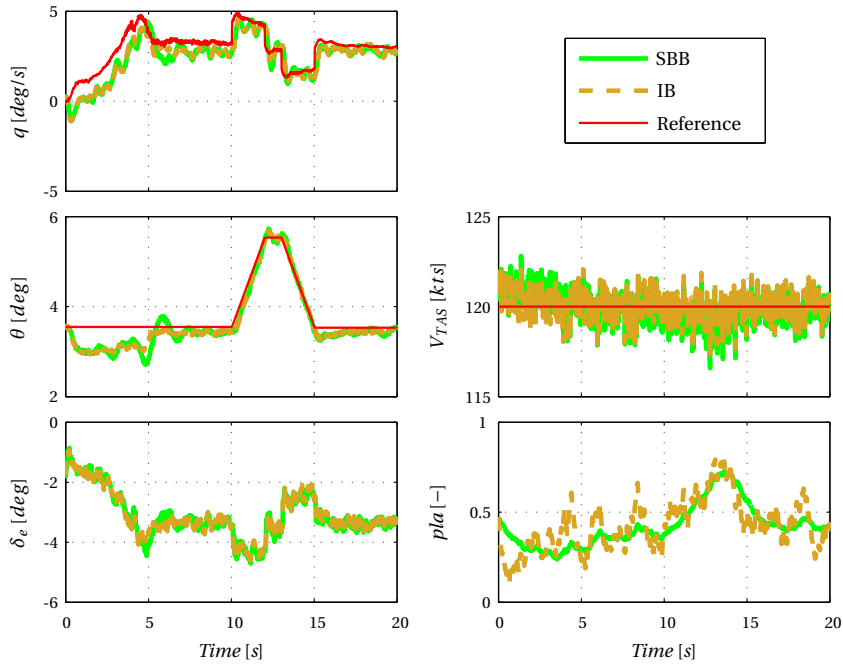


Figure 5.30: Longitudinal aircraft response in the presence of sensor noise, controlled by Sensor Based Backstepping and Incremental Backstepping.

5.6.5 Application to the DA 42 NAV Law

In order to construct the NAV law, system (5.121) must be extended. First, a relation between the aircraft position with respect to the earth fixed trajectory and the flight path angle is needed. Consider the point on the trajectory lying closest to the aircraft at a distance,

$$D = \begin{bmatrix} x_{T,O} \\ y_{T,O} \\ z_{T,O} \end{bmatrix} - \begin{bmatrix} x_O \\ y_O \\ z_O \end{bmatrix} \quad (5.138)$$

The distance vector can be expressed in the trajectory reference frame RF_T using,

$$\begin{bmatrix} \Delta Y \\ \Delta Z \end{bmatrix} = \begin{bmatrix} -\sin \chi_T & \cos \chi_T & 0 \\ 0 & 0 & 1 \end{bmatrix} D \quad (5.139)$$

The time-derivative of (5.139) while keeping X_T fixed, can be written as,

$$\begin{aligned} \Delta \dot{Y} &= V_{GS} \sin \chi_e \cos \gamma_k \\ \Delta \dot{Z} &= V_{GS} \sin \gamma_k \end{aligned} \quad (5.140)$$

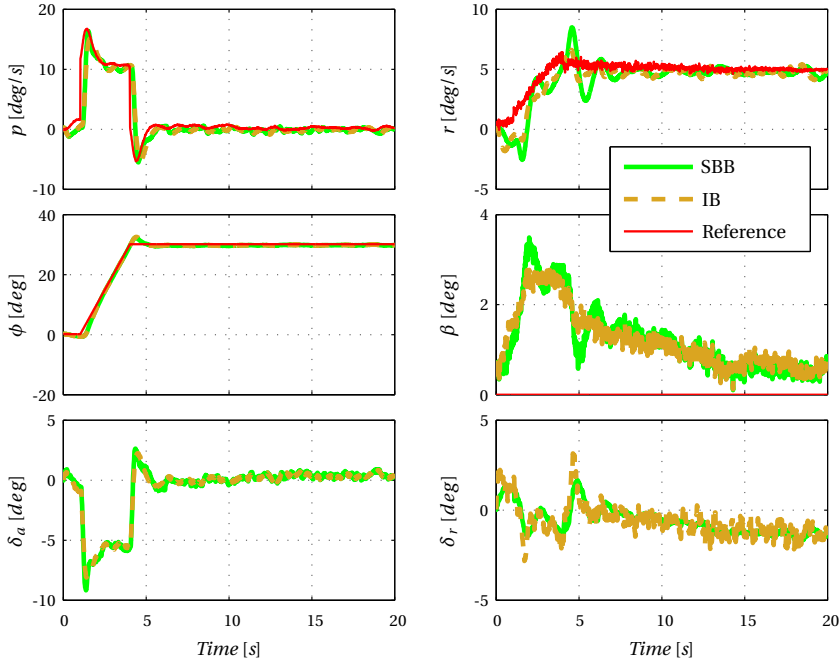


Figure 5.31: Lateral aircraft response in the presence of sensor noise, controlled by Sensor Based Backstepping and Incremental Backstepping.

with $\chi_e = \chi_T - \chi_k$. This expression can be used to define a flight path vector reference based on the position offset with respect to the trajectory to follow.

The second relation needed is one between the flight path vector and the attitude rates. This relation cannot be found as easily, especially if the influence of wind on the aircraft is non-negligible. Using Equation (2.7),

$$\begin{aligned} \dot{\gamma}_k &= \frac{-\dot{w}_E V_{GS} + \dot{V}_{GS} w_E}{\cos \gamma_k V_{GS}^2} \\ \dot{\chi}_k &= \frac{u_E \dot{v}_E - v_E \dot{u}_E}{u_E^2 + v_E^2} \end{aligned} \quad (5.141)$$

in which $A_E = [\dot{u}_E \ \dot{v}_E \ \dot{w}_E]^T$ directly depends on the forces acting on the aircraft expressed in RF_E , should lead to such an expression. These forces will not only depend on the attitude rates, but also on control surface deflections, thereby again violating the lower triangular form requirement of Backstepping. In addition, the altitude response of an airplane is non-minimum phase [46], which is an obstacle for application of SBB. Further derivation of this expression and the design of a SBB

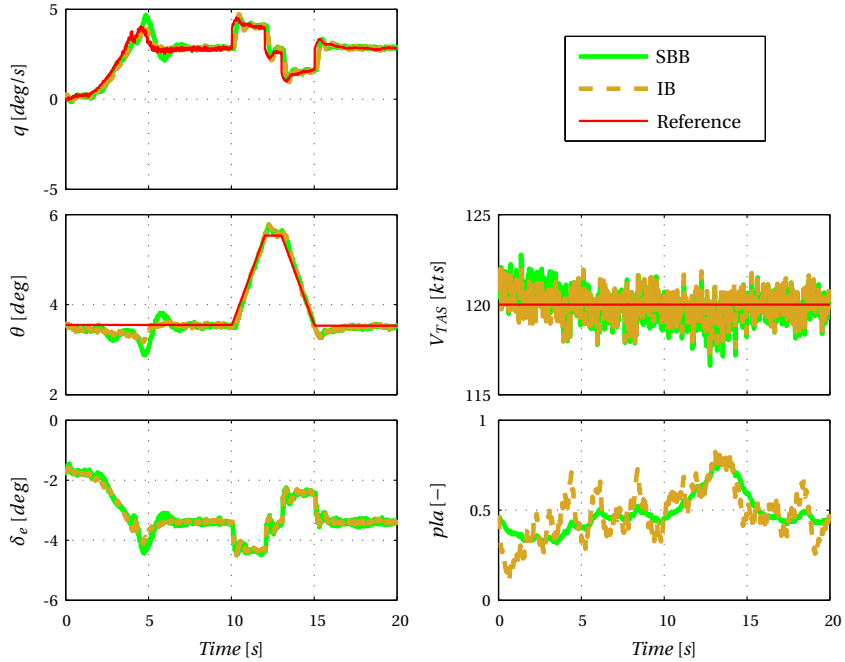


Figure 5.32: Longitudinal aircraft response in the presence of sensor noise, controlled by SBB and IB using differentiated angular rates.

FCL using that expression, is left for future work. Instead P and PD outer-loop controllers are assumed to properly construct the attitude rate reference from the flight path vector, i.e.,

$$\begin{aligned}\dot{\theta}_{ref} &= \frac{1}{V_{GS}} K_{P_\gamma} \gamma_e \\ \dot{\phi}_{ref} &= \frac{1}{V_{GS}} [K_{P_\chi} \chi_e + K_{D_\chi} \dot{\chi}_e]\end{aligned}\quad (5.142)$$

with $\gamma_e = \gamma_{k,ref} - \gamma_k$. With this simplification the resulting FCL does not have guaranteed closed-loop stability. For the indented use of the designed FCL, a simulation environment, this drawback is disregarded.

Example 5.22 (NAV law using Sensor Based Backstepping)

The autothrottle and sideslip compensating part of the NAV law can be directly copied from the ATT law. The position controller should be constructed in four steps. Since this derivation would be rather lengthy, instead a simpler outer-loop controller is added on top of the RCAH controller constructed in Example 5.18.

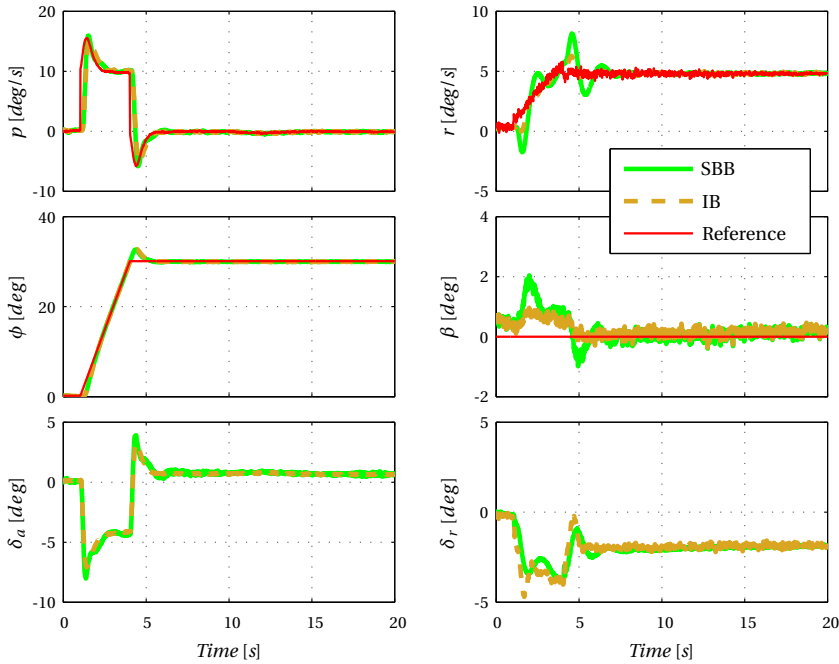


Figure 5.33: Lateral aircraft response in the presence of sensor noise, controlled by SBB and IB using differentiated angular rates.

Consider system (5.140). When χ_e and γ_k are small, this system can be simplified to,

$$\begin{bmatrix} \Delta \dot{Y} \\ \Delta \dot{Z} \end{bmatrix} = V_{GS} \begin{bmatrix} \chi_e \\ \gamma_k \end{bmatrix} \quad (5.143)$$

which is affine in control. If χ_e is not small the error signal can be saturated to remain in the validity range of the approximation. By inversion a reference for χ_k and γ_k is calculated as,

$$\begin{bmatrix} \chi_e \\ \gamma_{k,ref} \end{bmatrix} = \frac{1}{V_{GS}} \begin{bmatrix} \Delta \dot{Y} \\ \Delta \dot{Z} \end{bmatrix} \quad (5.144)$$

This reference only depends on the rate of change of the position offset and not the position offset itself. Rewriting (5.144) to a PID-like controller yields,

$$\begin{bmatrix} \chi_e \\ \gamma_{k,ref} \end{bmatrix} = \frac{1}{V_{GS}} \begin{bmatrix} K_{PDy} \Delta Y + K_{IDy} \int \Delta Y dt + K_{DDy} \Delta \dot{Y} \\ K_{PDz} \Delta Z + K_{IDz} \int \Delta Z dt + K_{DDz} \Delta \dot{Z} \end{bmatrix} \quad (5.145)$$

These reference values can be used in the P and PD controllers (5.142) which in turn determine reference values for $\dot{\phi}$ and $\dot{\theta}$. These reference values can be provided to the RCAH control law, thereby closing the entire control loop.

Figure 5.34 shows an trajectory intercept using the SBB controller described in this example. Clearly the trajectory is intercepted smoothly and without overshoot. The outer-loop controllers (5.145 and 5.142) could also be used to generate commands for the IB controller of Example 5.19. As this would lead to nearly identical results, this example is omitted from the thesis.

Table 5.2: SBB controller gains.

	D_y	D_z	χ	γ
K_P	1.6	1.2	52	22
K_I	0.2	0.1	-	-
K_D	3.1	2.0	200	-

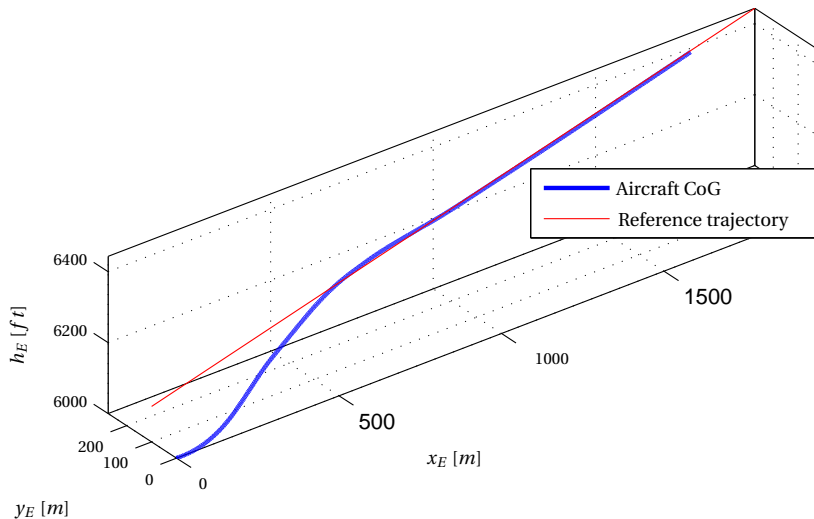


Figure 5.34: Time history of the aircraft intercepting a reference trajectory using the SBB controller.

5.6.6 Handling Quality Evaluation

This section shows the HQ evaluation of the SBB and IB controllers created in Examples 5.18 and 5.19. As mentioned in Section 5.3 HQ evaluations requires the identification of LOES models described in the frequency domain. Since the focus of this chapter lies on development of FCLs that require only little model information, the LOES models are not estimated by linearizing the entire closed loop of aircraft model, FBW platform and nonlinear FCL, but using the chirp z transform on simulation time histories.

A sum of sinusoids, each of which fitting an integer number of periods in the simulation length to prevent leakage, is provided subsequently to the pitch rate command and roll rate command input of the FCLs. The simulated time history is converted to the frequency domain using the chirp z transform and then fitted onto a LOES description using the optimization method described in Section 4.3. The validity of the LOES description can be checked using the Variance Accounted For (VAF) [131],

$$VAF(y(k), \hat{y}(k, \theta)) = \max \left(0, \left[1 - \frac{\frac{1}{N} \sum_{k=1}^N \|y(k) - \hat{y}(k, \theta)\|_2^2}{\frac{1}{N} \sum_{k=1}^N \|y(k)\|_2^2} \right] \right) \cdot 100\% \quad (5.146)$$

in which $y(k)$ is the output of the nonlinear model and $\hat{y}(k, \theta)$ the output of the LOES description. This measure shows the quality of the model in a quantitative way, high values correspond to close model fits and low values to poorer ones. System identification theory tells us that the input used to generate the VAF values should be uncorrelated to the signals used for identification. The VAF values for the LOES descriptions used in this section are therefore determined using a Schroeder sweep on the input [108, 77] and results are typically between the 85% and 99.5%.

Figure 5.35 shows the longitudinal HQs of the SBB and IB controllers. Both controllers again result in a too large equivalent pitch time-delay, but as mentioned in Section 4.6.5 this is due to the slow FBW platform, rather than the control laws themselves. Due to the high gain nature of the controllers, the short period damping is low and the eigenfrequencies are too high. This problem should be addressed before implementing the FCLs in reality.

Figure 5.36 shows the lateral HQs of the SBB and IB controllers. The lateral HQs are acceptable throughout the flight envelope, for both the SBB and the IB controller, except for the roll angle and roll rate oscillations. Again due to the high gains, the roll angle and roll rate oscillations can be up to 20%, which is uncomfortable for pilots and passengers. As already shown in Figure 5.29, the IB controller does a better job of suppressing sideslip.

The HQs can be improved by using a command filter to shape the reference signals provided by the pilot to the controller. This does not alter the closed loop of the controller, keeping the stability proofs intact. The command filter can just be a low pass filter,

$$CF = \frac{1}{\frac{1}{\omega_c} s + 1} \quad (5.147)$$

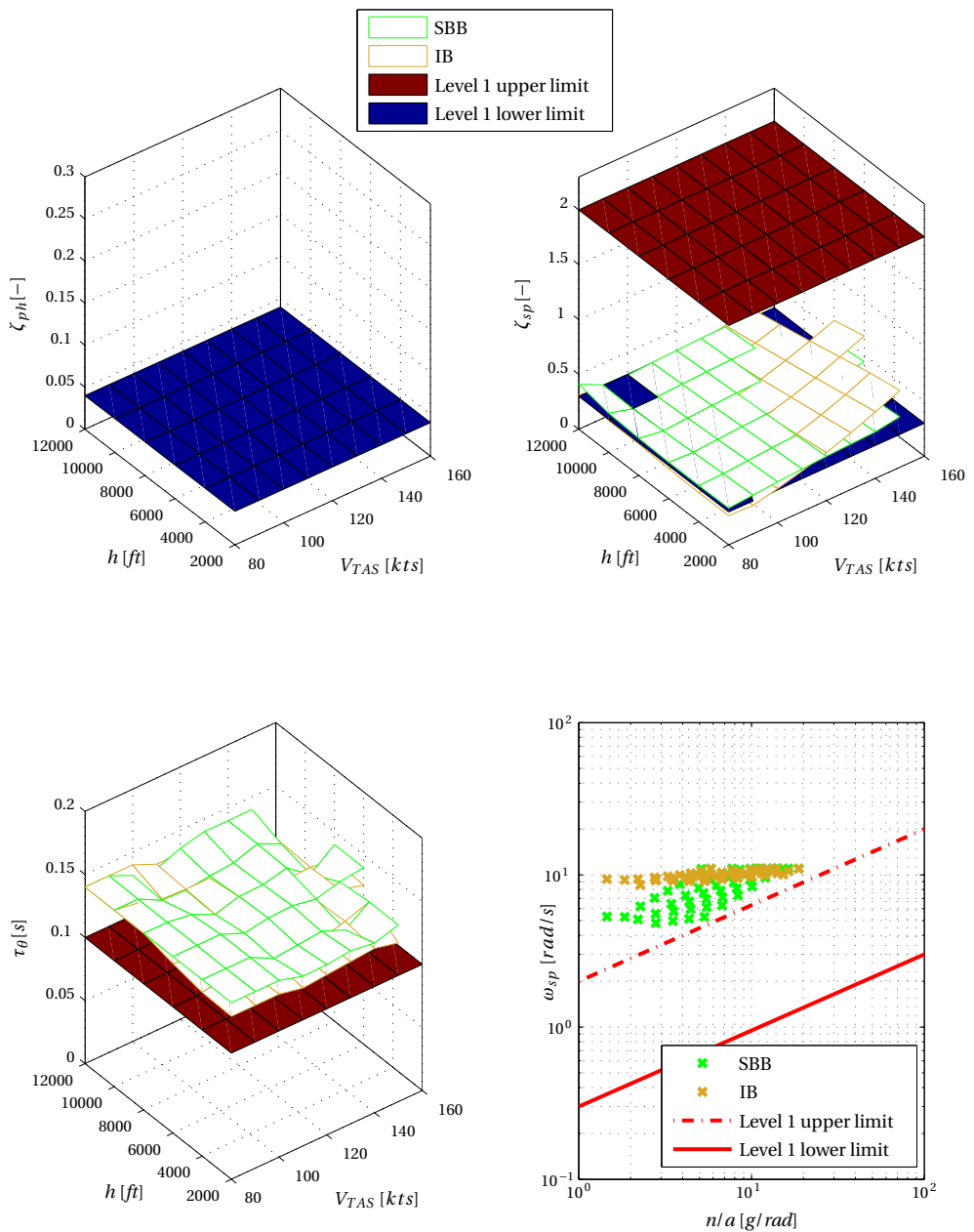


Figure 5.35: Longitudinal performance of the Sensor-Based Backstepping and Incremental Backstepping controlled system.

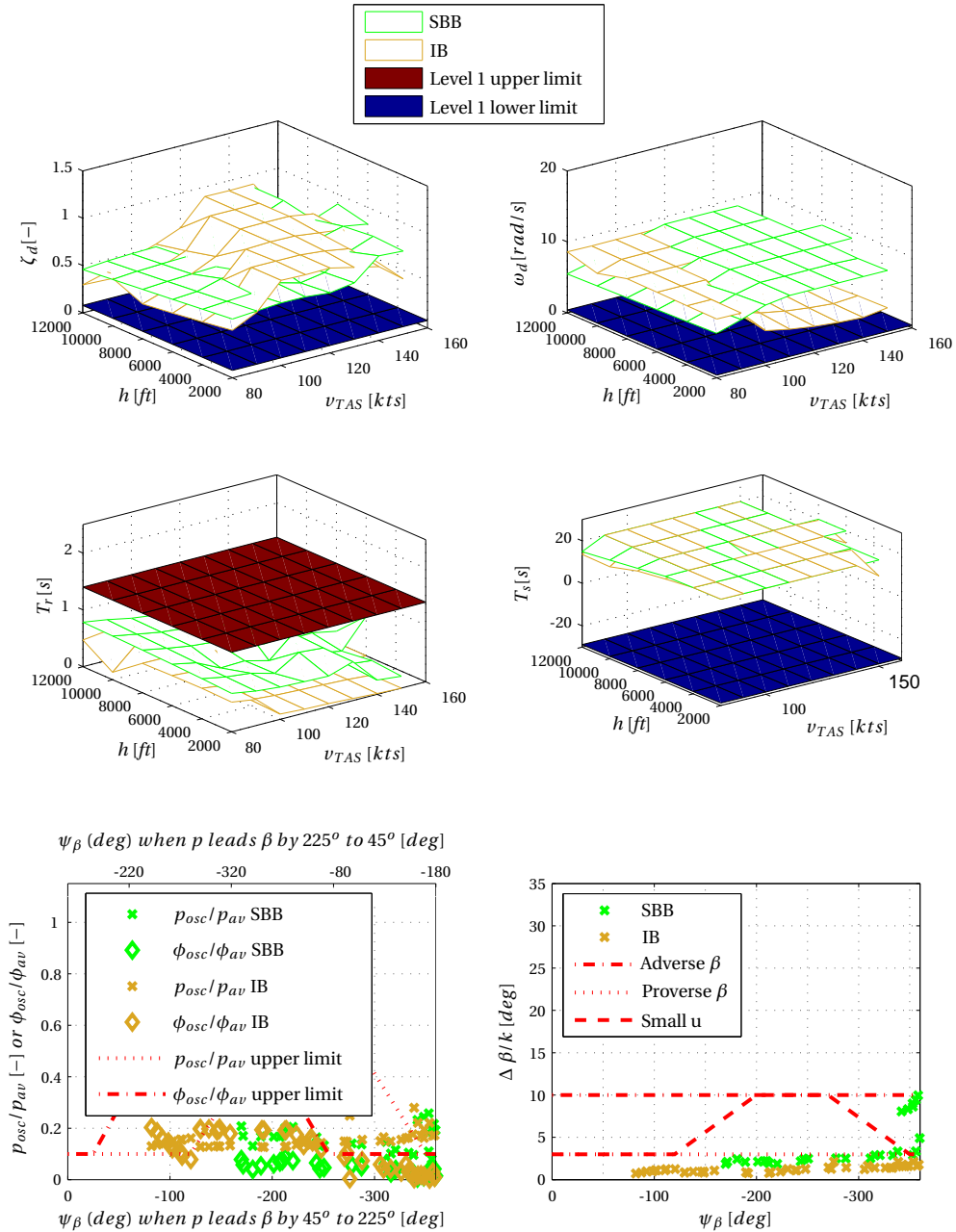


Figure 5.36: Lateral performance of the Sensor-Based Backstepping and Incremental Backstepping controlled system.

with ω_c the desired cutoff frequency of the filter. As indicated in Appendix E.3, this cutoff frequency is equivalent to the short period frequency when the short period damping is 0.7. However, implementing this filter also changes the damping, so it requires some trail and error. Figure 5.37 shows the SBB controller with and without a command filter. Choosing the cutoff frequency $\omega_c = 0.3\omega_{sp_{des}}$ rad/s, results in a short period damping of around 1.5 and acceptable short period frequencies throughout the flight envelope. Using this same command filter for the IB controller produces highly similar results and is therefore omitted from this thesis.

5.6.7 Performance Evaluation of the NAV Law

Table 5.3 provides the performance metrics for passively controlled FCLs as described in Section 4.3.2. The rise time, settling time, overshoot, ISE and ITEA metrics are determined using a step input of 50 meters. To obtain values that are comparable with the classical NAV FCL developed in Chapter 4, the aircraft response should be scaled to a equivalent response to a unit step input before determining the ISE, ITEA and M metric. Nonlinearities in the system distort results that would be obtained if an actual unit step response is used. As mentioned in Section 4.6.6, the M metric is determined using a reference (desired) dynamics given by the sigmoid function,

$$x_{ref}(t) = \frac{1}{1 + e^{-1.2t+4.4}} \quad (5.148)$$

The small M value for the V-NAV controller shows that this FCL intercepts the reference trajectory smoothly. Also the low rise time, settling time and overshoot make this a proper FCL design. The H-NAV controller does not perform as good as the V-NAV controller, due to the longer rise and settling times, but in terms of overshoot the design is good. Section 7.2.6 will show the comparison of the SBB NAV law with the classical NAV law.

Table 5.3: NAV law performance.

Metric	V – NAV	H – NAV
Rise time [s]	3.8	9.4
Settling time [s]	6.3	16.8
Overshoot [%]	0.8	0.7
ISE [ms]	2.8	4.7
ITEA [ms]	9.0	33.4
M [-]	0.04	0.43

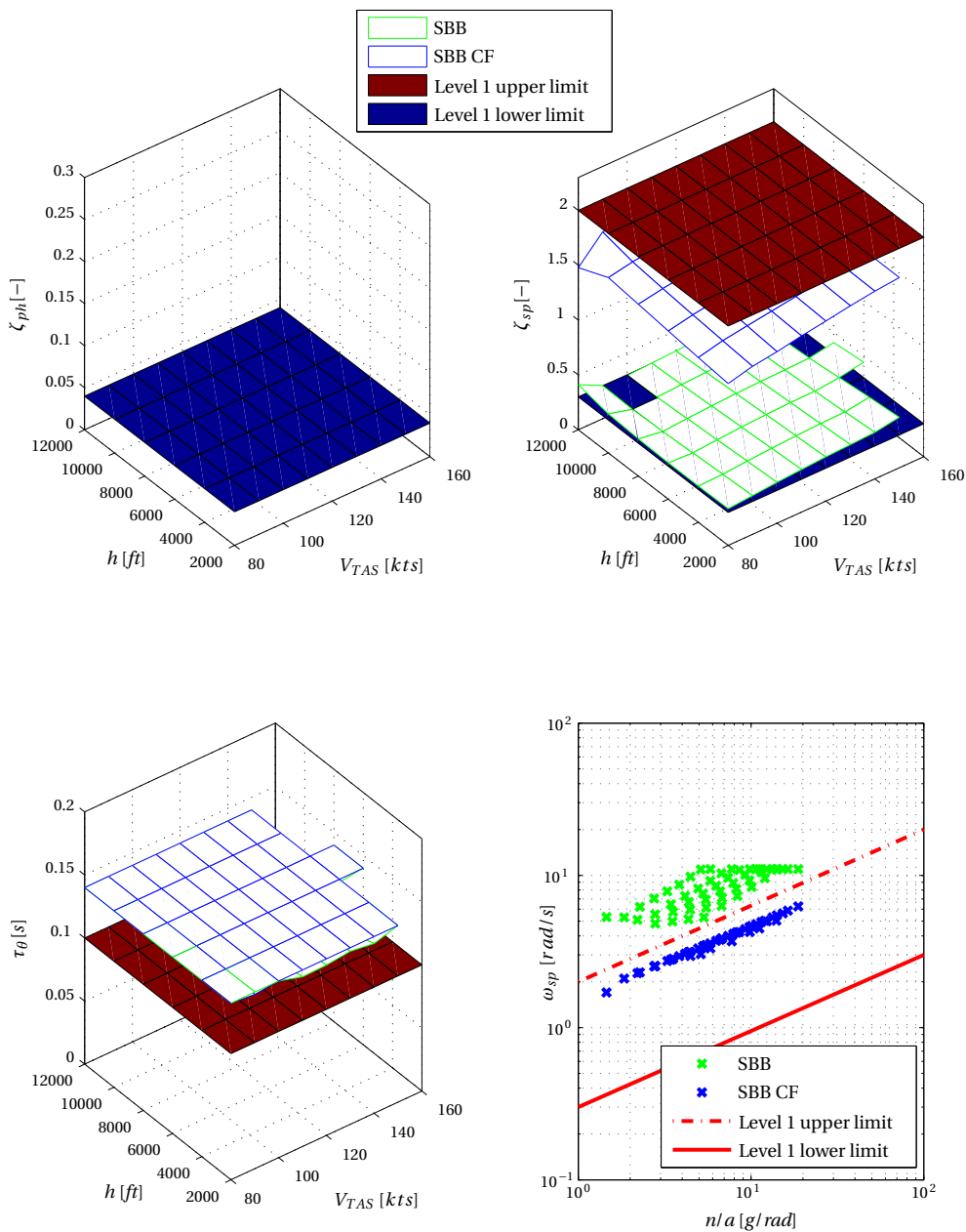


Figure 5.37: Longitudinal performance of the Sensor-Based Backstepping controlled system with and without a command filter.

5.7 Conclusions and Recommendations

This chapter presented two backstepping controller designs, one based on singular perturbation theory, named Sensor-Based Backstepping (SBB) and one based on Taylor expansions, called Incremental Backstepping (IB). Both methods use measurement data rather than model knowledge in their implementation and are therefore potentially usable on a broad family of small airplanes. Good tracking performance with or without uncertainty is obtained using either method for simple scalar systems, but also for flight control of the DA 42. The influence of measurement noise is shown to be small and comparable to that obtained using conventional backstepping. Since the Backstepping controllers are based on Lyapunov analysis, stability of the controlled system is guaranteed. The new controllers developed in this chapter have the advantage over conventional backstepping that model uncertainties have a smaller impact on performance and therefore they may very well be a significant step towards certification of advanced flight control laws.

The SBB controller can also be written into a Proportional-Integral (PI) controller form. Equivalent performance is obtained for both nominal and uncertain systems of relative degree one. For higher order systems, an equivalent PI form cannot be found. In the presence of sensor noise, SBB appears to provide better results. However, when the state derivative, used in the SBB controller, is not measured, but calculated by differentiating the state, this ‘advantage’ disappears.

The IB controller uses an inversion of the control function in its evaluation, whereas the SBB controller only uses the sign of this function. Both FCL designs result in similar responses, except for the sideslip and velocity controllers. When no sensor noise is taken into account, the IB controller is better able to track the reference signals for these states than the SBB controller. When sensor noise on angular acceleration measurements is taken into account, the SBB controller is favored, due to a smoother velocity controller output. For a general aviation aircraft, the assumed availability of angular accelerometers is questionable, however. Using differentiation of angular rate measurements instead of direct angular acceleration measurements also yields good results. Eventhough the noise levels are increased by differentiation, constant biases are removed as well. Both controllers result in poor handling qualities due to their high gain nature, but by filtering the command signals ideal handling qualities can be obtained.

Since both designs result in comparable responses, only a single design is selected for comparison with the classical FCL design in Chapter 7. This design is the SBB FCL, due to its complete model independence. Chapter 7 presents a more thor-

ough evaluation of the SBB FCL including the influence of parameter uncertainty and disturbances on the aircraft response.

Some practical considerations remain before actual implementation of either advanced FCL design is possible. The current main drawback of the new methods is that they require measurements of the actuator output in order to be robust to time delays. Preliminary simulations show that good results can also be obtained using a actuator model, and it would be worthwhile to investigate how accurate such a model needs to be in future work.

Also future work is needed to find a more scientific method for the selection of the controller gains. Most of the gains used in this chapter are selected by trail and error and could be improved. Perhaps a cost function of control effort, noise attenuation, disturbance rejection and tracking performance can be minimized to find optimal controller gains. Or the gains can be tuned using the control performance assessment provided by the ANOVA-like variance decomposition method, in order to find controller gains resulting in good noise attenuation.

The NAV mode created in this chapter does not fit entirely in the backstepping framework. The reason for this design flaw lies in that the system description for position control does not have a lower triangular form, nor is altitude control minimum phase. It would be worth investigating whether the influence of the control surface deflections can be ignored when calculating the flight path vector rate of change and whether the SBB method can be altered to support slightly non-minimum phase systems.

INVESTIGATION OF PRACTICAL FLIGHT ENVELOPE PROTECTION SYSTEMS FOR SMALL AIRCRAFT

Abstract

In commercial aviation fly-by-wire technology, equipped with flight envelope protection (FEP), is used to prevent accidents related to handling and control problems. This chapter focuses on a FEP system for small aircraft. Preliminary results are obtained from an empirical comparison study in the time domain, between a PID-based control-limiting approach, a command-limiting approach, a constrained-flight-control-law approach, using model-based predictive control and incremental nonlinear dynamic inversion (INDI), and a virtual-control-limiting approach that also uses INDI. Comparison is not only done using a nominal model, but also in the presence of parametric uncertainty, sensor noise, time delays, wind gusts and turbulence. Investigation of the results reveals that, for this study, control limiting should be avoided and that for practical implementation, command limiting is currently the best option.

6.1 Introduction

Commercial aviation has a long history in using control systems to shape ideal aircraft responses [125]. To increase safety, modern commercial aircraft, such as a Boeing 777 and an Airbus A380, are also equipped with Flight Envelope Protection (FEP) systems to protect for stall, exceeding over-speed, limit angle of attack and load factors. These techniques have greatly reduced the handling and control related accidents in the commercial aviation sector. The work in this chapter focuses on the design of a FEP control system by trading off several control strategies adopted by industry and academia. As such, it provides a preliminary comparison study between these control strategies and their implications on system requirements, performance, cost, and certification.

This chapter is structured as follows. First, a review is given of FEP strategies and their benefits and pitfalls. Second, the role of the aircraft model fidelity and accuracy on the FEP design will be described. Then, a test case will be presented utilizing classic and advanced control strategies on a low-fidelity aircraft model. Finally, a discussion of the results is provided, followed by the conclusions.

6.2 Review of Flight Envelope Protection Strategies

Modern FBW control systems have FEP, that prevents the pilots from entering state- and control regions outside the safe flight regime of the aircraft. In this section a review is given on several aspects of FEP. First the determination of the safe flight regime is investigated, both a priori and during flight. When the limits are known, there are four different strategies to protect the aircraft against exceeding its safe flight envelope: control limiting, command limiting, using a Constrained Flight Control Law (CFCL) and virtual-control limiting [126]. These strategies are reviewed in the second part of this section. Irrespective of the determination and protection method, the pilot authority at the boundary should be defined. The third and last part of the review concerns with the use of soft limits and hard limits.

6.2.1 Safe Flight Envelope Definition

The safe flight-regime can be described in terms of limitations on airspeed, pitch and roll angles, angle of attack, and load factor. Predefining this regime has the advantage that the limits can easily be interpreted and pose little or no sensor requirements. Given the system dynamics $\dot{x} = f(x, u)$, where $x \in \mathbb{R}^n$ denotes the state of the system, $u \in \mathbb{R}^m$ the input and $T \geq 0$ some time horizon. The fixed flight-envelope

limits, i.e., limitations on the aircraft state, can be written as:

$$\underline{x} \leq x(t) \leq \bar{x} \quad \forall t \in [0, T] \quad (6.1)$$

The largest drawback of using a predefined flight envelope is that in case of failures the limits are not accurate anymore. Due to a failure (e.g., actuator hard over, structural damage of the aircraft, etc.) the safe flight envelope will shrink and limits will narrow. When the old boundaries are still used, it cannot be guaranteed that the FEP system will keep the aircraft within the safe flight regime. Tang *et al.* suggest that it should be possible to use multiple predefined flight envelope sets and let the sensor information determine which set is currently used by the FEP system [122]. The flight envelope limits then become a function of time:

$$\underline{x}(t) \leq x(t) \leq \bar{x}(t) \quad \forall t \in [0, T] \quad (6.2)$$

Tang *et al.* also use a different approach where the safe flight envelope is not defined on forehand, but on-line through reachability and viability calculations. First an aircraft model is identified on-line. This model can be used to predict the effect of control surface deflections on state variations [71]. Then the flight envelope is determined as follows. Let $\mathcal{U}_{[t,t']}$ denote the set of Lebesgue measurable functions from the interval $[t, t']$ to the set of possible inputs $U \in \mathbb{R}^m$. Given the set of states $K \in \mathbb{R}^n$, the safe flight envelope can be estimated by gathering the initial states for which:

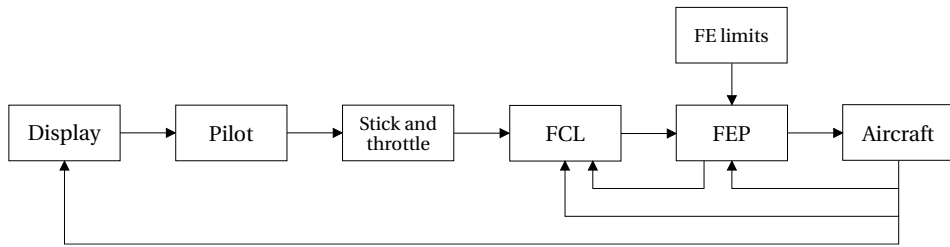
- There exists a $u(\cdot) \in \mathcal{U}_{[t,T]}$ for which the trajectory $x(\cdot)$ satisfies $x(\cdot) \in K \forall t \in [0, T]$.
- There exists a $u(\cdot) \in \mathcal{U}_{[t,T]}$ and a $t \in [0, T]$ such that the trajectory satisfies $x(t) \in K$.

The constraints calculated from the reachable set are then used in the protection system.

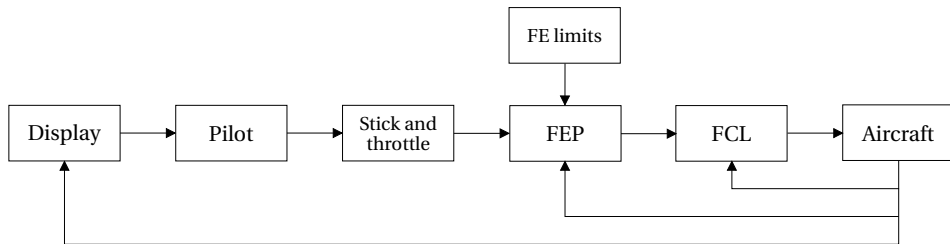
6.2.2 Flight Envelope Protection

When the flight envelope limits are known, either through on-line or off-line determination, the Flight Control Law (FCL) can be changed and/or extended in order to ensure that the aircraft stays within these boundaries. This section provides details on the four possibilities of FEP shown in Figure 6.1: control limiting, command limiting, using a CFCL and virtual-control limiting.

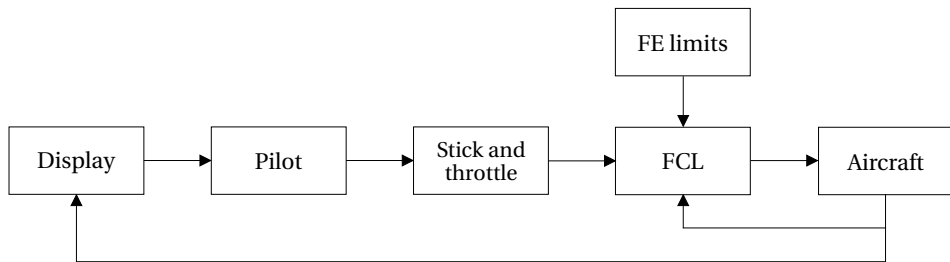
6. INVESTIGATION OF PRACTICAL FEP SYSTEMS FOR SMALL AIRCRAFT



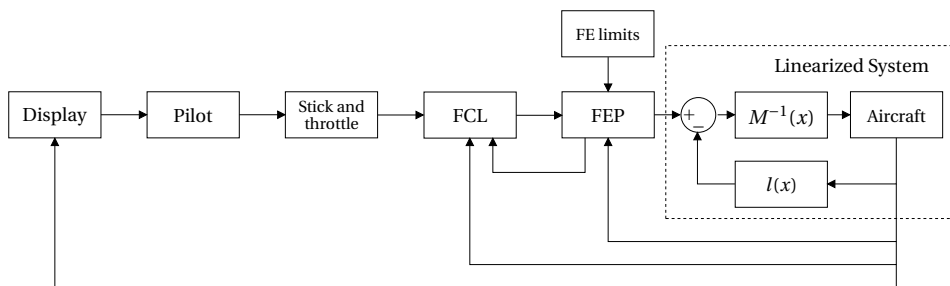
(a) FEP using Control Limiting.



(b) FEP using Command Limiting.



(c) FEP using a Constrained Flight Control Law.



(d) FEP using Virtual-control Limiting.

Figure 6.1: Different strategies for keeping the aircraft within the safe flight envelope.

Control Limiting

In a control-limiting setup, an additional block is placed between the FCL and the aircraft as shown in Figure 6.1(a). It performs two tasks. First, the envelope limits are mapped onto control-surface-deflection limits. This mapping is non-trivial and can be done in many ways, such as: inverting the input-output relation, using physical functions such as a force equilibrium function or approximating the control-surface-deflection limits by using safe flight envelope margins (i.e., when the aircraft is far away from its limits, large control surface deflections are allowed and when close to the limits control surface deflections are restricted). An advantage of control limiting is that only one set of mapping functions is required for all FCLs, i.e., only from the state limits onto control surface deflection limits irrespective of which FCL is selected. The second task of the FEP module is to keep the output of the FCL between the calculated control-surface-deflection limits,

$$\underline{u}(t) \leq u(t) \leq \bar{u}(t) \quad \forall t \in [0, T] \quad (6.3)$$

where $[\underline{u}(t) \quad \bar{u}(t)]^T = m_{f:\underline{x},\bar{x} \rightarrow \underline{u},\bar{u}}(x, \underline{x}, \bar{x}, t)$ with m_f denoting a set of mapping functions from state constraints onto input constraints. Reaching the control-surface-deflection limits is similar to reaching actuator limitations and should be included in anti-integrator-windup schemes or Pseudo Control Hedging [57] schemes of the FCL.

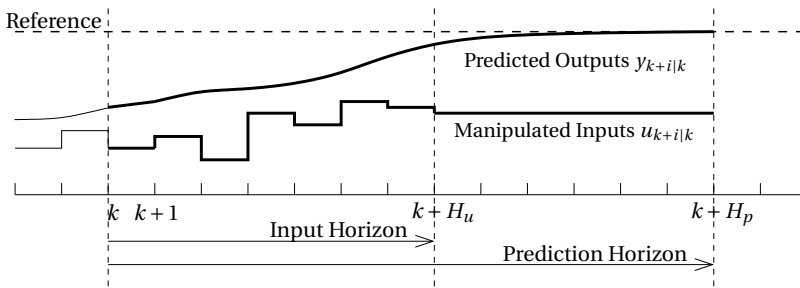
Command Limiting

In a command-limiting setup, an additional block is placed between the stick and the FCL as shown in Figure 6.1(b). The FEP block basically performs the same tasks as for control limiting. First, the flight envelope limits are mapped onto command limits. For each control mode a different set of mapping functions is needed, since different commands will be used for each control mode. This is a drawback of command limiting. The mapping functions themselves tend to be more simple, however. For example, mapping an altitude limit onto an altitude command limit for an altitude hold control law can be done straight forward with input saturation. Second, the stick commands are limited before they are fed to the FCL. This has the advantage that no additional integrator-windups will occur in the FCLs.

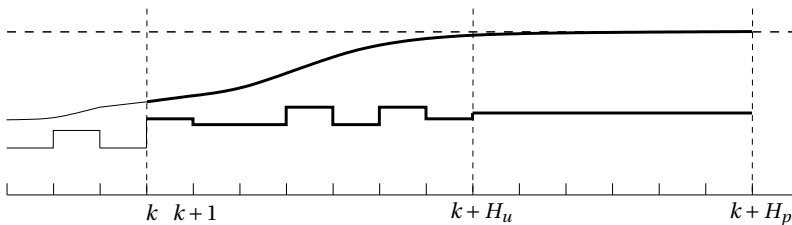
Constrained FCL

A third way to keep the aircraft within the safe flight envelope is to use a (state) constrained FCL as shown in Figure 6.1(c). Model-based Predictive Control (MPC) is a perfect candidate for this task, due to its explicit constraint-handling capabilities [73]. Originating from the process industry, MPC is capable of keeping multi-

variable systems within explicitly defined boundaries while tracking a desired trajectory with high performance [96]. MPC is a collective term for several control algorithms in which a dynamic model of the system is used to predict and optimize future states and needed inputs of the system. At each control interval, the MPC algorithm computes an open-loop sequence of the manipulated variables in such a way that the future behavior of the system is optimal. The first value in this optimal sequence is applied as an input to the system, and the optimization process is repeated at the subsequent control intervals [73]. This principle is called the receding horizon principle and is presented graphically in Figure 6.2. At time k an optimal control sequence, $u_{k+i|k}$, is calculated over a prediction horizon, H_p , in which the control is assumed to be constant after the input horizon, H_u , as shown in Figure 6.2(a). Only the first element of this sequence is used as an input to the system. Then the horizon is receded over one sample to $k + 1$ and the optimization is repeated with new measurements from the system, giving a new and possibly different optimal control sequence as shown in Figure 6.2(b).



(a) Optimal control sequence calculated at time k .



(b) New sequence is calculated after receding the horizon.

Figure 6.2: The Receding Horizon principle of MPC.

MPC is based on a discrete linear system. For these kinds of systems, future predictions can easily be made by simple matrix multiplications and additions. Con-

sider the discrete linear system,

$$x_{k+1} = A(k)x_k + B(k)u_k \quad (6.4)$$

Predictions of this system can be written as,

$$\begin{bmatrix} \hat{x}_{k+1|k} \\ \vdots \\ \hat{x}_{k+H_p|k} \end{bmatrix} = \Psi x_k + \Upsilon x_{k-1} + \Theta \Delta U_k, \quad (6.5)$$

where,

$$\Psi = \begin{bmatrix} A \\ \vdots \\ A^{H_p} \end{bmatrix}, \quad \Upsilon = \begin{bmatrix} B \\ \vdots \\ \sum_{i=0}^{H_p-1} A^i B \end{bmatrix}, \quad (6.6)$$

$$\Theta = \begin{bmatrix} B & \cdots & 0 \\ \vdots & & \vdots \\ \sum_{i=0}^{H_p-1} A^i B & \cdots & \sum_{i=0}^{H_p-H_u} A^i B \end{bmatrix}$$

The optimal sequence of manipulated variables can be found by solving the QP-problem,

$$\begin{aligned} \min_{\Delta U_k} \Delta U_k^T (\Theta^T Q \Theta + R) \Delta U_k - (2\Theta^T Q E_k)^T \Delta U_k \\ \text{subject to: } F \Delta U_k \leq c \end{aligned} \quad (6.7)$$

in which Q and R are weighing matrices, $E(k) = T_k - \Psi x_k - \Upsilon u_{k-1}$ represents the tracking error and F and c describe the state, input and incremental input constraints on the system. The outcome of the QP-solver is either in-feasibility or the optimal sequence of manipulated variables of which the first element can be applied to the system. Depending on the number of states of the system and the number of prediction steps used, the matrices may become large and solving the QP-problem could be time consuming.

Due to the nonlinearities at the boundaries of the flight envelope, the predictions made using such a linear model are incorrect. Nonlinear MPC exists, but unfortunately it is currently too slow for application in aircraft control [47, 6]. An alternative approach is using Nonlinear Dynamic Inversion [112, 54] (NDI) to obtain almost full linearity of the controllable system, on which a MPC controller can then be applied. NDI is a type of feedback linearization that continuously linearizes the

aircraft model by inverting the nonlinear dynamics. This method removes all nonlinearities from the system and can be seen as a special case of the backstepping method introduced in Chapter 5. Example 5.2 shows that this is not always beneficial, but the combination of NDI and aircraft dynamics results in a mere chain of integrators, which is perfect for MPC application. For demonstration purposes, suppose a nonlinear SISO system can be described by,

$$\begin{aligned} \dot{x} &= f(x) + g(x)u \\ y &= h(x) \end{aligned} \tag{6.8}$$

The control variable y is differentiated with respect to time until it becomes an explicit function of the input. Thus,

$$\dot{y} = \frac{\partial h}{\partial x} \dot{x} = \frac{\partial h}{\partial x} f(x) + \frac{\partial h}{\partial x} g(x)u \tag{6.9}$$

Feedback linearization is achieved using the control input,

$$u = M^{-1} (v - l) \tag{6.10}$$

where $M = \frac{\partial h}{\partial x} g(x)$ and $l = \frac{\partial h}{\partial x} f(x)$. Application of this input to the system results in the output y becoming the integral of the virtual-control input v . The linear system, $\dot{y} = v$, can easily be discretized and then used to predict the future behavior of the system in the MPC controller. Figure 6.3 shows the principle of NDI in a block diagram.

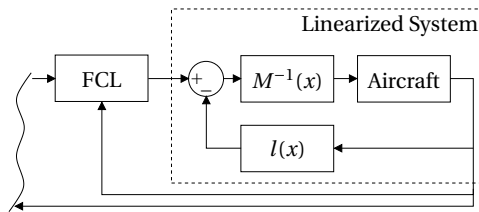


Figure 6.3: Feedback linearization using Nonlinear Dynamic Inversion.

For a low-fidelity aircraft model, the nonlinear dynamics are not accurately known and therefore inversion can be problematic. Using NDI with a linear fractional representation (LFR) of the uncertainty, shows that modeling errors can result in incomplete linearization [130] and therefore poor performance of the MPC

controller. When NDI on the incremental input of the system (also known as Incremental Nonlinear Dynamic Inversion) is used, a large part of the uncertain parameters drop out, thereby decreasing the sensitivity to parametric uncertainty [9]. This method is nearly identical to the IB method presented in Section 5.6.3 and will therefore be introduced briefly. Consider the moment equation,

$$M_a + M_c = J\dot{\omega} + \omega \times J\omega \quad (6.11)$$

where M_a represents the aerodynamic moment, M_c the aerodynamic moment due to control surface deflections, J the inertia tensor and ω the rotational velocity of the aircraft. Suppose that a change in control moment has a far greater effect on the angular acceleration than on the angular rate, or in other words that time scale separation may be applied [99]. The incremental moment equation can then be written as,

$$\partial M_c = J(\dot{\omega}_{new} - \dot{\omega}_{cur}) \quad (6.12)$$

In this equation the parametric uncertain M_a has dropped out. Using Equation (6.12) as a basis for NDI will therefore result in a control law that is less sensitive to parametric uncertainty. Equation (6.12) also shows that application of INDI requires knowledge on the angular accelerations of the aircraft $\dot{\omega}$. There are devices on the market that can measure the angular acceleration, but these are costly. An alternative approach is to use the angular rates available from IMU's and differentiate this signal. This procedure will put requirements on the noise level of that signal, however. Although similar, INDI and IB are not equivalent. For systems with a relative degree larger than one, the stabilizing functions from higher order subsystems are used in the IB control law, whereas INDI does not use this construct and results in fully linear system. Note that for systems with a relative degree of one both methods are identical.

Virtual-Control Limiting

Application of a recursive control-scheme such as NDI or Backstepping allows for the definition of a fourth FEP strategy, namely virtual-control limiting or stabilizing function limiting. In this setup, limitations are not applied on the control surface deflections, but on the virtual-control input (α) of the subsystem, as shown in Figure 6.1(d). In this way only one set of mapping functions is needed, i.e., from state constraints onto virtual-control input constraints, irrespective of the outer-loop control law used. These functions are more simple than the mapping functions needed for control limiting and can be written as,

$$\underline{\alpha}(t) \leq \alpha(t) \leq \bar{\alpha}(t) \quad \forall t \in [0, T] \quad (6.13)$$

where $[\underline{\alpha}(t) \quad \bar{\alpha}(t)]^T = m_{f:\underline{x},\bar{x} \rightarrow \underline{\alpha},\bar{\alpha}}(x, \underline{x}, \bar{x}, t)$.

6.2.3 Pilot Authority at the Boundary

Irrespective of the methods used for determining and protecting the flight envelope, control authority at the boundary must be defined. In commercial aviation control systems, there is an important distinction between the approaches to FEP being taken by Boeing & Airbus. The Boeing 777 has so called “soft” protections, meaning that the crew can override them by using excess force on the control column. So, the protection system will make it more difficult to do something it thinks should not be done, but will always leave the final decision to the crew. The main advantage of soft limits is that pilots can always operate the aircraft at its full capability whenever required. The disadvantage is that less-experienced pilots and ill-trained pilots can always control the aircraft into unsafe flight conditions. In other words, pilots have to be fully aware of the aircraft limitations. Otherwise, they still have the authority to make things worse.

In contrast, the protections on the A320 are so called “hard” limits that cannot be overridden. That is, you either get switched into an alternate control mode, or your inputs will be ignored. The advantage of hard limits is that the protection system will always keep the aircraft in safe flight regimes and therefore controllable, irrespective of pilot control actions. The main disadvantage is that it prevents the aircraft to be operated at its full capacity, which can also have some serious consequences. For example, in the China Airlines B 747 incident 300 nm northwest of San Francisco in 1985 [89], the crew was forced to overstress (and structurally damage) the horizontal tail surfaces to recover from a roll and near vertical dive following an automatic disconnect of the autopilot. At the time of disconnect, full rudder was engaged to one side and the crew was unaware of this. The crew recovered control with about 10,000 ft of altitude left from an original high altitude cruise. It is likely that if the aircraft had prevented the crew from initiating control commands that would lead to aircraft damage, the aircraft (and passengers) would have been lost.

6.3 Aircraft Model Requirements

This section provides some remarks on aircraft model requirements related to FEP system design. First the necessity of a nonlinear model is explained, followed by a brief description on how such a model may be obtained. The last part of this section shows the influence of the mapping functions on the required model accuracy.

6.3.1 Importance of Modeling Nonlinearities

In general, much effort is directed into creating an aircraft model suitable for controller design. This is quite logical since a good aircraft model will require a less

robust control-law and may therefore lead to a better performing controller. It is common practice that controller design is done using linearized aircraft models and classical control theory. A number of operating points are selected within the flight envelope around which the linear approximation is valid. These linearized models are then used in analysis and design tools, such as Root-Locus, Bode, Nyquist, etc. Whether this procedure will provide satisfactory results for the design of FEP systems can be questioned. FEP plays its role at the limits of the flight envelope, where most nonlinear effects are present. Therefore, a full nonlinear model is highly preferred. Chapter 2 describes the nonlinear model of the Diamond DA 42 used in this thesis.

6.3.2 Mapping Functions and Aircraft Model Fidelity

Another requirement on the aircraft model is posed by the choice in mapping functions used in the FEP system. High model accuracy is needed when physical functions, or inverted input-output relations, are used as mapping functions. For example, consider the transfer function from elevator deflection angle to pitch angle,

$$H(s) = \frac{\theta(s)}{\delta_e(s)} \quad (6.14)$$

This relation can be used to calculate the elevator deflection corresponding to the upper pitch angle limit,

$$\underline{\delta_e}(s) = H^{-1}(s)\bar{\theta}(s) \quad (6.15)$$

Clearly H should be invertible and it should also be accurate, since there is no correctional term present in the equation. Would an inaccurate model be used, the mapping may become inexact leading to the possibility of exceeding the safe flight envelope.

Using approximation functions, the mapping is more robust against small model uncertainties and therefore the fidelity of the aircraft model used may be lower. For example, suppose an elevator deflection limit can be related to the upper pitch angle limit as follows,

$$\underline{\delta_e} = \delta_{e,trim} + K_p(\theta - \bar{\theta}) \quad (6.16)$$

where K_p is a proportional gain. This relation is not dependent on model information and is therefore less sensitive to model uncertainty. However, the amount of freedom the pilot has within the safe flight envelope may be restricted unnecessarily, since the limits are not determined accurately.

6.4 Test Case Definition

The remainder of this chapter contains a comparison study. The performance, defined as the ability to keep the aircraft within the safe flight envelope, of four different FEP systems will be compared in the time domain. In this study the knowledge on the aircraft model and on the benefits and pitfalls of FEP strategies will be used to find the FEP system best suited for a certain test case. In this section, the method of this test case is described first. Next, the four FEP options are presented and in the end the results of the test case are given.

6.4.1 Method

Aircraft Model

The aircraft used in the test case is a Diamond DA 42, the dynamic behavior of which is described in Chapter 2. The aircraft will be trimmed at 120 kts, 6,000 ft and in cruise configuration. This condition is partly selected because of the available data, but also since most fatal accidents related to handling and control of the aircraft occur during the cruise and maneuvering phase [90]. The majority of all accidents occur during the landing phase, but, since the energy state of the aircraft (both potential and kinetic) is quite low during landing, many of those accidents are non-fatal.

Flight Control Law

Direct control of this model (and the aircraft) is not easy. Part of this is caused by the coupling of aircraft states, for example banking to the left will also pitch down the nose of the aircraft. Sections 4.2 and 4.6.2 explain that an attitude rate command attitude hold (RCAH) control law, as shown in Figure 6.4, could simplify aircraft handling and may be suitable for less-experienced pilots.

The drawback of a RCAH FCL is that it is not inherently stable. This means keeping a certain stick deflection will not result in a new equilibrium situation, but a constantly changing attitude angle. Even keeping the stick centered is not necessarily safe, because speed stability is removed from the dynamic behavior of the aircraft. Without application of FEP this behavior is dangerous. It should therefore be a good FCL for this test case.

The rudder and throttle are controlled without an interface to the pilot in this test case. The rudder controller will try to minimize the sideslip angle by directly reacting to β and an auto-throttle will try to keep the speed constant by directly reacting to V_{TAS} .

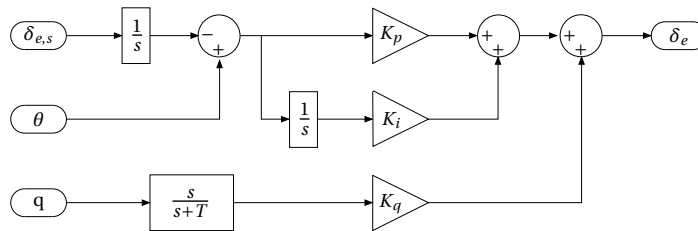


Figure 6.4: Attitude Rate Command Attitude Hold Control Law.

Input Signal

In order to test the performance of the FEP systems, a sufficiently large step is given as pitch-rate command. This will cause a sharp pull-up maneuver during which the angle of attack limit is reached followed by a pitch angle limit. The aircraft will decelerate in this condition until the stall speed limit is reached. After 20 seconds the input is reversed to check for integrator windups of the control system.

Flight Envelope Determination

The selected control law requires the use of FEP for safe flying. However, before the flight envelope can be protected, it must first be defined. Restriction to low-cost sensors limits the usefulness of on-line model identification. The noise of the sensors will lead to uncertainty in the model parameters, resulting in a conservative definition of the flight envelope. Moreover, determination of the flight envelope through reachability and viability calculations is currently too slow for on-line application. A predefined flight-envelope-limit set will therefore be used in the test case.

Available Mapping Functions

The four FEP strategies to compare are: control limiting, command limiting, replacing the FCL by a CFCL and virtual-control limiting. For all these strategies a mapping of the state constraints is required. Restriction to low-cost sensors affects the choice in mapping functions that can be used as well. The use of physical functions, such as a force equilibrium or an energy conservation function, require extensive knowledge on the aircraft state and would therefore pose considerable sensor requirements. Mapping functions that use inverted input-output relations are also less useful, since the fidelity of the model used in this test case is not high enough. The only mapping functions that can be used are therefore approximate mapping functions.

Authority at the Boundary

The pilot authority at the envelope boundary is defined using hard limits. In this way the system is usable for less-experienced pilots, since they are not able to structurally damage the aircraft. Furthermore the use of soft limits would require a force or force-feedback stick, which is more expensive and uses more space in the often already cramped cockpit.

Conditions

The goal of this chapter is the investigation of practical FEP systems. In order to increase the practical use of these systems, several off-nominal conditions need to be added to the test case. Due to the low-fidelity of the model, robustness to parameter changes is important. As the input in the test case is a longitudinal one, only longitudinal model parameters need to be altered. To check the robustness of the FEP systems to parameter uncertainty, the basic longitudinal force coefficient (C_{X_0}) is increased by 10%, while the influence of the angle of attack on the vertical force coefficient (C_{Z_α}) is decreased by 10%. The elevator effectiveness ($C_{m_{\delta_e}}$) is increased by 40%. Mass (m) and longitudinal center of gravity position (x_{cg}) are also subject to change during flight and have therefore been increased by 10% and 5% respectively.

With the use of low-cost sensors comes the necessity to deal with noisy signals. Checking the sensitivity to sensor noise is therefore crucial. In order to do so, the output of the aircraft is modified using the sensor models described in Section 3.2.4. The output of this sensor block is fed to the control system.

Besides sensor noise, time delays of the signals can have a severe impact on the performance of the FEP systems. Sensitivity to these delays is investigated using transport delays of 50, 100 and 150 milliseconds.

The last off-nominal condition examined in this chapter is flying through turbulence and wind gusts. This condition causes disturbances on the input as seen from the controller. It is therefore similar to the condition with sensor dynamics, however, the frequency and amplitude of the disturbance are completely different. Since the effect of turbulence on small aircraft is profound, this condition could have a large impact on the FEP system. The effects of turbulence have been modeled according to the mathematical representation in section 3.7 of the Military Specification MIL-F-8785C [79], as explained in Section 2.3.2. The intensity of the turbulence used is labeled as “moderate” by MIL-F-8785C. This means that at an altitude of 6,000 ft the root mean square of the turbulence amplitude is 10 ft/s. The

aircraft is flying at 120 kts so the increment in angle of attack caused by turbulence has a root mean square of $\arctan\left(\frac{10 \cdot 0.3048}{120 \cdot 0.51444}\right) = 0.049$ radians or 2.8 degrees. The wind gust is defined using a “1-cosine” shape. It starts after 10 seconds, has a length of 120 meters and an amplitude of 3.5 m/s.

6.4.2 Flight Envelope Protection Strategies

Control Limiting

In the control-limiting setup, multiple parallel PID controllers, one for each flight envelope limit, can be used for the mapping of state constraints onto control surface deflection constraint as shown in Figure 6.5. The output of each of these PID controller is interpreted as a control surface limit. For instance,

$$\underline{\delta}_e = \delta_{e,trim} + K_p(\theta - \bar{\theta}) + K_i \int (\theta - \bar{\theta}) dt + K_d \frac{d(\theta - \bar{\theta})}{dt} \quad (6.17)$$

where K_p , K_i and K_d are gains. Note that in order to prevent “suction” towards the limit while being in the safe flight envelope, the integral should be kept zero until the limit is reached. When the output of the currently selected FCL exceeds a control surface limit, control is switched to that limit hold controller. Additional switching logic is used to return control authority to the pilot on input reversal and prevent integrator-windups in the FCL and in the parallel PID controllers.

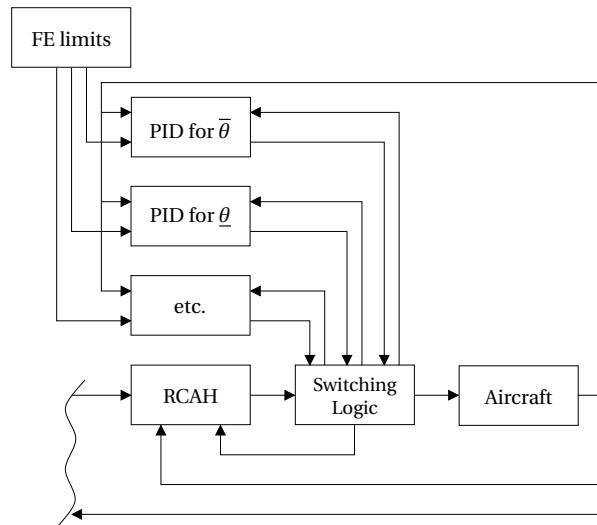


Figure 6.5: Control Limiting using multiple PID controllers.

Command Limiting

The second candidate used, is the command-limiting setup shown in Figure 6.6. In this setup the FEP controller will limit the attitude-rate commands fed to the FCL. The pitch angle limits are mapped onto pitch-rate command limits using parameter projection [64]. Let \mathcal{S} be a convex region defined as,

$$\mathcal{S} \triangleq \{\gamma \in \mathbb{R}^{p_\gamma} | g(\gamma) \leq 0\} \quad (6.18)$$

where $g: \mathbb{R}^{p_\gamma} \rightarrow \mathbb{R}$ is a smooth function. Parameter projection provides that the parameter γ will remain in \mathcal{S} , when,

$$\dot{\gamma} = \begin{cases} \dot{\gamma} & \text{if } \gamma \in \mathcal{S}^0 \text{ or if } \gamma \in \delta\mathcal{S} \text{ and } \nabla g^T \dot{\gamma} \leq 0 \\ \dot{\gamma} - \Gamma \frac{\nabla g \nabla g^T}{\nabla g^T \Gamma \nabla g} \dot{\gamma} & \text{otherwise} \end{cases} \quad (6.19)$$

where \mathcal{S}^0 is the interior of \mathcal{S} , $\delta\mathcal{S}$ is the boundary of \mathcal{S} , $\nabla g = \frac{dg}{d\gamma}$ and Γ is a design parameter. In the case of mapping the pitch angle limit onto a pitch-rate constraint, the following relations can be used. Since g is a scalar-function per parameter, first the upper and lower limits need to be captured in a single function,

$$g = (\theta - (\bar{\theta} + \underline{\theta})/2)^2 - (\bar{\theta} - (\bar{\theta} + \underline{\theta})/2)^2 \quad (6.20)$$

$$\nabla g = 2(\theta - (\bar{\theta} + \underline{\theta})/2) \quad (6.21)$$

The pitch angle limits can then be mapped onto pitch-rate constraints using,

$$q_{cmd} = \begin{cases} q_{cmd} & \text{if } g \leq 0 \text{ or if } g = 0 \text{ and } \nabla g q_{cmd} \leq 0 \\ 0 & \text{otherwise} \end{cases} \quad (6.22)$$

To prevent the aircraft from stalling, the upper pitch angle limit can be decreased on approaching the stall-speed (\underline{V}). This may be done using a hyperbolic tangent function,

$$\bar{\theta} = \bar{\theta} \cdot \tanh\left(c_1 \frac{V - \underline{V}}{c_2}\right) \quad (6.23)$$

where c_1 and c_2 are tuning parameters. Similar constructions are possible for the over-speed, angle of attack and load factor limits.

Constrained FCL

In the third candidate, the PID FCL is replaced by a MPC controller combined with INDI. This candidate is referred to as CFCL hereafter. The INDI control variables have to be chosen carefully since they have effect on the required mapping of the

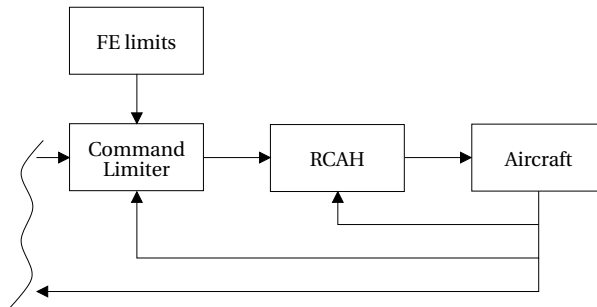


Figure 6.6: Command Limiting.

flight envelope limits onto the controller constraints. Here the state and input vectors of the linear system used by the MPC controller are chosen as follows:

$$\zeta = \begin{bmatrix} \phi \\ \theta \end{bmatrix}, \quad v = \begin{bmatrix} \dot{p} \\ \dot{q} \end{bmatrix}$$

In this way the pitch and bank angle limits can be fed straight to the MPC as state constraints. The other aircraft state limits can be protected using the same construction as used in the command-limiting setup, i.e., hyperbolic tangent functions. Figure 6.7 shows the CFCL in a block diagram.

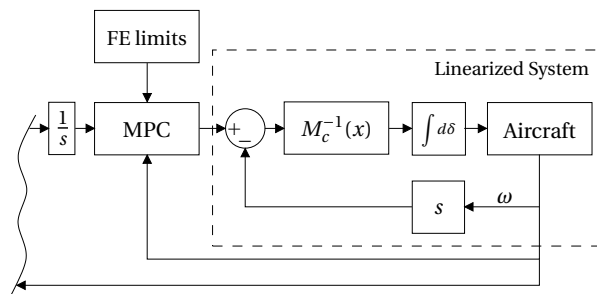


Figure 6.7: Replacing the FCL by MPC+INDI.

Virtual-control Limiting

In the fourth and last candidate, the RCAH FCL is combined with INDI. Again INDI linearizes the system using differentiated angular rate feedback. The linearized system has the virtual-input variables, $v = [\dot{p} \ \dot{q}]^T$. Adaptation of the gains of the FCL is needed, since the output of the FCL changes from δ_e to \dot{q} , but the structure remains the same. FEP is achieved by mapping the state constraint onto angular acceleration constraints using parameter projection and hyperbolic tangent functions. The

control-authority switching logic is copied from the control limiting FEP strategy. Figure 6.8 shows the FEP strategy in a block diagram.

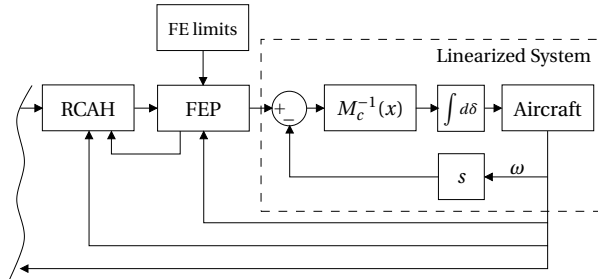


Figure 6.8: Virtual-control Limiting.

6.4.3 Results

The performance of the multiple PID control-limiting, the command-limiting, the CFCL and the virtual-control-limiting FEP systems is shown in Figure 6.9. This figure also shows the input signal in green and the safe flight envelope limits in red. Figure 6.10 shows the performance of the same systems, but now using altered aircraft model parameters. Figure 6.11 shows the effect of sensor noise and Figure 6.12 that of time delays. Figures 6.13 and 6.14 show the aircraft response in the presence of winds gusts and turbulence. The results are discussed in detail in the following section.

6.5 Discussion

6.5.1 Performance

The aircraft response to the earlier defined input using the different FEP systems is shown in Figure 6.9. It should be noticed that the PID control-limiting setup slightly overshoots the envelope limits. This is quite logical since each controller becomes active after the limit is reached and acts only as a hold controller. When using control limiting the safe flight envelope must therefore be chosen conservative. In the command-limiting setup the controllers already act when approaching the limit and prevent overshoots. This results in a smooth intercept of the limits, which is preferable for travel comfort and pilot awareness of approaching flight envelope limits. There is barely any difference between the command-limiting setup and CFCL setup. Using the virtual-control-limiting strategy, the pitch angle also overshoots it's limit. The limit mapping function is more exact than for normal control limiting, however, leading to a smaller overshoot. The velocity limit is handled

using the same hyperbolic tangent functions as used in the command-limiting and CFCL setup, which can clearly be seen from the response. All four controllers do not suffer from integrator windups and control is returned to the pilot immediately after input reversal.

6.5.2 Sensitivity to Parametric Uncertainty

Not only good performance is required, also robustness against modeling errors is crucial for practical use of the FEP system. Figure 6.10 shows the performance of the controllers in the presence of modeling errors. The control limiting setup is reasonably robust, but does get influenced by the uncertainties. Limits are exceeded slightly further and limit transitions, such as from pitch limit to stall speed limit, oscillate more. This fact can be explained by realizing that the mapping from state limits onto control surface deflection limits is largely dependent on the control surface effectiveness. Modifying the control surface effectiveness alters the state change caused by a control surface deflection and would therefore require a change in mapping. The command-limiting, CFCL and virtual-control-limiting setups are not sensitive to the changes in the altered parameters. For these setups the control laws handle the parameter changes and the mapping functions are not influenced. Since the aircraft was not re-trimmed after the model changes, some initial movement can be seen in the first two seconds for all FEP strategies.

6.5.3 Sensitivity to Sensor Noise and Bias

A low-cost system implies using low-cost hardware. Unfortunately low-cost hardware results in more sensor noise and bias. Figure 6.11 shows the performance of the controllers in the presence of these disturbances. Clearly the performance of the control limiting FEP system is unsatisfactory. The reason for this lies in the mapping of the velocity constraint onto the elevator deflection limit. The differential term of this hold controller is quite large and in the presence of sensor noise, this signal blows up. Figure 6.11(b) shows the aircraft response when stall speed protection is disabled for the control-limiting FEP system. The result is considerably better. For the command-limiting setup the added sensor noise and bias hardly influences the response of the aircraft. Even-though sensitivity to noise on the angular rate measurements was expected for the setups using INDI, the figure does not show this. Since the actuator dynamics act as a low-pass filter, the level of noise applied in this test case does not lead to significant problems.

6.5.4 Sensitivity to Time Delays

Besides sensor noise and bias, time delays play a significant role in a low-cost general aviation fly-by-wire system. The influence of time delays on the aircraft response is shown in Figure 6.12. The top Figure, 6.12(a), shows that all systems are hardly influenced by time delays smaller than 50 ms. In the presence of 100 ms time delay and 150 ms time delay, as shown in Figures 6.12(b) and 6.12(c) respectively, problems arise. Both the control-limiting system and the CFCL system show rapid oscillations in the pitch angle. The virtual-control-limiting setup even cause a more sluggish response to the input. All systems do succeed to keep the aircraft within the safe flight envelope, but travel comfort is lost for most of them. Command limiting is influenced the least by the addition of time delays in the system.

6.5.5 Sensitivity to Wind Gusts and Turbulence

Figure 6.13 shows the influence of wind gusts on the aircraft responses. The angle of attack build up after 10 seconds, due to the wind gust, is clearly shown in the response. The FEP controllers prevent the aircraft from exceeding the angle of attack limit, by lowering the nose of the aircraft. The CFCL performs best for this test case, by lowering the nose such that the angle of attack limit is not reached. The command limiting and virtual-control limiting controllers push the nose less far down and this results in a slight overshoot of the angle of attack limit. This behavior comes from a tuning choice in which a trade off is made between the allowance of rapid aircraft responses and strict enforcement of the limitations. The control limiting FEP controller reacts after the limit has been exceeded, but does push the nose down as far as the CFCL controller.

Figure 6.14 shows the influence of turbulence on the aircraft responses. The influence of turbulence on the angle of attack is attenuated by deflections of the elevator. The RCAH FCL clearly rejects the turbulence, as the response of the aircraft is highly similar to the nominal case. All FEP controllers are able to keep the aircraft within the flight envelope limits.

6.5.6 Implications for Small Aircraft

The cost of a FEP system is largely determined by sensor requirements and certification costs. Using predefined flight envelope limits and approximate mapping functions results in low sensor requirements and therefore potential cost savings. In terms of certification the use of predefined limits is also advisable. The choice between application of control limiting, command limiting, CFCL and virtual-control limiting is influenced by certification considerations as well. CFCL has a lower

functional visibility, mainly due to the use of a QP-solver in the MPC controller, and therefore requires a more extensive certification procedure than the other controllers [95]. In both INDI setups matrix inversion is required, which is potentially numerically unstable. Since a linear relation is assumed between the aerodynamic moment and the control surface deflections and cruise condition is selected as the operating point, this is not a problem for the presented test case, however. A smaller part of the total cost is determined by flight control system hardware. Using CFCL poses a higher demand on processing power than using PID controllers, which means more expensive hardware is needed.

6.5.7 Scope of the Test Case

The ultimate goal of a practical FEP system is of course to be used in real flight. In the SAFAR project, the objective is to install low-cost FBW technology in a Diamond DA 42 demonstrator aircraft. As a first step the FBW system will be switched on during cruise flight and a conservative set of limits will be used. On this platform, a RCAH FCL combined with a FEP system will aim to make flying this small aircraft easier and more safe. This chapter contributes to the selection of that FEP system.

The test case presented in this chapter therefore suits the needs of the project. Would the FBW system be used for full flight, additional requirements are posed on the FCL and RCAH may not be a good choice anymore. This will have impact on the mapping functions used in the FEP systems and may lead to different results. Also the degree of nonlinearity of the model will increase, making the INDI-based systems potentially more beneficial.

6.5.8 Future Investigations

Should installment of FBW and FEP contribute to decreasing the rate of handling and control accidents in cruise flight, focus can be diverted to the next major source of accidents. In general aviation as well as commercial aviation, planning and decision errors are responsible for a large part of the accidents. Much attention is already given to solving these issues in the commercial aviation sector and future investigations are needed in what way these solutions are applicable to the small aircraft market.

On the other hand, many non-fatal accidents occur during the landing phase. Before personal air transportation is an option, this figure must also be reduced drastically. In commercial aviation auto-land systems are installed to prevent landing phase accidents. This solution requires the support of costly airport services,

however. A typical airport where a general aviation aircraft will land, lacks this support and therefore future investigations are needed in how an auto-land system can be developed for the small aircraft market.

6.6 Conclusions

This chapter presents a study of Flight Envelope Protection (FEP) techniques for small aircraft. A comparison is made between a Proportional-Integral-Derivative (PID) based control-limiting approach, a command-limiting approach, an approach using a Constrained Flight Control Law (CFCL) in the form of Model Predictive Control (MPC) combined with Incremental Nonlinear Dynamic Inversion (INDI) and a virtual-control-limiting approach using INDI. All four controllers perform well when there are no model uncertainties present. However, full certainty is hardly the case when a low-cost system is considered. Model parameters are altered up to 40% and the test case is rerun without adapting the controllers. Command limiting, CFCL and virtual-control limiting proved far less sensitive to parametric changes than the control-limiting setup. Similar results are obtained when sensor noise and bias is considered. Especially the stall speed protection of the control limiting system proved highly sensitive to sensor noise and bias. In the presence of time delays only command limiting keeps performing well. The FEP controllers are all able to deal with atmospheric conditions, such as wind gusts and turbulence. Robustness against off-nominal conditions is not the only prerequisite for a well-functioning low-cost FEP system, however. When looking at hardware and certification requirements, command limiting and control limiting are potentially less expensive than CFCL and virtual-control limiting. Weighing all these considerations leads to the conclusion that command limiting is the preferred option for the chosen test case.

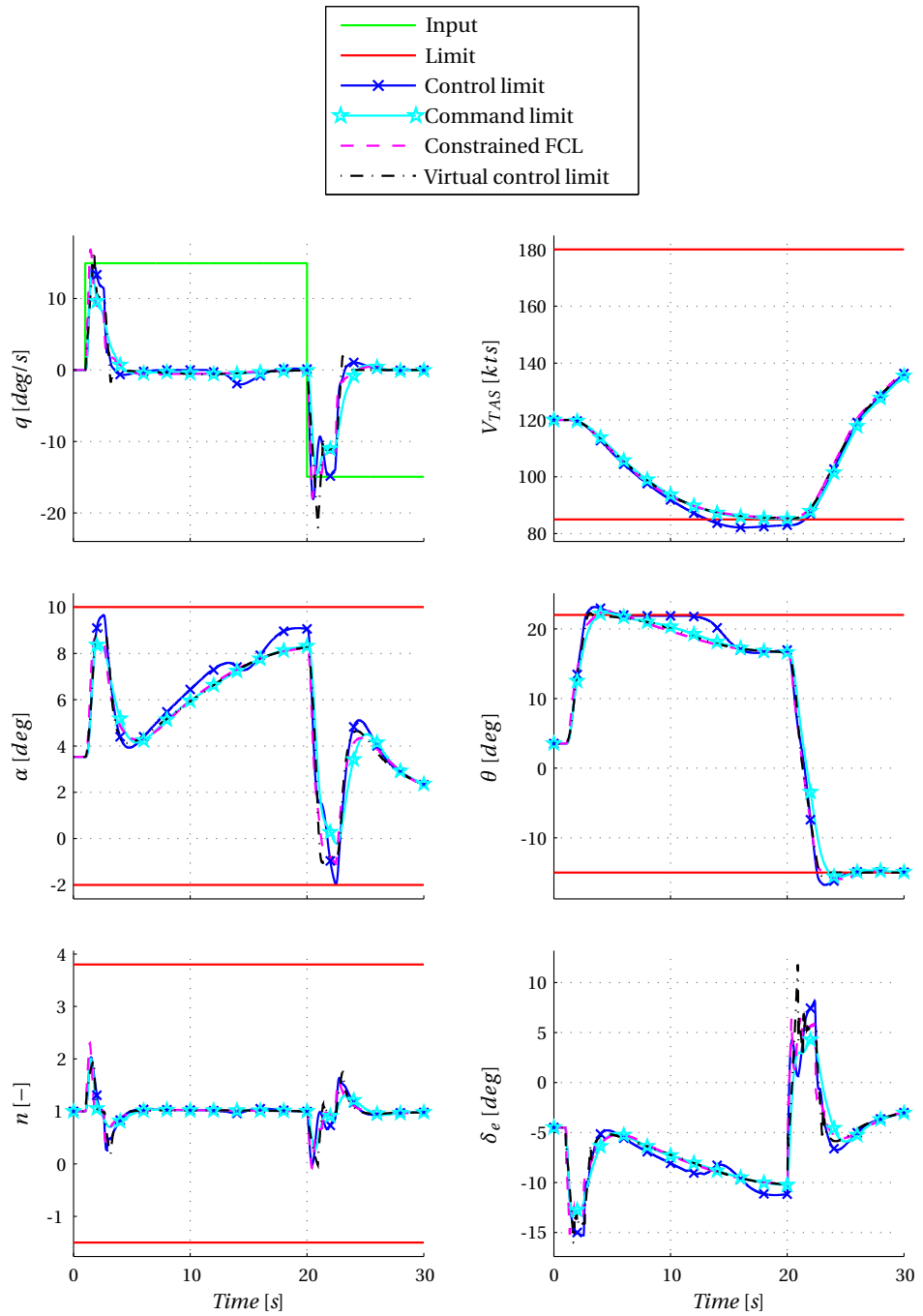


Figure 6.9: Aircraft response using different FEP strategies.

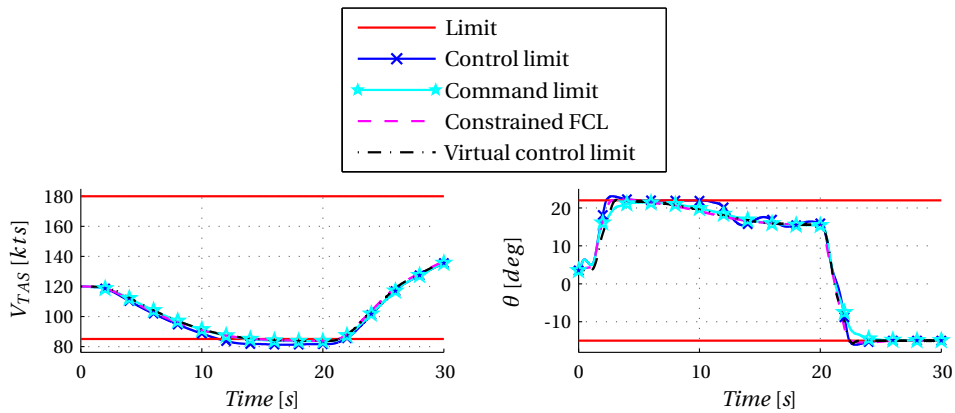
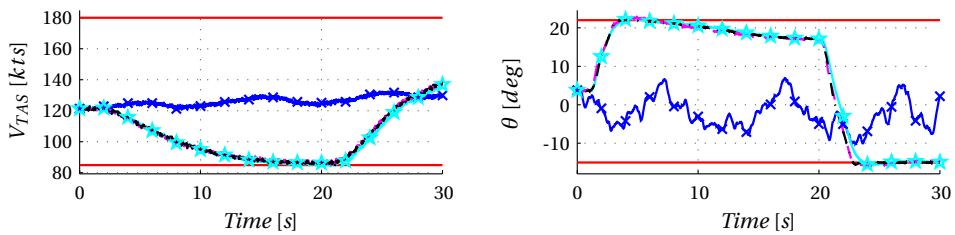
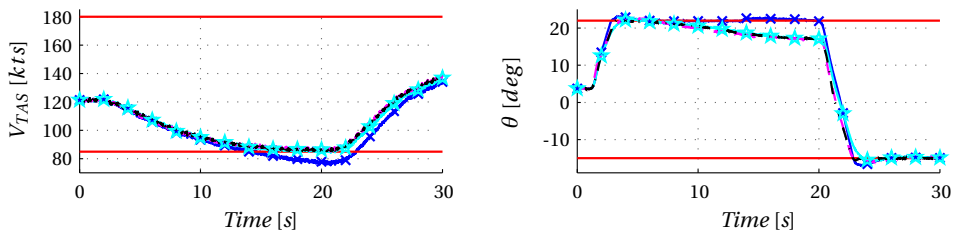


Figure 6.10: Aircraft response using different FEP strategies, sensitivity to parametric uncertainty.



(a) Control limiting with stall speed protection.



(b) Control limiting without stall speed protection.

Figure 6.11: Aircraft response using different FEP strategies, sensitivity to sensor noise.

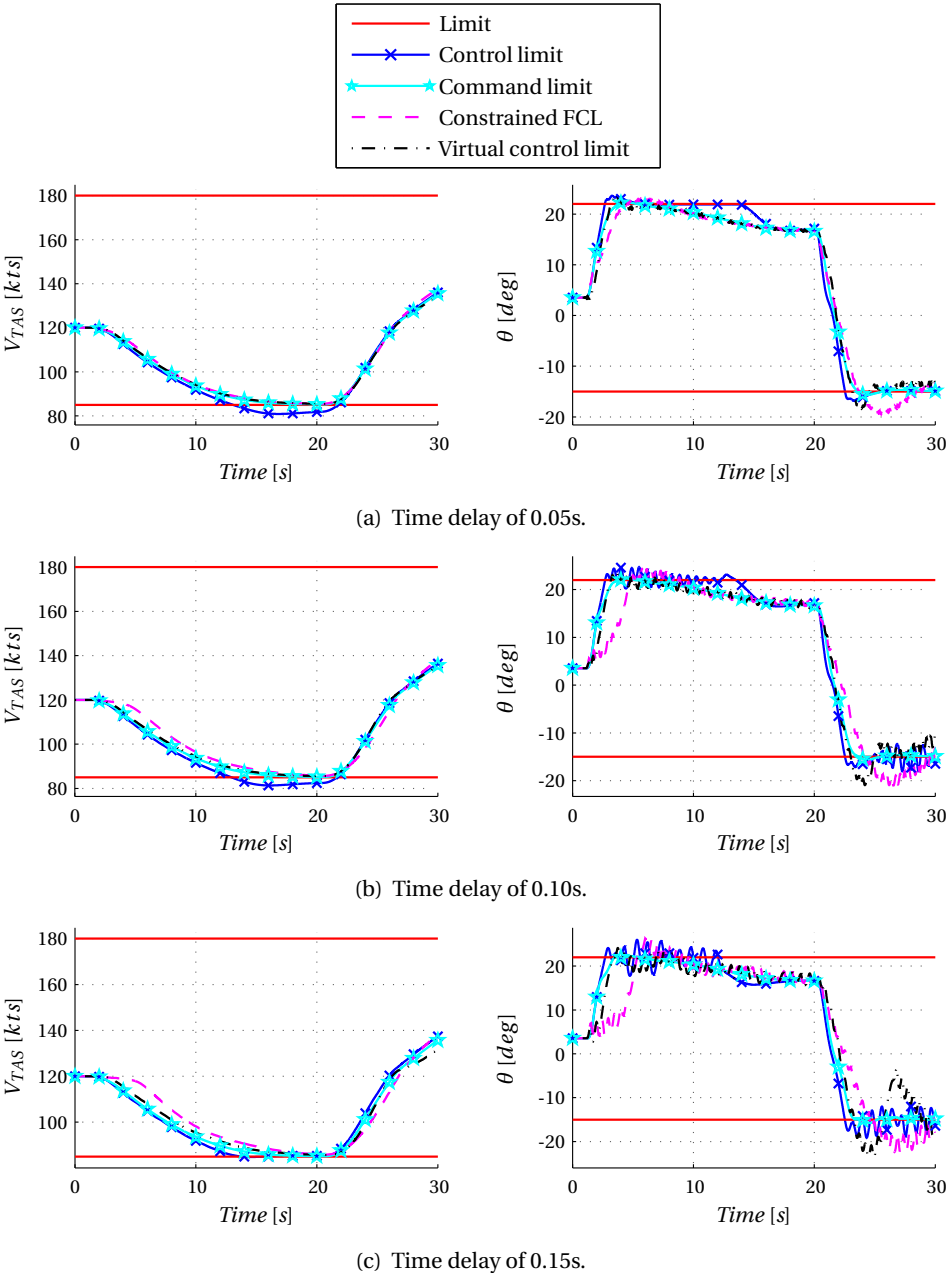


Figure 6.12: Aircraft response using different FEP strategies, sensitivity to time delay.

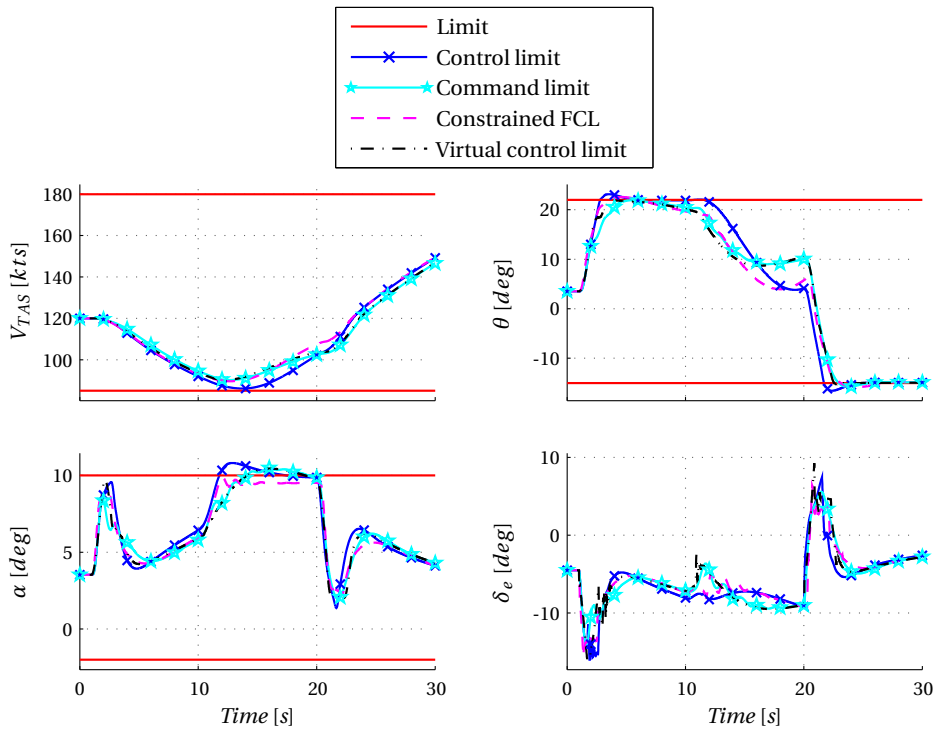


Figure 6.13: Aircraft response using different FEP strategies, sensitivity to wind gusts.

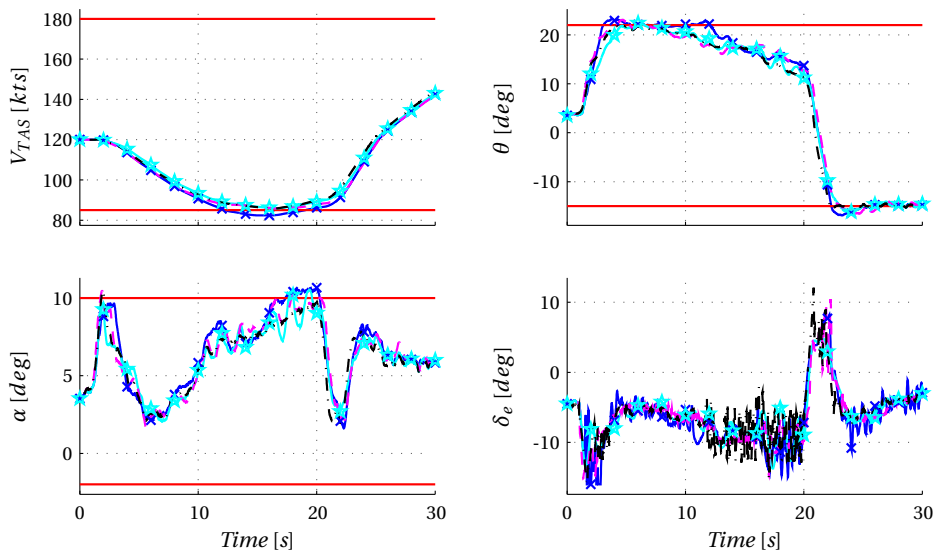


Figure 6.14: Aircraft response using different FEP strategies, sensitivity to turbulence.

EVALUATION

Abstract

This chapter shows a comparison between the Flight Control Laws (FCLs) developed using a classical method in Chapter 4 and a nonlinear method in Chapter 5, called the Sensor-Based Backstepping (SBB) controller. This comparison is done using faster than real-time simulations of the aircraft model developed in Chapter 2 combined with the Fly-By-Wire (FBW) platform presented in Chapter 3. Several aspects are reviewed in this chapter that the FCLs will face in reality, namely sensitivity to parametric uncertainty, sensor noise, disturbances and time delays. Performance is compared using Handling Qualities (HQs) for the manually controlled FCLs and other performance metrics for automatic FCLs. The chapter also briefly comments on design effort and certifiability of the FCL designs. Besides the offline FCL comparison, this chapter shows an exploratory study into the acceptance and appreciation of the manually controlled classical FCL design. This online (pilot-in-the-loop) evaluation is done using a single certified DA 42 test pilot and shows starting points for future statistical representative experiments needed to draw general conclusions on the online quality of the FCL designs.

7.1 Introduction

This chapter compares and evaluates the Flight Control Laws (FCLs) developed in Chapters 4 and 5. Section 7.2 presents the main part of this comparison, which is done offline, using faster than real-time simulations of the different FCLs combined with the aircraft model of Chapter 2 and the FBW platform of Chapter 3.

The success of a FCL design is determined not only by objective offline simulations, but also subjectively by the end user, i.e., the pilot. If they do not accept and appreciate the design, it will not be used. Due to time constraints, a statistical representative study into the acceptance of the FCL designs by general aviation pilots is beyond the scope of this thesis. Instead, Section 7.3 presents an exploratory study into the acceptance of one of the manually controlled FCL designs, by a certified Diamond DA 42 test pilot.

7.2 Offline Performance Comparison

To be able to answer the main research question of this thesis it is important to look at multiple aspects of each FCL design. This section investigates the sensitivity to uncertainties, sensor noise and bias, time delays and atmospheric disturbances of the FCL designs, thereby providing insight into the robustness and the performance degradation in off-nominal situations. The nominal performance is compared using the performance metrics described in Section 4.3 and also the differences in design effort and certifiability of the designs are investigated. This section ends with the comparison of the FCL designs in case of failures. Chapter 6 already showed that for Flight Envelope Protection (FEP) a nonlinear FCL does not present advantages (nor disadvantages) and therefore FEP is not a deciding factor in the FCL design choice.

Four FCL designs will be compared in this section. The first is the ATT mode described in Section 4.6 and is referred to as the PID control law. The second is the Sensor-Based Backstepping (SBB) FCL introduced in Section 5.6.4 and is called the SBB control law. In order to make a fair comparison, the SBB controller is given access to the same sensor suite as used for the PID FCL. This means the derivatives of the angular rate measurements are used rather than direct measurements of the angular accelerations in the SBB FCL evaluation. The third and fourth FCL designs are the PID NAV mode and the SBB NAV mode respectively. These latter two designs will only be compared using the performance metrics presented in Section 4.3.2.

7.2.1 Sensitivity to Parametric Uncertainty

To test the sensitivity of the FCLs to parametric uncertainties either the aircraft model can be altered, or in the extreme a model of an entirely different aircraft can be used. In both cases the FCL designs are not changed and this procedure will therefore give insight in the FCL behavior in case reality differs from simulation. The Delft University of Technology is co-owner of a Cessna Citation II, for which a high fidelity dynamic model is available [128]. Although not a small aircraft, compared to the Diamond DA 42, it is comparable in dynamic behavior. This aircraft is also inherently stable and controlled using aileron, elevator and rudder deflections and a power lever angle setting. Application of the FCLs on the Citation will not only provide information on the sensitivity to parametric uncertainties, but also on the usability of the FCLs on a range of small aircraft.

Figures 7.1 and 7.2 show the lateral and longitudinal motion respectively of the Cessna Citation II, trimmed at 180 kts and 6,000 ft and controlled by the PID and SBB FCLs. Although both controllers remain stable, the SBB controller has better tracking performance than the PID controller. Also in terms of control effort the SBB controller is preferred. Actually, the results obtained using the SBB controller are quite extraordinary and the SBB controller can be seen as a first step towards a plug-and-play type controller.

7.2.2 Sensitivity to Sensor Noise and Bias

This section compares the sensitivity of both FCL designs to sensor noise and bias. The description of the sensors used on the FBW platform can be found in Section 3.2.4. Results are shown in Figures 7.3 and 7.4. The SBB controller is a high bandwidth controller that relies on fast changes in the input to stabilize the error dynamics. It is therefore inherently susceptible to high bandwidth noise. The PID controllers are designed with noise attenuation in mind, yet the figures show that both FCLs are nearly equally sensitive to sensor noise. The reason for this lies in the integrating action and the anti-windup scheme of the SBB controller and of course the actuator dynamics of the FBW platform, all acting as noise attenuators on the input signal. From a noise sensitivity perspective the PID FCL is preferred, but the advantage over the SBB FCL is small.

7.2.3 Sensitivity to Time Delays

As explained in Chapter 3 time delays are a property of a general aviation aircraft FBW platform that cannot be neglected. Both controllers have been synthesized using expected values for each time delay source. This section will investigate the

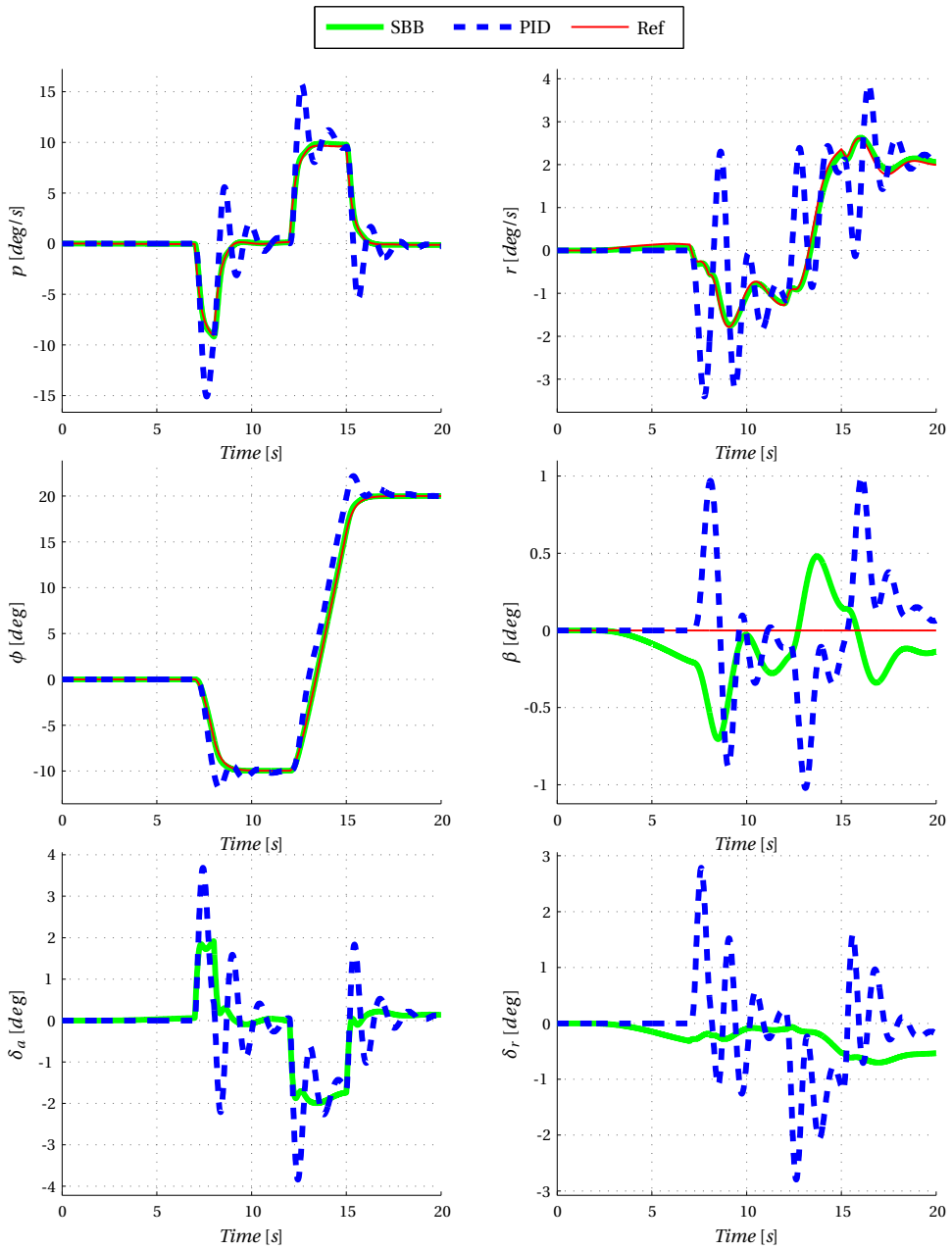


Figure 7.1: Time history of the lateral motion of the Cessna Citation II controlled by the PID and SBB FCLs.

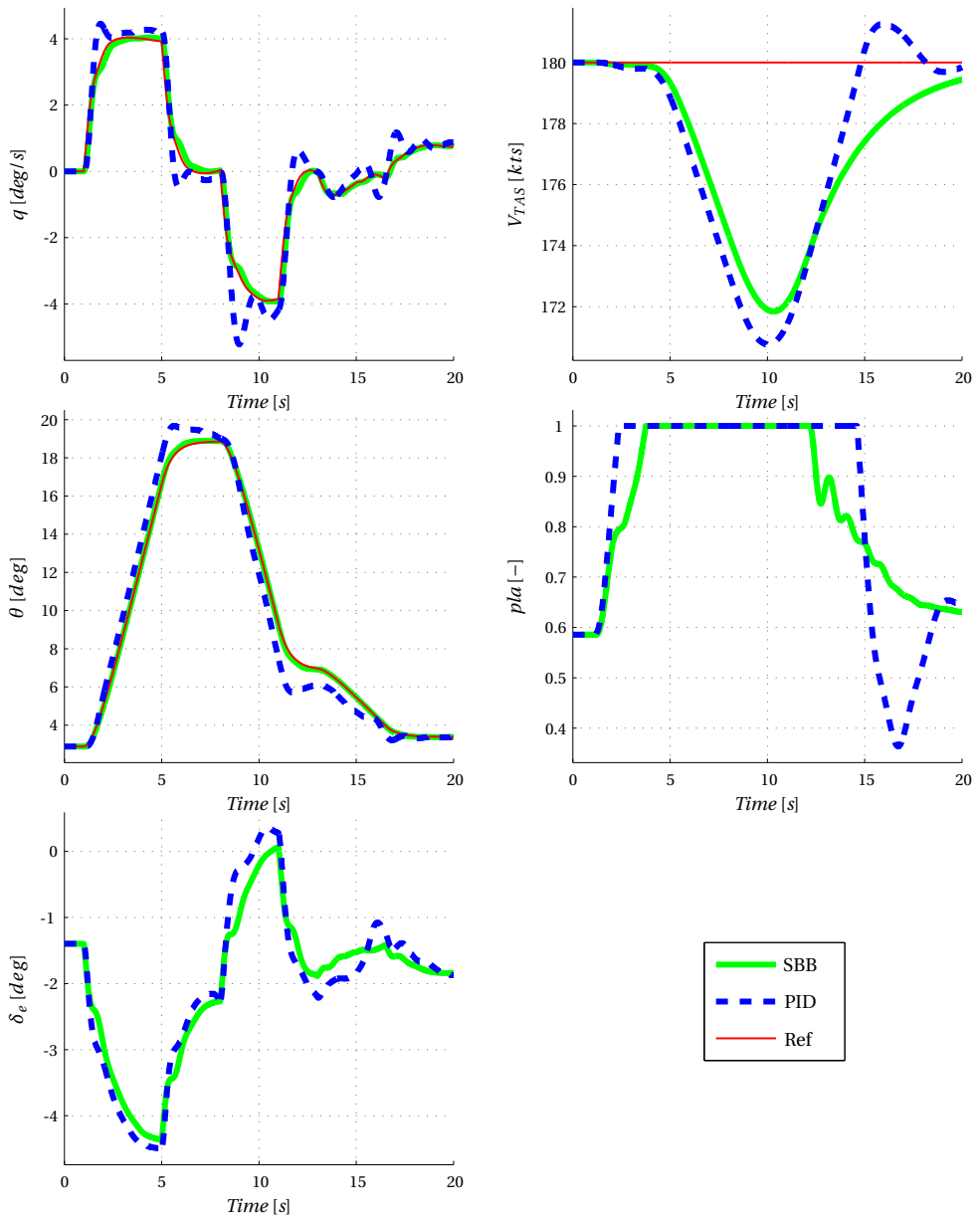


Figure 7.2: Time history of the longitudinal motion of the Cessna Citation II controlled by the PID and SBB FCLs.

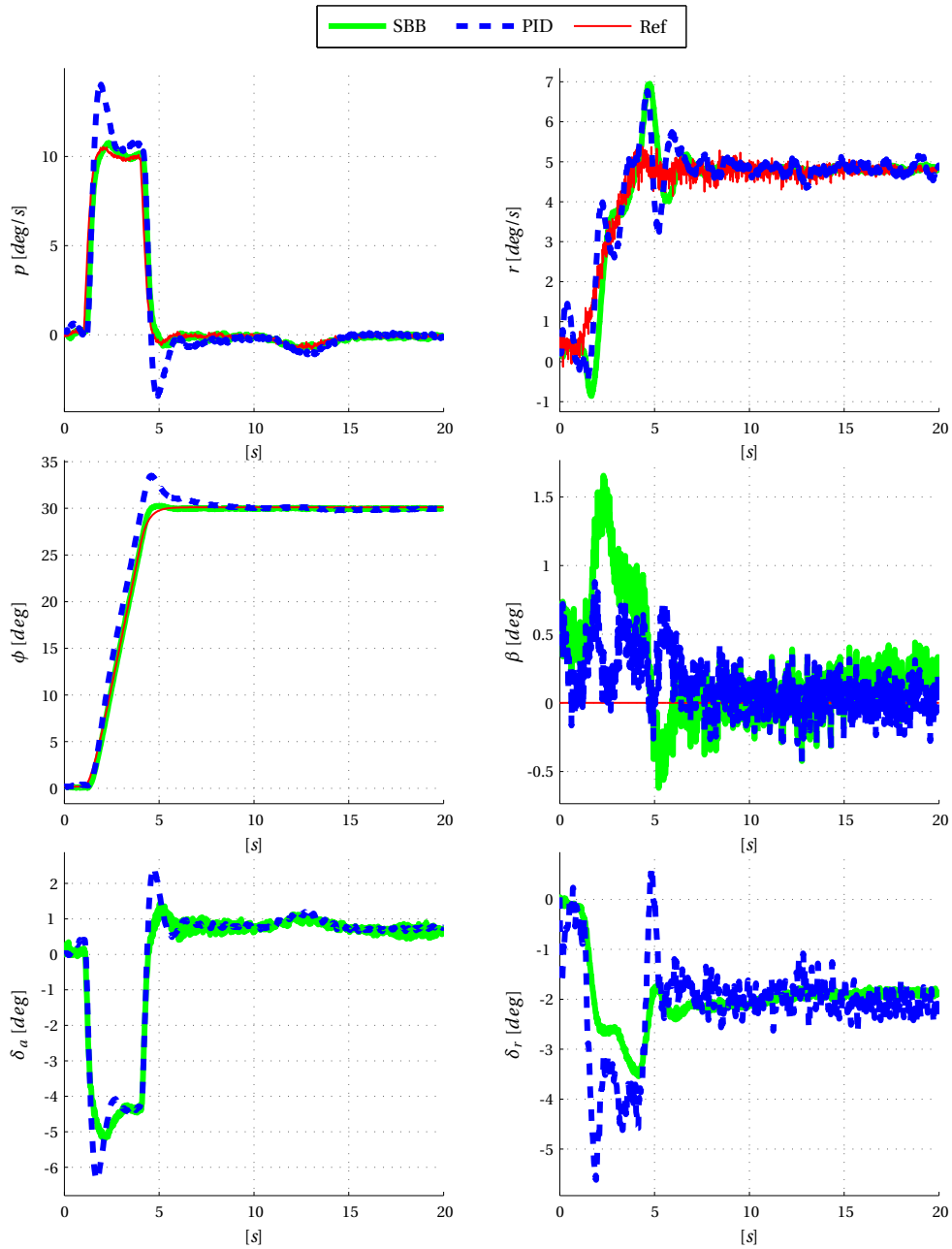


Figure 7.3: Time history of the lateral motion of the Diamond DA 42 with sensor noise and bias controlled by the PID and SBB FCLs.

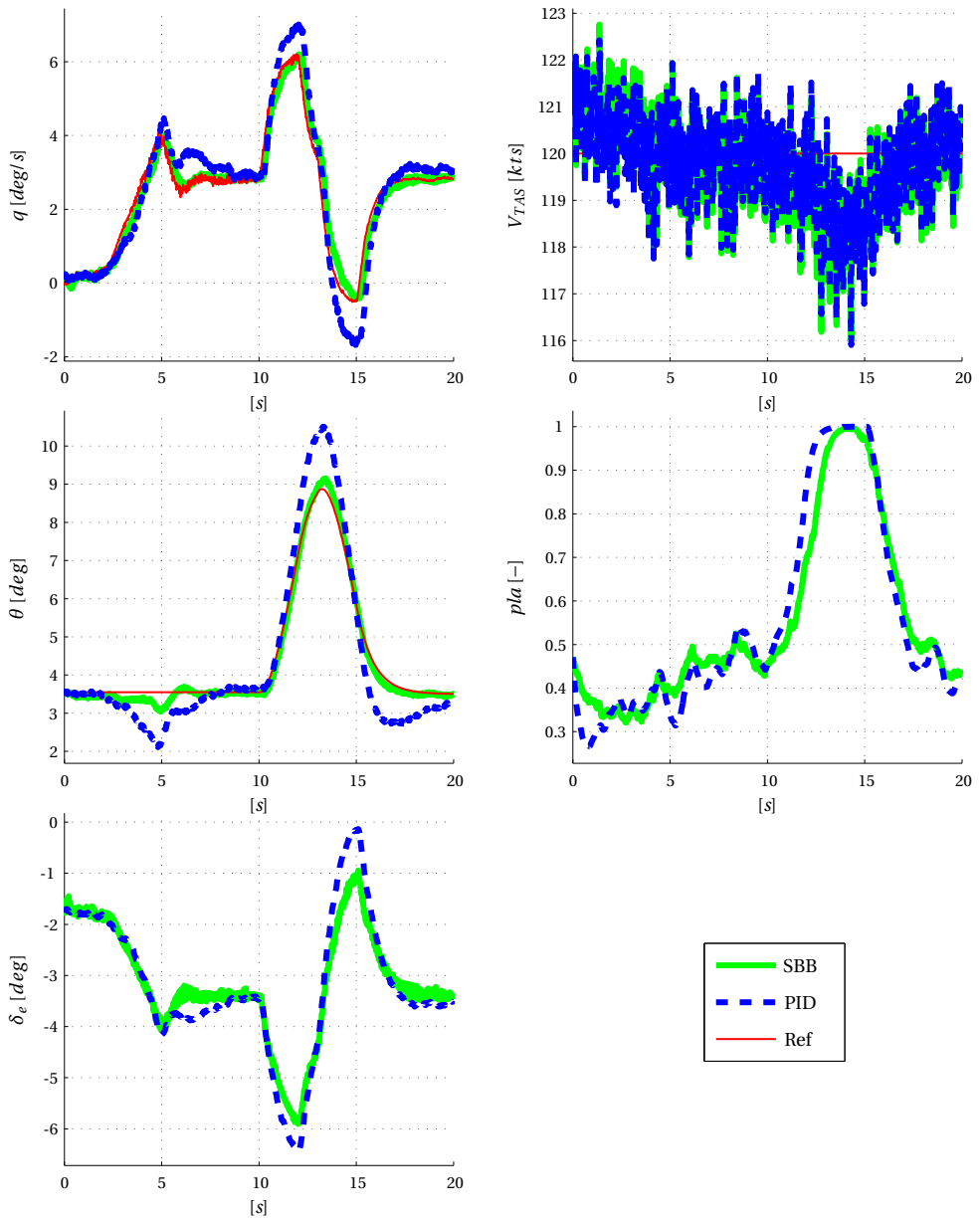


Figure 7.4: Time history of the longitudinal motion of the Diamond DA 42 with sensor noise and bias controlled by the PID and SBB FCLs.

behavior of the FCLs in the presence of extreme time delays. The extreme delays are chosen as $3t_s$ reference delay, $3t_s$ actuator delay and $7t_s$ measurement delay, in which $t_s = 16$ milliseconds is the time step for each platform update cycle. The total time delay in the system is 208 ms in this case. These delays are extreme for FBW platforms used in commercial aviation, but could be encountered in control of a UAV [81].

Figure 7.5 and 7.6 show the effect of these extreme time delays on the performance of the FCL designs. Both designs show increased oscillations, where for the SBB FCL this increase is larger than for the PID FCL. However, re-tuning the FCLs to improve performance requires adaptation of all gains in case of the PID FCL and changing only the anti windup parameter H in case of the SBB FCL.

7.2.4 Sensitivity to Wind Gusts and Turbulence

Turbulence and wind gust are atmospheric disturbances acting on the aircraft that should be rejected by the FCL designs. The dynamic models for turbulence and wind gusts can be found in Section 2.3.2 and the intensity in this offline simulation is set to “moderate” as defined by MIL-F-8785C. The wind gust is set to start after 5 seconds, with an onset length of $[d_x \ d_y \ d_z] = [120 \ 120 \ 80]$ meters and an intensity of $[u_g \ v_g \ w_g] = [3.5 \ 3.0 \ 3.0]$ m/s.

Figures 7.7 and 7.8 show the response of the DA 42 in turbulent air to both FCL designs. The influence of the wind gust is barely visible in the response and the turbulence is rejected adequately by both designs. In pitch control the PID controller is favorable, since this FCL generates smoother elevator commands, but at the cost of slightly lower tracking performance.

7.2.5 Handling Qualities

The ATT mode developed in SAFAR is a manually flown mode and therefore performance metrics can be specified in the form of Handling Qualities (HQs) as discussed in Section 4.3.1. Sections 4.6.5 and 5.6.6 show the handling qualities for the PID and SBB FCLs respectively and for better comparison this section presents a combination of the figures shown in those sections.

Figures 7.9 and 7.10 show the handling qualities of both FCL designs. Laterally the HQs are similar, except for the roll subsidence mode time constant, which is slightly higher for the SBB controller and the roll oscillations which are lower for the SBB controller. Both of these qualities can also be seen in the roll angle response of Figure 7.7, i.e., PID is slightly faster than SBB, but also has more overshoot. The

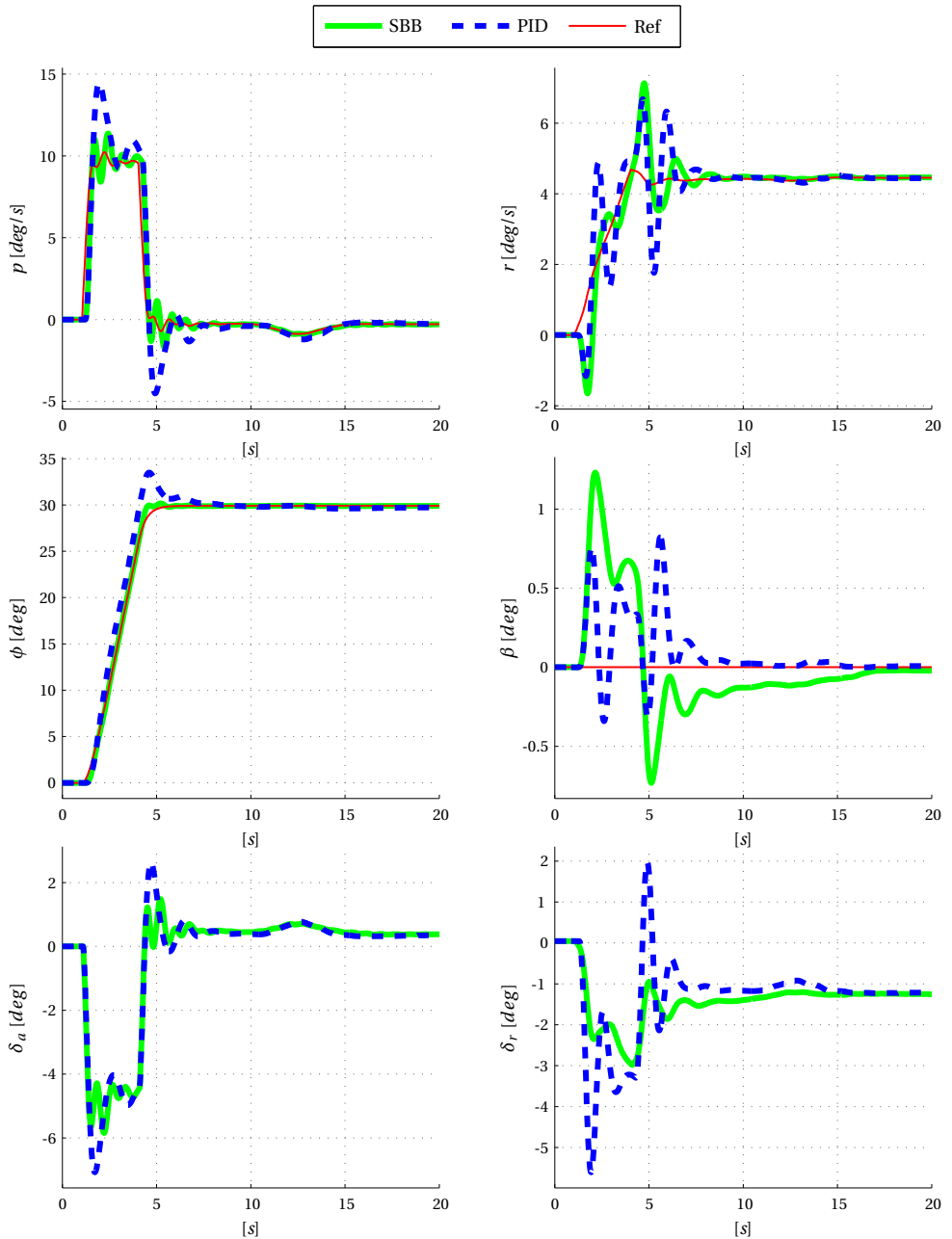


Figure 7.5: Time history of the lateral motion of the Diamond DA 42 with extreme time delays controlled by the PID and SBB FCLs.

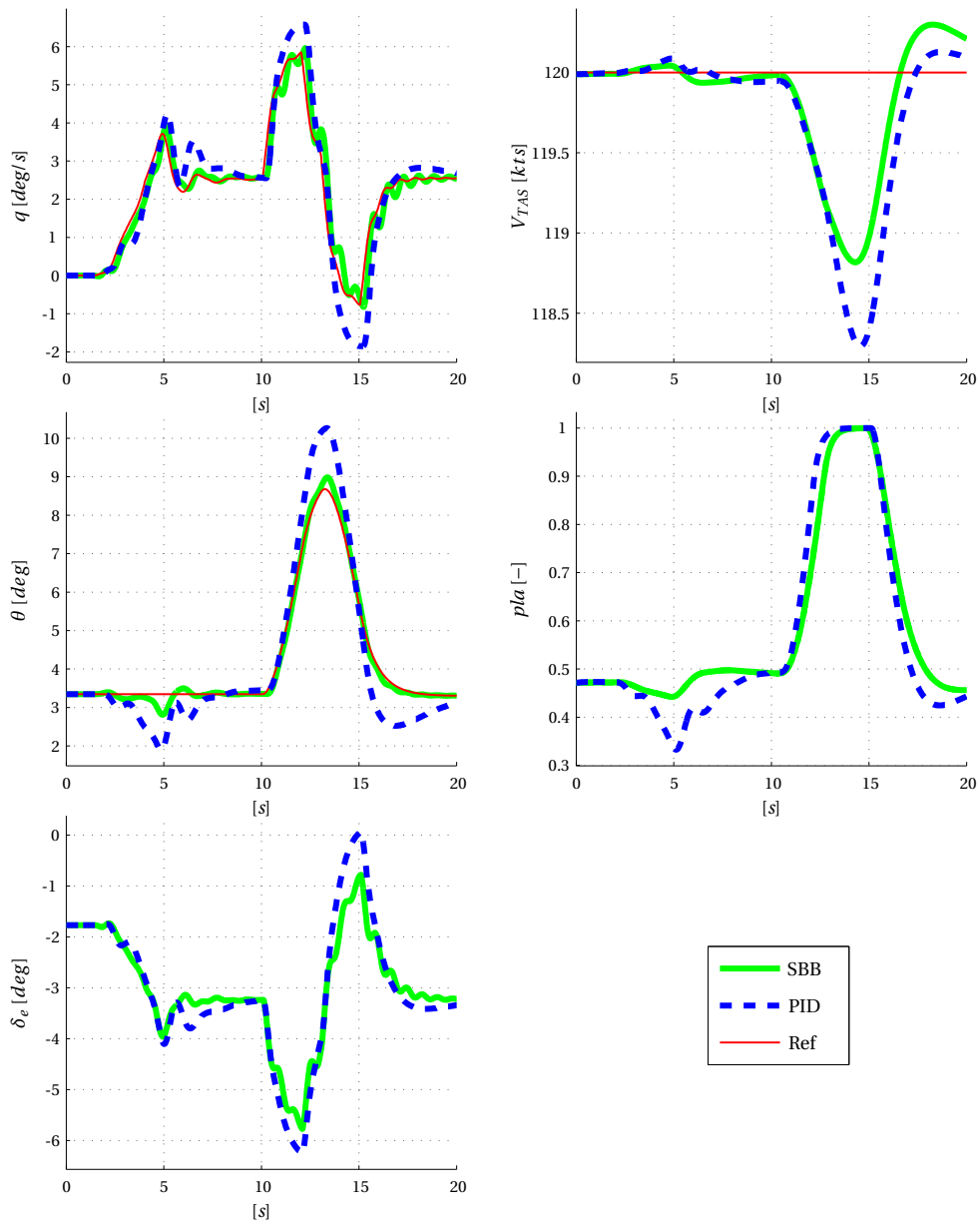


Figure 7.6: Time history of the longitudinal motion of the Diamond DA 42 with extreme time delays controlled by the PID and SBB FCLs.

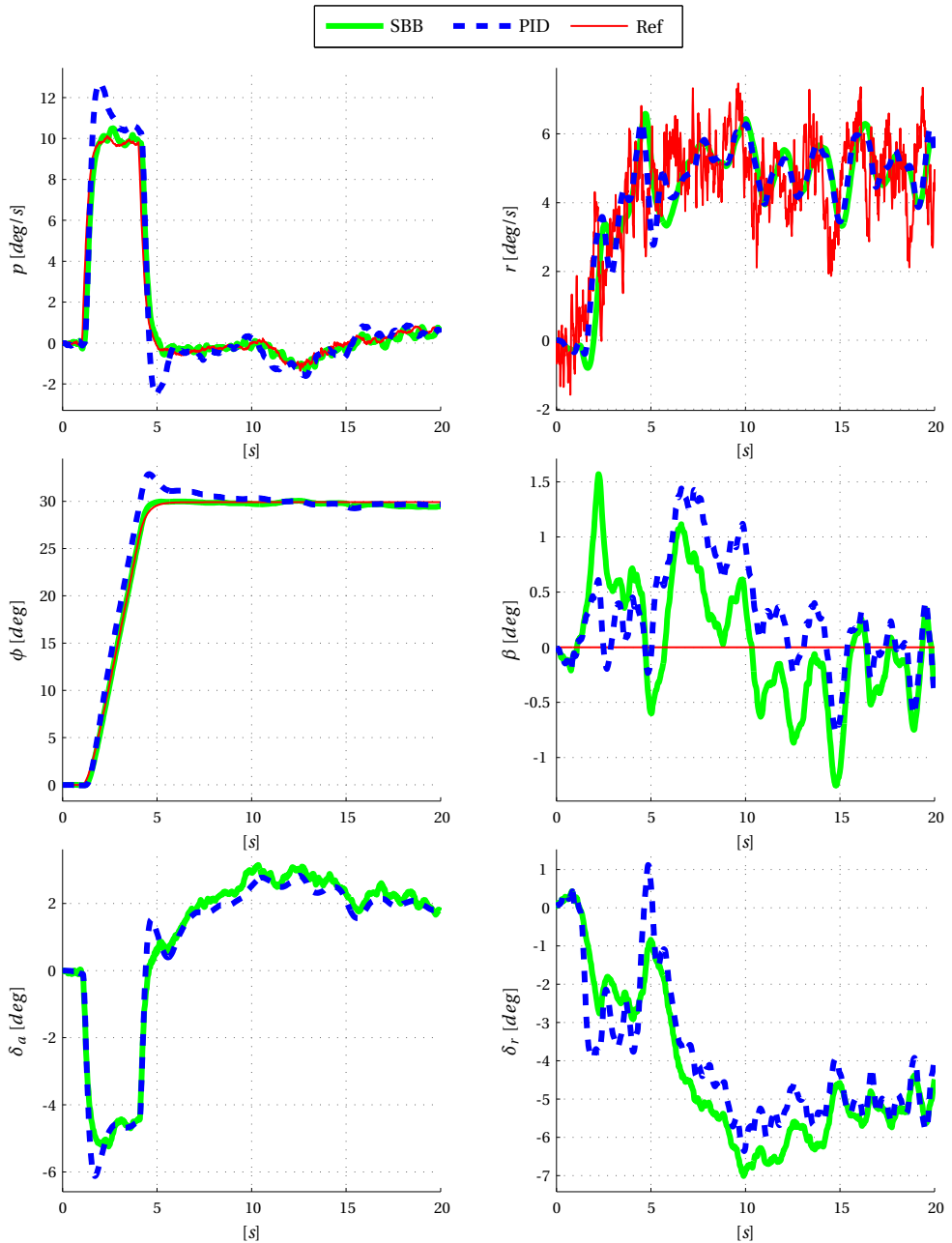


Figure 7.7: Time history of the lateral motion of the Diamond DA 42 with gust and turbulence controlled by the PID and SBB FCLs.

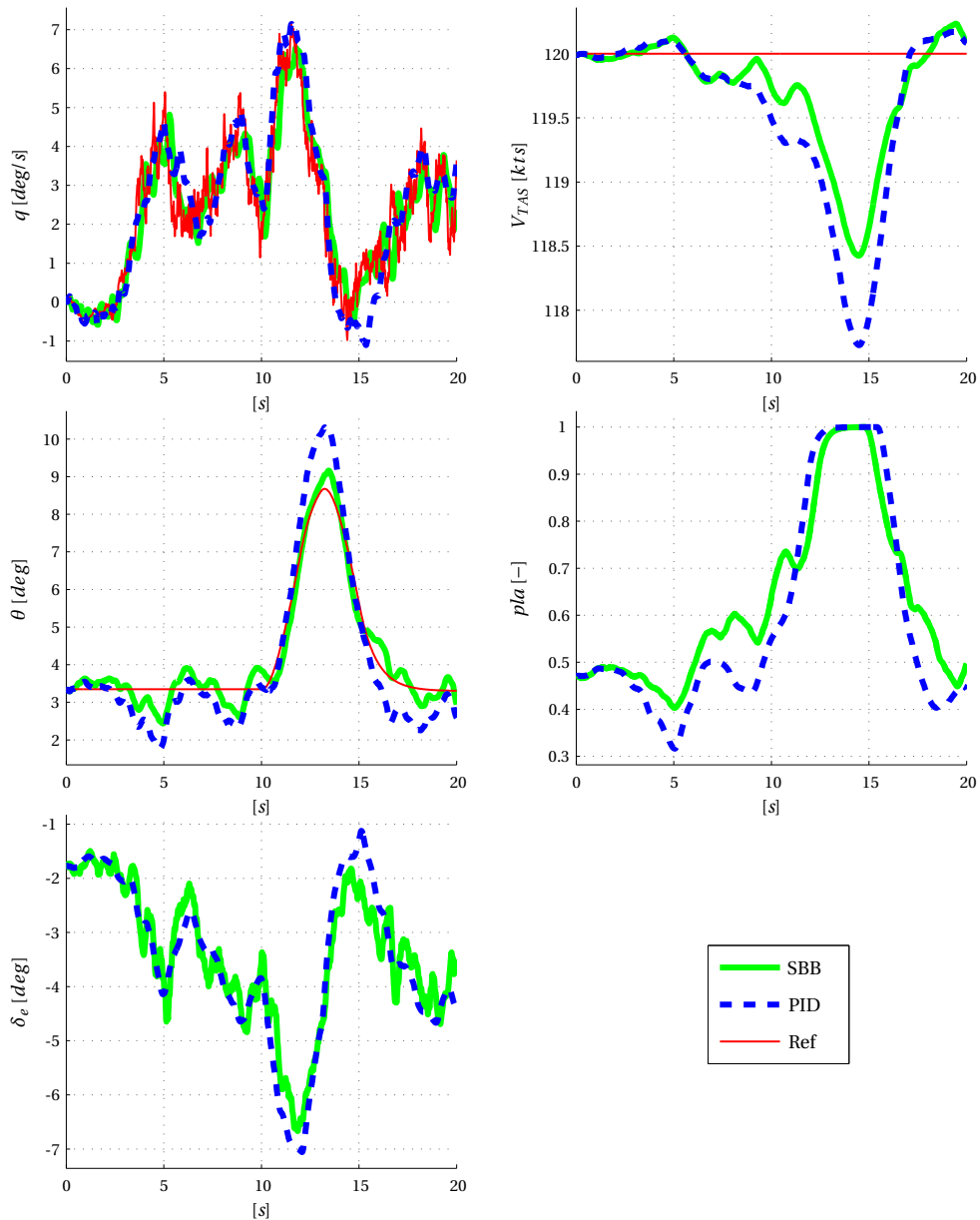


Figure 7.8: Time history of the longitudinal motion of the Diamond DA 42 with gust and turbulence controlled by the PID and SBB FCLs.

longitudinal HQs show that both FCLs remove the phugoid and result in the same equivalent time delay. The main difference is shown in the pitch damping. The SBB controller results in an over-damped response and the PID in an under-damped one. Both are acceptable from a HQ perspective though.

7.2.6 Performance Evaluation of the NAV Law

The NAV mode developed in SAFAR is an automatic FCL mode and therefore performance metrics can be used, that are specified in Section 4.3.2. Sections 4.6.6 and 5.6.7 show the performance metrics for the PID and SBB FCLs respectively and this section presents a combination of the tables presented in these sections.

Table 7.1 shows that similar performance can be obtained by using either PID or SBB for the NAV law. The choice of FCL design method will therefore not depend on the ability to expand the RCAH control to an automatic FCL mode, such as the NAV law.

Table 7.1: NAV law performance.

Metric	PID		SBB	
	V-NAV	H-NAV	V-NAV	H-NAV
Rise time [s]	3.2	5.4	3.8	9.4
Settling time [s]	23.8	9.8	6.3	16.8
Overshoot [%]	12.2	0.9	0.8	0.7
ISE [ms]	1.7	2.3	2.8	4.7
ITEA [ms]	31.3	25.5	9.0	33.4
M [-]	0.49	0.25	0.04	0.43

7.2.7 Design Effort

Although, the design effort of a FCL is only for a small part related to the adjustment or fine-tuning of the gains, this section comments on the gain selection procedures of both ATT mode FCL designs. A considerable part of the design effort is spent on certification, which is the topic of the next section [87].

The PID FCL uses 11 gains and 6 filters, such as lead-lag filters, low-pass filters and washout filters. Two of the gains are scheduled for altitude and velocity to obtain desired handling qualities. When an optimization problem is formulated using a cost function depending on the tracking error, noise attenuation and disturbance rejection, it will be non convex and minimizing the cost function is not straight forward.

7. EVALUATION

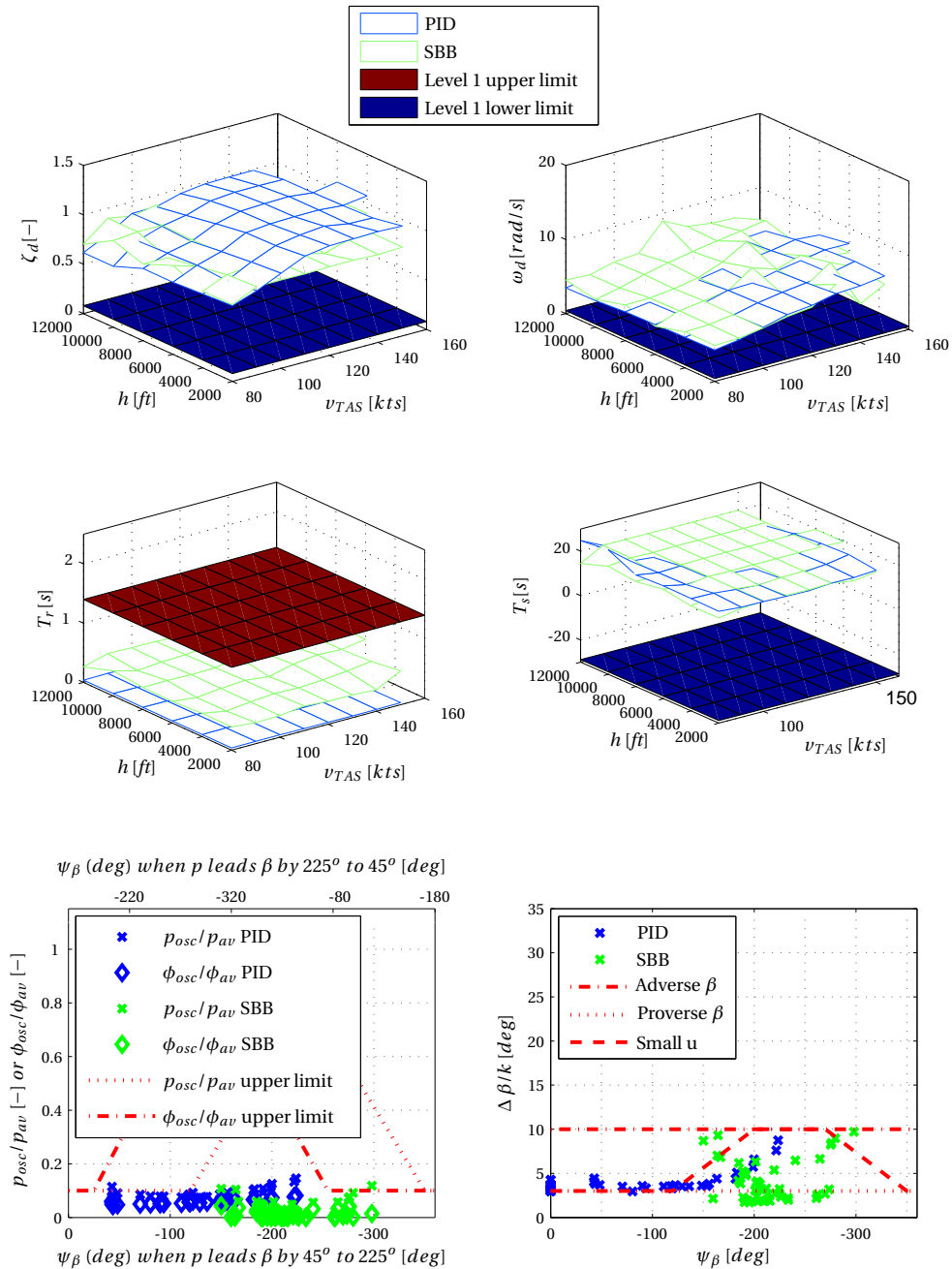


Figure 7.9: Lateral Handling Qualities of the Diamond DA 42 with PID or SBB.

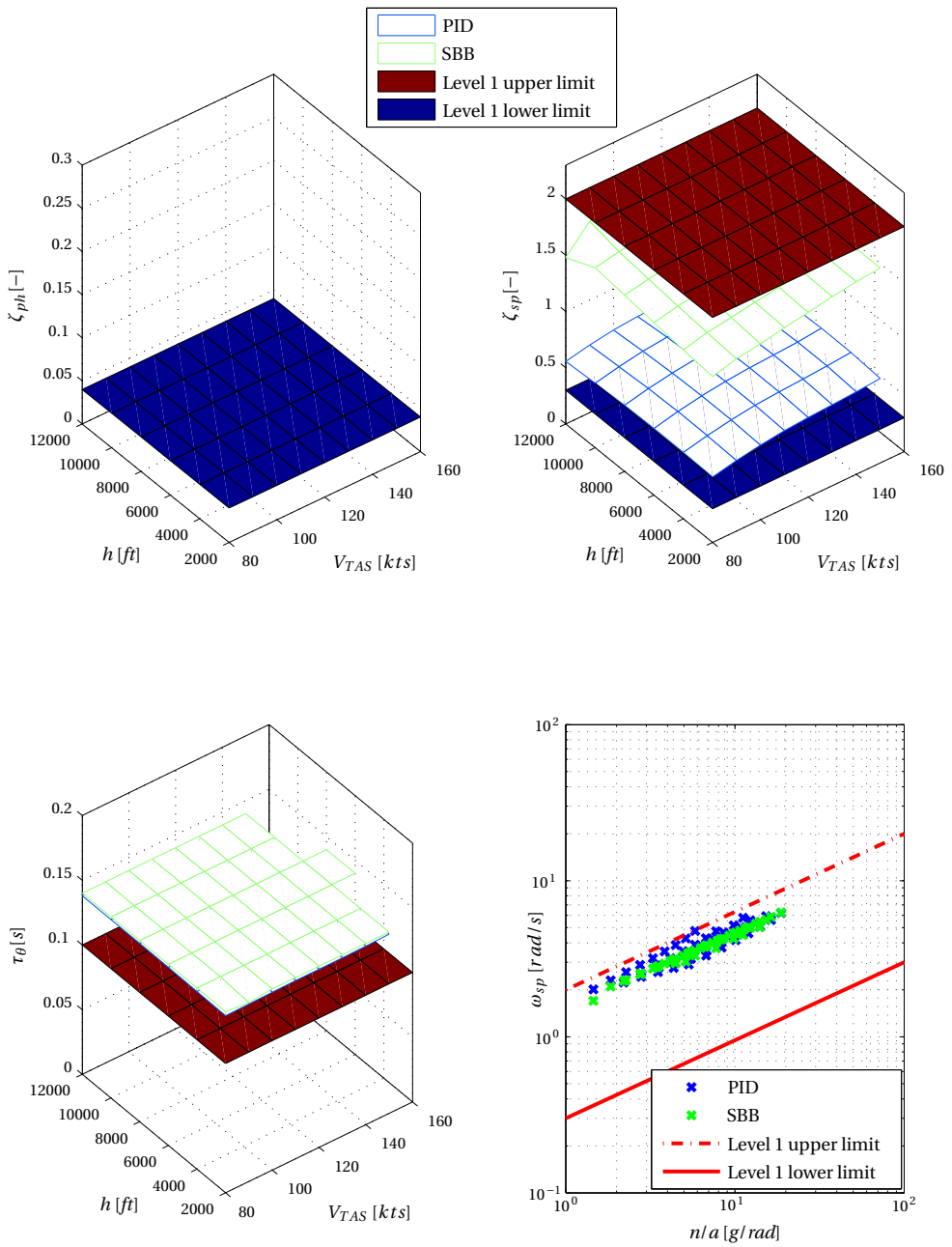


Figure 7.10: Longitudinal Handling Qualities of the Diamond DA 42 with PID or SBB.

The SBB FCL uses 17 gains and 2 low-pass filters for command filtering. The gains consist of two values for ϵ , three values for c_1 in the first step of the RCAH part of the SBB controller, three values for the second step k and if used three values for the integrating error k_I . For the autothrottle part of the SBB controller two gains are used and the remaining four gains are used in the anti windup scheme. When using engineering judgment it is easy to tune these gains by trial and error.

From the above description it can be concluded that the design effort for the SBB controller is lower, but not because it has fewer gains to tune. The sensitivity of the tracking performance, noise attenuation, disturbance rejection and time-delay robustness on the gain values is lower for the SBB FCL, making it more straightforward to select rough gain values by trial and error. This characteristic of the SBB method also shows in Section 7.2.1, where the FCL tuned for the DA 42 also performs well on the Citation.

7.2.8 Certifiability

Section 3.5 commented on the certification of FCLs. Intuitively one would say that certification of the classical FCL is less work than certification of the SBB FCL. However, the SBB controller for a system with relative degree one has an equivalent PI form, as described in Section 5.6.2, which could be interpreted as yielding an equal amount of work required for certification. The RCAH controller and sideslip compensator have a relative degree of two, resulting in a nonlinear feedback part in the FCL design. Future work should show whether this nonlinear part can also be achieved using gain scheduling. In that way an “equivalent” PI form may still be found. Other immediate obstacles in certification are not foreseen and starting the contact with the certification authorities is therefore recommended. It should be noted that the SBB controller has no adaptation, which is known to result in certification problems [55].

7.2.9 Fault Tolerance

One of the targeted advantages when installing a FBW platform on an aircraft, is improving flight safety. A measure to improve safety, named FEP, was already discussed in Chapter 6. Another measure to improve safety is the ability of a FCL to react quickly in case of failures. This section shows whether both FCLs are able to cope with an engine out scenario. Such a failure is not uncommon in general aviation and can lead to fatal accidents.

Figures 7.11 and 7.12 show the response of the aircraft influenced by either FCL, with an right engine failure after 10 seconds. Since the sideslip is compensated,

the rudder immediately deflects when the thrust becomes asymmetric. Also the pitch and roll angles are held by deflecting the ailerons and elevator. Finally, the power lever angle of the left engine is increased to maintain velocity. In summary, the aircraft continues flying without required interaction of the pilot. However, the operating envelope of the aircraft has shrunk due to the failure and when pulling up the engine is not able to maintain the velocity. It would therefore be dangerous if the pilot is unaware of the engine failure. The reduction in flight envelope should be communicated to the pilot, for example by showing the new safe flight envelope on the primary flight display accompanied by a warning that the engine has failed. The design of such a display is left for future work, however.

7.3 Exploratory Acceptance Study

The previous section showed a comparison between the PID and SBB FCLs based on offline simulations. As mentioned in the introduction, the success of a FCL design is determined not only by objective measures, but also by the opinion of the end users. An FCL, including FEP, is designed to change the dynamic behavior of the aircraft as seen from the pilots perspective. This change in human-machine interaction should therefore be examined during the FCL design as well. Due to time constraints, a statistical representative study, needed to draw general conclusions for general aviation pilots on the quality of each of the FCL designs, could not be performed. Instead this section presents an exploratory study into the acceptance and appreciation of the manually controlled classical FCL design, by a certified Diamond DA 42 test pilot. The quality of this FCL design is compared with the unaugmented DRCT mode. The comparison between DRCT and the classical FCL based ATT mode is chosen in particular, because both of these modes are implemented in the SAFAR validation airplane.

As the perception and action behavior of pilots is known to strongly depend on visual as well as vestibular cues, it is essential to employ a 6-DOF full flight simulator in the pilot-in-the-loop evaluation [135]. The control modes have therefore been evaluated in the SIMONA Research Simulator (SRS) 6-DOF full flight simulator, shown in Figure 7.13. In this study a DA 42 qualified test pilot participated on evaluating the new dynamic behavior of the simulated SAFAR validation plane. In Figure 7.14 the DA 42 test pilot is seated in the SRS flight deck.

This section starts with the definition of the method used in the online evaluation of the FCLs, followed by the definition of the different flight scenarios in the test campaign. The section ends with the results and a discussion thereof. The flight trials described in this thesis are a subset of the simulator trials done for SAFAR. For

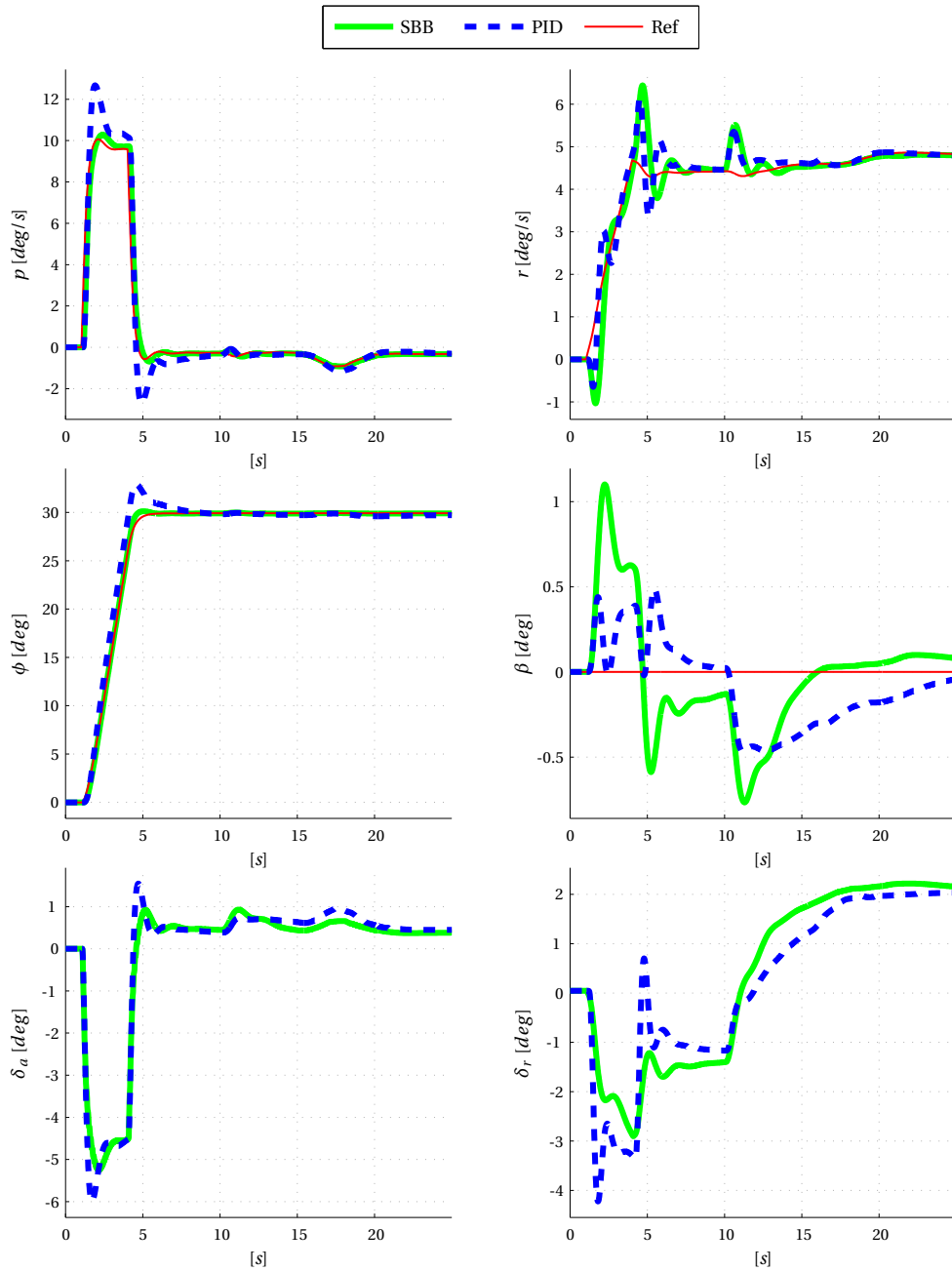


Figure 7.11: Time history of the lateral motion of the Diamond DA 42 with right engine failure controlled by the PID and SBB FCLs.

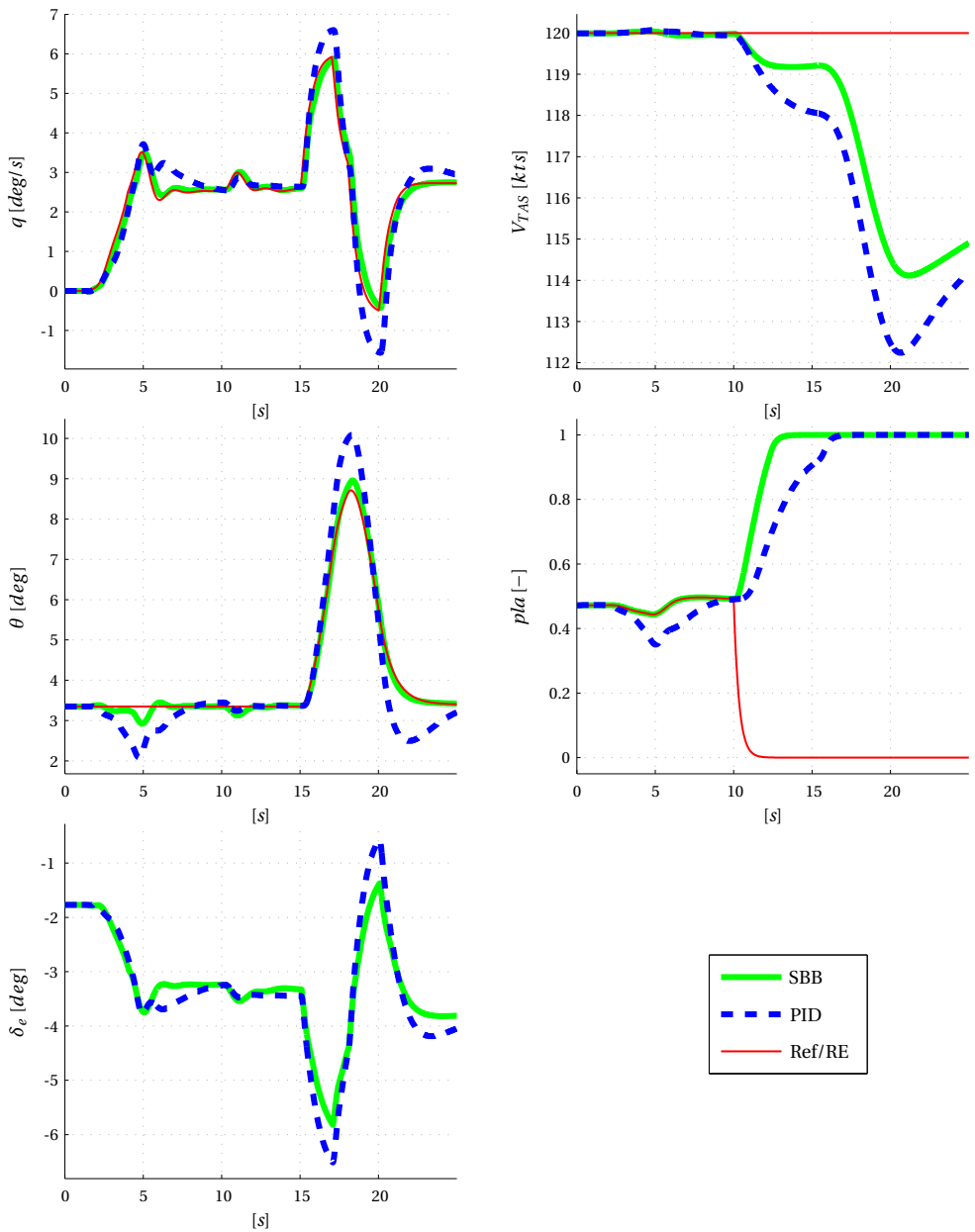


Figure 7.12: Time history of the longitudinal motion of the Diamond DA 42 with right engine failure controlled by the PID and SBB FCLs.

more information on the SAFAR simulator trials, the reader is referred to Appendix F in which the pilot instructions are provided.

7.3.1 Method

Test Subject Selection

A qualified DA 42 test pilot was invited to participate in the simulator trials. Test pilots have detailed knowledge of the dynamic behavior of an aircraft and will therefore also notice the difference in dynamic behavior due to the FCLs.

Model Implementations

The models used in this evaluation are the aircraft model described in Chapter 2 and the FBW platform model described in Chapter 3. The aircraft is trimmed at the operating point, which is used in the SAFAR flight test campaign, 120 kts and 6,000 ft in cruise configuration.

Flight Control Laws

The idea of the simulator flight trails is to prepare the SAFAR test pilot for flying the SAFAR validation plane. On this aircraft only the classical FCLs are implemented and therefore the online evaluation is also done using only the classical FCLs described in Chapter 4. Two modes are used during the online evaluation. The first mode, called DRCT, has no active FCL and is a direct stick-to-surface mode. The second mode is called ATT mode and uses a PID RCAFH controller, with sideslip compensation and velocity hold. In the third flight scenario, the ATT mode is expanded with the command limiting FEP system introduced in Chapter 6.

Displays

The synthetic vision display shown in Figure 7.15 is presented on the primary flight display in the SRS flight deck, directly in front of the right pilot seat. This display shows the current status of the aircraft as well as a tunnel in the sky which can be used for navigation. An outside visual system is switched on, that has a wide field of view and projects the image at infinity to match visual conditions in the real aircraft. The secondary flight displays are blank.

Implementation in the SRS

The SRS is controlled by a set of networked Personal Computers which run a flexible number of software modules within the Delft University Environment for Communication and Activation (DUECA) framework [121]. A simulation within DUECA is



Figure 7.13: SIMONA Research Simulator, source: W. R. Berkouwer



Figure 7.14: Cockpit view of the SRS, source: W. R. Berkouwer



Figure 7.15: SAFAR primary flight display, developed by dr. ir. C. Borst

subdivided into modules that each perform a part of the calculation. For SAFAR, these modules are the DA 42 aircraft model, the FBW controllers, the primary flight display, and a logging module. The DUECA modules of the DA 42 aircraft and the FCLs have been created by exporting their SIMULINK models to C-code using the Generic Real-time Workshop target with dynamic memory allocation (`grt_malloc`). Within a DUECA simulation on the SRS the Motion Limiter module plays a central role in the motion subsystem. It takes motion data from the aircraft model, filters and checks it before sending it to the motion base. In return it provides motion data, both calculated and measured by the motion base, which is useful for logging. Additionally, it provides a safety mechanism to bring the motion system in a safe state when something goes wrong within DUECA. The Motion Limiter uses a variety of input data such as, specific forces, (angular) velocities and (angular) accelerations, which are added as outputs to the aircraft model. In the simulation the aircraft state is updated at 300Hz and the FCLs at 60Hz. The FCL update rate almost matches the real FBW platform update of 16 milliseconds.

The outside visual is generated using the open-source flight simulation environment FlightGear [93]. Using DUECA, the current aircraft state, position and orientation, is communicated to FlightGear and this process is updated at 100Hz.

7.3.2 Flight Scenarios

Three flight scenarios are defined in this exploratory study, each with a different goal:

- Flight 1: Familiarization with the simulation. The goal of this flight is to accustom the pilot to the changes in human-machine interaction caused by installing the FBW platform. Both in DRCT and ATT mode the pilot is asked to make pitch and roll excursions from the trim state in increasing amplitude. After each excursion a short interview is held, whether the responsiveness of the aircraft is comparable to the real DA 42, or if stick gains needed tuning.
- Flight 2: Tracking the tunnel in the sky in DRCT law and ATT law. In order to get more quantitative data on the tracking performance and input activity of the pilot using each FCL, the pilot is asked to follow an earth fixed 3D trajectory in this scenario. Moderate turbulence is included in the simulation to increase the difficulty of the task. As a secondary goal, this scenario is also run with increased time delays, familiarizing the pilot with the effects of worst-case time delay.
- Flight 3: Intercepting the tunnel in the sky with and without FEP. This scenario is used to show the effect of FEP to the pilot. Starting 500 meters above and 1350 meters left of an earth fixed trajectory, the pilot is asked to fly towards, intercept and then follow this trajectory. The pilot was instructed to prevent exceeding a velocity of 135 kts during this scenario.

7.3.3 Results and Discussion

Evaluation of Flight 1

The first step is for the test pilot to get a basic feeling for the aircraft control and stick sensitivity in DRCT law and ATT law. A few remarks of the test pilot, after flying Flight 1, are:

“The DA 42 simulation is flyable and the responsiveness of the DA 42 is OK”

“There is more friction in the real DA 42 side-stick”

“There was no possibility to trim the aircraft in this simulation, but it’s flyable and I am happy with the simulated flight.”

“The ATT law is acceptable, it is flyable.”

“I experienced no problems regarding my intuitive reactions while flying in the ATT law.”

“The sideslip was suppressed a little bit, comparable to the real yaw damper implemented in the DA 42. It was acceptable for the flight condition.”

“The ATT law is perfect in the designed flight condition. Especially for a less-experienced pilot this is great!”

From the pilot’s comments it can be concluded that the simulated aircraft indeed behaves similar to a DA 42, except for the pilot controls. After enabling the ATT law it takes the pilot some time to get used to the changes in dynamic behavior, but eventually the benefit of the FCL becomes apparent.

Evaluation of Flight 2

The primary goal of the second flight trial is to compare the DRCT and ATT laws in terms of tracking performance and input activity. Second, larger time delays are introduced in the control loop to confront the pilot with a worst-case scenario of the dynamic qualities of the validation plane. A few remarks of the test pilot, after flying Flight 2 with nominal time delays, are:

“My initial reaction would be that no real difference exists between both laws while turning. After several test flights, the ATT law does not seem as easy in turns and constrained flight trajectories as the DRCT law. Perhaps this is also due to the turbulence present in the simulations.”

Figures 7.16 to 7.21 show the comparison between DRCT and ATT law, while the pilot is following a reference trajectory. The pilot controls the aircraft quite aggressively in the DRCT law. In ATT law the pilot is controlling more relaxed, resulting in slightly larger offsets to the reference trajectory. The root-mean-square values and standard deviations for each flight are shown in Table 7.2. The performance is comparable, whereas the control activity is smaller in ATT law.

After adding additional delay in the simulated FBW platform, the opinion of the pilot becomes more negative:

“You really feel the delay. This makes flying worse and results in PIO tendencies and not acceptable flying behavior. However, it is correctable and OK for testing purposes.”

From this comment the conclusion can be drawn that the time delays in the FBW platform must be kept at a minimum to retain acceptable flying behavior. However, the pilot comments can also be a reflection of the increase in oscillations show in Figures 7.5 and 7.6. It would therefore be useful to see whether a FCL tuned specifically for the worst-case time delays is perceived to have the same poor flying behavior. Again this is left for future work, however.

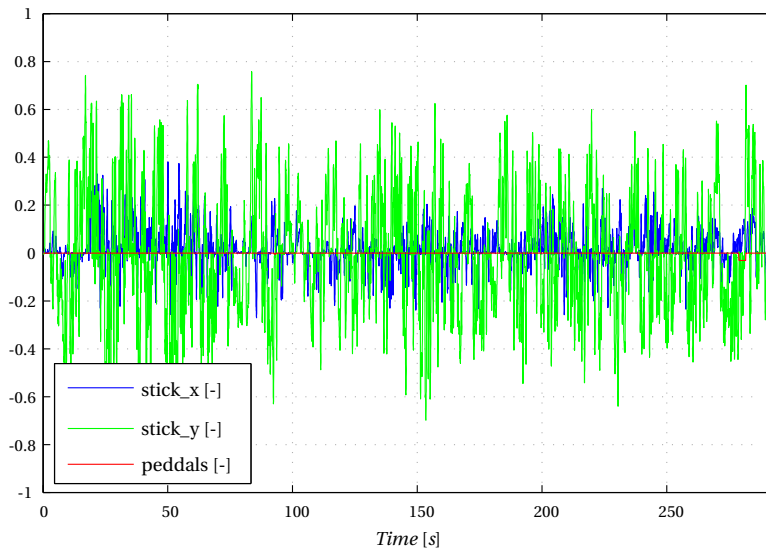


Figure 7.16: Pilot stick and rudder pedal input in DRCT law.

	DRCT		ATT	
	RMS	STD	RMS	STD
Horizontal offset [m]	8.7	7.5	9.7	8.9
Vertical offset [m]	3.0	2.7	3.4	3.4
Stick x [-]	0.08	0.08	0.04	0.04
Stick y [-]	0.25	0.25	0.15	0.15

Table 7.2: Root-mean-square and standard deviation of the input and position offsets from the reference trajectory.

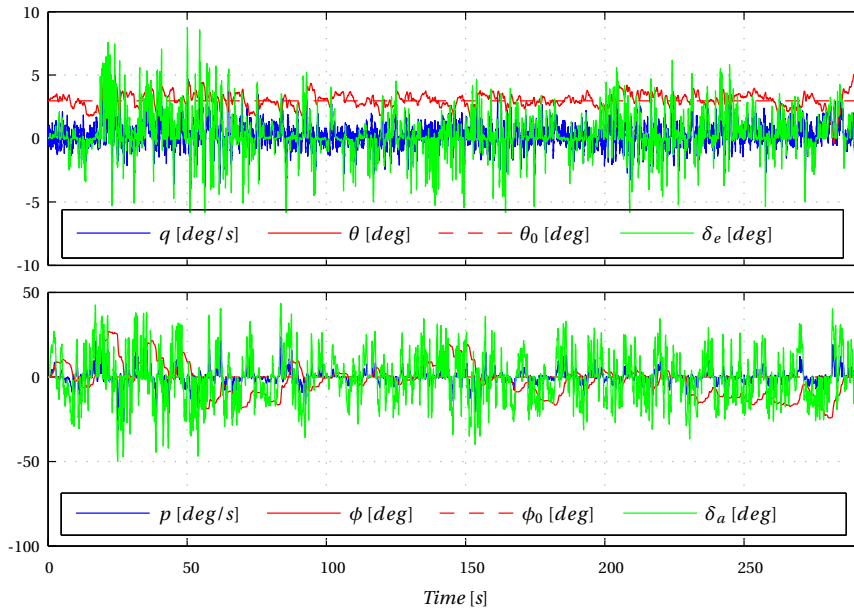


Figure 7.17: Aircraft responses to the pilot inputs in DRCT law, while the pilot tracks the reference trajectory.

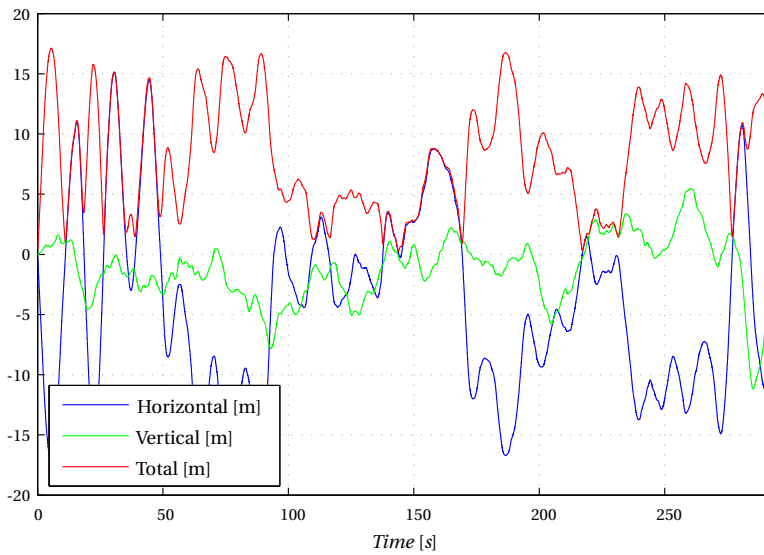


Figure 7.18: Offsets to the reference trajectory, when using the DRCT law.

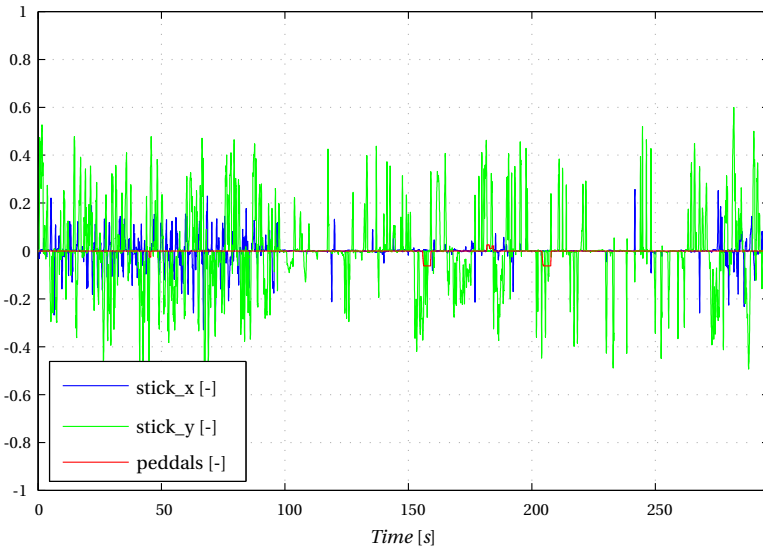


Figure 7.19: Pilot stick and rudder pedal input in ATT law.

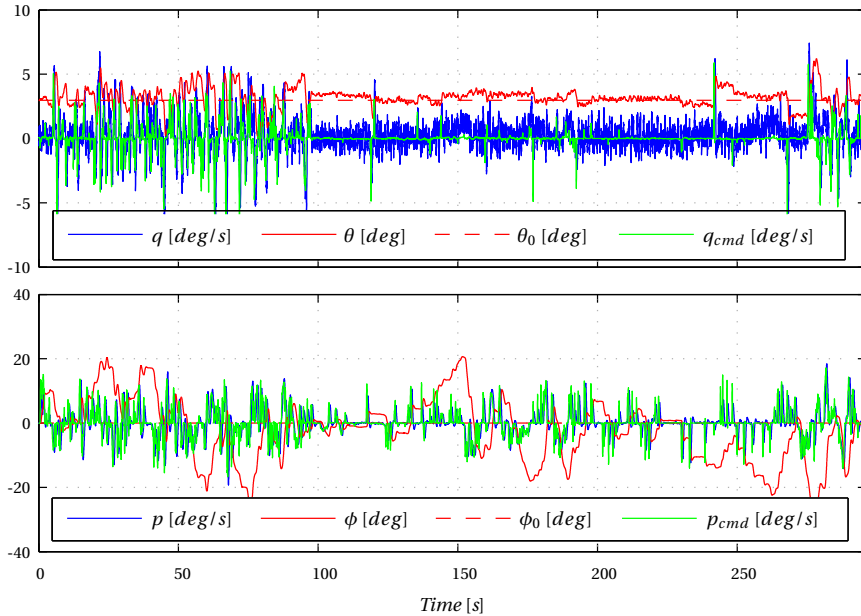


Figure 7.20: Aircraft responses to the pilot inputs in ATT law, while the pilot tracks the reference trajectory

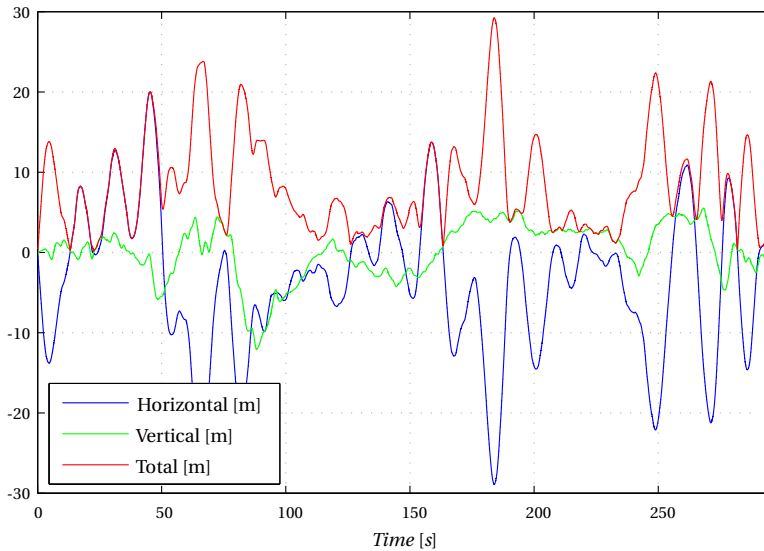


Figure 7.21: Offsets to the reference trajectory, when using the ATT law.

Evaluation of Flight 3

The goal of this flight is to evaluate the performance of the FEP system. A few remarks of the test pilot, after flying Flight 3, are:

“Protection will not help you in this scenario. The pilot has to deal with that you can’t push fully forward. This makes the transition during the intercept more dynamic. Without FEP there is no stick-blocking and therefore a more direct contact between pilot and aircraft. It is not normal operation to have your stick under stop. For less experienced pilots it could increase safety, but will also bring difficulty because of the loss in direct contact.”

“FEP restricts the pilots. Bank, pitch and speed limits should not be a problem for averagely experienced pilots.”

Figures 7.22 to 7.25 show the inputs and trajectory offsets for the pilot trying to intercept the reference trajectory from an initial position way outside the tunnel. Clearly the pilot is well able to intercept the tunnel without entering dangerous parts of the flight envelope. When FEP is enabled, the intercept performance is highly comparable with the FEP-disabled scenario. But, when looking at the pilot

input differences, we see that the FEP does a great job in rejecting undesired pilot inputs. From the large offsets in the pilot inputs, when FEP is enable, it is obvious that the pilot loses contact with the response of the aircraft. That is, the FEP has taken over control and puts the pilot out of the control loop. During the final part of the intercept, the abrupt transition in control authority may be undesirable from a human factors' perspective.

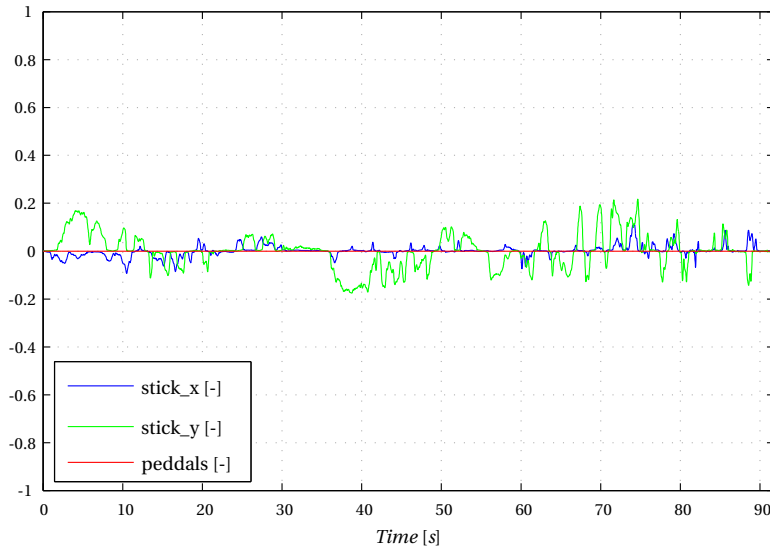


Figure 7.22: Pilot input during trajectory intercept in ATT law and without FEP.

Scope of the Study

The scope of the exploratory study presented in this section is limited. Clearly the remarks of one pilot cannot be extrapolated to the general opinion of all general aviation pilots. However, it is the opinion of a well trained DA 42 test pilot and therefore still worth noting.

Future Investigations

To improve the generality of the online evaluation, a larger set of test pilot should be invited to do the experiment. The experiment should then be split into four parts. In the first part the pilot compares the perceived performance of ATT law and DRCT law. The second part evaluates the ATT law performance at the worst-case time delays, with and without re-tuning. The third part investigates FEP acceptance with narrow and broad flight envelope limits. And in the fourth part the pilot compares the implementation of the ATT law using classical FCLs and the SBB FCLs.

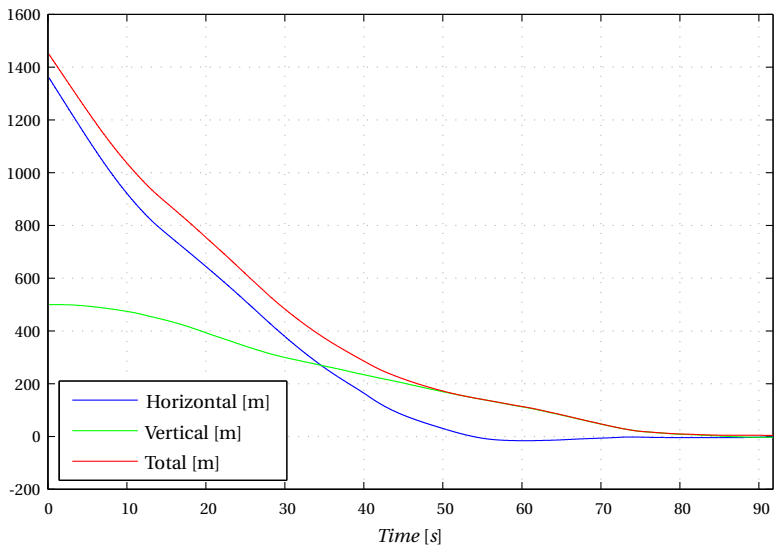


Figure 7.23: Trajectory offsets during trajectory intercept in ATT law and without FEP.

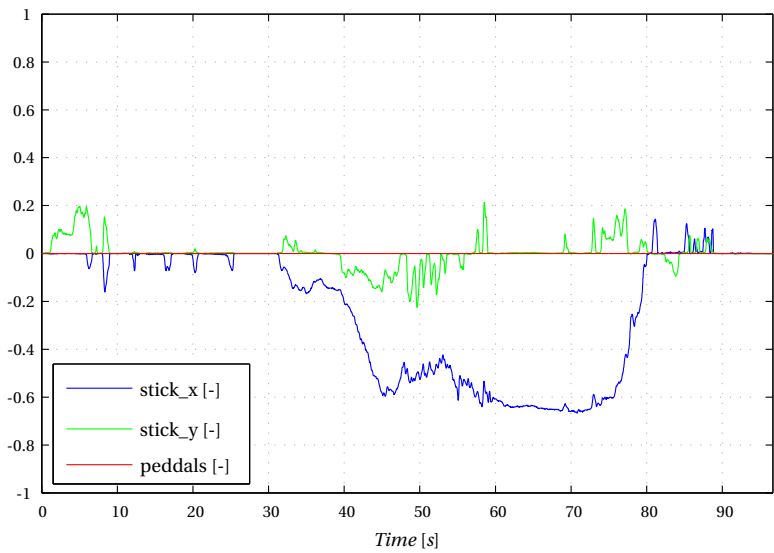


Figure 7.24: Pilot input during trajectory intercept in ATT law and with FEP.

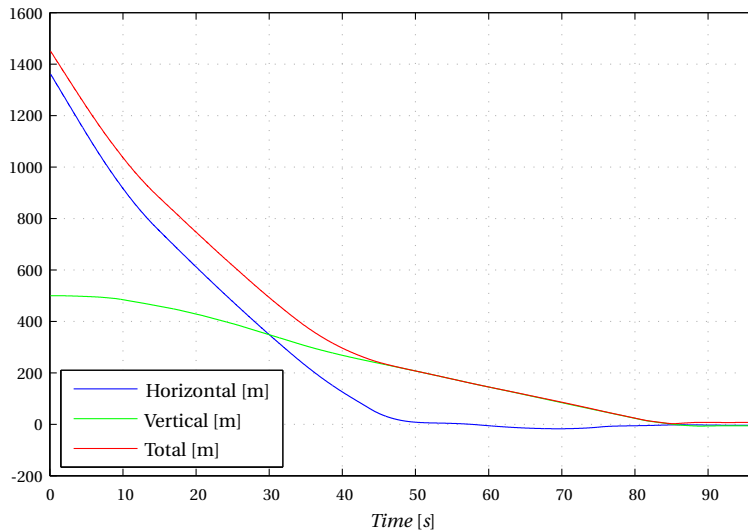


Figure 7.25: Trajectory offsets during trajectory intercept in ATT law and with FEP.

7.4 Conclusions

This chapter showed a comparison between the Flight Control Laws (FCLs) developed using a classical method in Chapter 4, called the Proportional-Integral-Derivative (PID) controller, and a nonlinear method in Chapter 5, called the Sensor-Based Backstepping (SBB) controller. This comparison is done using faster than real-time simulations of the aircraft model developed in Chapter 2 combined with the Fly-By-Wire (FBW) platform developed in Chapter 3.

Several aspects have been reviewed in this chapter that the FCLs will face in reality. Sensitivity to parametric uncertainty is analyzed by implementing the FCLs onto a completely different aircraft model, that of the Cessna Citation II. Without re-tuning the PID controller shows some oscillations, whereas the performance of the SBB controller remains excellent. The SBB controller could therefore be seen as a first step to a plug-and-play type FCL. However, it is slightly more susceptible to noise than the PID controller, but not as much as could be expected from a high bandwidth FCL design. Partly due to the integrating action of the SBB controller, the noise is attenuated. In the presence of severe time delays, both FCLs show oscillations. Re-tuning the SBB controller, for better performance in the presence of these time delays, can be done by changing only the anti-windup gain. Re-tuning the PID controller takes more effort. Simulations including wind gusts and turbulence show favorable characteristics of the PID controller. The PID controller pro-

vides smoother commands, but at the cost of slightly worse tracking performance compared with the SBB FCL.

Also the nominal performance of the PID and SBB FCLs is provided in this chapter, using the Handling Qualities (HQs) for the manual control mode and several other performance metrics for the automatic control mode. Both FCLs have good HQs and the difference is mainly found in the roll and pitch damping, which is low for the PID controller and high for the SBB controller. The performance of the automatic mode is comparable for both FCL designs.

The design effort and certifiability of each FCL design is briefly described in this chapter. The SBB controller is more easy to tune, yet it may be more difficult to certify and vice versa for the PID controller. For academic purposes, for which certification is of less importance, the SBB controller is a very good design option.

Finally the FCL designs are compared in an engine out scenario. Both FCLs cope with the failure and the aircraft continues flying without interaction of the pilot. The failure results in a smaller operational envelope of the aircraft and it could therefore be dangerous if the pilot is unaware of the failure. The failure should therefore be communicated to the pilot in a clear way, but this is left for future work.

Besides the offline FCL comparison, this chapter showed an exploratory study into the acceptance and appreciation of the classical FCL design. Unfortunately there was not enough time to do a statistical representative study, needed to draw more general conclusions, into the quality of both FCL designs. The online (pilot-in-the-loop) evaluation presented in this chapter is done by a single certified Diamond DA 42 test pilot. In the pilot's opinion the simulated aircraft behaves similar to a DA 42, except for the pilot controls. In the first few flights the pilot sees the benefits of the ATT law, but when asked to closely follow a reference trajectory the changes in dynamic behavior are not perceived as helpful. However, analysis of the flight data shows that the pilot controls the aircraft more relaxed in ATT mode than without a FCL, while the tracking performance is only slightly worse. According to the pilot, FEP was not useful while intercepting a reference trajectory and he commented that for less experienced pilots it is even worse to lose direct contact with the dynamics of the aircraft. He said FEP would introduce difficulties during the final part of the intercept when there is an abrupt transition in the control authority. Future studies should show if this opinion can be changed when broader flight envelope limits are used, that match the operational constraints of the aircraft more closely. Other studies into a different strategy in shifting control authority between pilot and FEP, such as using haptic feedback on the side-stick, can also be considered. For SAFAR these studies would not be useful, since the side-stick used in this project is passive.

CONCLUSIONS AND RECOMMENDATIONS

This thesis shows two successful Flight Control Law (FCL) designs for a personal air transportation system. One design is based on classical control theory and one on a newly developed nonlinear control method. Both designs are implemented and evaluated on a dynamic model of the Diamond DA 42, the test aircraft used in the seventh framework European project “Small Aircraft Future Avionics aRchitecture” (SAFAR). The SAFAR DA 42 is equipped with Fly-By-Wire (FBW) technology in order to change the pilot-aircraft interaction with the aim of improving safety and ease of aircraft handling.

8.1 Thesis Scope

The Diamond DA 42 is a small, light weight, four person, twin engine airplane and therefore a proper candidate for a personal air transportation system. The dynamic behavior of this airplane, which is the motion under influence of different forces and moments, can be described using the equations of motion. Several sources of forces and moments are identified and modeled in this thesis, including a propulsion model, an atmospheric disturbance model and an aerodynamic model. The aerodynamic model is validated using a Qualification Test Guide (QTG) provided by Diamond Simulation. This QTG is normally used to validate the correct operation of a level 5 flight training device, meaning that it describes a family of airplanes, rather than the DA 42 specifically. The FCLs are therefore designed with focus on

robustness to parameter uncertainties. The main research in this thesis is done for an undamaged airplane in nominal operation.

A flight control computer, at the heart of a FBW platform, uses FCLs to determine control effector settings (i.e., aileron deflection, elevator deflection, rudder deflection and throttle setting) based on measurement data. Although the FCLs aim at improving the dynamic behavior of the aircraft, they also have to deal with the dynamic behavior of the FBW platform itself. Measurement data contains noise and is not available instantaneous, actuator commands need time to take effect, redundancy management causes additional time delays, etc. This thesis therefore also describes the influence of the FBW platform on the system controlled by the FCLs. It is shown throughout the thesis that the characteristics of a FBW platform have a considerable effect that must be taken into account while designing the FCLs.

For each FCL design, two different control modes are developed in this thesis. The first is a manual control mode, using Rate-Command/Attitude-Hold (RCAH) for pitch and roll control, sideslip compensation and velocity hold, called the attitude (ATT) mode. RCAH decouples the flight controls, thereby simplifying flying the aircraft, it rejects turbulence and is a proven concept, used at low speeds in the Airbus A320/330 and 340. The ATT mode is particularly useful in cruise flight. For other flight phases different control strategies are more suitable, for example sideslip compensation is not desired in crosswind landings. The second control mode is a automatic 4D trajectory following mode, called the navigation (NAV) mode. This mode allows the aircraft to follow a predefined earth fixed trajectory and velocity profile without interaction of the pilot.

To increase safety, modern commercial aircraft, such as a Boeing 777 and an Airbus A380, are equipped with Flight Envelope Protection (FEP) systems to protect for stall, exceeding over-speed, limit angle of attack, load factors, etc. Since one of the main goals of adding FBW to a general aviation aircraft is to improve safety, FEP is a necessary addition to the FCL design. Even more so, due to the use of RCAH in the manual control mode. RCAH removes speed stability from the aircraft, meaning that pitch is maintained even when the aircraft decelerates. Without the use of FEP this behavior is quite dangerous.

8.2 Classical Flight Control Design

Common practice in industry for designing FCLs is still to linearize the aircraft model at different operating points and create a gain scheduled Proportional Integral Derivative (PID) controller. This thesis presents a successful classical con-

troller and uses it as a baseline for comparison with the more academic nonlinear FCL designs. The classical controller is designed using loop shaping with focus on tracking performance, disturbance rejection and noise attenuation. Gain selection is done using the combination of a rough pattern search method and a trust-region-reflective method.

Performance of the ATT mode is determined using the Handling Qualities (HQs) defined by the United States air force in MIL-F-8785C. Although it is shown that the unaugmented aircraft already possesses good HQs, the ATT mode still offers improvements. The main drawback of the ATT mode is a high equivalent time delay, which is due to the large time delays on the FBW platform. Performance of the NAV mode is demonstrated using a suite of performance metrics. These metrics are also used for comparison with the nonlinear FCL design.

8.3 Nonlinear Flight Control Design

The nonlinear FCL is designed with focus on model uncertainty. Adaptation or robustness are commonly used to deal with model uncertainty, but certification of these laws has proven to be difficult. The backstepping design method can be seen as a good candidate for a certifiable nonlinear FCL, due to its use of Lyapunov analysis thereby guaranteeing system stability. However, conventional backstepping is sensitive to model uncertainties and therefore a more sensor based approach is introduced in this thesis. Sensor-Based Backstepping (SBB) uses singular perturbation theory and provides a backstepping framework to Hovakimyan's approximate dynamic inversion controller.

Implementation of the RCAH controller with sideslip compensation, using the SBB method, is done in two steps and while the system is minimum phase, controllable and sufficiently time scale separated the designed FCL asymptotically stabilizes the error dynamics. Here the error dynamics refer to the difference between aircraft dynamics and reference dynamics, provided by the pilot. Tuning of the FCL gains is straight forward and is done using an engineering guess. HQ evaluation shows that the FCL is too fast and command filtering is needed to obtain proper behavior of the system throughout the flight envelope. A first order low-pass filter proves to be a good command filter and results in adequate handling characteristics. The SBB FCL uses direct measurement of angular rates, rather than the differential equations for the rotational motion of the aircraft, thereby avoiding influence of model uncertainties. Angular accelerometers are available commercial-off-the-shelf, but too costly for use in general aviation. Simulations show that differentiation of angular rate measurements result in very good behavior of the FCL as well.

Velocity control using the SBB method is done in a single step, due to the relative degree of one of this system. The good performance of this controller could also have been obtained using a PI controller, because this thesis shows that SBB and PI control are equivalent for systems with a relative degree of one. Looking at this statement the other way around, provides a theoretical background for the success of PI control on particular nonlinear systems.

Expanding the SBB FCL to the 4D trajectory following NAV mode is not straight forward, because the lower-triangular system requirement is violated in that case. Adding a PID outer-loop controller results in good NAV law performance, but the guarantee of full system stability is lost.

8.4 Addition of Flight Envelope Protection

This thesis investigates four FEP strategies. The first is control limiting, in which commands issued by the FCL are limited to stay within a safe flight envelope. The second is command limiting, in which commands to the FCL are limited. The third is replacing the FCL by a constrained FCL, such as model predictive control, which is able to handle state constraints. And the last strategy is virtual control limiting, in which commands to the inner-loop of a recursive nonlinear FCL design are limited. The use of nonlinear FCLs for FEP purposes is shown not have an advantage, nor disadvantage, and therefore FEP is not a deciding factor in the FCL design choice. Command limiting is a good FEP strategy for a small airplane and can be applied to classical FCL designs as well as a nonlinear ones.

8.5 Comparison of the Flight Control Designs

In order to make a proper choice which FCL design is best suited for the control of a personal air transportation system, more specifically a Diamond DA 42, several offline simulations have been performed. The influence of parametric uncertainties is tested by applying both FCL designs, without adaptation of the gains, to the airplane model of a Cessna Citation II. Performance of the PID controller in this scenario is not bad, but the response does show oscillations. Performance of the SBB controller remains excellent and this design can therefore be seen as a first step towards a plug-and-play type of FCL. Noise attenuation and disturbance rejection are specifically taken into account while designing the classical controller. It is therefore no surprise that the PID FCL performs slightly better than the SBB controller in this regard. In the presence of worst case time delays, both FCL designs suffer in performance, but re-tuning the SBB controller is considerable easier. Both designs have satisfactory HQs, but differ in short period and aperiodic roll damping. The

PID design is tuned to be fast and under-damped and the SBB design is inherently over-damped. Performance of the NAV mode is highly comparable for both FCL designs and is therefore not helpful in the FCL design choice. Design effort in terms of gain tuning is easier for the SBB design as compared with the PID design and vice versa for certification effort.

8.6 What is the Best Selection of a Practical Flight Control Law for Small Fixed Wing Aircraft

Taking all the considerations of the previous section into account allows us to answer the main research question: What is the best selection of a practical flight control law for small fixed wing aircraft? In the scope of this thesis, SBB is selected as the preferred FCL design. A SBB FCL is easy to tune and insensitive to parametric uncertainties, while providing adequate noise attenuation and disturbance rejection. No adaptation is used, meaning that this FCL design has a predictable output and therefore a chance at certification. In particular the possibility of developing a plug-and-play type FCL is an attractive property of the SBB design.

8.7 Beyond the Scope

This section lists some brief remarks on the impact of a change in the scope on the conclusion drawn in the previous section.

- Shifting the focus from small airplanes to helicopters may impact the conclusions. One of the differences between helicopters and airplanes from a control perspective is the non-affine-in-control nature of the helicopter. However, due to the use of the partial derivative of the state derivative to the input in the SBB method, this should not be a problem. Successful FCL designs using this kind of linearization can be found in literature.
- Not only for helicopters, but also for other airplanes, such as commercial airplanes, fighter planes or Unmanned Aerial Vehicles (UAVs) the time-scale separation property of a system may change the conclusion. As long as the changes in input commands can evolve much faster than the change in system dynamics, SBB will function properly and remains the preferred design.
- Increasing the flight envelope, beyond the single operating point of 120 kts at 6,000 ft, by improving the model validity, will not result in a change in the conclusion drawn in this thesis. This thesis shows that command filtering can be used in the SBB FCL design to obtain desired performance throughout the flight

envelope and increasing that flight envelope does therefore not change the conclusion.

- When failures occur, the sign of the control surface effectiveness could change and thereby (drastically) reduce the SBB performance. As mentioned in the thesis a crude form of failure detection may be used to make sure the correct sign is used in the SBB controller.
- Improving the FBW platform, by for example reducing time delays is beneficial for both the classical FCL design as well as the nonlinear FCL design, but will have no impact on the design choice.
- Application of SBB to control modes that close more control loops than the ATT mode, is shown not to be straight forward. When the FCLs are designed solely for automatic modes, such as for UAVs, the benefit of SBB decreases.
- For the same reason the benefit of SBB decreases when focus is shifted from cruise to the landing phase. During the landing phase position, rather than attitude, is important and therefore more control loops need to be closed.

8.8 Recommendations

The work presented in this thesis gives rise to new questions and research directions. This section provides recommendations for further studies.

The aircraft model developed for this thesis is a good starting point, but should be expanded for a more thorough evaluation of the FCL design. Validity is currently demonstrated in a single operating point, meaning that the resulting FCLs are limited to operate at that point as well. Expanding the validity of the aircraft model can be done using dedicated flight tests or by closer cooperation with Diamond Simulation.

Furthermore, the aircraft model should be expanded with structural dynamics and aeroelasticity effects. When the designed FCL excites the aircraft at frequencies associated with these dynamics, anything ranging from passenger discomfort to destruction of the aircraft due to aeroelastic instability can happen. Also control surface effect reversal due to aeroelasticity would have a large impact on the SBB FCL operation and should be carefully studied.

Many accidents in general aviation happen during landing, therefore it would be beneficial to implement a flare and auto-land mode for a small airplane. A landing model is already introduced in this thesis, but this model is not validated. Val-

Validation of this model can be done using static measurements of the landing gear components and by performing drop tests, bump test, etc. to determine dynamic properties of the model. As already indicated in this thesis, much more detail can be added to the landing model, but whether this is needed depends on the validation results and the intended use of the model. Note that the NAV law already showed altitude variations of several feet due to measurement noise. Additional filtering, or better sensors may be needed when a position-based FCL is designed for the landing phase. Also note that airport site measurement equipment, such as a localizer and glide path beacon, is not always available on small airports.

Other FCL modes can be implemented as well, such as a de-crab mode and an autothrottle thrust mode. In this way the FBW platform can be used more intensively in all flight phases.

The HQ analysis performed in this thesis has shown that the equivalent pitch time delay is slightly too large, especially when low-cost sensors are used. Reduction of this time delay might be possible by changing the method of redundancy management or by using faster hardware.

The connectivity of the FBW platform should also be improved before the mechanical backup can be removed. The pilot should be able to have rudder input and the elevator trim tab should be connected. Adding a low-frequency elevator trim system that controls the hinge moment to zero is absolutely recommendable to lower the risk of accidents.

The FCL designs presented in this thesis are of course not fully finalized products, but rather a good starting point for further research. Disturbances with a frequency around 1 rad/s have a large negative influence on the autothrottle performance of the classical FCL. When this FCL is used in further studies, sources of such disturbances should be identified and an autothrottle redesign may be needed. Also future work is needed to find a more scientific method for the selection of the controller gains for the nonlinear FCL design. Most of the gains used in this FCL are selected by trial and error and perhaps a cost function of control effort, noise attenuation, disturbance rejection and tracking performance can be minimized to find more optimal controller gains.

Furthermore the side stick currently chosen in SAFAR does not have considerable damping characteristics. While flying, the aircraft movements cause the pilot body to move as well and by holding the stick give inputs to the FCLs, thereby closing a loop. This effect is called ratcheting and could lead to hazardous situations, particularly in turbulence. This phenomenon can be studied in a moving base sim-

ulator and if needed the FCLs could filter high input frequencies or the damping of the stick can be adjusted. Also the stick shaping part of the flying quality evaluation should be addressed in future studies.

This thesis already showed a preliminary online evaluation of the FCL designs. As the perception and action behavior of pilots is known to strongly depend on visual as well as vestibular cues, it is essential to employ a 6-DOF full flight simulator in these tests. It is important to check whether the intended use of the FCLs are appreciated and accepted by the pilot. For example, a test flight using narrow flight envelope limits resulted in counter productivity of the FEP system. The pilot lost direct contact with the aircraft while FEP is active and when control authority is switched back the changes in dynamic behavior were abrupt, making flying with FEP less safe rather than safer. Further, it should be studied whether the FCL designs indeed lower the workload of the less-experienced general aviation pilot and make flying easier. Moreover, the SBB controller should also be evaluated online, to see whether the nice results that are shown in offline simulations are also experienced as such by the pilot.

RIGID BODY AIRCRAFT DYNAMICS

The dynamic behavior, or the motion of a vehicle under the influence of forces and moments, can be described in a set of equations, called the equations of motion. Since motion only has meaning in a frame of reference, first a set of reference frames is defined in Section A.1. The equations of motion are derived next, in Section A.2.

A.1 Reference Frames

The aircraft model, developed for this thesis, uses six reference frames.

The first reference frame is introduced to describe the motion of the vehicle with respect to the earth's surface. This reference frame is assumed to be inertial, meaning that the rotation and acceleration of the earth is neglected with respect to the motion of the vehicle.

- The Earth Fixed Reference Frame, RF_E , is a right-handed orthogonal axis system, of which the X_E -axis points to a fixed direction (e.g., the north), the Y_E -axis points to the right (perpendicular to the X_E -axis) and the Z_E -axis points downward (perpendicular to the $X_E Y_E$ -plane). The origin of the reference frame lies at the starting point of the maneuver considered.

The second reference frame has the same attitude as the first, but translates while the vehicle is moving. Integration of the velocity of this reference frame re-

sults in the position of the vehicle in RF_E . Inherently it will be non-inertial, as it will accelerate within RF_E .

- The Vehicle Carried Local-Earth Reference Frame, RF_O , is a right-handed orthogonal axis system, of which the X_O , Y_O and Z_O axes point in the same direction as the X_E , Y_E and Z_E respectively. The axes cross each other in the Center of Gravity (CoG) of the vehicle.

A third reference frame is introduced that not only translates while the vehicle is moving, but also rotates towards the direction of travel.

- The Kinematic Reference Frame, RF_K , is a right-handed orthogonal axis system, of which the X_K -axis points in the direction of the velocity vector of the aircraft with respect to the ground, V_{GS} , the Y_K -axis points to the right and the Z_K -axis points downward (perpendicular to the $X_K Y_K$ -plane). The axes cross each other in the CoG of the vehicle.

To simplify the derivation of the equations of motion a fourth reference frame is introduced. The position and attitude of this reference frame is fixed to the vehicle and it is therefore non-inertial. This means that the motion caused by the forces and moments needs to be corrected with fictitious forces introduced by the motion of the reference frame with respect to the inertial reference frame, RF_E ¹. The description of these corrective terms will follow in Section 2.2.2.

- The Body Fixed Reference Frame, RF_B , is a right-handed orthogonal axis system, of which the X_B -axis points in the direction of the nose of the vehicle, the Y_B -axis points to the right and the Z_B -axis points downward as seen from the pilot. The axes cross each other in the CoG of the vehicle.

The fifth reference frame is introduced in order to describe the aerodynamic forces and moments acting on the aircraft. These are caused by air flowing around the vehicle and therefore this reference frame points in the direction of the oncoming air.

¹In the case that RF_E would not be considered inertial either, additional fictitious forces should be introduced caused by the motion of RF_E with respect to an inertial reference frame.

- The Aerodynamic Reference Frame, RF_A , is a right-handed orthogonal axis system, of which the X_A -axis points in the direction of the velocity vector of the aircraft with respect to the air, V_{TAS} , the Y_A -axis points to the right and the Z_A -axis points downward (perpendicular to the $X_A Y_A$ -plane). The axes cross each other in the CoG of the vehicle.

Note that the difference between V_{TAS} and V_{GS} is the wind velocity vector V_{wind} . When no wind is present, X_A coincides with X_K .

A sixth reference frame is used to determine the distance of the aircraft with respect to an earth fixed trajectory.

- The Trajectory Fixed Reference Frame, RF_T , is a right-handed orthogonal axis system of which X_T points along an earth fixed trajectory, Z_T points in the same direction as Z_O and Y_T is perpendicular to the $X_T Z_T$ plane.

While flying, the vehicle can rotate in three different ways with respect to the earth. This means that the attitude of the RF_B with respect to RF_O may be determined using three Euler angles and two intermediate reference frames. Transformation of a vector (e.g., gravity), from RF_O to RF_B can be done by performing three subsequent transformations over ψ , θ and ϕ as depicted in Figure A.1. First, transformation of the vector from RF_O to $RF_{o'}$ using,

$$\begin{bmatrix} o'_1 \\ o'_2 \\ o'_3 \end{bmatrix} = \begin{bmatrix} \cos\psi & \sin\psi & 0 \\ -\sin\psi & \cos\psi & 0 \\ 0 & 0 & 1 \end{bmatrix} \begin{bmatrix} X_O \\ Y_O \\ Z_O \end{bmatrix} \quad (\text{A.1})$$

Second, transformation from $RF_{o'}$ to $RF_{o''}$ using,

$$\begin{bmatrix} o''_1 \\ o''_2 \\ o''_3 \end{bmatrix} = \begin{bmatrix} \cos\theta & 0 & -\sin\theta \\ 0 & 1 & 0 \\ \sin\theta & 0 & \cos\theta \end{bmatrix} \begin{bmatrix} o'_1 \\ o'_2 \\ o'_3 \end{bmatrix} \quad (\text{A.2})$$

and finally the vector defined in $RF_{o''}$ can be transformed to RF_B using,

$$\begin{bmatrix} X_B \\ Y_B \\ Z_B \end{bmatrix} = \begin{bmatrix} 1 & 0 & 0 \\ 0 & \cos\phi & \sin\phi \\ 0 & -\sin\phi & \cos\phi \end{bmatrix} \begin{bmatrix} o''_1 \\ o''_2 \\ o''_3 \end{bmatrix} \quad (\text{A.3})$$

Multiplying these three matrices, leads to the definition of the transformation matrix Q ,

$$\begin{bmatrix} X_B \\ Y_B \\ Z_B \end{bmatrix} = Q_{BO} \begin{bmatrix} X_O \\ Y_O \\ Z_O \end{bmatrix} \quad (\text{A.4})$$

where,

$$Q_{BO} = \begin{bmatrix} \cos\theta \cos\psi & \cos\theta \sin\psi & -\sin\theta \\ -\cos\phi \sin\psi + \sin\phi \sin\theta \cos\psi & \cos\phi \cos\psi + \sin\phi \sin\theta \sin\psi & \sin\phi \cos\theta \\ \sin\phi \sin\psi + \cos\phi \sin\theta \cos\psi & -\sin\phi \cos\psi + \cos\phi \sin\theta \sin\psi & \cos\phi \cos\theta \end{bmatrix}$$

From the way in which the transformations are defined, it can be deduced that the transformation matrix Q_{BO} is an orthonormal matrix. This implies that transformation of a vector from RF_B back to RF_O can be done with the useful property that the inverse equals the transpose, $Q_{OB} = Q_{BO}^{-1} = Q_{BO}^T$.

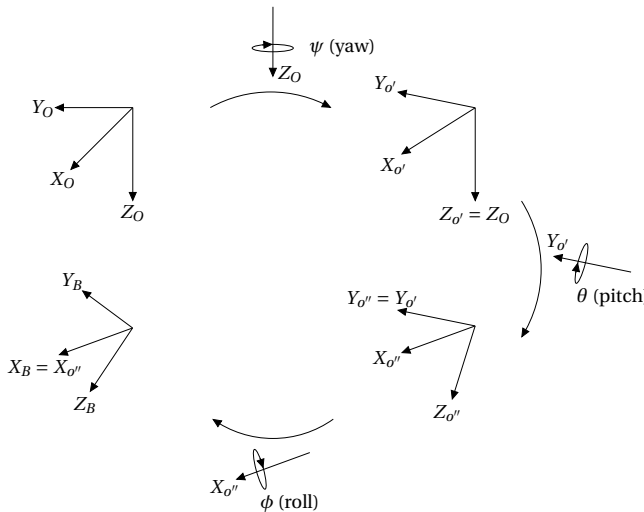


Figure A.1: Transformation from RF_O to RF_B using Euler angles

Transformation between the other reference frames can be defined in similar fashion.

- Q_{BA} is defined using two subsequent rotations over $-\beta$, α . Note that after these two rotations RF_A is already aligned to RF_B and no further rotations are needed.
- Q_{AO} is defined using three subsequent rotations over χ_a , γ_a and μ_a .

- Q_{KO} is defined using three subsequent rotations over χ_k , γ_k and μ_k .
- Q_{TO} is defined using a single rotation over χ_T .

Having defined the reference frames and transformations needed to describe the motion of the body, let us move on by looking into how the motion can be calculated in Section A.2.

A.2 Equations of Motion

This section presents a derivation of the equations of motion, which closely follows the one presented in Flight Dynamics [83]. First Newton's laws will be applied to the forces acting on the body described in the non-inertial reference frame RF_B . This leads to three differential equations for the translational velocity of the vehicle. Next, Newton's laws will be applied to the moments that act on the vehicle, leading to three additional differential equations for the rotational velocity of the body. Another three differential equations will be added to the equations of motion, since the transformation between RF_O and RF_B , defined in Section A.1, depends on Euler angles rather than body rotations. An additional three differential equations are introduced that describe the position of the aircraft in RF_E and this section ends with description of the equations of motion in RF_A and RF_K .

Differential Equations for the Translational Velocity of the Vehicle

Newton's second law for a point mass dm , which moves with time varying velocity V under the influence of a force dF , is expressed by Equation (A.5). When all forces and moments are summed about the CoG of the body and internal forces and moments are canceled according to Newton's third law, Equation (A.6) is obtained.

$$dF = \frac{d}{dt}(dm \cdot V) \quad (\text{A.5})$$

$$F = \int dF = \int_m \frac{d}{dt}(dm \cdot V) \quad (\text{A.6})$$

To simplify the following derivations, two assumptions are made:

- The vehicle is considered a rigid body, i.e., elastic deformations are neglected.
- The mass is assumed constant during the interval over which the motion is considered.

The mass element dm located at a point P of the vehicle has a velocity,

$$V_P = V_B + \frac{dr_P}{dt} \quad (\text{A.7})$$

where V_B is the velocity of the origin of the RF_B , i.e., the velocity of the CoG of the body and r_P is the length from the origin to a point P . The time derivative of a vector described in a rotating reference frame, depends on the time derivative of its length and the rotational change of the vector, so,

$$V_P = V_B + \frac{\partial r_P}{\partial t} + \Omega \times r_P \quad (\text{A.8})$$

However, since the body is assumed rigid, $\frac{\partial r_P}{\partial t} = 0$. Integration over all mass elements then yields,

$$\int_m dm V_P = \int_m dm (V_B + \Omega \times r_P) = m V_B + \Omega \times \int_m (r_P dm) \quad (\text{A.9})$$

The origin of the RF_B lies in the CoG, which means that $\int_m (r_P dm) = 0$. The total linear momentum of all particles in the body is therefore equal to,

$$L = \int_m dm V_P = m V_B \quad (\text{A.10})$$

Now Equation (A.6) can be rewritten as,

$$F = \frac{dL}{dt} = \frac{dm V_B}{dt} = m \frac{dV_B}{dt} = m \left(\frac{\partial V_B}{\partial t} + \Omega \times V_B \right) \quad (\text{A.11})$$

By using the notation $V_{B,x} = u$, $V_{B,y} = v$, $V_{B,z} = w$ and $\Omega_x = p$, $\Omega_y = q$, $\Omega_z = r$, the force equation becomes,

$$\begin{bmatrix} F_x \\ F_y \\ F_z \end{bmatrix} = m \left(\begin{bmatrix} \dot{u} \\ \dot{v} \\ \dot{w} \end{bmatrix} + \begin{bmatrix} p \\ q \\ r \end{bmatrix} \times \begin{bmatrix} u \\ v \\ w \end{bmatrix} \right) \quad (\text{A.12})$$

with $m\Omega \times V_B$ acting as fictitious (centrifugal) forces on the body resulting from motion of the reference frame. Expression (A.12) can also be written as a differential equation for the translational velocity of the body,

$$\begin{bmatrix} \dot{u} \\ \dot{v} \\ \dot{w} \end{bmatrix} = m^{-1} \begin{bmatrix} F_x \\ F_y \\ F_z \end{bmatrix} - \begin{bmatrix} p \\ q \\ r \end{bmatrix} \times \begin{bmatrix} u \\ v \\ w \end{bmatrix} \quad (\text{A.13})$$

Differential Equations for the Rotational Velocity of the Vehicle

Similar to the force equation, the moment equation can also be written as a change in momentum,

$$M = \frac{dB}{dt} = \frac{\partial B}{\partial t} + \Omega \times B \quad (\text{A.14})$$

where B is the angular momentum, $B = \int_m r_P \times V_P dm$. Inserting Equation (A.8) leads to,

$$B = \int_m r_P \times (V_B + \Omega \times r_P) dm = \int_m r_P \times V_B dm + \int_m r_P \times (\Omega \times r_P) dm \quad (\text{A.15})$$

Since V_B is independent of any mass element, it can be taken out of the integral. However, $\int_m (r_P dm)$ is zero and thus,

$$B = \int_m r_P \times (\Omega \times r_P) dm = \int_m \Omega (r_P \cdot r_P) dm - \int_m r_P (\Omega \cdot r_P) dm$$

or,

$$\begin{aligned} \begin{bmatrix} B_x \\ B_y \\ B_z \end{bmatrix} &= \int_m \begin{bmatrix} px^2 + py^2 + pz^2 \\ qx^2 + qy^2 + qz^2 \\ rx^2 + ry^2 + rz^2 \end{bmatrix} dm - \int_m \begin{bmatrix} px^2 + qxy + rxz \\ pxy + qy^2 + ryz \\ pxz + qyz + rz^2 \end{bmatrix} dm \\ &= \left(\int_m \begin{bmatrix} (y^2 + z^2) & -xy & -xz \\ -xy & (x^2 + z^2) & -yz \\ -xz & -yz & (x^2 + y^2) \end{bmatrix} dm \right) \Omega \end{aligned} \quad (\text{A.16})$$

By using moments and products of inertia the angular momentum can be written as,

$$B = J\Omega \quad (\text{A.17})$$

where,

$$J = \begin{bmatrix} I_{xx} & -I_{xy} & -I_{xz} \\ -I_{xy} & I_{yy} & -I_{yz} \\ -I_{xz} & -I_{yz} & I_{zz} \end{bmatrix}$$

Hence the moment equations become,

$$\begin{bmatrix} M_x \\ M_y \\ M_z \end{bmatrix} = J \begin{bmatrix} \dot{p} \\ \dot{q} \\ \dot{r} \end{bmatrix} + \begin{bmatrix} p \\ q \\ r \end{bmatrix} \times \left(J \begin{bmatrix} p \\ q \\ r \end{bmatrix} \right) \quad (\text{A.18})$$

Expression (A.18) can also be written as a differential equation for the rotational velocity of the body,

$$\begin{bmatrix} \dot{p} \\ \dot{q} \\ \dot{r} \end{bmatrix} = J^{-1} \begin{bmatrix} M_x \\ M_y \\ M_z \end{bmatrix} - J^{-1} \begin{bmatrix} p \\ q \\ r \end{bmatrix} \times \left(J \begin{bmatrix} p \\ q \\ r \end{bmatrix} \right) \quad (\text{A.19})$$

Differential Equations for the Euler Angles

The transformations between RF_O and RF_B , stated in Section A.1, depend on Euler angles rather than body angles and therefore the rate of change of the Euler angles must be obtained in order to calculate the motion of the vehicle with respect to the RF_E . The difference between Euler rates of change and body rotational rates lies in the axis about which they describe the rotational velocities. The body rotational rates (p , q and r) describe the velocity about the X_B , Y_B and Z_B axis and the Euler rates of change describe the rotational velocity about the o''_1 , o''_2 and Z_O axis. The Euler rates can be transformed to the RF_O by using the following relations,

$$\begin{aligned} \begin{bmatrix} \dot{\phi}_{X_B} \\ \dot{\phi}_{Y_B} \\ \dot{\phi}_{Z_B} \end{bmatrix} &= \begin{bmatrix} 1 & 0 & 0 \\ 0 & \cos\phi & \sin\phi \\ 0 & -\sin\phi & \cos\phi \end{bmatrix} \begin{bmatrix} \dot{\phi} \\ 0 \\ 0 \end{bmatrix} = \begin{bmatrix} \dot{\phi} \\ 0 \\ 0 \end{bmatrix} \\ \begin{bmatrix} \dot{\theta}_{X_B} \\ \dot{\theta}_{Y_B} \\ \dot{\theta}_{Z_B} \end{bmatrix} &= \begin{bmatrix} 1 & 0 & 0 \\ 0 & \cos\phi & \sin\phi \\ 0 & -\sin\phi & \cos\phi \end{bmatrix} \begin{bmatrix} \cos\theta & 0 & -\sin\theta \\ 0 & 1 & 0 \\ \sin\theta & 0 & \cos\theta \end{bmatrix} \begin{bmatrix} \dot{\theta} \\ 0 \\ 0 \end{bmatrix} = \begin{bmatrix} 0 \\ \dot{\theta} \cos\phi \\ -\dot{\theta} \sin\phi \end{bmatrix} \\ \begin{bmatrix} \dot{\psi}_{X_B} \\ \dot{\psi}_{Y_B} \\ \dot{\psi}_{Z_B} \end{bmatrix} &= \begin{bmatrix} 1 & 0 & 0 \\ 0 & \cos\phi & \sin\phi \\ 0 & -\sin\phi & \cos\phi \end{bmatrix} \begin{bmatrix} \cos\theta & 0 & -\sin\theta \\ 0 & 1 & 0 \\ \sin\theta & 0 & \cos\theta \end{bmatrix} \begin{bmatrix} \cos\psi & \sin\psi & 0 \\ -\sin\psi & \cos\psi & 0 \\ 0 & 0 & 1 \end{bmatrix} \begin{bmatrix} 0 \\ 0 \\ \dot{\psi} \end{bmatrix} \\ &= \begin{bmatrix} -\dot{\psi} \sin\theta \\ \dot{\psi} \cos\theta \sin\phi \\ \dot{\psi} \cos\theta \cos\phi \end{bmatrix} \end{aligned}$$

By combining these results, the body rotational velocities can be written in their Euler rate parts as,

$$\begin{bmatrix} p \\ q \\ r \end{bmatrix} = \begin{bmatrix} \dot{\phi}_{X_B} + \dot{\theta}_{X_B} + \dot{\psi}_{X_B} \\ \dot{\phi}_{Y_B} + \dot{\theta}_{Y_B} + \dot{\psi}_{Y_B} \\ \dot{\phi}_{Z_B} + \dot{\theta}_{Z_B} + \dot{\psi}_{Z_B} \end{bmatrix} = \begin{bmatrix} 1 & 0 & -\sin\theta \\ 0 & \cos\phi & \cos\theta \sin\phi \\ 0 & -\sin\phi & \cos\theta \cos\phi \end{bmatrix} \begin{bmatrix} \dot{\phi} \\ \dot{\theta} \\ \dot{\psi} \end{bmatrix} \quad (\text{A.20})$$

or by calculating the inverse, a differential equation is obtained for the Euler angles,

$$\begin{bmatrix} \dot{\phi} \\ \dot{\theta} \\ \dot{\psi} \end{bmatrix} = \begin{bmatrix} 1 & \sin\phi \tan\theta & \cos\phi \tan\theta \\ 0 & \cos\phi & -\sin\phi \\ 0 & \frac{\sin\phi}{\cos\theta} & \frac{\cos\phi}{\cos\theta} \end{bmatrix} \begin{bmatrix} p \\ q \\ r \end{bmatrix} \quad (\text{A.21})$$

Note that Equation (A.21) has a singularity for $\theta = \pm\pi/2$. However, since a DA 42 will not perform any acrobatic maneuvers, this singularity will not be problematic.

Differential Equations for the Position

Integration of the velocity of the aircraft expressed in RF_E results in the aircraft position with respect to the origin of RF_E . The set of differential equations used to

calculate the position of the aircraft is also known as the navigation equation and can be written as,

$$\begin{bmatrix} \dot{x}_E \\ \dot{y}_E \\ \dot{z}_E \end{bmatrix} = Q_{BO}^T \begin{bmatrix} u \\ v \\ w \end{bmatrix} + V_{wind,E} \quad (A.22)$$

with $V_{wind,E}$ the constant velocity of the air with respect to the earth.

Differential Equations in the Aerodynamic Reference Frame

Additional equations of motion can be defined in RF_A . The differential equation for the translational velocity of the aircraft in RF_A can be written as,

$$\begin{bmatrix} \dot{V}_{TAS} \\ 0 \\ 0 \end{bmatrix} = m^{-1} \begin{bmatrix} F_{A_x} \\ F_{A_y} \\ F_{A_z} \end{bmatrix} - \begin{bmatrix} p_A \\ q_A \\ r_A \end{bmatrix} \times \begin{bmatrix} V_{TAS} \\ 0 \\ 0 \end{bmatrix} \quad (A.23)$$

This set of differential equations can be combined with Equation (A.19) when the relation between $[p_A \ q_A \ r_A]^T$ and $[p \ q \ r]^T$ is determined.

Similar to the differential equations for the Euler angles, it is possible to describe the rotational rate of RF_A with respect to RF_B as,

$$\begin{bmatrix} \dot{\alpha}_{X_B} \\ \dot{\alpha}_{Y_B} \\ \dot{\alpha}_{Z_B} \end{bmatrix} = \begin{bmatrix} \cos \alpha & 0 & -\sin \alpha \\ 0 & 1 & 0 \\ \sin \alpha & 0 & \cos \alpha \end{bmatrix} \begin{bmatrix} 0 \\ \dot{\alpha} \\ 0 \end{bmatrix} = \begin{bmatrix} 0 \\ \dot{\alpha} \\ 0 \end{bmatrix}$$

$$\begin{bmatrix} \dot{\beta}_{X_B} \\ \dot{\beta}_{Y_B} \\ \dot{\beta}_{Z_B} \end{bmatrix} = \begin{bmatrix} \cos \alpha & 0 & -\sin \alpha \\ 0 & 1 & 0 \\ \sin \alpha & 0 & \cos \alpha \end{bmatrix} \begin{bmatrix} \cos -\beta & \sin -\beta & 0 \\ -\sin -\beta & \cos -\beta & 0 \\ 0 & 0 & 1 \end{bmatrix} \begin{bmatrix} 0 \\ 0 \\ -\dot{\beta} \end{bmatrix} = \begin{bmatrix} \dot{\beta} \sin \alpha \\ 0 \\ -\dot{\beta} \cos \alpha \end{bmatrix}$$

The rotational rate of RF_A with respect to the inertial reference frame RF_E can then be determined from the difference between the rotational rate of RF_B with respect to RF_E and the rotational rate of RF_A with respect to RF_B or,

$$\begin{bmatrix} p_A \\ q_A \\ r_A \end{bmatrix}_B = \begin{bmatrix} p \\ q \\ r \end{bmatrix} - \begin{bmatrix} \dot{\beta} \sin \alpha \\ \dot{\alpha} \\ -\dot{\beta} \sin \alpha \end{bmatrix} \quad (A.24)$$

Note that Equation (A.24) is expressed in RF_B and should be transformed to RF_A to be used in the differential equations describing the forces in RF_A . This leads to the following result,

$$\begin{bmatrix} p_A \\ q_A \\ r_A \end{bmatrix} = Q_{BA}^T \left(\begin{bmatrix} p \\ q \\ r \end{bmatrix} - \begin{bmatrix} \dot{\beta} \sin \alpha \\ \dot{\alpha} \\ -\dot{\beta} \sin \alpha \end{bmatrix} \right) \quad (A.25)$$

Combining Equation (A.13) and Equation (A.24) results in the following three differential equations,

$$\begin{bmatrix} \dot{V}_{TAS} \\ \dot{\alpha} \\ \dot{\beta} \end{bmatrix} = \begin{bmatrix} 0 & 0 & 0 \\ -\cos \alpha \tan \beta & 1 & -\sin \alpha \tan \beta \\ \sin \alpha & 0 & -\cos \alpha \end{bmatrix} \begin{bmatrix} p \\ q \\ r \end{bmatrix} + \begin{bmatrix} V_{TAS} & 0 & 0 \\ 0 & 0 & 1/\cos \beta \\ 0 & -1 & 0 \end{bmatrix} \frac{F_A}{mV_{TAS}} \quad (\text{A.26})$$

When the forces on the aircraft are not described in RF_A , but in RF_B , it is possible to evaluate the rate of change of the aerodynamic reference frame parameters by substituting $F_A = Q_{BA}^T F_B$ in Equation (A.26), i.e.,

$$\begin{bmatrix} \dot{V}_{TAS} \\ \dot{\alpha} \\ \dot{\beta} \end{bmatrix} = \begin{bmatrix} 0 & 0 & 0 \\ -\cos \alpha \tan \beta & 1 & -\sin \alpha \tan \beta \\ \sin \alpha & 0 & -\cos \alpha \end{bmatrix} \begin{bmatrix} p \\ q \\ r \end{bmatrix} + \begin{bmatrix} V_{TAS} \cos \alpha \cos \beta & V_{TAS} \sin \beta & V_{TAS} \sin \alpha \cos \beta \\ -\sin \alpha / \cos \beta & 0 & \cos \alpha / \cos \beta \\ -\cos \alpha \sin \beta & \cos \beta & -\sin \alpha \sin \beta \end{bmatrix} \frac{F_B}{mV_{TAS}} \quad (\text{A.27})$$

Substituting Equation (A.12) in Equation (A.27) and using the relations,

$$\begin{aligned} V_{TAS} &= \sqrt{u^2 + v^2 + w^2} \\ \tan \alpha &= w/u \\ \sin \beta &= v/V_{TAS} \end{aligned} \quad (\text{A.28})$$

yields the shorter expressions,

$$\begin{aligned} \dot{V}_{TAS} &= \frac{u\dot{u} + v\dot{v} + w\dot{w}}{V_{TAS}} \\ \dot{\alpha} &= \frac{u\dot{w} - w\dot{u}}{u^2 + w^2} \\ \dot{\beta} &= \frac{v\dot{V}_{TAS} - V_{TAS}\dot{v}}{\cos \beta V_{TAS}^2} \end{aligned} \quad (\text{A.29})$$

Please note that Equation (A.29) is also exactly the derivative of Equation (A.28), which implies that the derivations are correct.

Differential Equations in the Kinematic Reference Frame

Eventhough the forces and moments acting on an aircraft are generally not expressed in RF_K , a result similar to Equation (A.29) can be obtained for the rate of change of the kinematic reference frame parameters. Differentiation of the expressions,

$$\begin{aligned} V_{GS} &= \sqrt{u_E^2 + v_E^2 + w_E^2} \\ \sin \gamma_k &= -w_E/V_{GS} \\ \tan \chi_k &= v_E/u_E \end{aligned} \quad (\text{A.30})$$

yields,

$$\begin{aligned} \dot{V}_{GS} &= \frac{u_E \dot{u}_E + v_E \dot{v}_E + w_E \dot{w}_E}{V_{GS}} \\ \dot{\gamma}_k &= \frac{-\dot{w}_E V_{GS} + w_E \dot{V}_{GS}}{\cos \gamma_k V_{GS}^2} \\ \dot{\chi}_k &= \frac{u_E \dot{v}_E - v_E \dot{u}_E}{u_E^2 + v_E^2} \end{aligned} \quad (\text{A.31})$$

PARAMETER DETERMINATION USING FLIGHT TEST DATA

This appendix analyses log files that were provided by Diamond Aircraft Industries GmbH with the aim to obtain aerodynamic model parameters.

A method that can be used for aerodynamic model parameter estimation is the two-step method [82]. In this method the first step is to combine the sensor data and estimate the state of the aircraft at each time-step using a Kalman filter. Then, in the second step, the parameters of the model are estimated using least squares estimation. In order to use the log data for step one, data synchronization and several data corrections are needed.

Data Synchronization

The data used in step one, is measured by different sensors.

- The output of an Inertial Measurement Unit (IMU) consists of angular rates ω and specific forces f , which are also referred to as total accelerations. The output is updated at rates from 50 Hz to 1000 Hz.
- Global Positioning System (GPS) receivers measure the position and velocity of the aircraft in RF_E . From these measurements the ground speed V_{ground} , track

angle χ and flight path angle γ can be reconstructed. The receiver updates the measurement at 1 Hz.

- The Air Data Probe (ADP) measures, true airspeed V_{TAS} , angle of attack α and angle of sideslip β . Probes with an update rate of 100 Hz are commercial-of-the-shelf available.
- The DA 42 has a Full Authority Digital Engine Control (FADEC) system and the throttle setting δ_{th} can be read directly from this system at a rate of 70 Hz.
- Finally, potentiometers or synchros, with update rates of 1000 Hz, can be used to measure control surface deflections $\delta_a, \delta_e, \delta_r$.

The log-files provided by Diamond Aircraft Industries GmbH contain three timestamps, GPS time, PC1 time and PC2 time. Correct synchronization of the data is only possible when all clocks are synchronized at the start of the flight trails, or when the time delay between the clocks is known. Interpolation of the data is not needed, as explained in step one of the two-step method. Several corrections for each sensor are needed, and will be introduced in the following two paragraphs.

Inertial Measurement Unit Data Corrections

Measurements from the Inertial Measurement Unit (IMU) must be corrected for off-CoG position, also known as lever arm effects, and initial attitude with respect to RF_B . Temperature dependent and axis misalignment effects are usually already corrected for by the manufacturer and therefore not treated here.

Corrections for initial attitude can be made using,

$$f_{I_B} = Q_{I_B I} f_I \quad (\text{B.1})$$

$$\omega_B = \omega_{I_B} = Q_{I_B I} \omega_I \quad (\text{B.2})$$

where RF_I represents the reference frame aligned to the IMU, RF_{I_B} the reference frame aligned to RF_B but located at the position of the IMU and $Q_{I_B I}$ the transformation matrix between RF_I and RF_{I_B} , defined using three subsequent rotations over ψ_0, θ_0 and ϕ_0 . $Q_{I_B I}$ can be simplified for small misalignment angles using,

$$Q_{I_B I} \approx \begin{bmatrix} 1 & 0 & -\theta_0 \\ 0 & 1 & \phi_0 \\ \theta_0 & -\phi_0 & 1 \end{bmatrix} \quad (\text{B.3})$$

After leveling the aircraft with a spirit level and putting the IMU in alignment mode, the angles θ_0 and ϕ_0 can be read directly from the IMU [65]. Determination of ψ_0 is

not possible using this technique and is therefore assumed to be zero in Equation (B.3).

The position difference between IMU and the CoG results in false measurements of specific force in the presence of rotation. The velocity of a point P can be written as introduced in Equation (A.8),

$$V_P = V_B + \frac{\partial r_P}{\partial t} + \omega_B \times r_P \quad (\text{B.4})$$

Suppose the distance between IMU and CoG is fixed, i.e., $\frac{\partial r_P}{\partial t} = 0$. Then the total acceleration of this point is calculated, by differentiating both sides of the equation,

$$A_P + \omega_B \times V_P = A_B + \omega_B \times V_B + \dot{\omega}_B \times r_P + \omega_B \times (\omega_B \times r_P) \quad (\text{B.5})$$

The total acceleration of P is the specific force measured by the IMU, $A_P + \omega_B \times V_P = f_{I_B}$ and the total acceleration of the body can be written as, $A_B + \omega_B \times V_B = f_B$. Equation (B.5) then becomes,

$$f_B = f_{I_B} - \dot{\omega}_B \times X_{IMU} - \omega_B \times (\omega_B \times X_{IMU}) \quad (\text{B.6})$$

The corrections given by Equations (B.1) and (B.6) need to be applied to the data measured by the IMU to relate this data to the state variables used in the equations of motion.

Air-Data Probe Data Corrections

Measurements from an Air-Data Probe (ADP) need to be corrected for the measured airflow due to the rotational velocity of the aircraft, the up- and side-wash caused by the aircraft itself and movement of the ADP due to bending and torsion of the wing under load. Corrections for temperature and air density effects are made by most manufacturers and therefore not treated here. Also, the assumption is made that the ADP is closely aligned to RF_B using a spirit level.

The errors introduced by the up- and side-wash due to the aircraft are also known as aerodynamic position errors. Laban provides a detailed investigation of these effects in his Ph.D. thesis [65]. Many manufacturers supply guidelines for the minimum distance, at different places on the aircraft, at which the ADP should be installed in order to make these errors negligible. The assumption is made that these guidelines were followed during the installment of the ADP used to create the log-files and that no further corrections are needed.

The errors introduced by the rotation of the aircraft are also known as kinematic position errors. Correction is possible by again using Equation (A.8) and setting $\frac{\partial r_P}{\partial t} = 0$, assuming that the position of the ADP is fixed with respect to the center of gravity. The measured airspeed can be converted to airspeed expressed in RF_B using,

$$V_B = V_{ADP} - \omega_B \times X_{ADP} \quad (\text{B.7})$$

In the case the ADP is mounted on the wing other errors are introduced by the torsion and bending of the wing under load. This can be demonstrated by an example. Suppose the wing bends 5 cm with a sinusoidal motion of 5 Hz, which is of course overly simplified. An ADP, mounted at the wing tip, then moves with a vertical velocity of $0.5\pi \cos(10\pi t)$. When flying at 60 m/s, the angle of attack introduced by this movement is, $\alpha_{bending} = \arctan\left(\frac{0.5\pi \cos(10\pi t)}{60}\right)$ rad, or $\approx 1.5 \cos(10\pi t)$ deg. This leads to a maximum error due to the bending of the wing of $\alpha_{bending,max} = 1.5$ deg, a considerable error. Both torsion and bending can be seen as a disturbance (noise), acting on the ADP measurements. Correcting these errors would require measurements of the amount of bending and torsion that occurred during the flight. These measurements are not available. Since the Kalman filter in step one should be able to filter out this noise, no further correction steps are taken.

Step One

An Extended Kalman Filter (EKF) may be used to combine (fuse) the different measurement signals into an estimated state. This filter first predicts the current state using the state at the previous time step and a nonlinear system function f . It also predicts the estimate covariance using a linearized and discretized system matrix

$$F_{k-1} = e^{\left. \frac{\partial f}{\partial x} \right|_{\hat{x}_{k-1|k-1}, u_{k-1}}} \Delta t,$$

$$\begin{aligned} \hat{x}_{k|k-1} &= f(\hat{x}_{k-1|k-1}, u_{k-1}) \\ P_{k|k-1} &= F_{k-1} P_{k-1|k-1} F_{k-1}^T + W_{k-1} Q_{k-1} W_{k-1}^T \end{aligned} \quad (\text{B.8})$$

where \hat{x} is the state prediction vector, u is a vector of measurements, P is the estimate covariance matrix, W is a discrete process noise matrix and Q is a diagonal matrix containing the noise variances of u . Since the measurements of the IMU are available at a high update rate and have a small noise level it is common practice to use these measurements in the prediction step.

The second step, or update step, of the EKF corrects the predicted values. This step can run at a lower frequency and compares a nonlinear observation vector h to GPS and ADP measurements z , thereby providing a measurement residual. It

also provides a covariance for the measurement residual using a linearized and discretized observation matrix $H_k = e^{\frac{\partial h}{\partial x}|_{\hat{x}_{k|k-1}} \Delta t}$,

$$\begin{aligned}\tilde{y}_k &= z_k - h(\hat{x}_{k|k-1}) \\ S_k &= H_k P_{k|k-1} H_k^T + R_k\end{aligned}\tag{B.9}$$

where \tilde{y} is the measurement residual, S is the residual covariance and R is a discrete diagonal matrix containing the noise variances of z . The residual covariance is used to compute the optimal Kalman gain, in order to weigh the correction term with the amount of “trust” of each data source,

$$K_k = P_{k|k-1} H_k^T S_k^{-1}\tag{B.10}$$

The update part is finally calculated, using the Kalman gain, as,

$$\begin{aligned}\hat{x}_{k|k} &= \hat{x}_{k|k-1} + K_k \tilde{y}_k \\ P_{k|k} &= (I - K_k H_k) P_{k|k-1}\end{aligned}\tag{B.11}$$

The updated state estimate is used in the subsequent prediction step, thereby reducing the influence of the IMU drift on the state estimate.

A disadvantage of the EKF is that rapid divergence of the estimated parameters is possible, due to the linearization of $f(\hat{x}_{k-1|k-1}, u_{k-1})$ and $h(\hat{x}_{k|k-1})$. To reduce this risk, the update step can be iterated until convergence is reached. The Iterated Extended Kalman Filter (IEKF) will be used in step one of the two-step method for estimating the state at each data point in the log-file. For a more in-depth treatment of Kalman filters, the reader is referred to [136].

Step Two

The estimated state from step one can be used to estimate the parameters of the aerodynamic model of a DA 42. Since the model uses a linear combination of the parameters, a simple approach would be to use linear least squares for this second step,

$$\begin{aligned}y &= A\theta \\ \theta_{LS} &= [A^T A]^{-1} A^T y\end{aligned}\tag{B.12}$$

where y is a vector containing dimensionless force and moment coefficients at every time step $k = 0, 1, \dots, n$, A is a matrix containing the product parts of the Taylor expansion at every time step and θ is a vector containing the aerodynamic model parameters. Note that the Moore-Penrose pseudo inverse is used, since A is not a square matrix.

The variables used in the least square method may still contain errors, however. The total least squares method takes the presence of errors into account and uses a singular value decomposition to determine the parameters. Suppose the error in the variables can be written as,

$$y + f = (A + e)\theta \quad (\text{B.13})$$

where f and e are error matrices. The total least squares method finds θ that minimizes f and e for A and y . This is done using the singular value decomposition of $[A \ y]$,

$$[A \ y] = U\Sigma \begin{bmatrix} V_{AA} & V_{Ay} \\ V_{yA} & V_{yy} \end{bmatrix}^* \quad (\text{B.14})$$

The parameter vector θ is then found using,

$$\theta = -V_{Ay}V_{yy}^{-1} \quad (\text{B.15})$$

Results

Analysis of the log files for parameter estimation using the two-step method reveals several recording flaws,

- The recorded data does not contain body angular rate measurements ω_I .
- The location of the IMU is recorded, but initial attitude is not.
- It is unclear whether off-CoG corrections are applied to the measurements or not.
- X_{accel} could mean the acceleration of the vehicle in X_B -direction, but also the specific force, or total acceleration of the IMU in its X -direction.
- It is neither recorded whether GPS time was used for time stamping the measurements or PC time, nor whether the PC1 and PC2 clocks have been synchronized.

In order to apply the two-step method, the angular rates are reconstructed by differentiating the roll, pitch and yaw measurements and transforming these rotational rates to RF_B , using Equation (2.3). The assumption is made that PC1 and PC2 times are synchronized, such that the data in the log files can be combined. However, filtering the data using the IEKF, with and without sensor corrections, produces poor results. Estimating the aerodynamic model parameters using the reconstructed state has not even been tried.

AIRCRAFT MODEL EIGENMOTIONS

This appendix contains the figures used for validation of the DA 42 aircraft model.

Figure C.1 shows the short period, a heavily damped longitudinal eigenmotion. Although this motion is usually flown with a step input on the elevator rather than an impulse, the figure still clearly shows the influence of this input on the state parameters.

Figure C.2 shows the phugoid, a lightly damped longitudinal eigenmotion. A singlet is given to the elevator, letting the pitch angle θ reach 20 degrees. Controls are released and the aircraft exchanges potential energy for kinetic and vice versa for over three minutes.

Figures C.3 and C.4 show the Dutch roll, a well-damped lateral eigenmotion. With a doublet on the rudder the aircraft is given a yawing motion. This accelerates one wing while decelerating the other, causing a difference in lift generation. Due to this difference in lift the aircraft starts rolling. However, the aircraft is dynamically stable and tries to return to the equilibrium situation. The decelerated wing starts accelerating and vice versa, creating a rolling motion in opposite direction. The aircraft overshoots the equilibrium situation several times before the motion is completely damped out. Figure C.4 shows the relation between roll rate and yaw rate during this motion.

Figure C.5 shows the aperiodic roll, or roll subsidence mode, an aperiodic lateral eigenmotion. A doublet is given to the aileron and the roll rate p accelerates to a certain value and no further. Without input the roll rate rapidly decelerates back to zero. The small oscillations shown in the roll rate plot are caused by the Dutch roll and short period acting on top of the aperiodic roll eigenmotion.

Figure C.6 shows the spiral, also an aperiodic lateral eigenmotion. A singlet is given to the aileron until 20 degrees bank angle ϕ is reached. There the controls are released and for most aircraft the bank angle keeps increasing until the aircraft gets into a high-speed spiral dive. The DA 42 has spiral stability, however. After releasing the controls the aircraft rotates back towards the equilibrium situation. This behavior is caused by a sufficiently large dihedral angle of the wing, causing a rolling moment under sideslip β , and a sufficiently long vertical tail arm, increasing the yaw damping of the aircraft.

Since the Figures C.1 until C.6 show results highly comparable to the QTG provided by DS, the assumption is made that the aircraft model behaves similar to a DA 42 in the neighborhood of the operating point of 120kts at 6,000 ft and in cruise configuration. Rough validation is therefore complete.

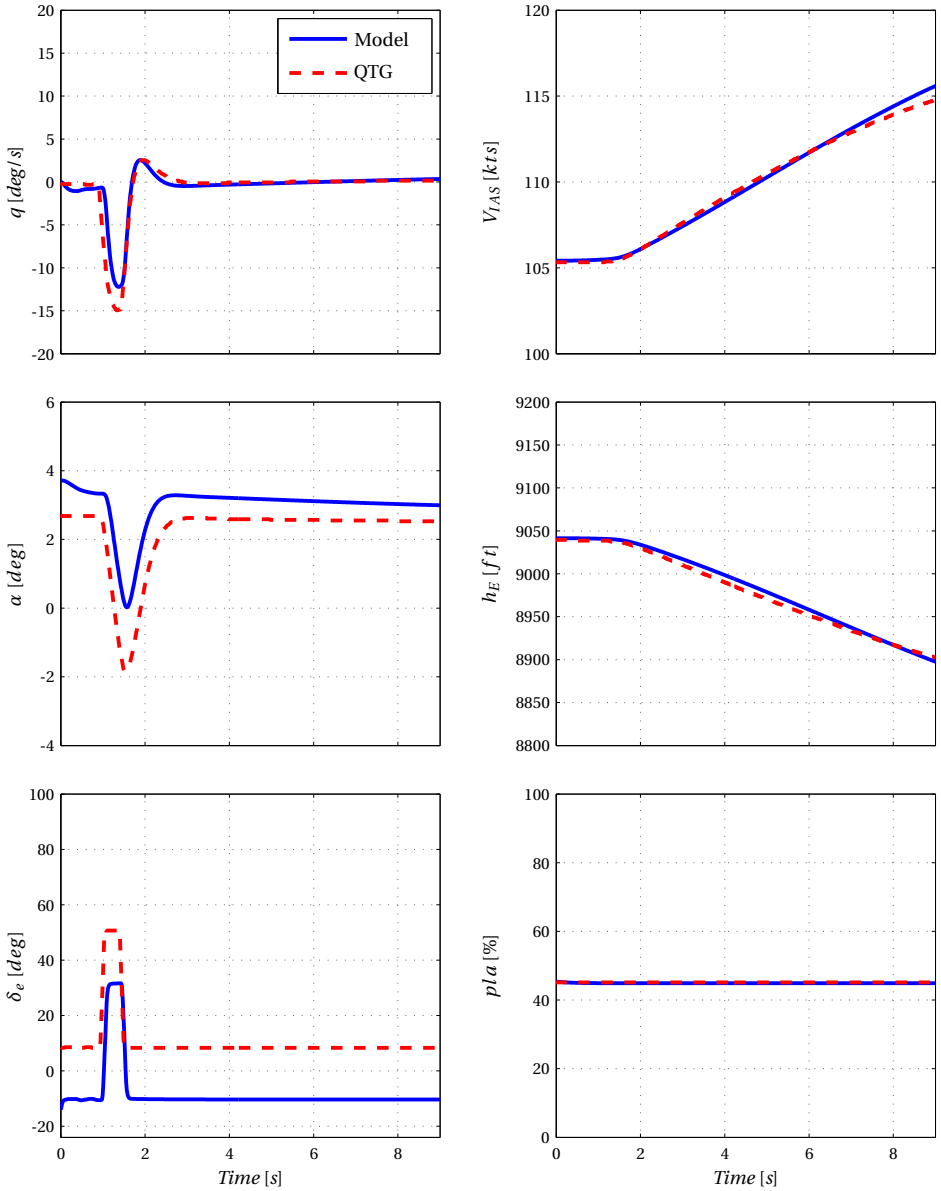


Figure C.1: Short Period

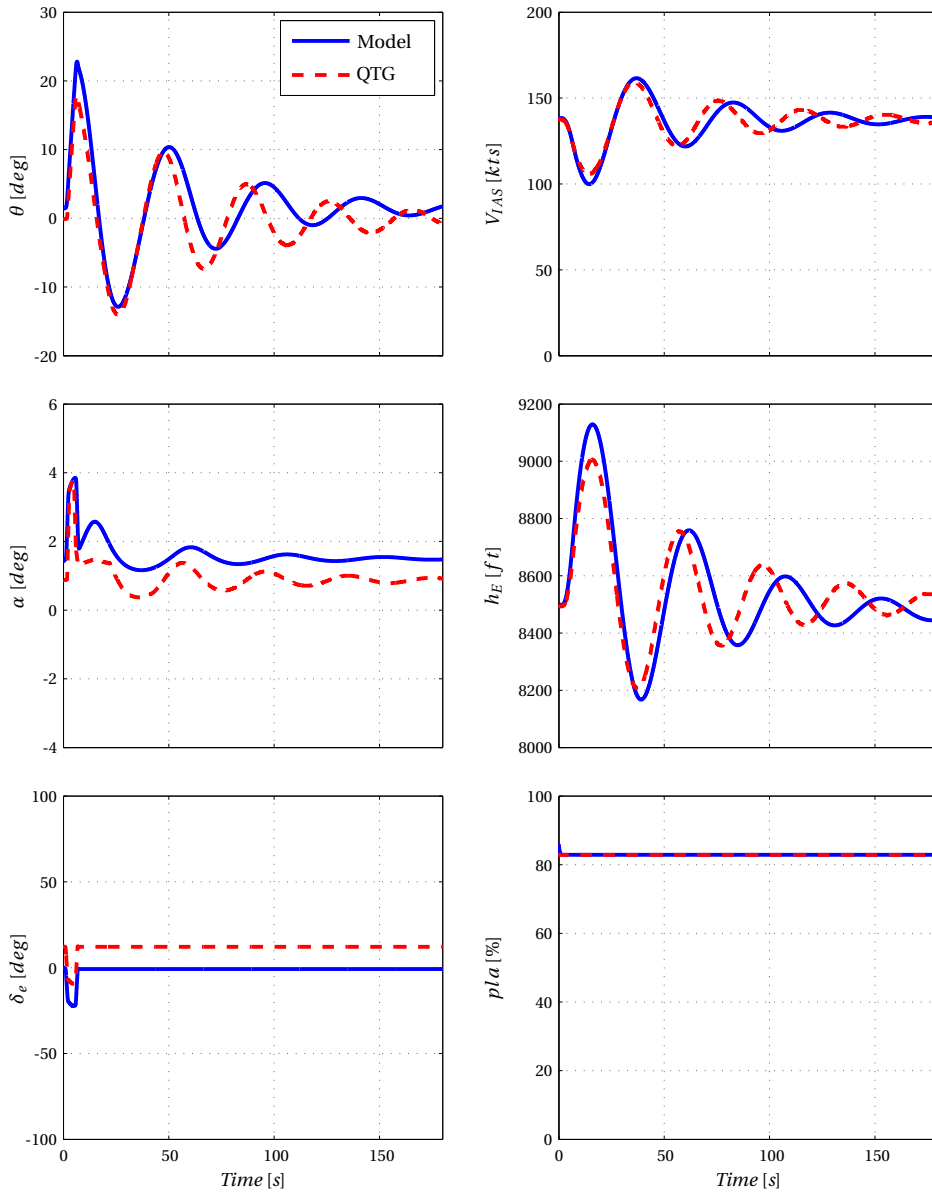


Figure C.2: Phugoid

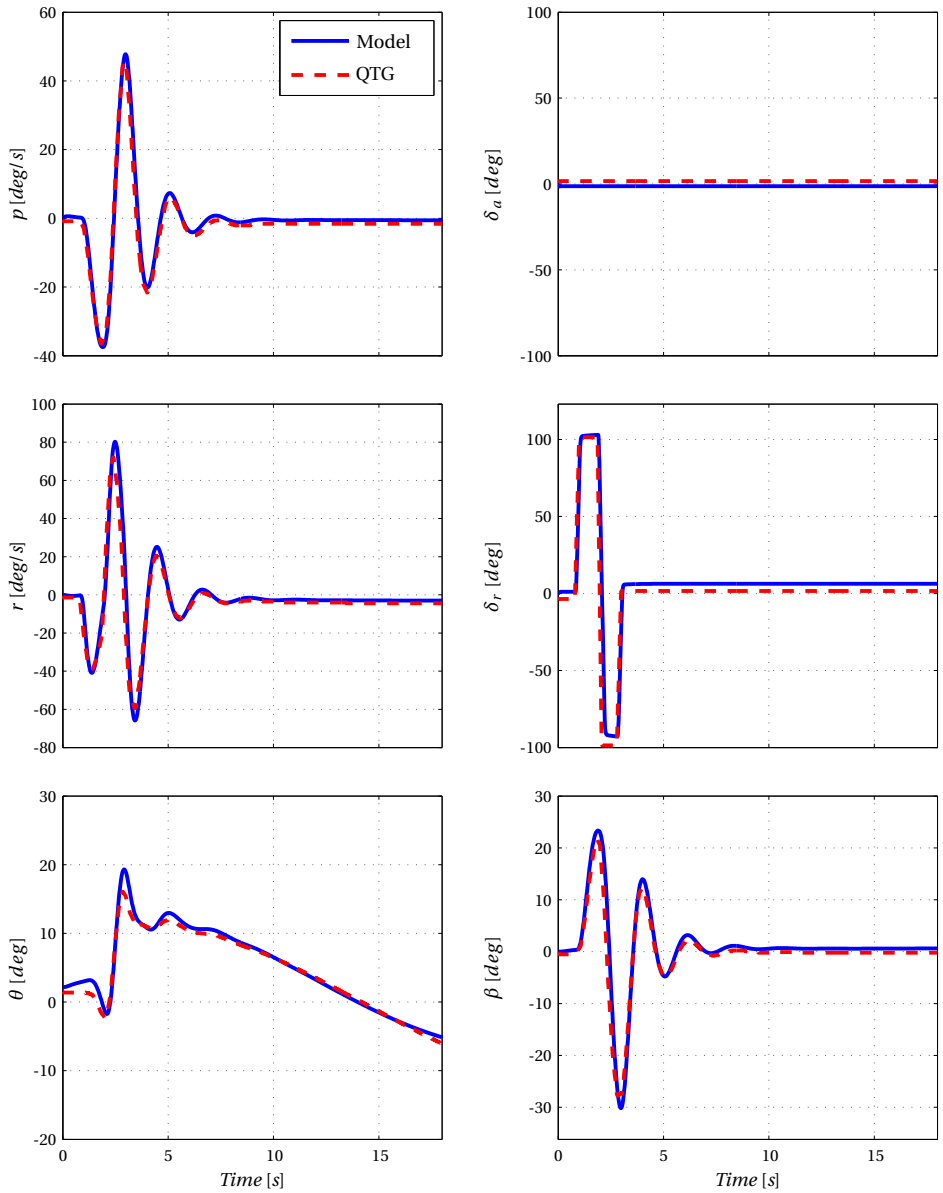


Figure C.3: Dutch roll

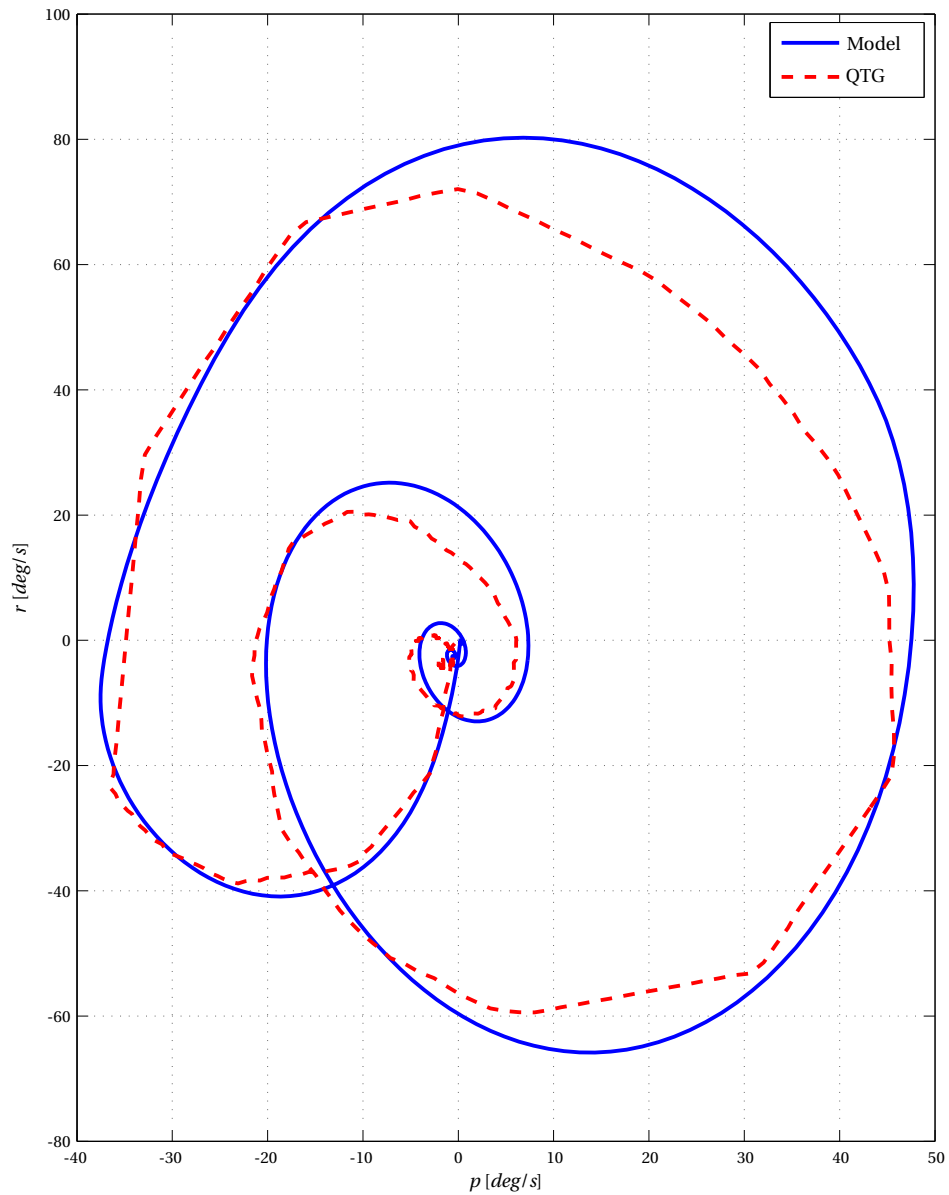


Figure C.4: Dutch roll, roll rate vs. yaw rate

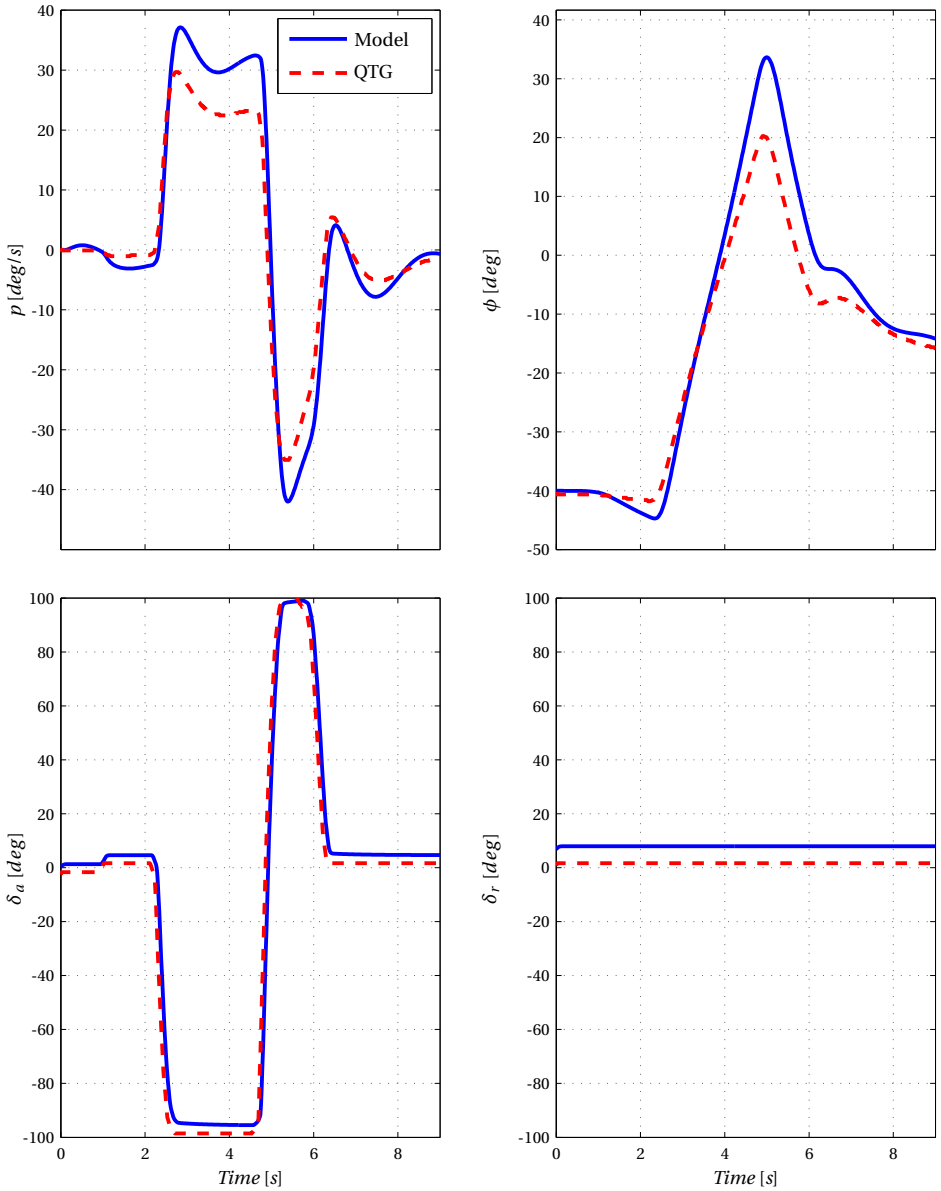


Figure C.5: Aperiodic roll

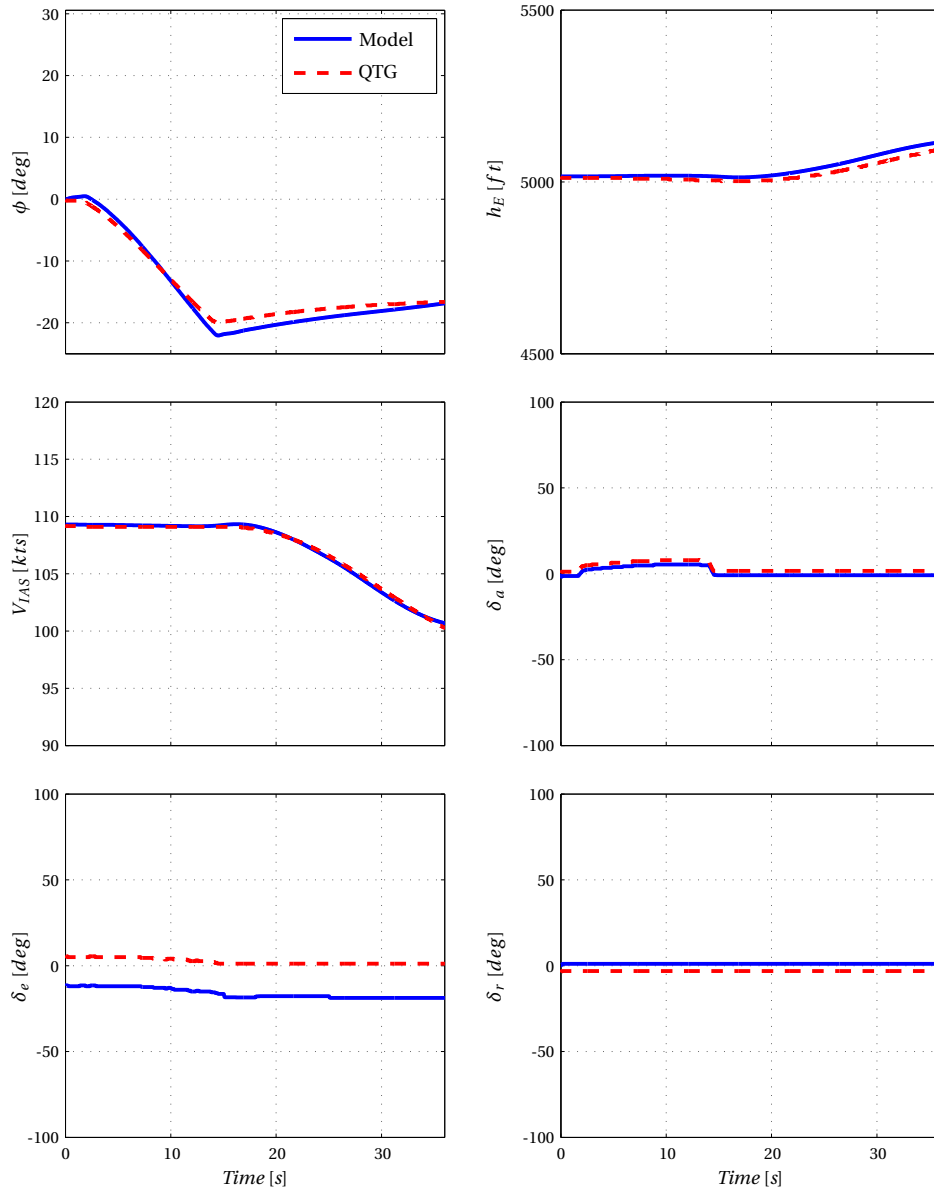


Figure C.6: Spiral

ADDITION OF A LANDING MODEL

The basis of the DA 42 dynamical model is given in Sections 2.3 and 2.4. With this framework in place, an extension can be made to the model that increases the usability. This extension is made for theoretic purposes and will not be used for control law design. Validation of this extension is therefore beyond the scope of interest.

When the aircraft is considered to be a point mass, the normal force due to the aircraft-ground interaction can be modeled as a spring damper system as shown in Figure D.1,

$$F_{G,Z_B} = \begin{cases} 0, & \text{if } d < 0 \\ -kd - c\dot{d}, & \text{if } 0 \leq d \leq d_{max} \\ -kd_{max} - c\dot{d}, & \text{if } d > d_{max} \end{cases} \quad (D.1)$$

where k is the spring constant and c is the damping constant. The deflection distance of the landing gear d can be calculated using,

$$d = z_G - (h_e - h_{ground}) \quad (D.2)$$

with z_G the distance between the CoG and the bottom of the landing gear.

The friction caused by the interaction between the tires and the runway pavement is a complex phenomenon and can be modeled in different ways varying in complexity. Complex methods such as, LuGre [18] and Pacejka's Magic Formula

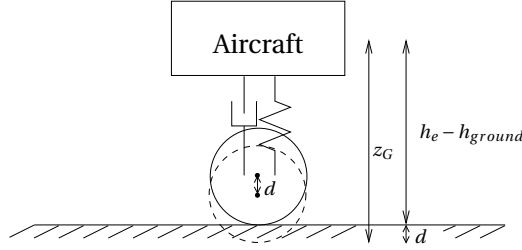


Figure D.1: Simple landing model: point mass-spring-damper system

[94] account for many properties of tire-ground interaction. For example, LuGre includes: Coulomb friction, stiction, viscous friction, pre-sliding displacement, frictional lag, varying brake-away force and stick-slip motion. The landing model used in this thesis only incorporates Coulomb and viscous friction, using the following simple relations,

$$\begin{aligned} F_{G,X_B} &= \mu_{roll} F_{G,Z_B} u^* \\ F_{G,Y_B} &= \mu_{side} F_{G,Z_B} v^* \end{aligned} \quad (D.3)$$

where μ_{roll} is the rolling resistance coefficient, μ_{side} is the lateral displacement resistance coefficient, u^* and v^* are the forward respectively lateral velocity of the vehicle saturated between ± 1 meters per second.

When the aircraft is not considered to be a point mass, the total landing forces and moments consist of the forces and moments at each part of the aircraft connected to the runway. In the uncompressed situation, a wheel is located at X_{G_i} , where i indicates the i -th wheel on the aircraft. The deflection distance of this wheel and landing strut is given by,

$$d_i = [-\sin\theta \ \sin\phi \ 1] X_{G_i} - (h_e - h_{ground_i}) \quad (D.4)$$

in which the approximation is made that $\cos\theta = \cos\phi = 1$. Figure D.2 shows the longitudinal situation for the landing gears of the aircraft.

The rate of change of deflection then follows from,

$$\dot{d}_i = [-q \cos\theta \ p \cos\phi \ 0] X_{G_i}^* - \dot{h}_e \quad (D.5)$$

where $X_{G_i}^*$ represents the bottom of the wheel in deflected state. When $d_i > 0$, the

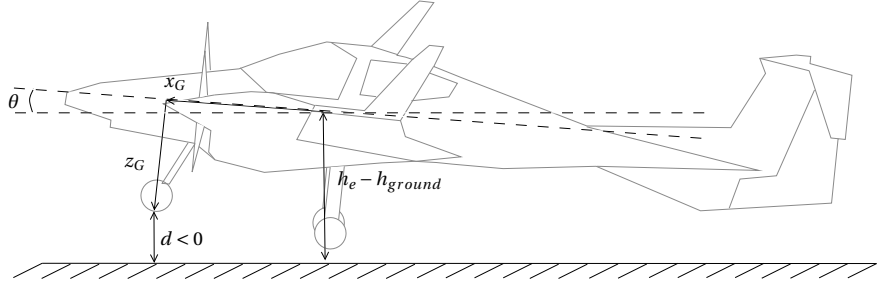


Figure D.2: Three point landing model

i -th landing gear touches the runway and the reaction forces follow from,

$$\begin{aligned}
 F_{G,X_{W_i}} &= \mu_{roll_i} F_{G,Z_{W_i}} u_{W_i}^* \\
 F_{G,Y_{W_i}} &= \mu_{side_i} F_{G,Z_{W_i}} v_{W_i}^* \\
 F_{G,Z_{W_i}} &= \begin{cases} 0, & \text{if } d_i < 0 \\ -k_i d_i - c_i \dot{d}_i, & \text{if } 0 \leq d_i \leq d_{max_i} \\ -k_i d_{max_i} - c_i \dot{d}_i, & \text{if } d_i > d_{max_i} \end{cases} \quad (D.6)
 \end{aligned}$$

in which the velocity of the aircraft expressed at the landing gear position V_{W_i} can be described using Equation (A.8),

$$\begin{aligned}
 V_{W,B_i} &= V_B + \omega_B \times X_{G_i}^* \\
 V_{W_i} &= Q_{BW}^T V_{W,B_i} \quad (D.7)
 \end{aligned}$$

where,

$$Q_{BW} = Q_{BO} \begin{bmatrix} \cos \psi & \sin \psi & 0 \\ -\sin \psi & \cos \psi & 0 \\ 0 & 0 & 1 \end{bmatrix}^T \begin{bmatrix} \cos \psi_{wheel} & \sin \psi_{wheel} & 0 \\ -\sin \psi_{wheel} & \cos \psi_{wheel} & 0 \\ 0 & 0 & 1 \end{bmatrix} \quad (D.8)$$

is a reference frame partly aligned to RF_O , but attached to the heading of the wheel ψ_{wheel} . Note that only the front wheel is steered and that for the rear wheels $\psi_{wheel,rear} = 0$, aligning $RF_{W,rear}$ to the heading of the aircraft ψ . Since the landing gear forces are generated at the point of contact between landing gear and runway, they should be translated to RF_B . This causes a moment on the aircraft,

$$F_{G_{B,i}} = Q_{BW} F_{G_{W,i}} \quad (D.9)$$

$$M_{G_{B,i}} = X_{G_i}^* \times F_{G_{B,i}} \quad (D.10)$$

Once translated the total forces and moments generated by all contact points is calculated as,

$$\begin{aligned} F_{G_B} &= \sum_{i=1}^n F_{G_{B,i}} \\ M_{G_B} &= \sum_{i=1}^n M_{G_{B,i}} \end{aligned} \tag{D.11}$$

Figure D.3 shows the spring deflections for each wheel during the landing of a slightly banked aircraft. The left wheel touches the ground slightly after the right one and oscillations are shown in the deflections of both landing gears. On the ground the aircraft brakes, which causes an increase in effective weight felt by the spring in the nose wheel. After 38 seconds the aircraft comes to a complete stop and the main wheels, which are closer to the CoG, take on the major part of the weight. The figure indicates that the landing model works properly. This does not mean that the landing model reflects the actual landing behavior of a DA 42.

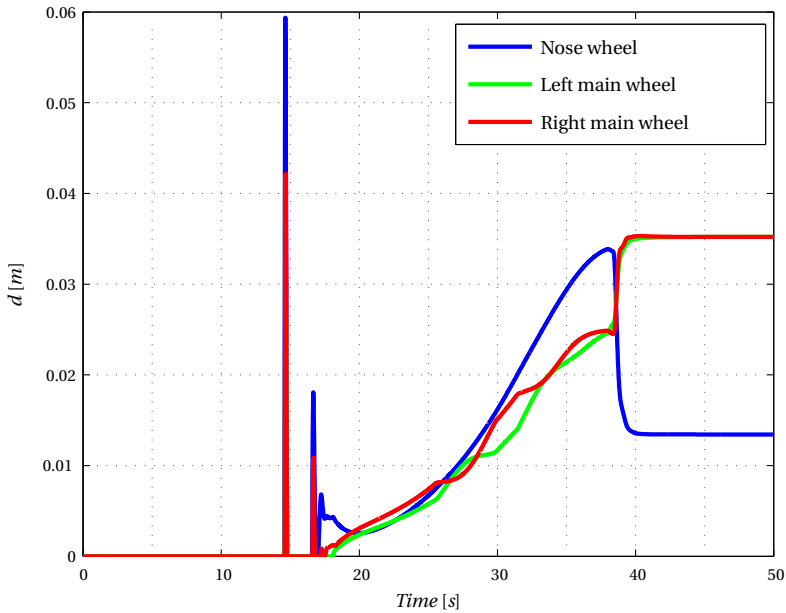


Figure D.3: Spring deflections during the landing of a slightly banked aircraft.

CLASSICAL FLIGHT CONTROL DESIGN

This appendix provides the design steps taken to develop the classical FCLs used in SAFAR. Bode plots are used to indicate open and closed-loop characteristics of the controlled aircraft. This is common practice in control design [103] and gives insight into the performance and robustness of the FCL. Note that the model validity was only demonstrated in Chapter 2 for flying 120kts at 6,000ft in cruise configuration. The FCLs designed in this Appendix should therefore be used with caution at operating points laying farther from this design point.

E.1 Sideslip Compensator

Figure E.1 shows the sideslip compensator in a block diagram. The system transfer function β/δ_r is obtained by linearizing the aircraft model combined with FBW platform at the design point, 120 kts and 6,000 ft. Whether gain scheduling is needed for the other parts of the flight envelope is checked further on in the design. Selecting a Proportional (P) controller with a gain of 1, i.e.,

$$C(s) = K_P \tag{E.1}$$

with $K_P = 1$, results in the open and closed loop behavior shown in Figure E.2. Clearly $|Y(s)/D(s)|$ is large in the low frequency range, meaning that disturbance rejection is inadequate. This can also be seen from the small loop gain in the open-loop response. The gain and phase margins are satisfactory, and also the noise attenuation $|Y(s)/N(s)|$ is good for high frequencies. Adding an Integral (I) gain to the

controller,

$$C(s) = K_P + K_I/s \quad (\text{E.2})$$

with $K_P = 0.4$ and $K_I = 0.8$, results in the open and closed loop behavior shown in Figure E.3. Disturbance rejection has improved, while keeping adequate gain and phase margins. The gains for this controller are obtained by minimizing $|Y(s)/D(s)|$, using MATLABs nonlinear least square solver *lsqnonlin*, while keeping $GM \geq 9.5$ dB and $PM \geq 35$ degrees. The disturbance rejection shows a peak at 3.2 rad/s, similar to the peaks shown in Figure 4.16 due to the time delays in the system. Adding a Differential (D) term to the controller, contributes lead to the closed-loop response and could solve the peak problem. However, the sideslip measurements contain a significant amount of noise. Differentiation would amplify this noise and cause the command signal to be noisy as well. Instead yaw-rate feedback can be used in an inner loop, as shown in Figure E.4. The inner-loop controller is again selected as a P controller with gain 1, i.e., $C_{IL} = K_P = 1$. The feedback term H_{IL} is designed using a mild washout filter as suggested in Section 4.2,

$$H_{IL}(s) = K_{IL} \frac{\tau s}{\tau s + 1} \quad (\text{E.3})$$

with $K_{IL} = -0.4$ and $\tau = 1.53$ seconds. Figure E.5 shows the open and closed-loop behavior of this system. The disturbance rejection has improved significantly, but still shows a minor peak and the phase margin has decreased. Adding a lead-lag filter in the outer-loop controller, i.e.,

$$C(s) = \left(K_P + \frac{K_I}{s} \right) \left(\frac{s + 1/T_1}{1 + \gamma/T_1} \right) \left(\frac{s + 1/T_2}{s + 1/(\beta T_2)} \right) \quad (\text{E.4})$$

with $K_P = 1.7$, $K_I = 0.6$, $T_1 = 0.56$ s, $T_2 = 0.91$ s, $\gamma = 2.77$ and $\beta = 3.71$, results in the open and closed loop behavior shown in Figure E.6. The peak in the disturbance response has decreased without negatively affecting the gain and phase margin.

Section 4.2 remarked that slow lateral oscillations could be introduced by adding a sideslip compensator. Figure E.7 shows a pole-zero map of the unaugmented and the sideslip compensated closed-loop systems. Several additional imaginary poles are present in the latter system, suggesting that the FCL indeed introduces extra lateral dynamical modes. By looking at the extra poles with the smallest damping ($\zeta = 0.45$) and the corresponding natural frequency ($\omega_n = 5.0$ rad/s), the sideslip compensator seems to cause fast and properly damped oscillations, rather than a slow and poorly damped one. The SISO design of the sideslip compensator at the design operating point is thereby finished.

Figure E.8 shows the gain margin, phase margin and two disturbance rejection measures, at different operating conditions. Clearly the gain and phase margin re-

main adequate throughout the flight envelope. The first disturbance rejection measure is calculated as,

$$DR = \sum_{k=1}^n \left| \frac{Y(\omega(k))}{D(\omega(k))} \right| d\omega_d \quad (\text{E.5})$$

in which $\omega(k) = 10^{-2+(k-1)\omega_d}$ and $\omega_d = 4/(n-1)$ with $n = 100$. In other words DR is the summation of the magnitude (in gain [-]) of the closed-loop transfer function from disturbance to output evaluated over n logarithmically equi-spaced points in the frequency range from 0.01 rad/s to 100 rad/s. Since DR does not change much over the flight envelope, comparable disturbance rejection can be expected at every operating point. The second disturbance rejection measure is the maximum magnitude (in [dB]) of the closed-loop transfer function from disturbance to output. This plot shows that the disturbances are rejected by at least -4.7 dB throughout the flight envelope. It can therefore be concluded that gain scheduling is not needed for the sideslip compensator.

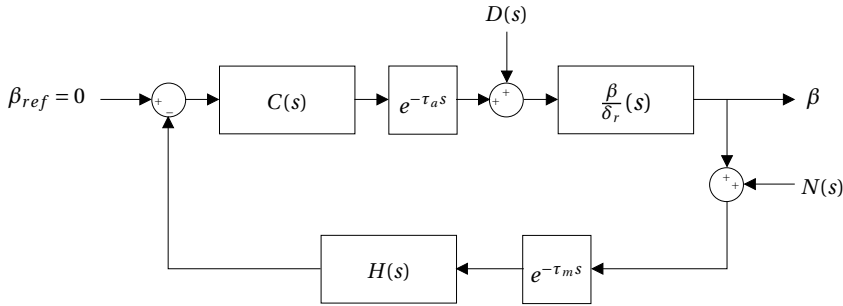


Figure E.1: Block diagram for the sideslip compensator, in which β/δ_r represents the transfer function of the sideslip response due to rudder input of the aircraft combined with the FBW platform, $C(s)$ the FCL and $H(s)$ the measurement filter.

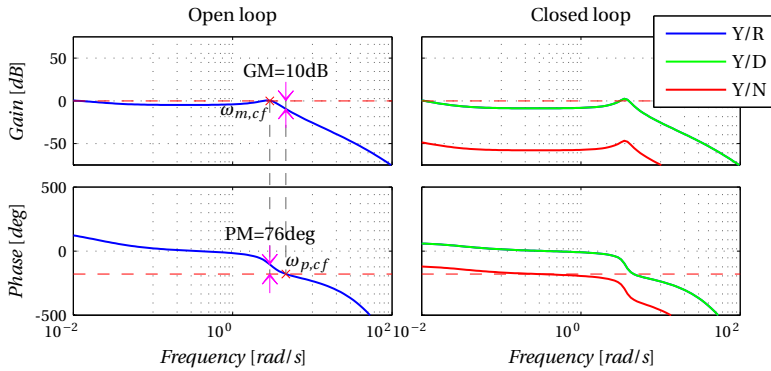


Figure E.2: Bode plot of the sideslip controller with $C = 1$ and $H = 1$.

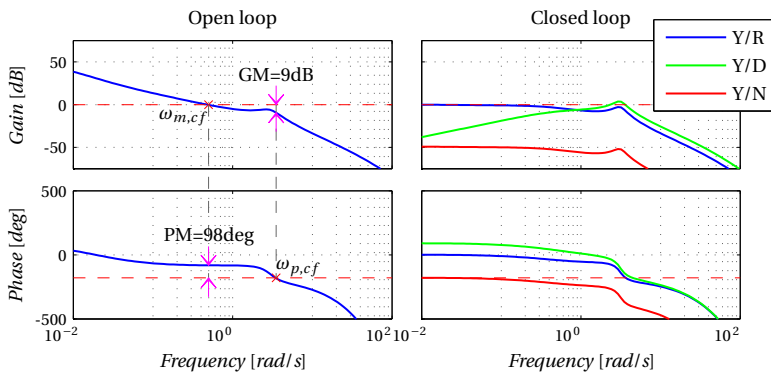


Figure E.3: Bode plot of the sideslip controller with $C = 0.4 + 0.8/s$ and $H = 1$.

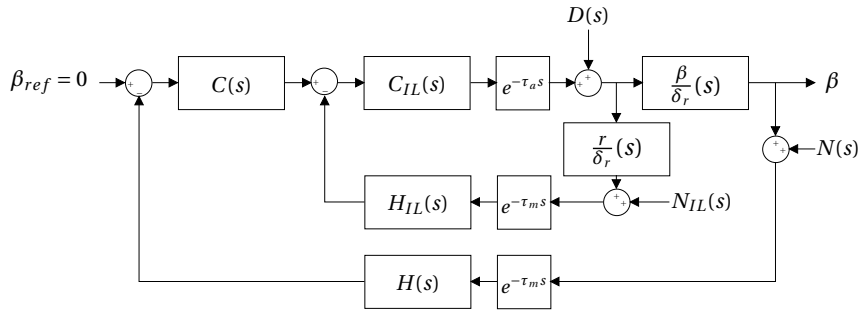


Figure E.4: Block diagram for the sideslip compensator with yaw-rate feedback in the inner loop.

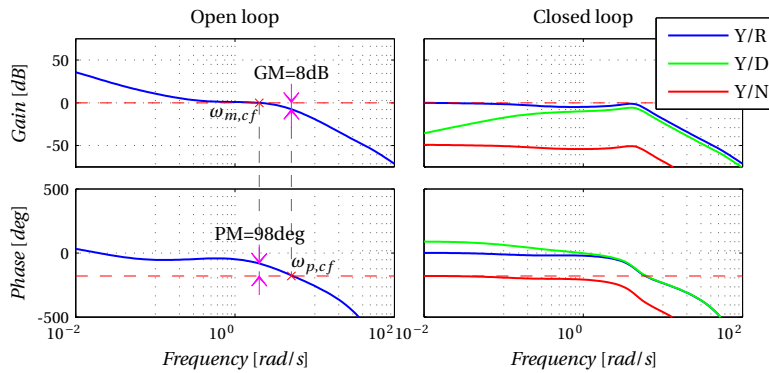


Figure E.5: Bode plot of the sideslip controller with $C = 1.7 + 0.6/s$, $H = 1$, $C_{IL} = 1$ and $H_{IL} = -0.4 \cdot 1.53s / (1.53s + 1)$.

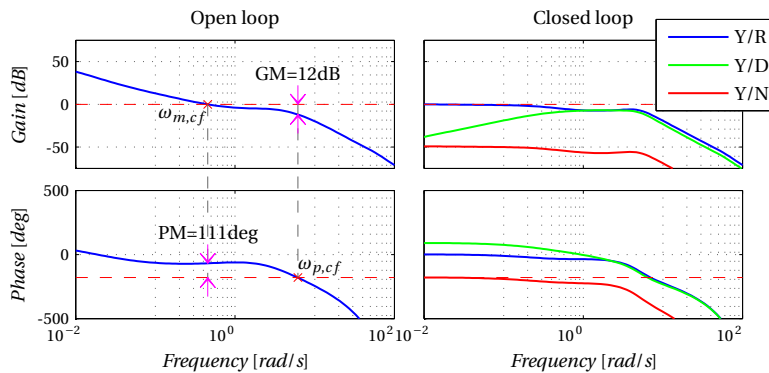


Figure E.6: Bode plot of the sideslip controller with $C = (1.7 + 0.6/s)(s + 1/0.56)/(1 + 2.77/0.56)(s + 1/0.91)/(s + 1/(3.71 \cdot 0.91))$, $H = 1$, $C_{IL} = 1$ and $H_{IL} = -0.4 \cdot 1.53s / (1.53s + 1)$.

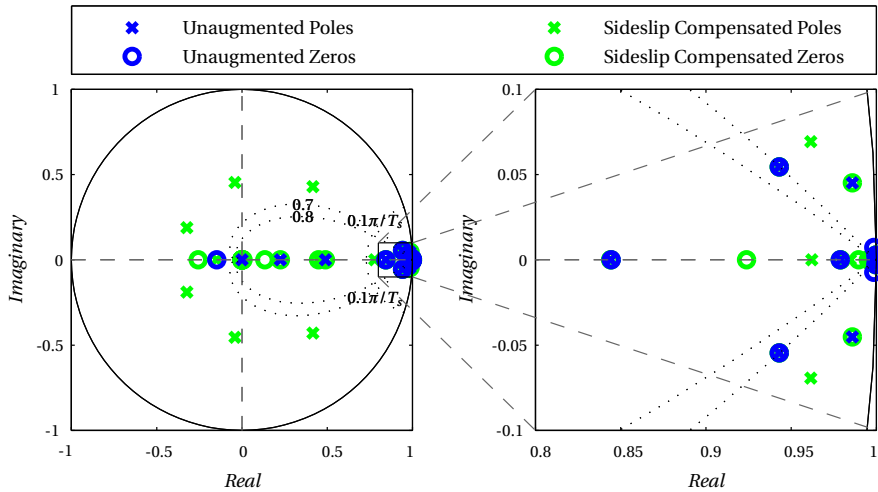


Figure E.7: Pole-zero map of the unaugmented system and the sideslip compensated system.

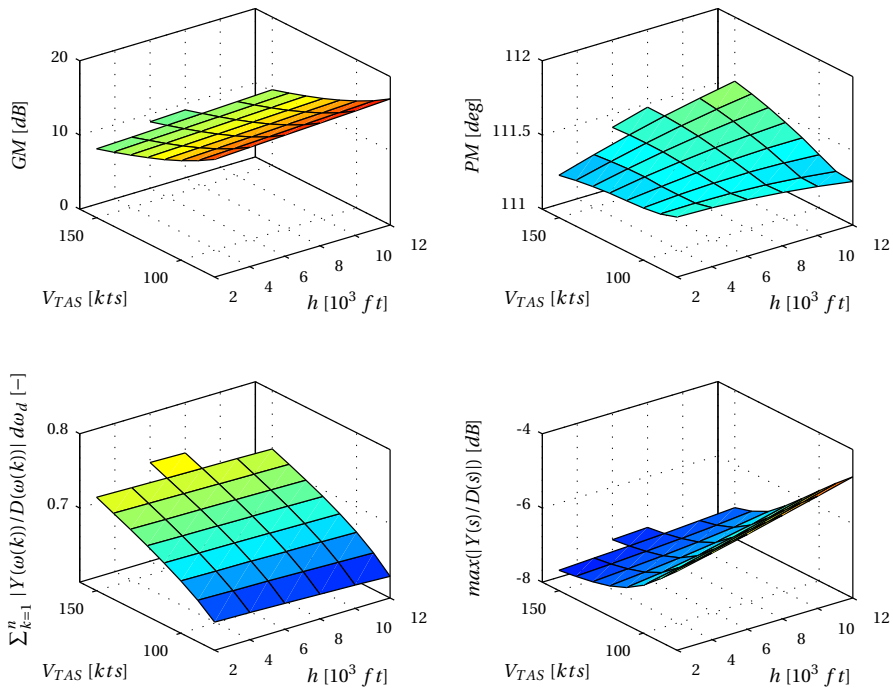


Figure E.8: Controller characteristics at different operating conditions.

E.2 Autothrottle

The autothrottle is designed using a similar strategy as applied to the sideslip controller. Since the autothrottle is designed for cruise flight only, it is implemented as a speed mode. In this mode the autothrottle follows a reference airspeed using engine throttle commands. In other flight phases a thrust mode may be more appropriate, in which the engine throttle is fixed and speed is controlled via the elevator.

Figure E.9 shows a block diagram of the autothrottle control loop. Again using a P controller with gain 1, i.e., $C(s) = K_P = 1$, results in the open and closed-loop behavior shown in Figure E.10. Clearly the disturbance rejection is poor and therefore the controller is rewritten as $C(s) = K_P + K_I/s = 1 + 0.2/s$. Figure E.11 shows the open and closed-loop behavior when PI control is used.

Figure E.12 shows the influence of measurement noise on the input signal, i.e., the power lever angle command. The presented controller causes too much noise on the input signal and the PI-gains should be lowered to $C(s) = 0.4 + 0.15/s$ for more acceptable noise levels. To reduce the noise level even further, a sensor filter can be added to the feedback part of the control loop. Using, $H(s) = 1/(1 + Ts)$, with the first-order low-pass filter time constant $T = 0.2$ seconds, results in the open and closed-loop behavior shown in Figure E.13. Noise attenuation is improved, but at the cost of a slight amplification of the disturbances around 1 rad/s. For now this controller is regarded as acceptable.

Figure E.14 shows the gain and phase margins at different operating conditions. The robustness of the autothrottle seems to be adequate for the full flight envelope. The figure also shows two noise attenuation metrics. The bottom left plot is created using a metric similar to the DR metric used for the sideslip compensator assessment,

$$NA = \sum_{k=n/2}^n \left| \frac{Y(\omega(k))}{D(\omega(k))} \right| d\omega_d \quad (\text{E.6})$$

in which $\omega(k) = 10^{-2+(k-1)\omega_d}$ and $\omega_d = 4/(n-1)$ with $n = 100$. Note that only the noise attenuation in the higher frequency part, $\omega \geq \omega(n/2) \approx 1$ rad/s, is used. The bottom right plot of the figure shows that the noise at a frequency of 10 rad/s is attenuated by at least -44 dB. Both plots show good noise attenuation throughout the flight envelope and therefore the autothrottle design is complete.

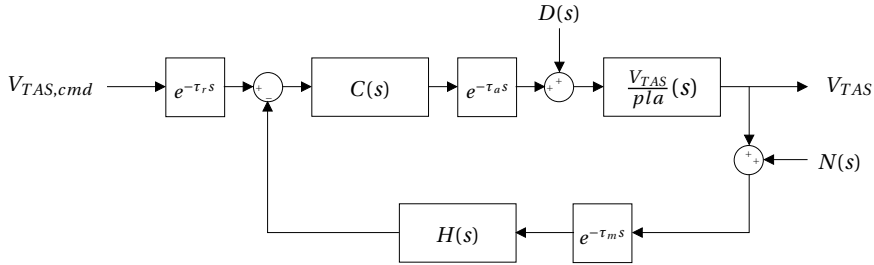


Figure E.9: Block diagram for the autothrottle, in which V_{TAS}/pla represents the transfer function of the true airspeed response due to power lever angle input of the aircraft combined with the FBW platform, $C(s)$ the FCL and $H(s)$ the measurement filter.

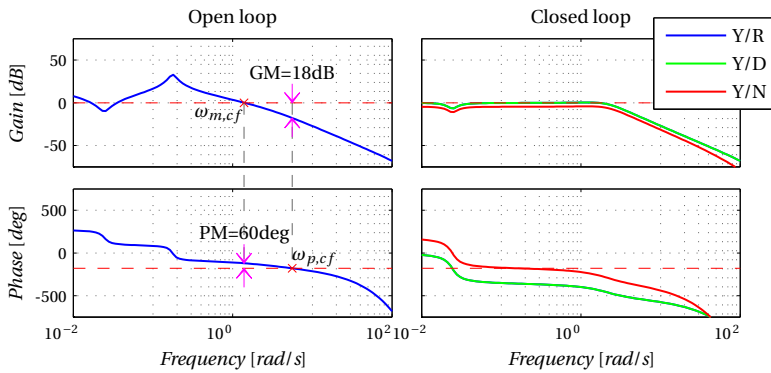


Figure E.10: Bode plot of the autothrottle with $C = 1$ and $H = 1$.

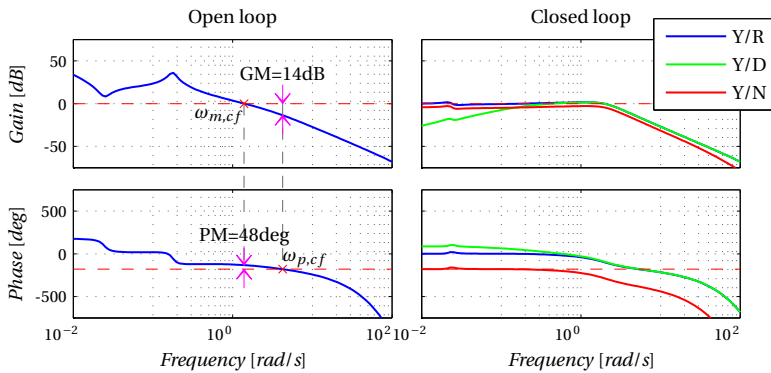


Figure E.11: Bode plot of the autothrottle with $C = 1 + 0.2/s$ and $H = 1$.

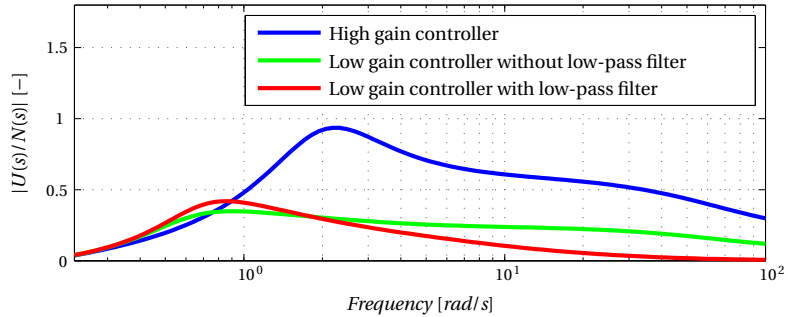


Figure E.12: Bode plot of the influence of measurement noise on the control input determined by the autothrottle.

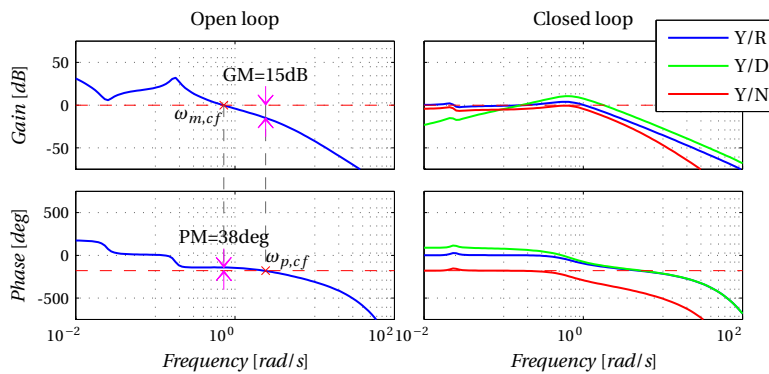


Figure E.13: Bode plot of the autothrottle with $C = 0.4 + 0.15/s$, $H = 1/(1 + 0.2s)$.

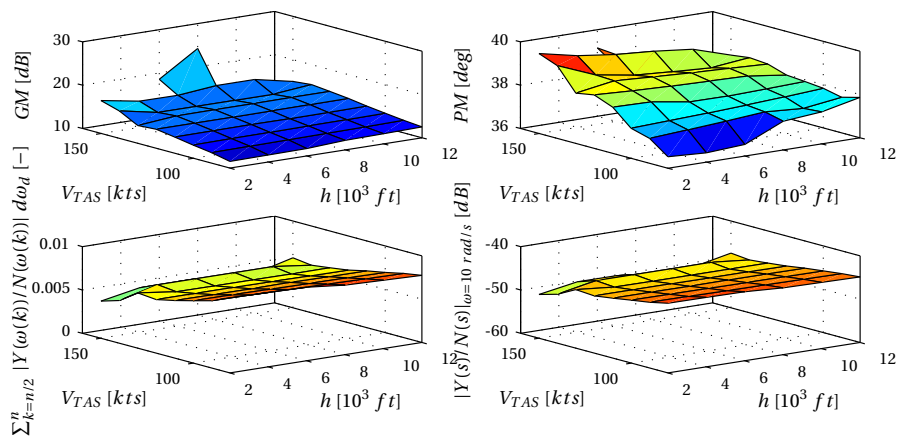


Figure E.14: Characteristics of the autothrottle at different operating conditions.

E.3 Pitch Rate Command/Attitude Hold Controller

The RCAH controller is designed using a similar strategy as applied to the sideslip controller and the autothrottle. The design is split into two parts. One for the elevator and one for the ailerons. Figure E.15 shows a block diagram of the elevator control loop. Note that the pitch rate command is integrated to a pitch angle reference, which the FCL should follow.

Figure E.16 shows the open and closed-loop behavior when a P controller is used, $C(s) = K_P$, with $K_P = -1$. Disturbances are not rejected properly and therefore again I control is added, i.e., $C(s) = K_P + K_I/s$, with $K_P = -0.6$ and $K_I = -0.2$. The result of using this controller is shown in Figure E.17. The bandwidth of this controller is only 1.1 rad/s, which is too small for manual control. Humans averagely control pitch with frequencies up to 4 rad/s [103]. In case of pitch RCAH control with a damping coefficient of 0.7, the bandwidth is equal to the equivalent short period natural frequency, ω_{sp} [92]. Performance specifications for ω_{sp} are provided in Section 4.3.1. At 120 kts and 6,000 ft the bandwidth should therefore be around 3.6 rad/s. To improve disturbance rejection and the controller bandwidth a pitch-rate inner-loop is added as shown in Figure E.18. The feedback term H_{IL} is designed using a washout filter as suggested in Section 4.2, i.e., $H_{IL}(s) = K_{IL}\tau s/(\tau s + 1)$, with $K_{IL} = -1.0$ and $\tau = 5$ seconds. Figure E.19 shows the open and closed-loop behavior of this system. The bandwidth has increased to 1.6 rad/s, which is still insufficient. Adding a lead-lag filter in the outer-loop controller, i.e.,

$$C(s) = \left(K_P + \frac{K_I}{s} \right) \left(\frac{s + 1/T_1}{1 + \gamma/T_1} \right) \left(\frac{s + 1/T_2}{s + 1/(\beta T_2)} \right) \quad (\text{E.7})$$

with $K_P = -1$, $K_I = -0.3$, $T_1 = 0.54$ s, $T_2 = 0.1$ s, $\gamma = 3.0$ and $\beta = 6.2$, results in the open and closed loop behavior shown in Figure E.20. The bandwidth has increased to 3.6 rad/s, which is sufficient. Note that the downside of requiring a high bandwidth is that noise attenuation deteriorates. Fortunately the attitude measurements have low noise power, as can be seen from $|Y(s)/N(s)|$.

Figure E.21 shows the gain and phase margins, the NA metric and the bandwidth of the pitch RCAH controller at different operating conditions. Section 4.3.1 shows that ω_{sp} , and therefore the bandwidth, should increase with speed and decrease with altitude. Currently the opposite is true. In order to compensate for this change in dynamics, the inner-loop gain K_{IL} and the P-gain K_P can be scheduled to change with altitude and speed variations. Figure E.22 shows a gain map that improves the bandwidth as demonstrated in Figure E.23. The gain scheduled controller is satisfactory throughout the flight envelope and the pitch RCAH design is therefore complete.

E.3. Pitch Rate Command/Attitude Hold Controller

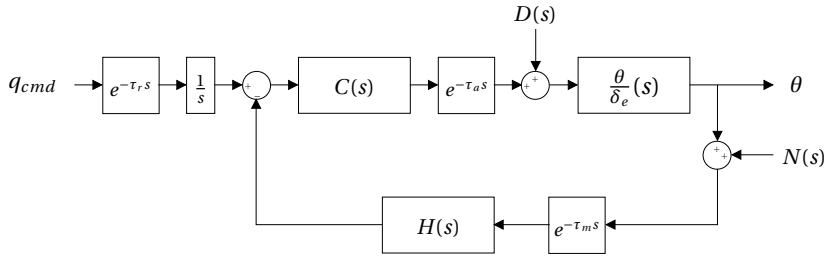


Figure E.15: Block diagram for the pitch RCAH controller, in which θ/δ_e represents the transfer function of the pitch angle response due to elevator deflections of the aircraft combined with the FBW platform, $C(s)$ the FCL and $H(s)$ the measurement filter.

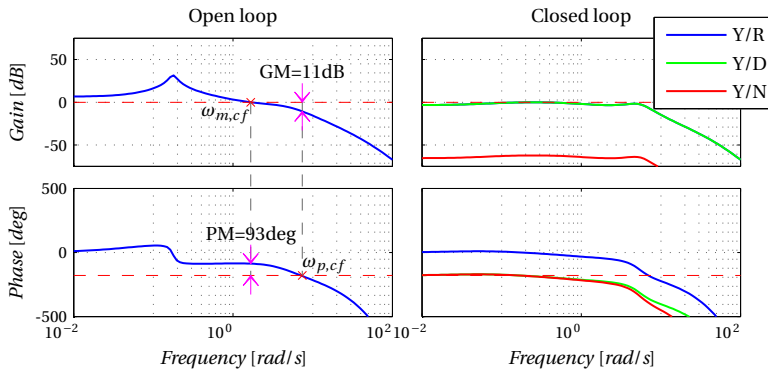


Figure E.16: Bode plot of the pitch RCAH controller with $C = -1$ and $H = 1$.

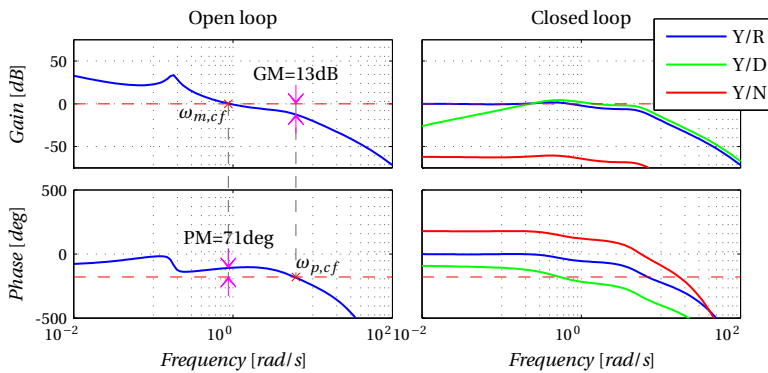


Figure E.17: Bode plot of the pitch RCAH controller with $C = -0.6 - 0.2/s$ and $H = 1$.

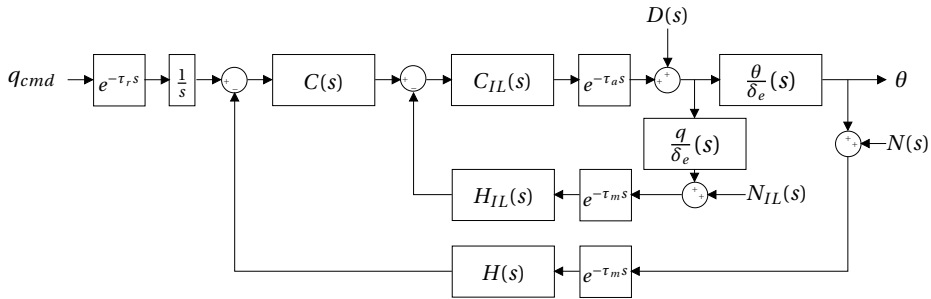


Figure E.18: Block diagram for the pitch RCAH controller with pitch-rate feedback in the inner loop.

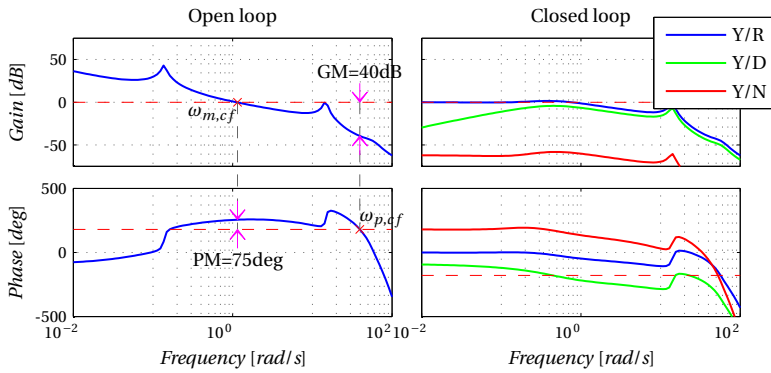


Figure E.19: Bode plot of the pitch RCAH controller with $C = -2.2 - 0.3/s$, $H = 1$, $C_{IL} = 1$ and $H_{IL} = -5s/(5s + 1)$.

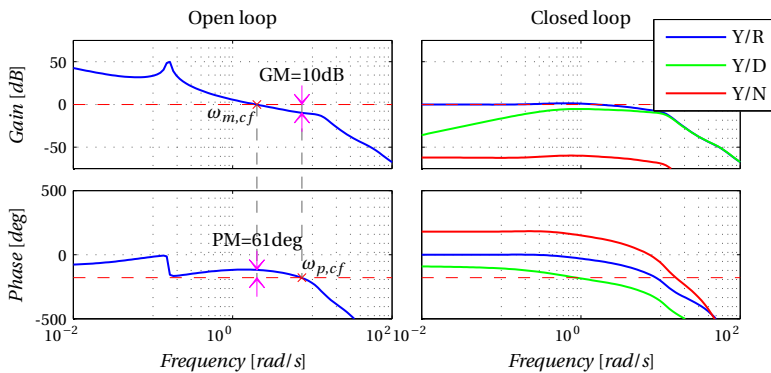


Figure E.20: Bode plot of the pitch RCAH controller with $C = (-1 - 0.3/s)(s + 1/0.54)/(s + 3.0/0.54)(s + 1/0.1)/(s + 1/(6.2 \cdot 0.1))$, $H = 1$, $C_{IL} = 1$ and $H_{IL} = -0.4 \cdot 5s/(5s + 1)$.

E.3. Pitch Rate Command/Attitude Hold Controller

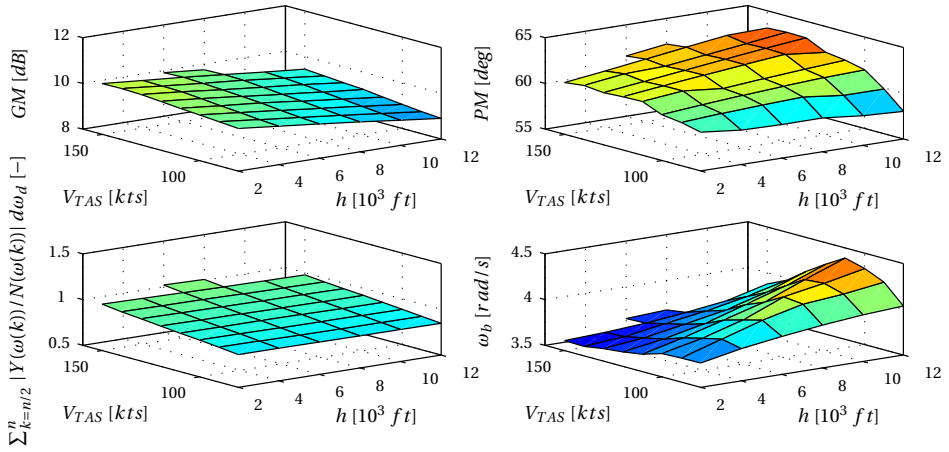


Figure E.21: Characteristics of the pitch RCAH controller at different operating conditions.

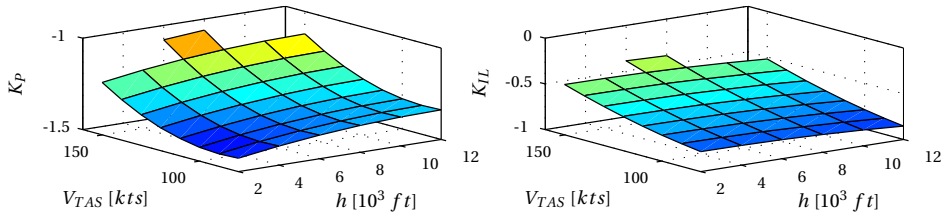


Figure E.22: Gain schedule of K_P and K_{IL} for altitude and speed.

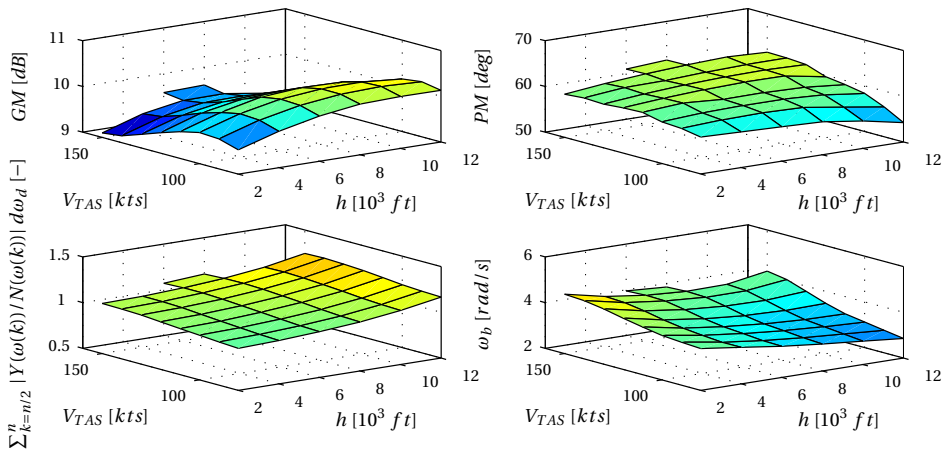


Figure E.23: Characteristics of the pitch RCAH controller with gain scheduling of K_P and K_{IL} , at different operating conditions.

E.4 Roll Rate Command/Attitude Hold Controller

Figure E.24 shows a block diagram for the aileron control loop. Using a P controller with gain 1, $C(s) = K_P = 1$, results in the open and closed-loop behavior shown in Figure E.25. Disturbance rejection is poor at low frequencies, indicated by the relatively high $|Y(s)/D(s)|$. Figure E.26 shows that adding I control, i.e., $C(s) = K_P + K_I/s$, with $K_P = -1.3$ and $K_I = -0.7$, improves disturbance rejection. Another slight improvement is possible by adding a roll-rate inner-loop. Figure E.27 shows a block diagram of this control loop and Figure E.28 shows the open and closed-loop behavior for a controller with washout filter, i.e.,

$$H_{IL}(s) = K_{IL} \frac{\tau s}{\tau s + 1} \quad (\text{E.8})$$

with $K_{IL} = -0.2$ and $\tau = 5$ seconds. Lead-lag compensation is not needed, since the bandwidth of the roll RCAH controller is already 5.6 rad/s and the phase margin is 61 degrees. The latter indicates that the equivalent dutch roll damping ζ_d is approximately $PM/100 = 0.61$ which is sufficient from a performance perspective as shown in Section 4.3.1. With this damping, the dutch roll natural frequency ω_d is approximately equal to the bandwidth and is therefore also sufficient.

Figure E.21 shows the gain and phase margins, the NA metric and the bandwidth of the pitch RCAH controller at different operating conditions. The gain margin is too low at high velocity, so again gain scheduling is needed. Figure E.30 shows a gain map that improves the gain margin as demonstrated in Figure E.31. However, at higher velocity the bandwidth drops to 2 rad/s, which is insufficient. Adding a lead-lag filter in the outer-loop controller, i.e.,

$$C(s) = \left(K_P + \frac{K_I}{s} \right) \left(\frac{s + 1/T_1}{1 + \gamma/T_1} \right) \left(\frac{s + 1/T_2}{s + 1/(\beta T_2)} \right) \quad (\text{E.9})$$

with $K_P = -3.6$, $K_I = -0.6$, $T_1 = 0.11$ s, $T_2 = 0.07$ s, $\gamma = 6.0$ and $\beta = 2.7$ and rescheduling the gains as shown in Figure E.32, leads to the characteristics depicted in Figure E.33. The gain scheduled controller is satisfactory throughout the flight envelope and the roll RCAH design is therefore complete.

E.4. Roll Rate Command/Attitude Hold Controller

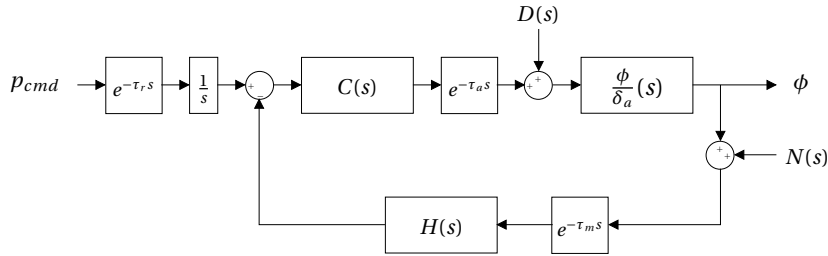


Figure E.24: Block diagram for the roll RCAH controller, in which ϕ/δ_a represents the transfer function of the roll angle response due to aileron deflections of the aircraft combined with the FBW platform, $C(s)$ the FCL and $H(s)$ the measurement filter.

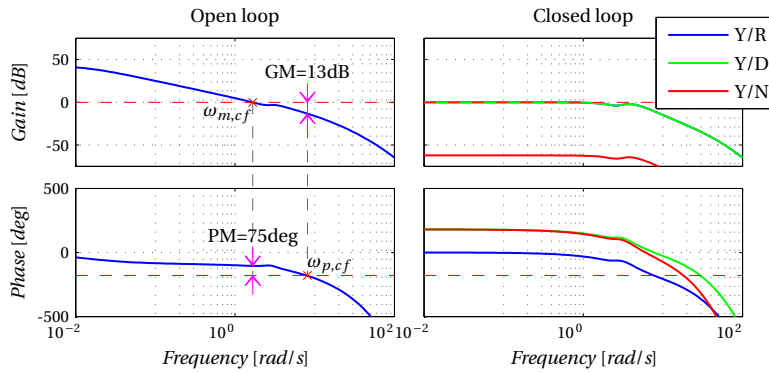


Figure E.25: Bode plot of the roll RCAH controller with $C = -1$ and $H = 1$.

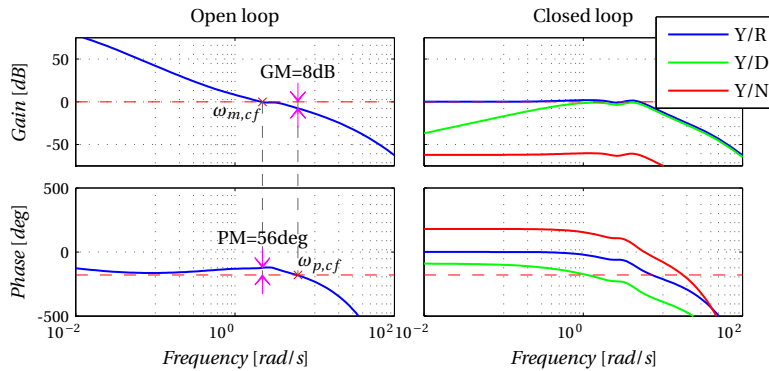


Figure E.26: Bode plot of the roll RCAH controller with $C = -1.3 - 0.7/s$ and $H = 1$.

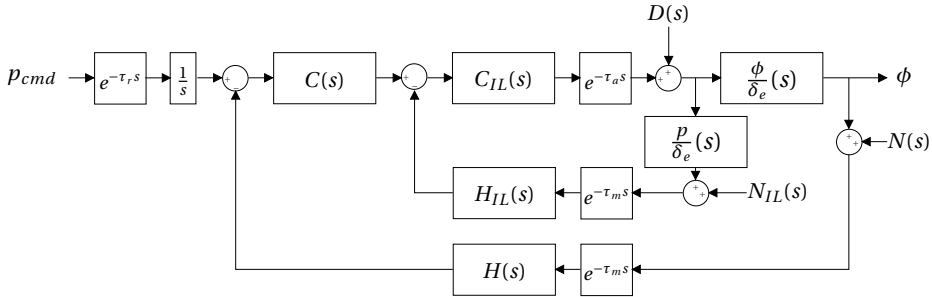


Figure E.27: Block diagram for the roll RCAH controller with roll-rate feedback in the inner loop.

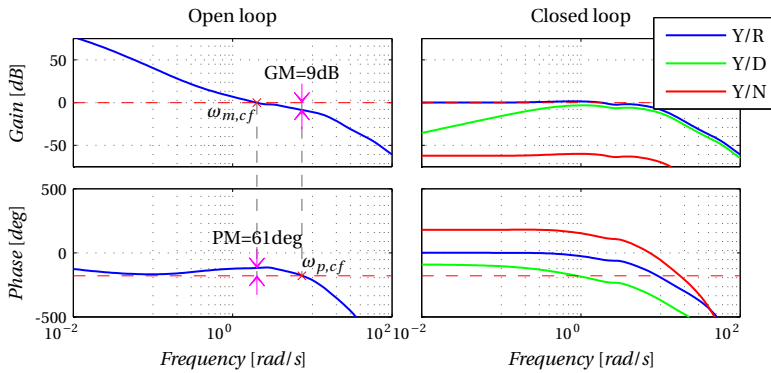


Figure E.28: Bode plot of the roll RCAH controller with $C = -1.6 - 0.6/s$, $H = 1$, $C_{IL} = 1$ and $H_{IL} = -s/(5s + 1)$.

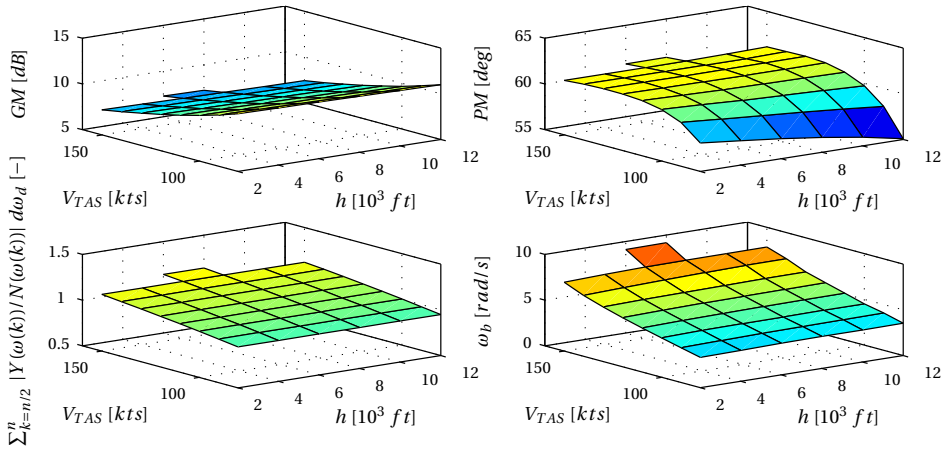


Figure E.29: Characteristics of the roll RCAH controller at different operating conditions.

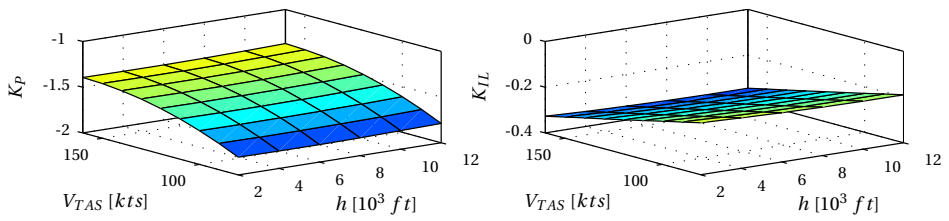


Figure E.30: Gain schedule of K_P and K_{IL} for altitude and speed.

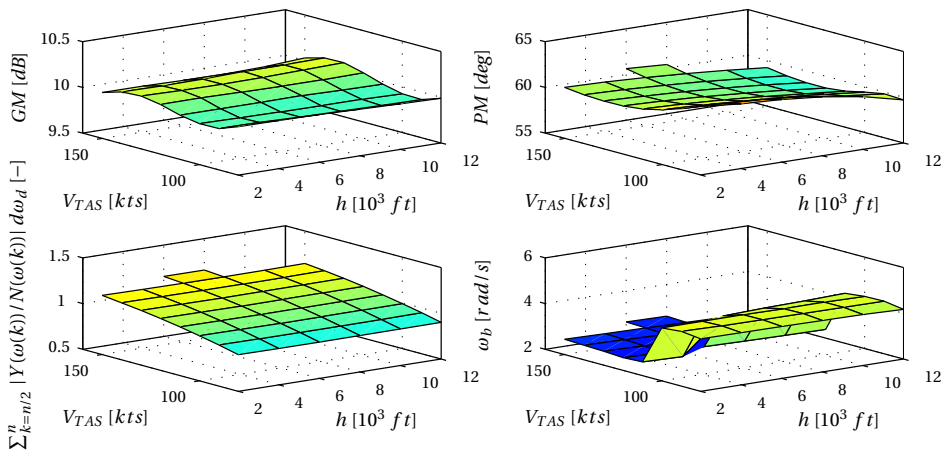


Figure E.31: Characteristics of the roll RCAH controller with gain scheduling of K_P and K_{IL} , at different operating conditions.

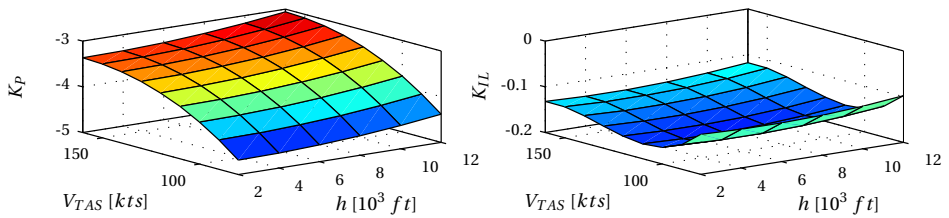


Figure E.32: Gain schedule of K_P and K_{IL} for altitude and speed.

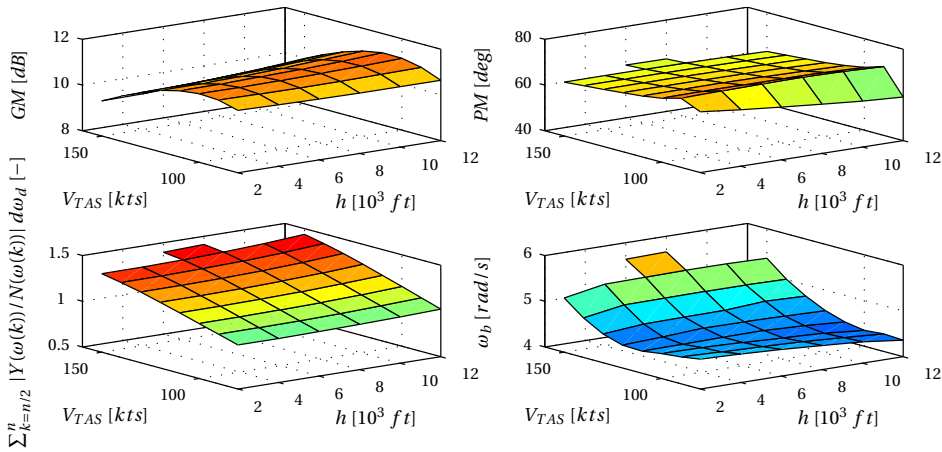


Figure E.33: Characteristics of the roll RCAH controller with gain scheduling of K_P and K_{IL} and lead-lag compensation, at different operating conditions.

E.5 3D Trajectory Following Controller

The 3D trajectory following controller closes two additional control loops on top of the RCAH controller. First the flight-path vector loop will be closed, second the position loop.

Figure E.34 shows a block diagram of the vertical trajectory following controller with flight-path-angle feedback. The open and closed loop characteristics of this system using a controller with $C = 1 + 1/s$ and a measurement filter $H = 1$ are shown in Figure E.35. The controller already seems to be adequate and no additional inner loop or lead-lag filter is needed. Figure E.36 shows the characteristics throughout the flight envelope. The gain and phase margin stay adequate and also the bandwidth is fine in every operating condition. Gain scheduling is therefore not needed.

Figure E.37 shows a block diagram of the complete vertical trajectory following controller. The open and closed loop characteristics of this system using a controller with $C = (10 + 1/s)/1000$ and a measurement filter $H = 1$ are shown in Figure E.38. Note that this FCL causes substantial altitude changes due to disturbances and measurement noise. To get a feeling for the impact of the measurement noise on the elevator deflection and the altitude, Figure E.39 shows the changes in these parameters. In the cruise phase slow variations of several feet are not a problem and no additional filtering is required. The damping of the closed-loop response is approximately $PM/100 = 0.55$, and therefore the vertical trajectory is intercepted

with overshoots. This is regarded as less comfortable for passengers of the aircraft and the damping should be increased to prevent overshoots. Instead of adding a D term to the controller an additional vertical-velocity inner loop can be added to the FCL as shown in Figure E.40. Figure E.41 shows the resulting open and closed-loop behavior of this system. The phase margin has improved, while maintaining adequate gain margin. Figure E.42 shows that gain scheduling is not needed for the outer-loop controller.

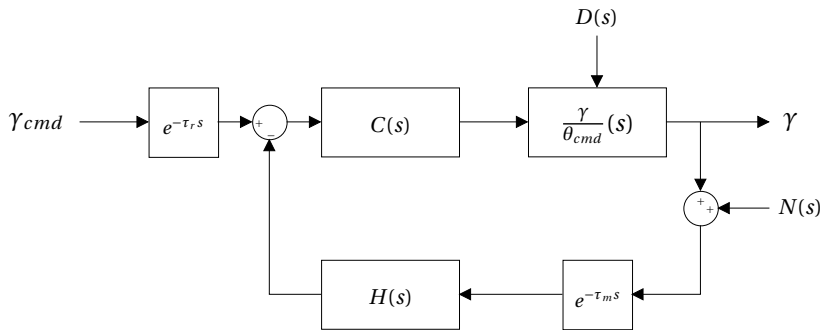


Figure E.34: Block diagram for the vertical trajectory following controller with flight-path-angle feedback. The transfer function $\gamma/\theta_{cmd}(s)$ represents the aircraft with FBW platform and the attitude-hold mode developed in Section E.3.

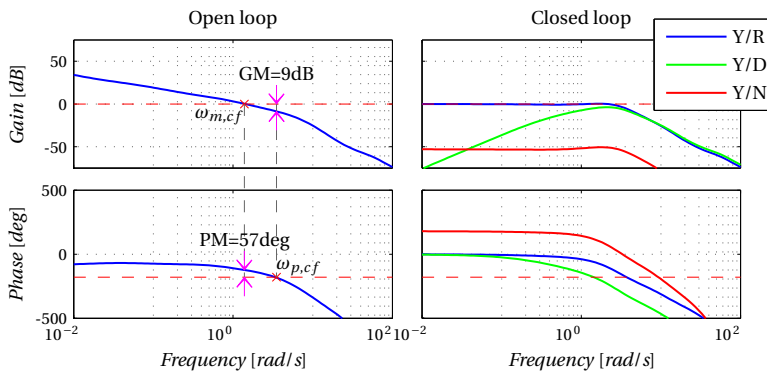


Figure E.35: Bode plot of the vertical trajectory following controller with $C = 1 + 1/s$ and $H = 1$.

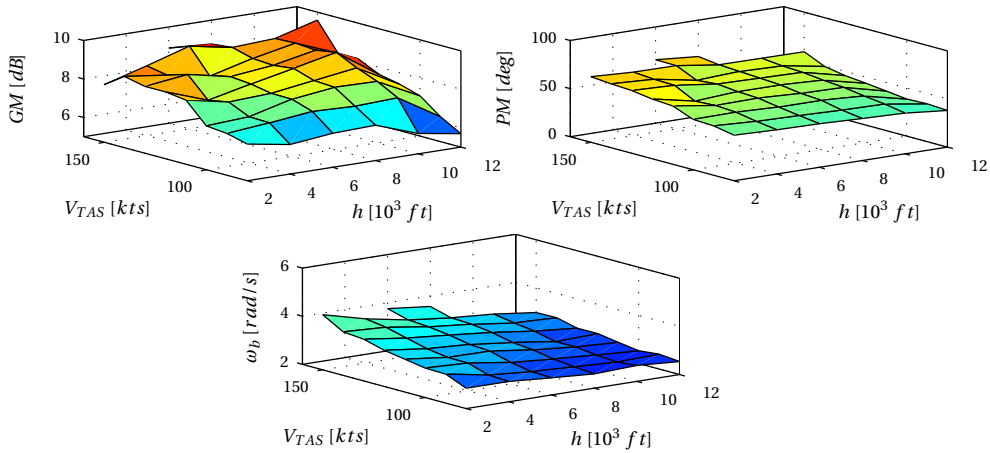


Figure E.36: Characteristics of the vertical trajectory following controller at different operating conditions.

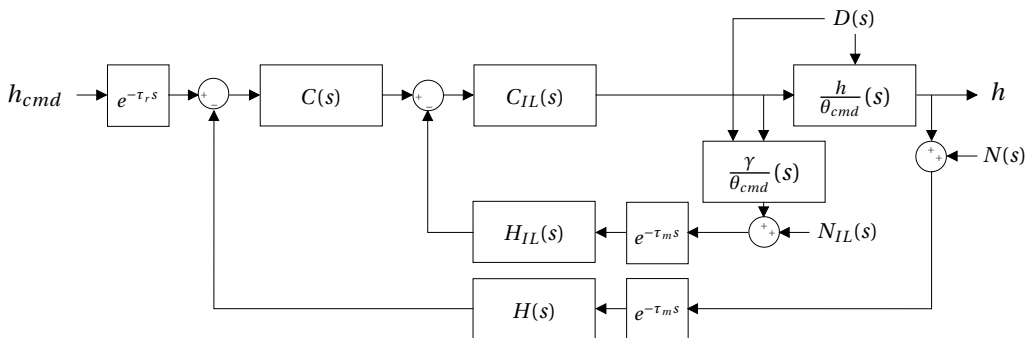


Figure E.37: Block diagram for the vertical trajectory following controller with flight-path-angle feedback in the inner loop and vertical position feedback in the outer loop.

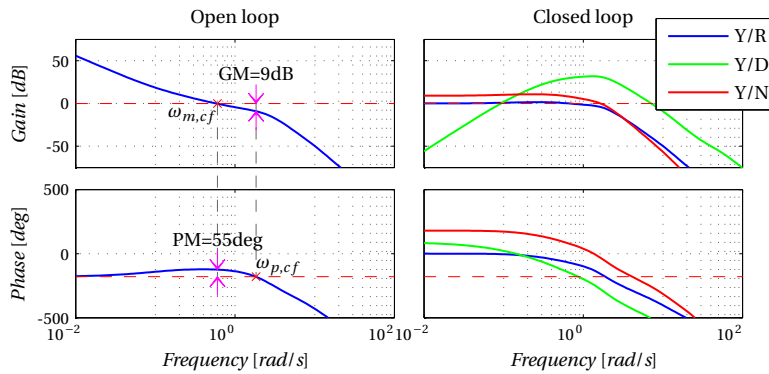


Figure E.38: Bode plot of the vertical trajectory following controller with $C_{IL} = 1 + 1/s$, $H_{IL} = 1$, $C = (10 + 1/s)/1000$ and $H = 1$.

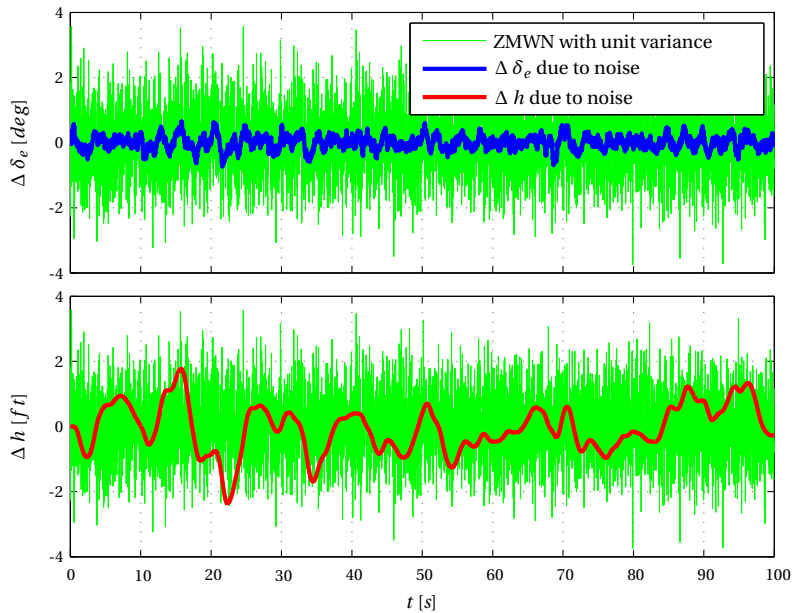


Figure E.39: Time history of evelator deflection and altitude variations caused by measurement noise.

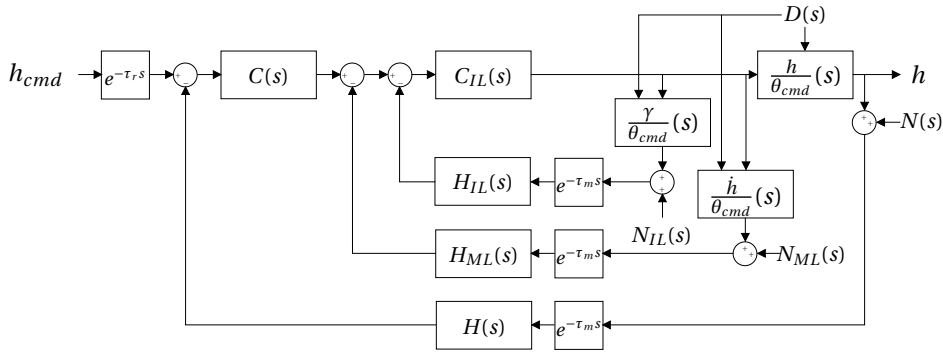


Figure E.40: Block diagram for the vertical trajectory following controller with flight-path-angle feedback in the inner loop, vertical speed feedback in the middle loop and vertical position feedback in the outer loop.

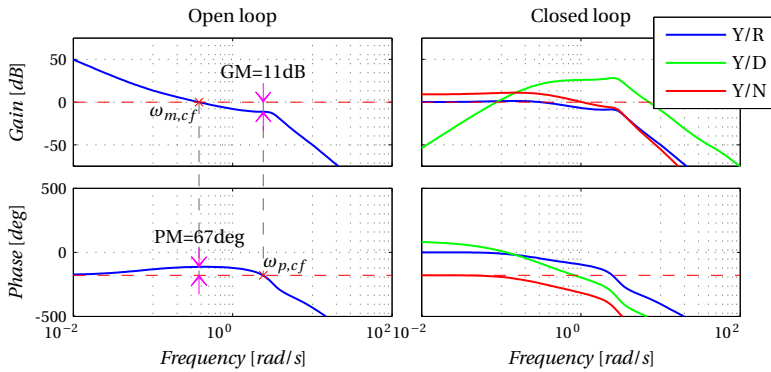


Figure E.41: Bode plot of the vertical trajectory following controller with $C_{IL} = 1 + 1/s$, $H_{IL} = 1$, $H_{ML} = 10/1000$, $C = (10 + 0.8/s)/1000$ and $H = 1$.

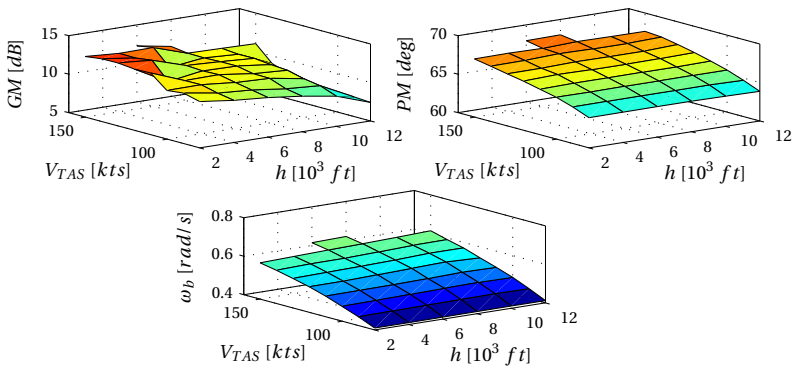


Figure E.42: Characteristics of the vertical trajectory following controller at different operating conditions.

Figure E.43 shows a block diagram of the horizontal trajectory following controller with track-angle feedback. The open and closed loop characteristics of this controller with $C = 5$ and $H = 1$ are shown in Figure E.44. Figure E.45 shows that gain scheduling is needed due to the low gain and phase margin at low velocity. Figure E.46 shows that scheduling the P gain results in adequate characteristics in every operating point.

The complete horizontal trajectory following controller is shown in Figure E.47. The open and closed loop characteristics of this controller with $C = 0.006 + 0.0005/s$ and $H = 1$ are shown in Figure E.48. The damping of the closed-loop response is approximately $PM/100 = 0.5$, and therefore also the horizontal trajectory is intercepted with overshoots. Again the damping should be increased for passenger comfort. Figure E.49 show a block diagram of the controller with an additional horizontal-velocity feedback loop. Figure E.50 shows the resulting open and closed-loop behavior of this system. The phase margin has improved, while maintaining adequate gain margin. Finally, Figure E.51 shows that gain scheduling is not needed for the outer-loop controller.

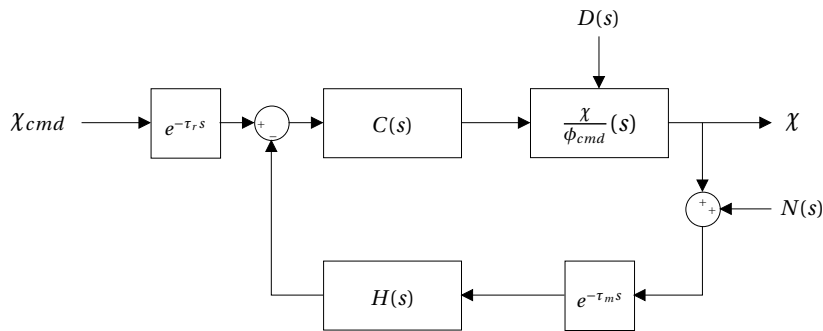


Figure E.43: Block diagram for the horizontal trajectory following controller with track-angle feedback. The transfer function $\chi/\phi_{cmd}(s)$ represents the aircraft with FBW platform and the attitude-hold mode developed in Section E.4.

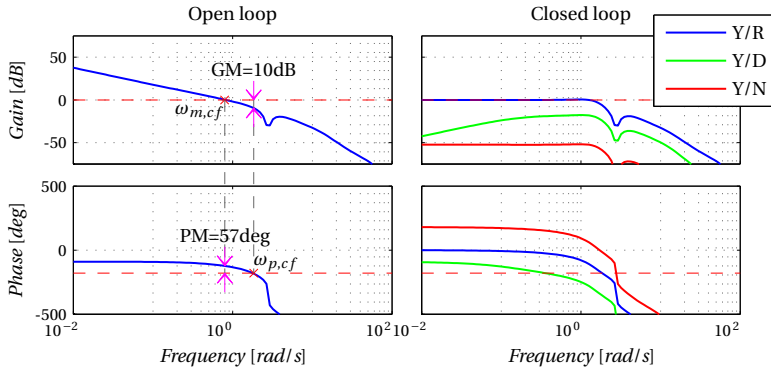


Figure E.44: Bode plot of the horizontal trajectory following controller with $C = 5$ and $H = 1$.

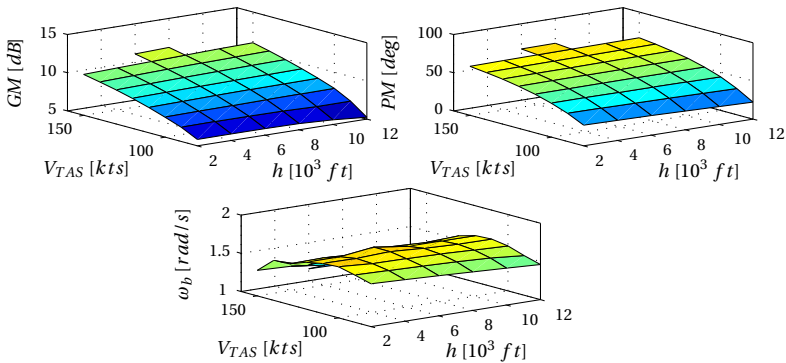


Figure E.45: Characteristics of the horizontal trajectory following controller at different operating conditions.

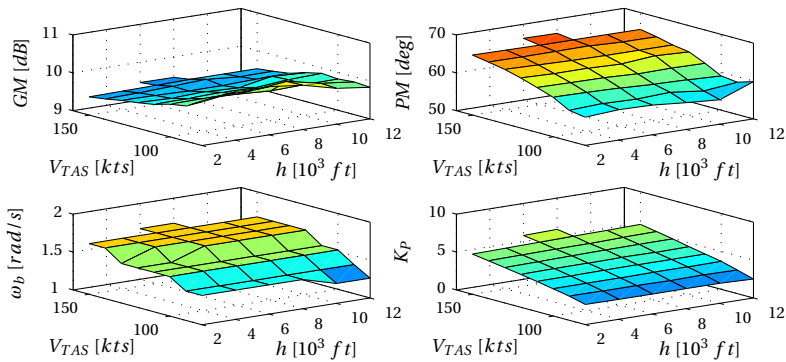


Figure E.46: Characteristics of the horizontal trajectory following controller with gain scheduling of the P-gain, at different operating conditions.

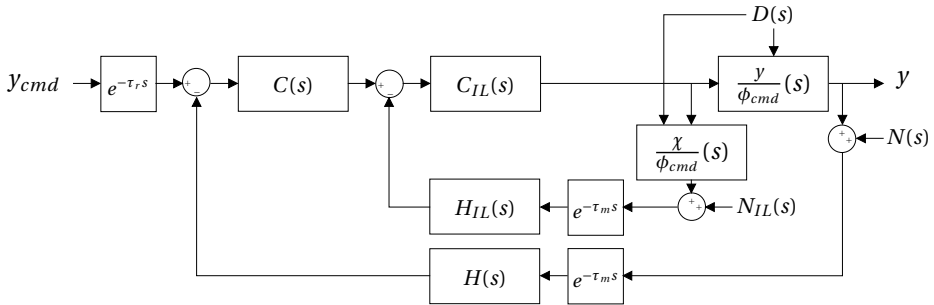


Figure E.47: Block diagram for the horizontal trajectory following controller with track-angle feedback in the inner loop and horizontal position feedback in the outer loop.

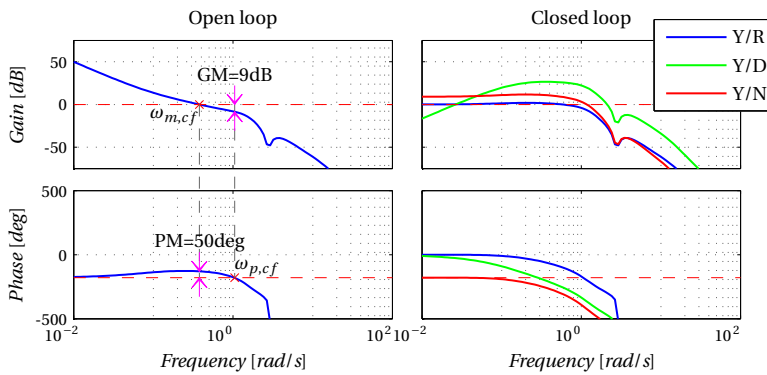


Figure E.48: Bode plot of the horizontal trajectory following controller with $C_{IL} = 5$, $H_{IL} = 1$, $C(s) = (6 + 0.5/s)/1000$ and $H = 1$.

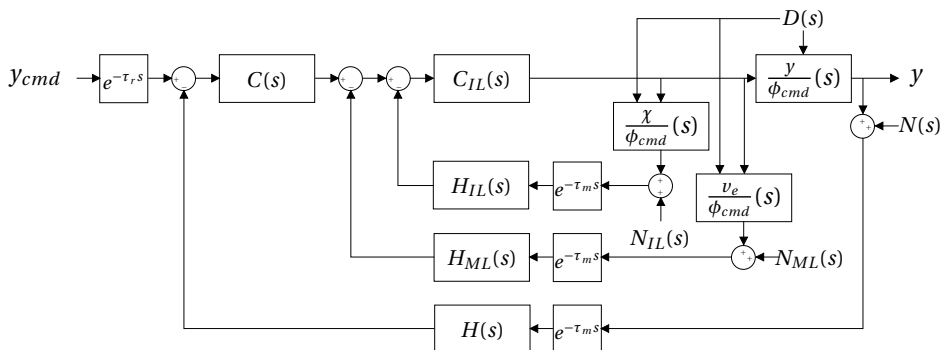


Figure E.49: Block diagram for the horizontal trajectory following controller with track-angle feedback in the inner loop, horizontal velocity in the middle loop and horizontal position feedback in the outer loop.

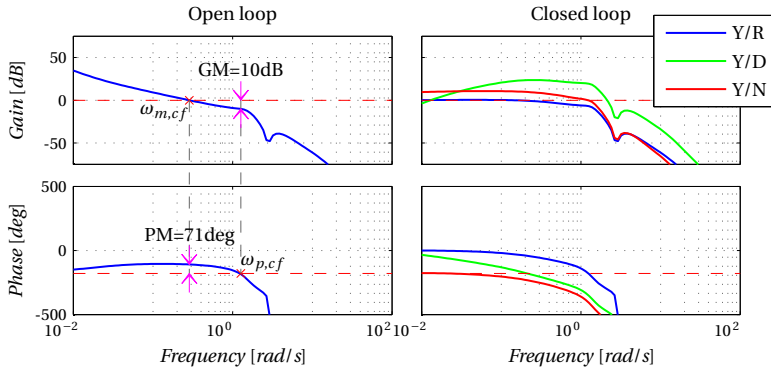


Figure E.50: Bode plot of the horizontal trajectory following controller with $C_{IL} = 5$, $H_{IL} = 1$, $H_{ML} = 5/1000$, $C(s) = (6 + 0.1/s)/1000$ and $H = 1$.

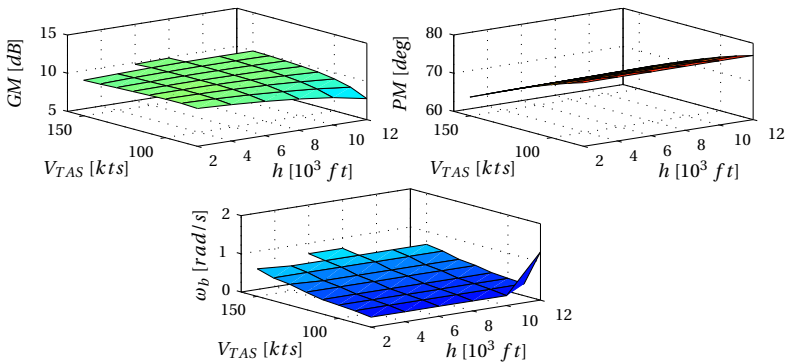


Figure E.51: Characteristics of the horizontal trajectory following controller at different operating conditions.

E.6 Nonlinear Simulations using the ATT law

The classical FCLs designed in this appendix are implemented on linearized SISO system descriptions. The actual aircraft dynamics are nonlinear as demonstrated in Chapter 2 and therefore the classical FCLs need to be implemented and tested on the nonlinear model as well. Ideally the dynamic behavior resulting from control actions should be the same for both the linear and nonlinear models. In this way the designed performance and robustness characteristics are maintained on the nonlinear system.

Figures E.52 and E.53 show time histories of the nonlinear aircraft dynamics under influence of the RCAH controller, combined with sideslip compensator and autothrottle. The roll and pitch commands are followed adequately even when the velocity reference is changed. However, these figures do not provide a good measure to show that the linear FCLs work equally well on the nonlinear system as on the linearized system for which they were designed. When the aircraft state is kept close to the linearization point and when measurement noise is not taken into account, there should be no difference between the dynamic behavior of the linear and the nonlinear system. Figure E.54 shows the comparison between the response of the linear and nonlinear system to a sinusoidal input of different amplitudes to the pitch RCAH. The results are indeed highly comparable, except when the amplitude becomes large enough to saturate the elevator deflection actuator. Figure E.55 shows that also for input signals with increasing frequency similar results are obtained from the linear and the nonlinear model. Figures E.56 and E.57 show the system responses when not only the pitch RCAH receives a nonzero input, but also the roll RCAH and the autothrottle. When control saturation is avoided, the linear and nonlinear system respond almost identically to the inputs. Similar properties are found throughout the flight envelope and the conclusion can be drawn that the classical FCLs properly control the nonlinear aircraft model in the neighborhood of the linearization points.

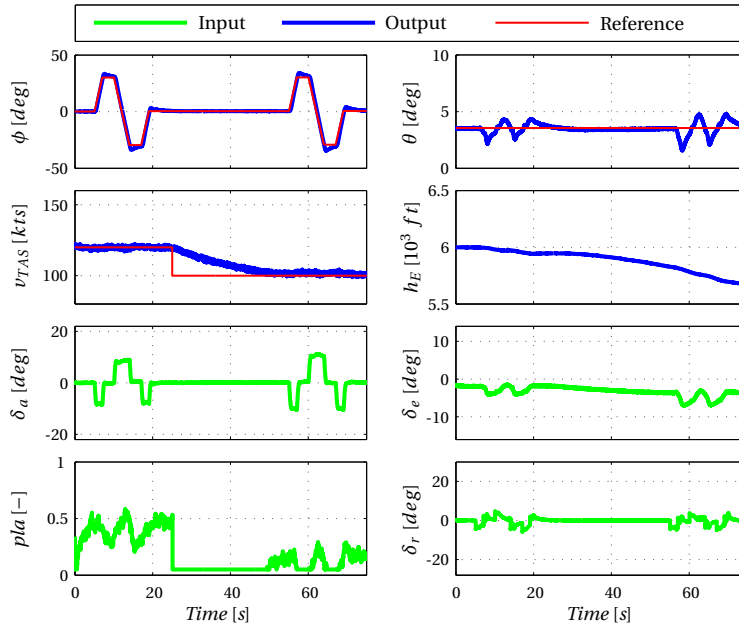


Figure E.52: Time histories of the aircraft dynamics influenced by the ATT law.

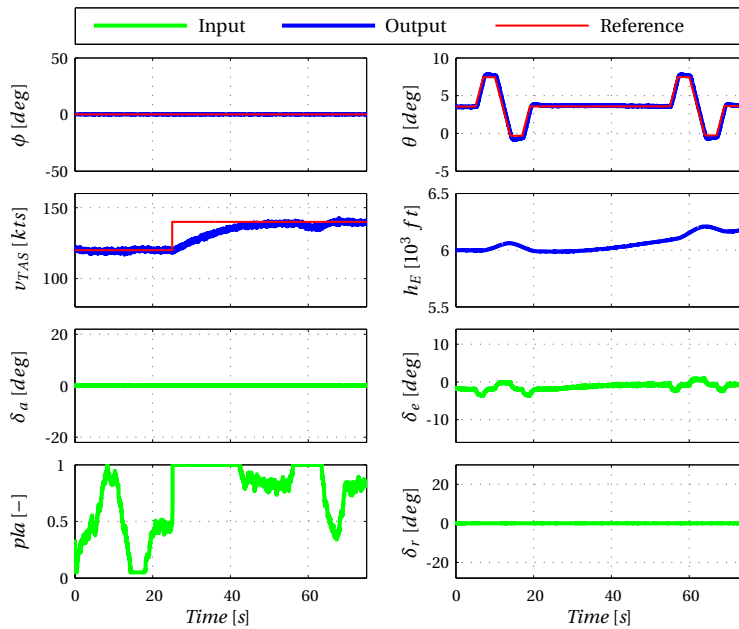


Figure E.53: Time histories of the aircraft dynamics influenced by the ATT law.

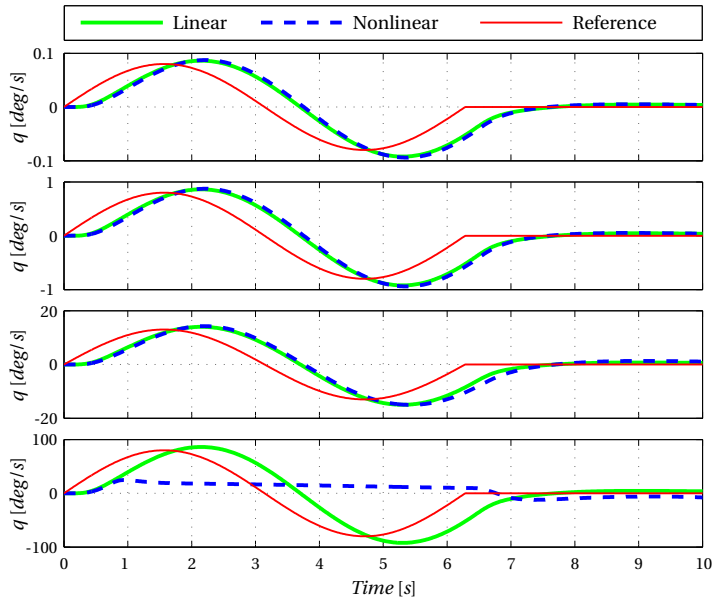


Figure E.54: Time histories of the (non)linear aircraft dynamics influenced by the pitch RCAH controller.

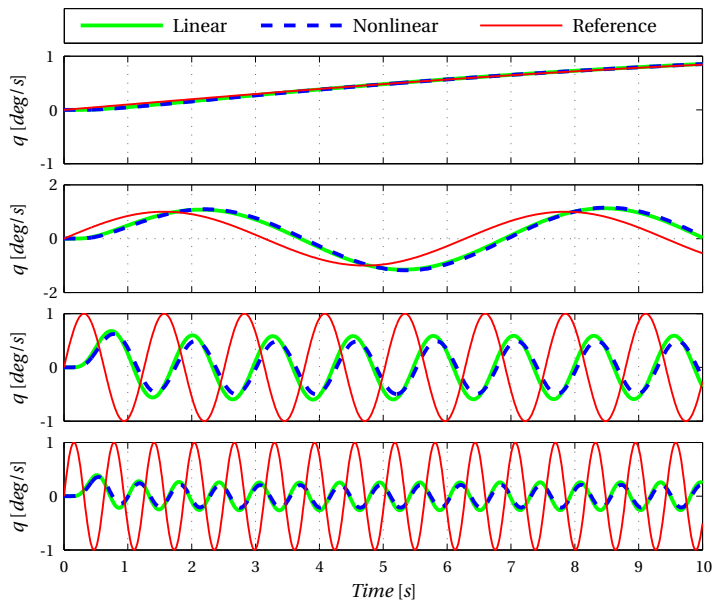


Figure E.55: Time histories of the (non)linear aircraft dynamics influenced by the pitch RCAH controller.

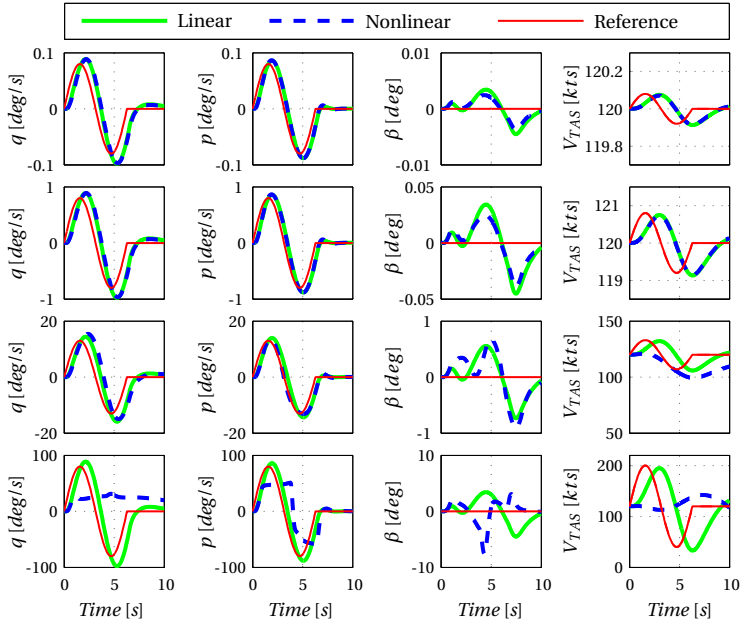


Figure E.56: Time histories of the (non)linear aircraft dynamics influenced by the ATT law.

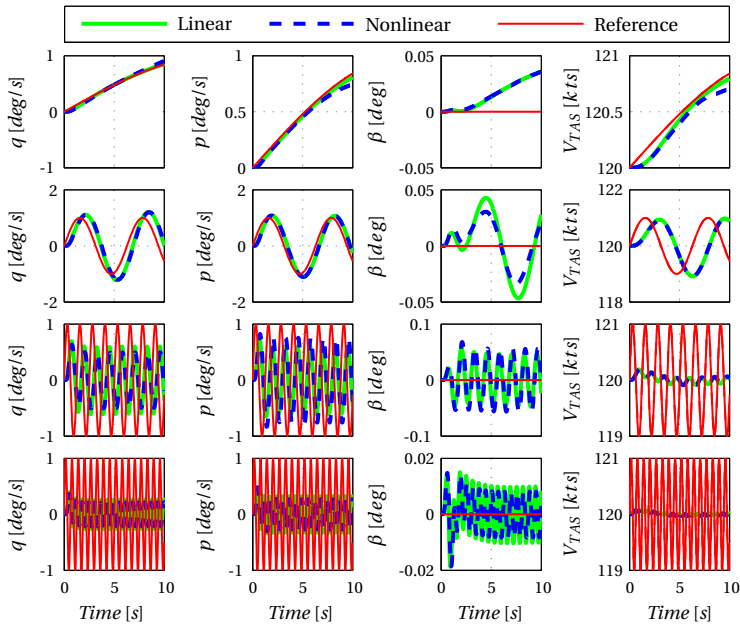


Figure E.57: Time histories of the (non)linear aircraft dynamics influenced by the ATT law.

E.7 Nonlinear Simulations using the NAV law

The NAV law designed using classical control theory should be tested on the nonlinear system in the same way as the ATT law. Figure E.58 shows the behavior of the linear and nonlinear system to an altitude command of different amplitude and frequency. Again the responses of both systems are highly comparable when control saturation does not occur. When not only altitude commands are given, but also horizontal position and velocity commands the models behave as shown in Figures E.59 and E.60. Clearly also the NAV law performs equally well on the linear and nonlinear model when the aircraft remains in the neighborhood of the operating condition. Again similar results are obtained throughout the flight envelope and the NAV law therefore properly controls the nonlinear aircraft model in the neighborhood of the linearization points.

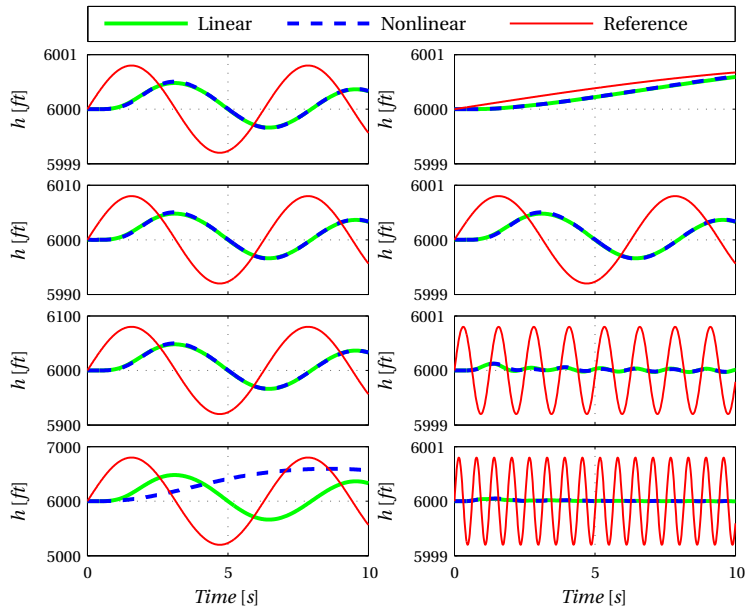


Figure E.58: Time histories of the (non)linear aircraft dynamics influenced by the NAV law.

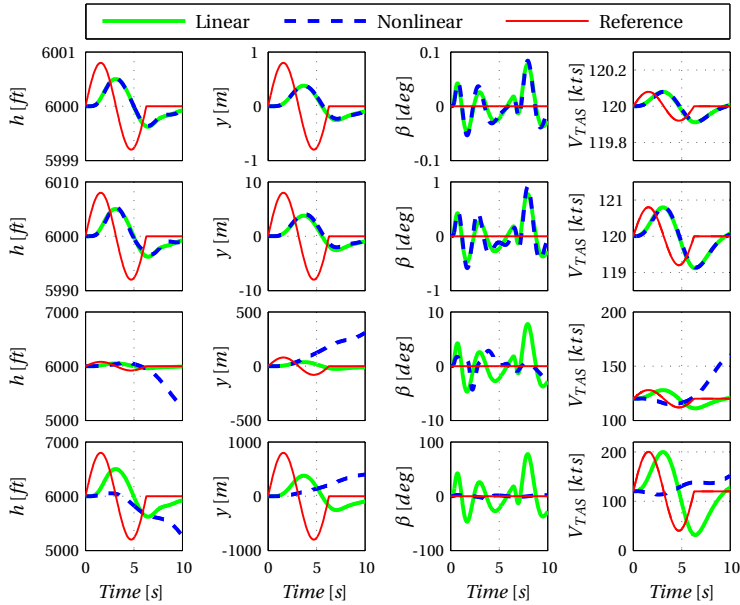


Figure E.59: Time histories of the (non)linear aircraft dynamics influenced by the NAV law.

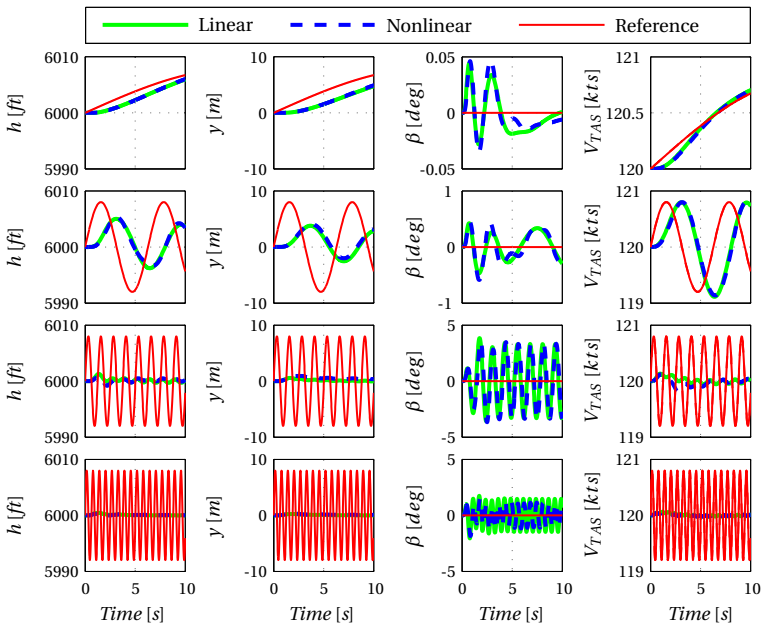


Figure E.60: Time histories of the (non)linear aircraft dynamics influenced by the NAV law.

PILOT INSTRUCTIONS FOR SIMULATOR TRIALS

F.1 SAFAR Flight Control Law Concept

Two separate FCLs will be used in SAFAR. The first is called the direct (DRCT) law and directly sends the pilot's commands to the control surfaces and engines. This mode should closely match the conventional (mechanical) way of controlling the aircraft, although aerodynamic forces will not be felt on the side-stick. The second FCL is an attitude-rate-command/attitude-hold (ATT) mode. The pilot will provide attitude-rate-commands using the side-stick and the FCL will try to hold the attitude (roll and pitch angles) by itself. This means the control inputs will be decoupled. For example, when giving a roll-rate command, to initiate a turn, the FCL will try to maintain the pitch angle and therefore deflect the elevator automatically. In the ATT mode, yawing is not controlled by the pilot, but the rudder is automatically deflected to cancel sideslip. Finally, the throttle will behave as a speed selector in ATT mode. In this way also the speed control is decoupled from steering. For example, when pitching upwards the FCL will try to maintain speed and therefore automatically increases the engine throttle. Removing speed stability from the aircraft behavior could be dangerous, however. When a certain large pitch angle is maintained, the throttle setting will be at its maximum, but the aircraft still decelerates. To prevent the aircraft from stalling, Flight Envelope Protection (FEP) is added to the ATT FCL. When approaching stall speeds this system automatically pushes

the nose down until a constant velocity climb is achieved. FEP also protects against over speed, large pitch and roll angles, angle of attack limits and load factor limits.

F.2 Objectives

The main objectives of the SAFAR simulator flight trials are to familiarize the pilot with the changes in dynamic behavior of the aircraft and to determine the best parameters for the FCLs. To achieve the goals of this test campaign, several flights will be simulated in different scenarios. The objectives per flight are defined as follows,

- Flight 1: Determine the DRCT law stick gains
- Flight 2: Determine the ATT law stick gains
- Flight 3: Test the FEP system
- Flight 4: Compare DRCT law and ATT law by tracking a tunnel in the sky
- Flight 5: Evaluate the FEP system by intercepting a tunnel in the sky

F.3 Control Task

For each flight a flight card is available, containing step-by-step instructions to the pilot as shown in table F.1. These flight cards are available in the cockpit for your convenience. In the first flight, you will get familiarized how the aircraft reacts with the FBW platform and report whether flying the aircraft with the side-stick is too sensitive or too relaxed. In the second flight, the ATT law is engaged and you are asked whether the ATT law makes flying more easy. The third flight pushes the aircraft to its limits and the safety aspect of the ATT+FEP law will be demonstrated. In the fourth flight you are asked to follow the centerline of a tunnel-in-the-sky, as shown in Figure 7.15, as closely as possible. This can be done by keeping the flight path indicator (green symbol in Figure 7.15) in the center of the tunnel frame. Both DRCT law and ATT law will be flown in this way and the results are used for comparison. The fifth flight again focuses on FEP. The initial position of the aircraft in this flight is several miles outside the tunnel and you are asked to intercept the tunnel. Specific instructions will be given before each flight.

F.4 Apparatus

The SAFAR simulator trials will take place in the SIMONA Research Simulator (SRS) shown in Figure 7.13. This is a six-degrees-of-freedom hydraulic motion system,

that can provide the crew with realistic linear accelerations and rotation rates. During the experiment you will be seated in the right pilot seat in the SRS cockpit. The side-stick and throttle will be used to control the aircraft dynamics. The side-stick will be calibrated to have the same characteristics as the stick used in the SAFAR demonstrator aircraft. The synthetic vision display depicted in Figure 7.15 will be presented on the primary flight display directly in front of the right pilot seat. An outside visual system will be switched on, that has a wide field of view and projects the image at infinity to match visual conditions in the real aircraft. The secondary flight displays will be blank.

F.5 Procedure

The procedure for each flight is as follows:

- The experimenter applies the settings for the next flight.
- The experimenter starts the control task after a countdown of 3-2-1.
- The participant performs the control task indicated on the flight card.

In flights 1 and 2 the participant reports on the responses of the aircraft and the experimenter will update the FCLs, after which the procedure list is continued from 1. until satisfactory characteristics are achieved.

In flight 3 the participant will experience the effect of FEP. Flights 4 and 5 are divided into several runs. Each run ends automatically, 5 minutes after the start of the control task, after which the procedure list is continued from 1. until all runs are completed.

The participant fills out a questionnaire.

The experimenter and participant check the questionnaire.

Continue with the next flight.

The total duration of the experiment will be approximately 5 hours including breaks. Coffee and tea will be available during all breaks and a lunch will be provided. The table below shows the agenda for the flight trials.

F. PILOT INSTRUCTIONS FOR SIMULATOR TRIALS

Table F.1: Flight Card for Flight 1

PROJECT		SAFAR Simulator Trails	
TEST CARD NUMBER		1	
SUBJECT		DRCT law stick shaping	
REFERENCE		-	
EST. DURATION OF TEST POINT		10 min.	
HAZARD CATEGORY 1		ROUTINE / LOW / MEDIUM / HIGH	
INITIAL CONDITIONS			
ALT/FL	Follow scheme	ENGINE SETTINGS	As required
IAS	Follow scheme	FLAP SETTINGS	O/R
MACH	-	LANDING GEAR	O/R
MASS	-	OTHER	-
C.G.	-		
TEST PROCEDURE			REC. NRS
<p>Flight crew:</p> <ol style="list-style-type: none"> 1. Climb to level flight at 6,000 ft 2. Clean configuration: establish a speed of 120 kts IAS 3. Minor pull-up 200ft/min [20 seconds] 4. Minor push-down -200ft/min [20 seconds] 5. <i>Establish straight and level flight (120 kts IAS and 6,000 ft)</i> 6. Minor bank left 10 degrees [30 seconds] 7. Minor bank right 10 degrees [30 seconds] 8. <i>Establish straight and level flight (120 kts IAS and 6,000 ft)</i> 9. If all feels OK, continue, if not inform simulator operator 10. Pull-up 400ft/min [15 seconds] 11. Push-down 400ft/min [15 seconds] 12. <i>Establish straight and level flight (120 kts IAS and 6,000 ft)</i> 13. Bank left 25 degrees [30 seconds] 14. Bank right 25 degrees [30 seconds] 15. <i>Establish straight and level flight (120 kts IAS and 6,000 ft)</i> 16. If all feels OK, continue, if not inform simulator operator 17. Pull-up 1000ft/min [10 seconds] 18. Push-down 1000ft/min [10 seconds] 19. <i>Establish straight and level flight (120 kts IAS and 6,000 ft)</i> <p>NOTE: The goal is to tune the stick gains. The simulation should react similar to the real aircraft, although the forces on the side-stick are absent. After the trial you may give comments during a small interview.</p>			

BIBLIOGRAPHY

- [1] Jürgen Ackermann and Paul Blue. *Robust Control: The Parameter Space Approach*. Springer-Verlag London Limited, 2002.
- [2] Paul J. Acquatella B. Robust nonlinear spacecraft attitude control: an incremental backstepping approach. Master's thesis, Delft University of Technology, 2011.
- [3] AFM. *Airplane Flight Manual DA42*. Diamond Aircraft Industries GmbH, N. A. Otto-Strasse 5 A-2700 Wiener Neustadt, Austria, 3rd edition, October 2005.
- [4] Luis Antonio Aguirre. Controllability and observability of linear systems: Some noninvariant aspects. *IEEE Transactions on Education*, 78(1):33–39, February 1995.
- [5] David W. Allen. Statistics of atomic frequency standards. *Proceedings of the IEEE*, 54(2):221–230, February 1966.
- [6] F. Allgöwer and A. Zheng. *Nonlinear Model Predictive Control*. Birkhäuser Verlag, 2000. Pages 219 - 245.
- [7] Adolfo Anta, Rupak Majumdar, Indranil Saha, and Paulo Tabuada. Automatic verification of control system implementations. In *EMSOFT'10, October 24-29, 2010, Scottsdale, Arizona, USA*, 2010.
- [8] Z. Artstein. Stabilization with relaxed controls. *Nonlinear Analysis*, 7:1163–1173, 1983.
- [9] Barton J. Bacon, Aaron J. Ostroff, and Suresh M. Joshi. Reconfigurable ndi controller using inertial sensor failure detection & isolation. *IEEE Transactions on Aerospace and Electronic Systems*, 37(4):1373–1383, October 2001.
- [10] BEA. *Rapport de la commission d'enquête sur l'accident survenu le 20 janvier 1992 près du Mont Sainte-Odile (Bas Rhin) à l'Airbus A 320 immatriculé F-GGED exploité par la compagnie Air Inter*. Bureau d'Enquêtes et d'Analyses

pour la Sécurité de l'Aviation Civile, Building 153, Le Bourget Airport, Paris, April 14 2010. F-ED920120.

- [11] BEA. *Safety Investigation into the accident on 1 June 2009 to the Airbus A330-203, flight AF447*. Bureau d'Enquêtes et d'Analyses pour la Sécurité de l'Aviation Civile, Building 153, Le Bourget Airport, Paris, July 29 2011.
- [12] C. Bohn and D. P. Atherton. An analysis package comparing pid anti-windup strategies. *IEEE Control Systems*, 15(2):34–40, April 1995.
- [13] C. Borst, M. Mulder, M. M. Van Paassen, and J. A. Mulder. An Ecological Approach to Support Pilot Terrain Awareness After Total Engine Failure. *AIAA Journal of Aircraft*, 45(1):159–171, 2008.
- [14] Clark Borst. *Ecological Approach to Pilot Terrain Awareness*. PhD thesis, Delft University of Technology, Ridderkerk. ISBN/EAN:978-90-5335-196-3. Download: <http://repository.tudelft.nl/>, 2009.
- [15] Dominique Brière and Pascal Traverse. Airbus a320/a330/a340 electrical flight controls - a family of fault-tolerant systems. In *FTCS-23. Digest of Papers., The Twenty-Third International Symposium on Fault-Tolerant Computing*, pages pp. 616–623, 2002. ISBN 0818636807.
- [16] Peter Brooker. Sesar and nextgen: Investing in new paradigms. *The Journal of Navigation*, 61(2):195–208, 2008.
- [17] Kevin R. Bruce. Nasa b737 flight test results of the total energy control system. Technical report, Boeing Commercial Airplane Company, 1987. Report No. NASA CR-178285.
- [18] C. Canudas de Wit, H. Olsson, K. J. Åström, and P. Lischinsky. A new model for control of systems with friction. *IEEE Transactions on Automatic Control*, 40(3):419–425, March 1995.
- [19] CFR. *Code of Federal Regulations (CFR), Title 14, Parts 1 to 59*. US Government Printing Office, Superintendent of Documents, Mail Stop SSOP, Washington DC, 1 January 1992. (NOTE: FAR 35 and FAR 25 are components of CFR, Title 14).
- [20] Alan Chao and Michael Athans. Stability robustness to unstructured uncertainty for linear time invariant systems. In William S. Levine, editor, *The Control Systems Handbook, Second Edition*, pages 9–1 – 9–31. CRC Press, 2010.

-
- [21] T. F. Coleman and Y. Li. On the convergence of reflective newton methods for large-scale nonlinear minimization subject to bounds. *Mathematical Programming*, 67(2):189–224, 1994.
- [22] T. F. Coleman and Y. Li. An interior, trust region approach for nonlinear minimization subject to bounds. *SIAM Journal on Optimization*, 6:418–445, 1996.
- [23] R. P. G. Collinson. *Introduction to Avionics Systems*. Springer Dordrecht Heidelberg London New York, 3rd edition, 2011. ISBN 9789400707078, Paragraph 4.3.2.
- [24] Coen C. de Visser. *Global Nonlinear Model Identification with Multivariate Splines*. PhD thesis, Delft University of Technology, 2011. ISBN: 9789085707707.
- [25] C. A. Desoer and M. Vidyasagar. *Feedback Systems: Input-Output Properties*. New York: Academic, 1975.
- [26] Richard C. Dorf and Robert H. Bishop. *Modern Control Theory*. Prentice Hall, Upper Saddle River, New Jersey 07458, 12th edition, 2011.
- [27] Christopher Edwards, Thomas Lombaerts, and Hafid Smaili. *Fault Tolerant Flight Control: A Benchmark Challenge*. Springer-Verlag Berlin Heidelberg, 2010. ISBN 9783642116896, Page 15.
- [28] George Ellis. *Control System Design Guide*. Elsevier Academic Press, 525 B Street, Suite 1900, San Diego, California 92101-4495, USA, 2004. Chapter 16.
- [29] Kenneth Eriksson, Donald Estep, and Claes Johnson. *Applied Mathematics: Body and Soul*, volume 1. Springer, 2004. ISBN 978-3-540-00890-3, Chapter 12.
- [30] Bernard Etkin. Turbulent wind and its effect on flight. *Journal of Aircraft*, 18(5):327–345, May 1981.
- [31] EUROCAE. *Software Considerations in Airborne Systems and Equipment Certification, ED-12B*. EUROCAE, 1992.
- [32] L. P. Faleiro and A. A. Lambregts. Analysis and tuning of a 'total energy control system' control law using eigenstructure assignment. *Aerospace Science and Technology*, 3(3):127–140, 1999.
- [33] W. Falkena, C. Borst, Q. P. Chu, and J. A. Mulder. Investigation of practical flight envelope protection systems for small aircraft. *Journal of Guidance, Control, and Dynamics*, 34(4):976–988, July-August 2011.

- [34] W. Falkena, C. Borst, and J.A. Mulder. Investigation of practical flight envelope protection systems for small aircraft. In *AIAA Guidance, Navigation, and Control Conference, 2 - 5 August 2010, Toronto, Ontario Canada*, 2010.
- [35] W. Falkena, C. Borst, E. R. van Oort, and Q. P. Chu. Sensor-based backstepping. *Journal of Guidance, Control, and Dynamics*, Accepted for Publication.
- [36] W. Falkena, E. R. van Oort, , and Q. P. Chu. Towards certifiable advanced flight control systems, a sensor based backstepping approach. In *AIAA Guidance, Navigation, and Control Conference, 08 - 11 August 2011, Portland, Oregon*, 2011.
- [37] C. Favre. Fly-by-wire for commercial aircraft: the airbus experience. *International Journal of Control*, 59(1):139–157, March 2007.
- [38] GAMA. Statistical databook & industry outlook. General Aviation Manufacturers Association, 2009.
- [39] Patrick Goudou. *Certification Specifications for Large Aeroplanes: CS-25*. European Aviation Safety Agency, 2003.
- [40] Patrick Goudou. *Certification Specifications for Normal, Utility, Aerobatic, and Commuter Category Aeroplanes: CS-23*. European Aviation Safety Agency, 2003.
- [41] Patrick Goudou. *Executive Director Decision 2003/14/RM*. European Aviation Safety Agency, November 2003.
- [42] Patrick Goudou. *General Acceptable Means of Compliance for Airworthiness of Products, Parts and Appliances: AMC-20*. European Aviation Safety Agency, 2003.
- [43] Keqin Gu, Vladimir L Kharitonov, and Jie Chen. *Stability of Time-Delay Systems*. Birkhauser Boston, 1st edition, June 2003.
- [44] Jack K. Hale. *Theory of Functional Differential Equations*. Springer Verlag New York Inc., 1977.
- [45] Don Harris, editor. *Human Factors for Civil Flight Deck Design*. Ashgate Publishing Ltd, 2004. Chapter 8 by Sidney Dekker.
- [46] John Hauser, Shankar Sastry, and George Meyer. Nonlinear control design for slightly nonminimum phase systems: Application to v/stol aircraft. *Automatica*, 28(4):665–679, 1992.

-
- [47] M. Henson. Nonlinear model predictive control: Current status and future directions. *Computers and Chemical Engineering*, 23(2):187–202, 1998.
- [48] C. N. Hewitt and A. V. Jackson. *Handbook of Atmospheric Science: Principles and Applications*. Blackwell Science Ltd, 2003.
- [49] Nicholas J. Higham. *Accuracy and Stability of Numerical Algorithms*. SIAM, 2nd edition, 2002. ISBN: 0898715210, Chapter 18.2.
- [50] D. E. Hoak and E. E. Ellison. United states air force stability and control dat-com (and subsequent revisions). Technical report, United States Air Force, 1965.
- [51] John Hodgkinson. A history of low order equivalent systems for aircraft handling qualities analysis and design. In *AIAA Atmospheric Flight Mechanics Conference and Exhibit, 11-14 August 2003, Austin, Texas, 2003*.
- [52] Naira Hovakimyan, Eugene Lavretsky, and Amol Sasane. Dynamic inversion for nonaffine-in-control systems via time-scale separation part i. *Journal of Dynamical and Control Systems*, 13(4):451–465, October 2007.
- [53] iMAR, Im Reihersbruch 3, D-66386 St. Ingbert / Germany. *iIMU-MM-02-C datasheet*, 2009. Version 1.21.
- [54] A. Isidori. *Nonlinear Control Systems*. Springer-Verlag London Limited, 1995. Chapter 4.
- [55] Stephen A. Jacklin. Closing the certification gaps in adaptive flight control software. In *AIAA Guidance, Navigation, and Control Conference, Honolulu, Hawaii, Aug 18-21, 2008, 2008*.
- [56] JAR-VLA. *Joint Aviation Requirements, JAR-VLA Very Light Aeroplanes*. Civil Aviation Authority, Printing and Publication Services, Greville House 37 Gratton Road, Cheltenham, Glos. GL50 2BN, United Kingdom, 1 January 1992.
- [57] Eric N. Johnson and Anthony J. Calise. Pseudo-control hedging: A new method for adaptive control. In *Advances in Navigation Guidance and Control Technology Workshop*, November 2000.
- [58] James Justus. Ecological and lyapunov stability. *Philosophy of Science*, 75(4):421–436, October 2008.
- [59] R. E. Kalman. Contributions to the theory of optimal control. *Boletin de la Sociedad Matematica Mexicana*, 5:102–119, 1960.

- [60] Hassan K. Khalil. *Nonlinear Systems*. Prentice Hall, 3rd edition, 2002. Chapter 11 and Section 14.3.
- [61] Petar V. Kokotović. The joy of feedback: Nonlinear and adaptive: 1991 bode prize lecture. *IEEE Control Systems Magazine*, 12(3):7–17, June 1992.
- [62] Johann Koschorke. Advanced flight control design and evaluation: An application of time delayed incremental backstepping. Master's thesis, Delft University of Technology, 2012.
- [63] N. N. Krasovskii. *Stability and Motion: Applications of Lyapunov's Second Method to Differential Systems and Equations with Delay*. Stanford University Press, 1963. Translated by J. L. Brenner.
- [64] Miroslav Krstić, Ioannis Kanellakopoulos, and Petar V. Kokotović. *Nonlinear and Adaptive Control Design*. John Wiley & Sons, Inc. New York, NY, USA, 1995. Section 2.2.
- [65] Martin Laban. *On-Line Aircraft Aerodynamic Model Identification*. PhD thesis, Delft University of Technology, 1994.
- [66] A. A. Lambregts. Vertical flight path and speed control autopilot design using total energy principles. In *Guidance and Control Conference, Gatlinburg, TN, August 15-17, 1983*, 1983.
- [67] Isabelle Laplace, Clelia Chertier, Alfred Baron, and Maciej Maczka. D2.1 potential transfer of passenger demand to personal aviation by 2020. Technical report, EPATS, ASA6-CT-2006-044549, 2007.
- [68] William S. Levine, editor. *Control System Fundamentals*. CRC Press, 2011. Chapter 9.
- [69] B. L. Lewis and F. L. Stevens. *Aircraft Control and Simulation*. John Wiley and Sons, 1992. pp. 83-88.
- [70] R. M. Lewis and V. Torozon. Pattern search algorithms for bound constrained minimization. *SIAM Journal on Optimization*, 9(4):1082–1099, 1999.
- [71] T. J. J. Lombaerts, H. O. Huisman, Q. P. Chu, J. A. Mulder, and D. A. Joosten. Nonlinear reconfiguring flight control based on on-line physical model identification. *AIAA Journal of Guidance, Control and Dynamics*, 32(3):727–748, May–June 2009 2009.

-
- [72] A. M. Lyapunov. *General Problem of the Stability Of Motion*. Taylor & Francis in London, Washington, DC, 1st edition, 1992. Translated and edited by A.T. Fuller.
- [73] J. M. Maciejowski. *Predictive Control with Constraints*. Prentice Hall, 2002. Chapters 1, 2 and 3.
- [74] J. F. Magni, S. Bennani, and J. Terlouw. *Robust Flight Control: A Design Challenge*. Lecture Notes in Control and Information Sciences. Springer, 1997.
- [75] The Mathworks, The MathWorks, Inc., 3 Apple Hill Drive, Natick, MA 01760-2098. *Real-Time Workshop Embedded Coder: User's Guide Version 3*, 2002.
- [76] The Mathworks, The MathWorks, Inc., 3 Apple Hill Drive, Natick, MA 01760-2098. *Simulink Control Design User's Guide*, 2011.
- [77] L. K. Mestha and C. W. Planner. Application of system identification techniques to an rf cavity tuning loop. Technical report, RAL-89-101, 1989.
- [78] Wim Michiels and Silviu-Iulian Niculescu. *Stability and Stabilization of Time-Delay Systems*. Society for Industrial and Applied Mathematics, 2007.
- [79] MilSpec. *MIL-F-8785C, Military Specification: Flying Qualities of Piloted Airplanes*. U.S. Military, Airforce Flight Dynamics Laboratory, WPAFB, Dayton, Ohio, 05 November 1980. Section 3.7.
- [80] MilSpec. *MIL-STD-1797A, Flying Qualities of Piloted Airplanes*. U.S. Military, Airforce Flight Dynamics Laboratory, WPAFB, Dayton, Ohio, 30 January 1990. Section 3.7.
- [81] Anusha Mujumdar and Radhakant Padhi. Nonlinear geometric and differential geometric guidance of uavs for reactive collision avoidance. Technical report, Department of Aerospace Engineering Indian Institute of Science Bangalore, India., 2009.
- [82] J. A. Mulder, Q. P. Chu, J. K. Sirdar, J. H. Breeman, and M. Laban. Non-linear aircraft flight path reconstruction review and new advances. *Progress in Aerospace Sciences*, 35:673–726, 1999.
- [83] J. A. Mulder, W. van Staveren, J. C. van der Vaart, and E. de Weerd. Flight dynamics, lecture notes ae3-302. Technical report, Delft University of Technology, 2006.

- [84] M. Mulder and J. A. Mulder. Cybernetic analysis of perspective flight-path display dimensions. *AIAA Journal of Guidance, Control, and Dynamics*, 28(3):398–411, May-June 2005.
- [85] M. Mulder, A. R. Veldhuijzen, M. M. van Paassen, and J. A. Mulder. Integrating fly-by-wire controls with perspective flight-path displays. *AIAA Journal of Guidance, Control and Dynamics*, 28(6):1263–1274, November-December 2005.
- [86] Max Mulder and J. A. Mulder. *AE4-304 Aircraft Response to Atmospheric Turbulance*. Delft University of Technology, 2005.
- [87] NATO. Flight control design - best practices. Technical report, The Research and Technology Organization (RTO) of NATO, December 2000. (RTO TR-029).
- [88] Nhan T. Nguyen, Abraham K. Ishihara, Kalmanje S. Krishnakumar, and Maryam Bakhtiari-Nejad. Bounded linear stability analysis - a time delay margin estimation approach for adaptive control. In *AIAA Guidance, Navigation, and Control Conference, 10 - 13 August 2009, Chicago, Illinois*, 2009.
- [89] NTSB. *Aircraft Accident Report China Airlines Boeing 747-SP (NTSB/AAR-86/03)*. National Transportation Safety Board Bureau of Accident Investigation, 490 L'Enfant Plaza, S.W. Washington, D.C. 20594, 1985.
- [90] NTSB. *Annual Review of Aircraft Accident Data U.S. General Aviation, Calendar Year 2005*. National Transportation Safety Board Bureau of Accident Investigation, 490 L'Enfant Plaza, S.W. Washington, D.C. 20594, May 26 2009.
- [91] NTSB. *Review of U.S. Civil Aviation Accidents, Review of Aircraft Accident Data 2007-2009*. National Transportation Safety Board Bureau of Accident Investigation, 490 L'Enfant Plaza, S.W. Washington, D.C. 20594, March 31 2011. NTSB/ARA-11/01, PB2011-113050.
- [92] Katsuhiko Ogata. *Modern Control Engineering*. Prentice Hall, Upper Saddle River, New Jersey 07458, 3rd edition, 1997.
- [93] open source community. *FlightGear*: <http://www.flightgear.org/>.
- [94] H. B. Pacejka. *Tire and Vehicle Dynamics*. Society of Automotive Engineers, Warrendale, PA, October 2002.
- [95] Roger Pratt. *Flight Control Systems: Practical Issues in Design and Implementation*. Institution of Electrical Engineers, 2000. Page 173.

-
- [96] S. Joe Qin and Thomas A. Badgwell. A survey of industrial model predictive control technology. *Control Engineering Practice*, 11:733–764, 2003.
- [97] L. R. Rabiner, R. W. Schafer, and C. M. Rader. The chirp z-transform algorithm. *IEEE Transactions on Audio and Electroacoustics*, 17(2):86–92, June 1969.
- [98] R. Reichel, S. Görke, F. Cake, S. Polenz, and R. Riebeling. Flexible avionics platform. In *Proceedings of the 61. Deutscher Luft- und Raumfahrtkongress 2012, 10.-12. Sept. 2012, Estrel Berlin*, 2012.
- [99] J. Reiner, G. J. Balas, and W. L. Garrard. Flight control design using robust dynamic inversion and time-scale separation. *Automatica*, 32(11):1493–1504, 1996.
- [100] Michal Reinštein. *Use of Adaptive Filtering Methods in Inertial Navigation Systems*. PhD thesis, Czech Technical University in Prague, Faculty of Electrical Engineering, Department of Measurement, 2010.
- [101] Danlel E. Rivera, Manfred Morarl, and Slgurd Skogestad. Internal model control: Pid controller design. *Ind. Eng. Chem. Process Des. Dev.*, 25(1):252–26, January 1986.
- [102] Jan Roskam. *Airplane Flight Dynamics and Automatic Flight Controls - Part I*. Design, Analysis and Research Corporation, 120 East Ninth Street, Suite 2, 2001.
- [103] Jan Roskam. *Airplane Flight Dynamics and Automatic Flight Controls - Part II*. Design, Analysis and Research Corporation, 120 East Ninth Street, Suite 2, 2001.
- [104] Clarence W. Rowley and Belinda A. Batten. Dynamic and closed-loop control. In R. D. Joslin and D. N. Miller, editors, *Fundamentals and Applications of Modern Flow Control*, volume 231, chapter 5. AIAA Progress in Astronautics and Aeronautics, 2009.
- [105] Prateep Roy. Studies on the convergence of information theory and control theory. *Informatics in Control Automation and Robotics - Lecture Notes in Electrical Engineering*, 85:285–299, 2011.
- [106] RTCA. *Software Considerations in Airborne Systems and Equipment Certification, DO-178B*. Radio Technical Commission for Aeronautics Inc., 1994.
- [107] SAFAR. *Small Aircraft Future Avionics Architecture*. European Union, ACP7-CT-2007-0213374, <http://www.fp7-safar.de>.

- [108] M. Schroeder. Synthesis of low-peak-factor signals and binary sequences with low autocorrelation. *IEEE Transactions on Information Theory*, 16(1):85–89, January 1970.
- [109] R. Sepulchre, M. Jankovic, and P. Kokotovic. *Constructive Nonlinear Control*. Springer, 1996. ISBN: 3540761276.
- [110] S. Sieberling, Q. P. Chu, and J. A. Mulder. Robust flight control using incremental nonlinear dynamic inversion and angular acceleration prediction. *AIAA Journal of Guidance, Control, and Dynamics*, 33(6):1732–1742, November 2010.
- [111] Simtec. *Icasim Smart Air Data Boom*. Simtec Buergel AG, Im Soerlibrunnen 15, CH-4106 Therwil, www.simtec.ch. Version 5.
- [112] Jean-Jacques E. Slotine and Weiping Li. *Applied Nonlinear Control*. Prentice Hall, 1991. Chapter 6.
- [113] L. Sonneveldt, Q. P. Chu, and J. A. Mulder. Nonlinear flight control design using constrained adaptive backstepping. *AIAA Journal of Guidance, Control, and Dynamics*, 30(2):322–336, March-April 2007.
- [114] E. D. Sontag. A universal construction of artstein’s theorem on nonlinear stabilization. *Systems & Control Letters*, 13:117–123, 1989.
- [115] Cary R. Spitzer, editor. *The Avionics Handbook*. CRC Press, 2001. ISBN 084938348, Chapters 11 and 27.
- [116] Willem Hendrik Jan Joseph van Staveren. *Analyses of aircraft responses to atmospheric turbulence*. PhD thesis, Delft University of Technology, 2003. ISBN: 90-407-2453-9.
- [117] Vahram Stepanyan, Kalmanje Krishnakumar, Nhan Nguyen, and Laurens Van Eykeren. Stability and performance metrics for adaptive flight control. In *AIAA Guidance, Navigation, and Control Conference, 10 - 13 August 2009, Chicago, Illinois, 2009*.
- [118] Dr. Walter Stockwell. *Bias Stability Measurement: Allan Variance*. Crossbow Technology, Inc., <http://www.xbow.com>.
- [119] Karl J. Åström and Richard M. Murray. *Feedback Systems: An Introduction for Scientists and Engineers*. Princeton University Press, Princeton, NJ, 2008. Chapter 9.

-
- [120] Karl Johan Åström. *Introduction to Stochastic Control Theory*. Elsevier, 1970. Chapter 6.
- [121] Olaf Stroosma, M. M. van Paassen, and Max Mulder. Using the SIMONA Research Simulator for human-machine interaction research. In *Proceedings of the AIAA Modeling and Simulation Technologies Conference and Exhibit, Austin, Texas, Aug. 11-14, 2003*, pages 1–8, August 2003.
- [122] Liang Tang, Michael Roemer, Jianhua Ge, Agamemnon Crassidis, J. V. R. Prasad, and Christine Belcastro. Methodologies for adaptive flight envelope estimation and protection. In *AIAA Guidance, Navigation, and Control Conference and Exhibit*, 2009.
- [123] Justin Teo, Jonathan P. How, and Eugene Lavretsky. Proportional-integral controllers for minimum-phase nonaffine-in-control systems. *IEEE Transactions on Automatic Control*, 55(6):1477–1482, 2010.
- [124] A. N. Tikhonov. Systems of differential equations containing small parameters in the derivatives. *Mathematical Sb. (N.S.)*, 31(73)(3):575–586, 1952. (in Russian).
- [125] Pascal Traverse, Isabelle Lacaze, and Jean Souyris. Airbus fly-by-wire: A total approach to dependability. *IFIP International Federation for Information Processing*, 156:191–212, 2004.
- [126] Suraj Unnikrishnan. *Adaptive Envelope Protection Methods for Aircraft*. PhD thesis, School of Aerospace Engineering, Georgia Institute of Technology, August 2006.
- [127] Stijn B. J. Van Dam, Max Mulder, and M. M. Van Paassen. Ecological Interface Design of a Tactical Airborne Separation Assistance Tool. *IEEE transactions on Systems, Man, and Cybernetics part A*, 38:1221–1233, 2008.
- [128] C. A. A. M. van der Linden. *DASMAT - Delft University Aircraft Simulation Model and Analysis Tool*. Delft University Press, Delft, The Netherlands, 1998.
- [129] E. van Kampen. *Global Optimization using Interval Analysis*. PhD thesis, Delft University of Technology, 2010. ISBN: 9789085705871.
- [130] Eduard van Oort, Q. P. Chu, and J. A. Mulder. Robust model predictive control of a feedback linearized f-16/matv aircraft model. In *AIAA Guidance, Navigation, and Control Conference and Exhibit*, 2006.

- [131] Michel Verhaegen and Vincent Verdult. *Filtering and System Identification: A Least Squares Approach*. Cambridge University Press, 2007.
- [132] J. H. Wall and D. M. Bevely. Characterization of inertial sensor measurements for navigation performance analysis. In *Proceedings of the 19th International Technical Meeting of the Satellite Division of The Institute of Navigation (ION GNSS 2006)*, pages 2678 – 2685. Fort Worth, TX, September 2006.
- [133] Douglas A. Wiegmann, Scott A. Shappell, Albert Boquet, Cristy Detwiler, Kali Holcomb, and Troy Faaborg. Human error and general aviation accidents: A comprehensive, fine-grained analysis using hfacs. Technical report, Aviation Human Factors Division Institute of Aviation, 1 Airport Road Savoy, Illinois 61874, May 2005.
- [134] W. Yu, D. I. Wilson, and B. R. Young. Control performance assessment for nonlinear systems. *Journal of Process Control*, 20:1235–1242, 2010.
- [135] Peter M. T. Zaal. *Pilot Control Behavior Discrepancies Between Real and Simulated Flight Caused by Limited Motion Stimuli*. PhD thesis, Delft University of Technology, 2011. ISBN: 9789085704706.
- [136] Paul Zarchan and Howard Musoff. *Fundamentals of Kalman filtering: a practical approach*. American Institute of Aeronautics and Astronautics, 2nd revised edition edition, March 2005.
- [137] N. M. Zoumakis. The dependence of the power-law exponent on surface roughness and stability in a neutrally and stably stratified surface boundary layer. *Atmosfera*, 6:pp. 79–83, 1993.

SAMENVATTING

Onderzoek naar Praktische Besturingssystemen voor Kleine Vliegtuigen

Wouter Falkena

In het toekomstige luchtruim wordt een groei verwacht in het aantal vluchten van kleine vliegtuigen volgens het Amerikaanse Small Aircraft Transportation System (SATS) en het European Personal Air Transportation System (EPATS) programma. De belangrijkste reden voor deze groei is een toenemende vraag van mensen om naar meer plaatsen in minder tijd te kunnen reizen. Daarnaast zal, vanwege de introductie van verbeterde en kosten-efficiënte technologieën, de luchtvaart zelfs een aantrekkelijk alternatief voor vervoer over de weg worden. In het algemene luchtvaart segment zijn dodelijke en niet-dodelijke ongevallen echter niet zeldzaam. Op dit moment domineert een gemiddeld aantal van zeven ongevallen per 100.000 vliegreuren dit segment. Omdat de algemene luchtvaart naar verwachting sterk zal groeien in de komende jaren, moeten maatregelen worden genomen om deze groei in een veilige baan te leiden.

Door nauwkeurig te kijken naar ongeval analyses, kunnen veel voorkomende oorzaken worden herleid tot fouten in de besturing van het vliegtuig (72 %) en fouten in de besluitvorming van de piloot (36 %). Het gelijktijdig uitvoeren van taken, zoals het besturen van het vliegtuig, navigatie, planning en communicatie, is vooral voor minder ervaren piloten tamelijk moeilijk. Qua vliegtuigbesturing, kan het verkeerd inschatten van de koppeling in het vlieggedrag, zoals het stampen en gieren van het vliegtuig bij het inzetten van een bocht, en de effecten van externe verstoringen, piloten naar onveilige gebieden in het vluchtregime leiden. En qua de besluitvorming kan dubbelzinnige en tegenstrijdige informatie van de boordsystemen resulteren in het slechte “bewustzijn van de situatie” van de piloot en in slechte besluitvorming.

Om deze situaties te voorkomen kunnen technieken voor het verbeteren van de vliegtuigbesturing worden gebruikt, om eenvoudige en veilige vliegeigenschappen te creëren. Daarnaast kunnen nieuwe manieren van het gebruik en presenteren van informatie op de vluchtmonitoren worden onderzocht om het “situatie bewustzijn” en de besluitvorming te verbeteren. Dit proefschrift houdt zich echter alleen bezig met het verbeteren van de vliegveiligheid en het versimpelen van de vliegtuigbesturing.

De commerciële luchtvaart heeft een lange geschiedenis in het gebruik van regelsystemen om het ideale vliegtuiggedrag vorm te geven. Om de veiligheid te verhogen worden moderne commerciële vliegtuigen, zoals een Boeing 777 en een Airbus A380, ook uitgerust met een vluchtregimebeschermings systeem (FEP). Deze beschermt tegen overtrekken, een te hoge snelheid, invalshoeklimieten en belastinglimieten. Dit heeft het aantal ongevallen, door fouten in besturing van het vliegtuig, sterk verminderd in de commerciële luchtvaart sector. Toch is schaalverkleining van deze geavanceerde Fly-By-Wire (FBW) platformen naar vliegtuigen in de algemene luchtvaart sector geen optie omdat dit de kostprijs van een dergelijk vliegtuig aanzienlijk zou verhogen. In het “Small Aircraft Future Avionics Architecture” (SA-FAR) programma, een lopend Europees project, zal een betaalbaar FBW platform worden ontwikkeld voor kleine vliegtuigen met behulp van een “Flexible Avionics Platform Approach”. Deze aanpak leidt tot potentiële kostenbesparingen, maar introduceert ook een unieke omgeving voor de gebruikte regelsystemen. In deze omgeving zijn FCL ontwerpen nodig die robuust zijn tegen model onzekerheden, sensor afwijkingen, sensor ruis en tijdvertraging, terwijl ze snel en nauwkeurig genoeg zijn om de relatief wendbare dynamische eigenschappen van een klein vliegtuig te kunnen accommoderen. Ook moeten deze FCL ontwerpen in de nabije toekomst bruikbaar zijn om de groei in de algemene luchtvaart te kunnen ondersteunen. FCL ontwerpen welke aan deze eisen voldoen worden in dit proefschrift betiteld als praktische FCL ontwerpen. Om de kosteneffectiviteit van deze ontwerpen te vergroten, is het van belang dat de FCLs makkelijk overdraagbaar zijn naar andere kleine vliegtuigen, idealiter zonder enige aanpassing.

Met het gebruik van FEP kan vliegen veiliger worden gemaakt. Dit systeem maakt vliegen echter niet gemakkelijker. Rate-Command/Attitude-Hold ontkoppelt de besturing, hetgeen een vereenvoudiging van het vliegen bewerkstelligt. Daarnaast verwerpt het systeem turbulentie en is een bewezen concept, gebruikt bij lage snelheden in de Airbus A320/330 en 340. Daarom is deze handmatige besturingsmodus geselecteerd als één van de modi waarvoor FCL ontwerpen in dit proefschrift worden gecreëerd. Een tweede, geautomatiseerd 4D traject-volgend modus (NAV modus) wordt in dit proefschrift ook gebruikt voor FCL ontwerpen. De nadruk zal

echter op de handmatige modus liggen, omdat een FCL met eenvoudige bediening als van essentieel belang wordt gezien in het geval van een noodsituatie en voor het plezier van het vliegen zelf.

Op basis van een dynamisch model van een Diamond DA 42 en met een beschrijving van de dynamische eigenschappen van het FBW platform, zijn twee verschillende FCL ontwerpen voor beide modi gesynthetiseerd en geanalyseerd in dit proefschrift. Het eerste ontwerp maakt gebruik van klassieke regeltheorie, of nauwkeuriger, lus vorming met de nadruk op volgpresetaties, verstoring verwerping en ruisonderdrukking. Selectie van de versterkingsfactoren van de FCL werd gedaan met behulp van de combinatie van een ruw patroon zoekmethode en een “Trust-Region-Reflective” methode. Het tweede FCL ontwerp maakt gebruik van een nieuw ontwikkelde niet-lineaire ontwerpmethod, gebaseerd op backstepping, singuliere verstoringstheorie en geschatte dynamische omkering. Deze methode, genaamd Sensor-Based Backstepping (SBB), maakt geen gebruik van informatie van het dynamische model, maar baseert zich uitsluitend op metingen. Beide FCL ontwerpen zijn vergeleken op gevoeligheid voor parametrische onzekerheid, sensor ruis, verstoringen, vertragingen, vliegeigenschappen (HQ), prestatie-indicatoren voor de geautomatiseerde FCLs, de ontwerp inspanning, certificeerbaarheid en de mogelijkheid tot het toevoegen van FEP.

De invloed van parametrische onzekerheden werd getest door beide FCL ontwerpen, zonder aanpassing van de versterkingsfactoren, toe te passen op het vliegtuig model van een volledig ander vliegtuig, een Cessna Citation II. De prestaties van de klassieke regelaar in dit scenario zijn niet slecht, maar de responsie toont wel oscillaties. De prestaties van de SBB-regelaar blijven uitstekend en dit ontwerp kan dus worden gezien als een eerste stap richting een plug-and-play FCL. Ruis onderdrukking en verstoring verwerping werden specifiek meegenomen tijdens het ontwerpen van de klassieke regelaar. Het is dan ook geen verrassing dat de klassieke FCL iets beter presteert dan de SBB-regelaar in dit opzicht. In aanwezigheid van tijdsvertragingen welke in het slechtste geval kunnen optreden in de FBW platform componenten, lijden beide FCL ontwerpen in prestaties, maar opnieuw afstemmen van de SBB-regelaar is veel gemakkelijker. HQs bleken bevredigend voor beide ontwerpen, maar verschillen in de demping van de korte periode en aperiodische roll. Het klassieke ontwerp is afgestemd op snelheid en is onder-gedempt en het SBB ontwerp is van nature over-gedempt. De prestaties van de NAV modus zijn zeer vergelijkbaar voor beide FCL ontwerpen en zijn dus niet nuttig voor de keuze in FCL ontwerpmethod. Ontwerp inspanning op het gebied van afstemming van de versterkingsfactoren is gemakkelijker voor het SBB ontwerp in vergelijking met het PID ontwerp en vice versa voor de certificatie inspanning.

In het kader van dit proefschrift, is SBB gekozen als gewenste FCL ontwerp. Deze methode levert goede vliegeigenschappen op zolang het systeem minimale fase heeft, bestuurbaar is en voldoende gescheiden is in tijdsschaal. Verder onderzoek is nodig voor een meer wetenschappelijke manier van het selecteren van de versterkingsfactoren. Piloot-in-de-lus simulaties moeten aantonen of een minder ervaren algemene luchtvaart piloot de veranderingen in het dynamisch gedrag veroorzaakt door het installeren van een FBW platform met FCLs waardeert en accepteert.

ACKNOWLEDGEMENTS

This thesis is the result of four years of research within the Aerospace Software and Technology Institute (ASTI) at the Delft University of Technology. Finishing this research project would not have been possible without the support of many people. I am very grateful to all of these people, but I would like to mention some of them in particular.

Above all I would like to thank my wife Ester for loving and supporting me. Without her I would not be the person that I am today. Equally much I would like to thank my parents, Sjoerd and Anke for believing in me, for supporting me and for pushing me to study harder when needed. Without them my path in life would be fully different. I would like to thank my brother, Rogier, for being an example in life.

After my M.Sc. graduation my promotor Prof. Bob Mulder provided me the opportunity to work as a researcher in an European project. While working on this project he also convinced me to pursue a Ph.D. degree. For both these pushes in the right direction I am truly grateful. I would also like to express my gratitude to my co-promotor Dr. Ping Chu, who has contributed much to the academic quality of this thesis.

Of course I would like to thank Dr. Clark Borst, not only for being my daily supervisor, as whom he kept a close eye on the structure of the text, but also for being my co-worker in the SAFAR project. I will always remember the trips and the fun, especially at the end of the day.

I also want to express my gratitude to my other daily supervisors, Dr. Erik-Jan van Kampen and Dr. Coen de Visser. Your comments have been of much help to improve the thesis.

The exploratory acceptance study in the evaluation part of the work would not have been possible without the SIMONA support team. I would therefore like to say, thank you Ir. Olaf Stroosma.

ACKNOWLEDGEMENTS

ASTI has been a very pleasant and productive working environment and I would like to thank Walter Berkouwer, Meine Oosten and Vera van Bracht for their administrative support, for the memorable dinners and for the interesting coffee breaks.

My thanks also goes to my roommates, Jan, Laurens, Deniz, Rolf, Liguó, Jia and Yazdi. In particular I would like to thank Deniz for the “candy” from Turkey and I would like to say to Jan, we will finish that roller coaster some day!

Ir. Paul Acquatella and Ir. Johann (Raphael) Koschorke, it has truly been a pleasure working with you on your M.Sc. graduation projects. The discussions we had were also very helpful for me and your abilities to grasp this many new and difficult subjects in such short amount of time still amazes me.

Last, but certainly not least, I would like to thank my volleyball teammates, and close friends, Tobie and Bastiaan van den Berg for helping me loose stress both on and off the court. And I would like to thank the VvLR for keeping aerospace engineering interesting all those past years.

Wouter Falkena

Delft, November 2012

CURRICULUM VITAE

Wouter Falkena was born on February 17, 1983 in Leek, the Netherlands. He attended the primary school De Tweesprong in Leek from 1987 to 1995 and the high school De Waezenburg in Leek from 1995 to 2001 to obtain his Atheneum certificate.

He enrolled at the Faculty of Aerospace Engineering at the Delft University of Technology in 2001. In 2005 he participated in the design synthesis exercise, which is a team assignment of 10 weeks. The study object of this assignment was the Superbus and Wouter's part consisted of the guidance and navigation of this vehicle, using radar, GPS and IMUs. He obtained his M.Sc. degree in Aerospace Engineering at the Control and Simulation Division in 2008 with a study into an auto-drive system for the Superbus. During this study he created a vehicle model as well as a model-based control system.

In 2008 he started as a researcher at the Delft University of Technology within the Aerospace Software and Technologies Institute (ASTI). His research was part of the Small Aircraft Future Avionics architecture (SAFAR) program, a seventh framework European project with the goal to create an affordable fly-by-wire platform for small general aviation aircraft. Wouter's part in this program consisted of the development of an aircraft model and the design of the flight control laws for a Diamond DA 42. Both of these items are also included in this thesis. In 2010 he continued the research with more academic flight control laws and in 2012 the SAFAR program finished with several test flights of the DA 42 with the SAFAR platform on-board.

